N°d'ordre NNT : 2019LYSEI033

THESE de DOCTORAT DE L'UNIVERSITE DE LYON
opérée au sein de
l'Institut National des Sciences Appliquées de Lyon

Ecole Doctorale MEGA ED162
Mécanique, Energétique, Génie Civil, Acoustique

Spécialité/discipline de doctorat :
Génie Mécanique

Soutenue publiquement le 06/06/2019, par :
MAQUART Tristan

TRIVARIATE MODELS GENERATION FROM UNSTRUCTURED SURFACE MANIFOLDS FOR ISOGEOMETRIC ANALYSIS - APPLICATION TO REDUCED ORDER MODELING WITH GEOMETRIC PARAMETERS

Devant le jury composé de :

LEGRAIN, Grégory	Maître de conférences HDR, École Centrale de Nantes	Rapporteur
RASSINEUX, Alain	Professeur, UTC Compiègne	Rapporteur
BARANGER, Thouraya	Professeur, UCBL	Examinatrice
NERON, David	Professeur, ENS Paris-Saclay	Examinateur et président
REMACLE, Jean-François	Professeur, Université Catholique de Louvain	Examinateur
ELGUEDJ, Thomas	Professeur, INSA de Lyon	Directeur de thèse
GRAVOUIL, Anthony	Professeur, INSA de Lyon	Invité et co-directeur de thèse
ROCHETTE, Michel	Docteur, ANSYS France	Invité et co-encadrant de thèse

Mathematics is the art of giving the same name to different things.
Henri Poincaré
If a machine is expected to be infallible, it cannot also be intelligent.
Alan Turing
Every surface homeomorphic to a sphere must have at least one singularity: every horse must have at least one mane.
Poincaré-Hopf theorem corollary

Remerciements

Sacrée aventure menée jusqu'ici ! une histoire touche à sa fin et une autre commence. 3 années formidables mais à la fois particulièrement agrémentées de rencontres enrichissantes, de moments difficiles et joyeux mais surtout intenses. Tout ce travail n'aurait pas été réalisable sans plusieurs personnes et institutions qui m'ont fait confiance durant ces trois années qui resteront gravées dans ma mémoire.

Tout premièrement, mes premières pensées sont dirigées vers mes encadrants de thèse, Thomas ELGUEDJ, Anthony GRAVOUIL et Michel ROCHETTE. D'abord, je tiens particulièrement à remercier Thomas pour sa disponibilité, sa confiance sans faille mais aussi sa franchise et par dessus tout, sa maîtrise de l'IGA (Analyse isogéométrique pour les intimes de la méthode). Et oui, Thomas m'a fait découvrir l'IGA. Étant encore jeune diplômé et inconscient de la montagne de travail qui se dessinait devant moi, il m'a donné goût à un sujet novateur et passionnant. De plus il a su montrer de grandes qualités humaines diverses et variées. En fait Thomas, c'est quelqu'un qui est proche du doctorant sauf qu'il est professeur. Il a su aussi démontrer plusieurs de ses aptitudes au fil de nombreuses "conférences vacances travail" à l'étranger. Anthony est quant à lui un maître de la pédagogie. Je le remercie personnellement pour son expérience et sa solidité dans le domaine. Pour lui, un travail de recherche n'est jamais terminé, il est à "suivre". Bref toujours matière à faire mieux, faire évoluer et/ou peaufiner les détails. Il a su m'apporter une certaine rigueur et méthode. Michel est remercié pour son implication dans ses travaux. En effet, cette thèse est un travail personnel qui s'articule et s'inscrit dans un travail d'équipe. Ils m'ont transmis la passion de la recherche. Au travers de tout cela, ils m'ont accordé leur confiance, donné leurs conseils avisés et ont fait preuve d'une grande rigueur scientifique. Pour finir, grâce à eux, je suis clairement devenu bilingue avec cette rédaction en anglais ! (boutade...).

Tous les membres du jury sont grandement remerciés. Pour commencer, je souhaite exprimer ma reconnaissance envers Thouraya BARANGER. Un parcours qui n'aurait pas été possible sans elle. Pour la petite histoire, après mon stage de Master Recherche, Thouraya a cru en moi et s'est démenée pour me trouver un sujet de thèse qui a été avec le recul, passionnant et enrichissant. Sebastien BAGUET est aussi à l'origine de cette aventure, merci à lui. Mes rapporteurs, Grégory LEGRAIN et Alain RASSINEUX qui ont eu la tâche complexe de relire ces travaux, sont grandement remerciés. De plus, David NERON et Jean-François REMACLE m'ont fait l'honneur de composer ce jury et d'y apporter leur touche personnelle. J'ai particulièrement apprécié leurs interventions et les échanges qui ont suivi. Je remercie tout particulièrement David NERON pour avoir présidé ce jury de thèse.

Je souhaite également remercier l'équipe de recherche ANSYS. Merci tout particulièrement à Christelle et Valéry mais aussi à Wenfeng pour l'aide qu'ils m'ont fournie dans diverses projets internes. Merci à Martijn et Claire pour votre réactivité et professionnalisme. Travailler chez ANSYS c'est travailler dans un endroit proche de son bureau de l'INSA histoire de faire un aller retour en deux minutes. Non, sérieusement c'est travailler avec des gens très compétents, humains mais surtout motivés par la tâche qu'ils accomplissent. L'esprit d'équipe y permet un travail de qualité. Merci à Christine pour son professionnalisme.

Ceux avec qui j'ai partagé mon quotidien au sein du LaMCoS vont être particulièrement (cela est sûr) et chaleureusement (cela dépendra...) remerciés dans ce paragraphe qui est annoncé plutôt long. Le LaMCoS est une ruche de doctorants plus ou moins présents, plus ou moins expressifs, plus ou moins chauds pour aller boire un verre, mais ils sont tous grandement appréciables de part leur personnalité. En effet, cultures, origines et passions ce mêlent dans cette boite à doc (certains l'appelleront aussi la boite à chomdu, ce que je réfute totalement). C'est plutôt clairement enrichissant. D'abord si tu es en train de lire cette phrase, je te conseille de continuer. Ne lisez pas les remerciements en anglais, il sont moins complets. Commençons par le commencement. Premièrement nous allons débuter par le début. Je remercie Thibaut à qui je donne le trophée de la patience et du Inkscapeur de ouf. Où Thibaut passe les prix de posters n'ont qu'à bien se tenir. Tu mérites d'autres palmes pour les autres qualités dont tu as fait preuve pour avoir été mon co-bureau (joli tandem) pendant presque 3 ans. Merci aussi au passage d'avoir refait la terrasse de mes voisins (moi j'ai fait un peu mieux...). Matthieu merci pour tous les voyages vacances que l'on a partagé (Austin, San diego, Pavie et Giens 2017), en particulier NYC. Sacré coloc à New York ! Tristan (le végé et non-fumeur) s'en souvient je pense ! Mes pensées vont aussi à ceux qui codent avec les ieps (pieds), la team dite des scatter-interpolants. Et oui, de nos jours il y a des gens qui codent avec un fond blanc et sur Matlab. Pire, ils font leur thèse avec de genre d'outils : je les remercie. Thomas tu est nommé (merci pour les c***treuses aussi). Alexis aussi tu as scatterisé. Zi est apprécié pour sa grande connaissance de la France, Zi connait tout : surtout les Zilôts de Giens 2019. Vincent le bidouilleur de l'extrême, toujours opérationnel pour faire de l'Arduino ou du Raspberry. Pipo à qui je dois ce bureau. Pierre pour être naturellement fêtard. Nico pour ses conseils et son expertise grandement appréciable de papi de la mécanique. Médéric pour sa motivation sans faille. Florian pour son support de co-bureau. Marie pour avoir récemment choisi Hughes (on va en parler ci-après) et l'IGA pour 3 ans de bonheur. Tous les autres sont aussi grandement remerciés, Etoe et Efel (les jeunes skieurs), Étienne (les bières de Glasgow), Yvan, Arthur, Ye, Zhaofeng, Meng, Haoming, Tyty, Mouhamadou, Tarek, Fatima, Salvatore, Damien, Nico L, Yanick et le autres doctorants du laboratoire que j'ai pu côtoyer. Pour certains, nous avons tissé des liens qui sont forts. Merci pour les palets bretons à Giens ! Robin (le jeune papa) que je remercie pour nous avoir accompagné à plusieurs conférences. Je tenais aussi à remercier l'équipe des permanents, bref il fait bon travailler au LaMCoS. Pour finir, merci à Isabelle pour sa grande efficacité.

Un petit paragraphe est dédié à mon mentor de l'ombre : Hughes. L'IGA c'est une religion, tu y crois ou tu y crois pas. Religion avec pas mal d'avantages comparé à la FEA, mais avec deux trois inconvénients aussi, il faut être objectif. Merci Hughes pour cette passion que tu nous as transmis. Tu as su NURBSER toutes nos approches scientifiques.

C'est maintenant le moment de remercier des personnes qui me sont chères depuis longtemps. Mes amis sans qui rien n'aurait été de la sorte. Ils ont su me porter et me soutenir jusqu'à l'aboutissement de ces travaux. Certains sont présents depuis très longtemps et je les remercie vivement. Tout ce qu'on a partagé durant ces trois ans m'a aidé à surmonter quelques épreuves difficiles mais surtout à m'épanouir dans ce monde de la recherche. Il y a tellement à dire que je vais essayer de synthétiser. Je donnerai que 2 prénoms, deux qui ont marqué cette dernière année de thèse tout particulièrement. Merci à Thomas pour la sous-loc et la vaisselle, Matteo pour les bonnes pâtes et les repas ou je mettais les pieds sous la table à 21h. Merci à mes copains d'enfance avec qui j'ai grandi et avec qui je me suis construit, ils se reconnaitront. Merci aux autres, les "autres" qui sont arrivés après mais qui méritent aussi ma plus profonde gratitude.

Pour finir, je dédie ces travaux à ma famille, qui m'ont soutenu jusqu'au bout. À mes parents André et Françoise et ma soeur Ambre qui m'ont donné leur soutien inconditionnel. Ils ont cru en moi du début à la fin et m'ont poussé à arriver jusqu'ici. À mon frère jumeau Guillaume qui a su trouver les mots et l'attitude adéquate pour me faire avancer et me conforter dans cette épreuve singulière. Il n'y a pas de mots pour lui témoigner toute ma reconnaissance. Ils ont un peu rien compris à tout ce blabla mécanique mais je les remercie très chaleureusement de m'avoir apporté autant durant ces 3 années.

Figure 1: Le gâteau IGA.

Figure 2: Île de Porquerolles, CSMA 2019, Giens, FRANCE.

Acknowledgements

There are numerous people, institutions and ANSYS France that deserve deep gratitude for supporting my work during this 3 years.

Firstable, I would like to thank my thesis advisors Thomas ELGUEDJ and Anthony GRAVOUIL, for their excellent knowledge and support but also for giving me your confidence.

Additionally for being my co-supervisor, I want to thank Michel ROCHETTE and all people of ANSYS France for the great working environment and their scientific expertise.

Furthermore, I would like to thank all members of my thesis jury for supporting me and my work. In particular my thesis reviewers Grégory LEGRAIN and Alain RASSINEUX for the quality work they have produced. Moreover, I wish to thank Jean-François REMACLE and David NERON. David NERON is especially thanked for being my jury president.

It was and it will always a pleasure to work within the MIMESIS and MULTIMAP research teams. I want to express my gratitude to all members of the LaMCoS for letting me grow in a fruitful environment with friends and competent colleagues. Numerous co-workers are gratefully acknowledged for their sympathy but also for the friendship we have built together.

Without my Master's internship supervisor Thouraya BARANGER, nothing would have been possible. That is why i want to thank you in particular for your wonderful trust without that I would never have done this work. The same thanks are dedicated to Sébastien BAGUET.

To finish, I want to thank my close friends and my family for their unequalled and strong support. I am thankful to my parents André and Françoise but also to my sister Ambre and my twin brother Guillaume. Without them, such work would have been different.

We wish to thank the LTSI at Rennes, France for providing the scanned aorta meshes. Moreover, the startup Sim&Cure is gratefully thanked for sharing his innovative approach concerning cerebral aneurysms treatments but also for providing the scanned aneurysm meshes.

Résumé

Ce travail présente un cadre générique pour la construction de maillages isogéométriques volumiques à partir d'une géométrie complexe avec une topologie arbitraire pour des applications relatives aux modèles d'ordres réduits. En effet, les maillages structurés tels que les maillages isogéométriques ou hexahédriques sont difficiles à obtenir de manière automatique. Les analyses statistiques de formes et les modèles d'ordres réduits nécessitent des données structurées et ordonnées pour être construits efficacement. Pour ce faire, nous utilisons les limites du modèle solide triangulé, la B-Rep CAD (Boundary Representation in Computer Aided Design). Tout d'abord, cette thèse inclut une intégration d'un algorithme de décomposition en pantalons et en cuboïdes prenant en compte les caractéristiques géométriques. La décomposition en cuboïdes divise une surface en un ensemble de patchs quadrilatéraux qui peuvent aider à définir un volume associé. Des champs de croix (cross fields), c'est-à-dire des champs de directions à 4 symétries, sont utilisés pour guider une paramétrisation globale alignée de la surface. Ce paramétrage est optimisé afin de minimiser la distorsion des éléments. Le processus d'optimisation est pensé pour concevoir des champs de croix avec des contraintes topologiques et géométriques. En utilisant la décomposition optimisée en cuboïdes, une structure volumétrique est extraite. Sur la base de la paramétrisation globale et de la structure volumétrique précédemment calculée, une paramétrisation isogéométrique trivariée est déduite. Les propriétés topologiques invariantes sont analysées tout au long du processus proposé. Pour finir, pour différentes occurrences géométriques de même topologie mais possédant des géométries différentes, notre méthode permet d'avoir la même représentation : des maillages isotopologiques isogéométriques trivariés détenant la même connectivité. L'efficacité et la robustesse de l'approche proposée sont illustrées par plusieurs exemples de modèles d'ordres réduits en utilisant l'IGA (IsoGeometric Analysis).

Mots clés : Analyse IsoGéométrique ; Modèle d'Ordre Réduit ; Analyse Statistique de Forme ; Topologie ; Paramétrisation ; Décomposition en cuboïdes ; Géométrie Paramétrique.

Summary

This work presents a generic framework to construct trivariate isogeometric meshes of complicated geometry and arbitrary topology required for reduced order model applications. Indeed, structured meshes such as isogeometric or pure hexahedral ones are difficult to obtain in an automatic manner. Statistical shape analysis and reduced order modeling require structured and ordered data to be efficient. For that purpose, we use the triangulated solid 3D model's boundary provided from B-Rep CAD (Boundary-Representation in Computer Aided Design) models. Firstable, the workflow includes an integration of a geometry-feature-aware pants-to-cuboids decomposition algorithm. The input triangulated mesh is decomposed into a set of cuboids in two steps: pants decomposition and cuboid decomposition. Cuboid decomposition splits a surface into a set of quadrilateral patches which can define a volumetric layout of the associated boundary surface. Cross fields, i.e., 4-symmetry direction fields are used to guide a surface aligned global parameterization. Optimizing this parameterization, patches of the quadrilateral layout inherited from the cuboid decomposition are re-positioned on the surface in a way to achieve low overall distortion. The optimization process is thought to design cross fields with topological and geometrical constraints. Using the optimized cuboid decomposition, a volumetric layout is extracted. Based on the global parameterization and the structured volumetric layout previously computed, a trivariate isogeometric parameterization is deducted. Learning generalized forms of theorems in the topology field, invariant topological properties are analyzed throughout the proposed process. To finish, for different geometrical instances with the same topology but different geometries, our method allows to have the same representation: trivariate isogeometric isotopological meshes holding the same connectivity. The efficiency and the robustness of the proposed approach are illustrated through several examples of reduced order models using IGA (IsoGeometric Analysis).

Keywords: IsoGeometric Analysis; Reduced Order Modeling; Statistical Shape Analysis; Topology; Parameterization; Cuboid Decomposition; Parametric Geometry.

Contents

List of Figures

List of Tables

Résumé étendu

0.1 Introduction et motivations

L'Analyse IsoGéométrique (IGA) est une technique d'analyse numérique qui utilise les mêmes fonctions de base pour représenter la géométrie et pour les calculs numériques des solutions approchées des éventuelles équations aux dérivées partielles appliquées aux domaines concernés [Hughes, Cottrell et Bazilevs 2005 ; Cottrell, Hughes et Bazilevs 2009]. L'un des défis les plus importants impliquant l'analyse isogéométrique est de construire des modèles 3D appropriés pour le calcul à l'aide des volumes donnés par leur représentation de bords tel que les modèles B-Rep (Boundary Representation) issus de la CAO (Conception Assistée par Ordinateur). On pourra remarquer que l'IGA est une approche prometteuse pour combler l'écart entre la CAO et la FEA (Finite Element Analysis), le besoin de repasser par la géométrie pour raffiner le maillage n'étant plus nécessaire. Nous invitons les lecteurs à se référer à la Figure 3 pour plus de détails.

Depuis quelques années, beaucoup d'applications dans le domaine des méthodes numériques pour la mécanique sont dédiées aux modèles d'ordres réduits. De plus en plus de simulations numériques demandent la détermination en temps réel ou quasi réel de solutions complexes [Chinesta, Ammar et Cueto 2010 ; Chinesta, Ladeveze et Cueto 2011 ; Lu, Blal et Gravouil 2018]. Les applications embarquées en sont un exemple. Les modèles rencontrés récemment sont multi-paramétriques et possèdent de plus en plus d'étapes gourmandes en temps de calcul afin de satisfaire une certaine exigence de précision. On pourra se référer à la Figure 4 pour comprendre la démarche générale. Dans ces travaux de thèse, nous nous concentrerons sur la qualité, mais aussi grandement sur les propriétés géométriques des modèles mathématiques réalisés pour construire ces modèles réduits.

Néanmoins, une condition préalable à l'IGA est la disponibilité de modèles CAO représentés par des NURBS (Non Uniform Rational B-Splines) volumiques. Cependant, les modeleurs CAO utilisent habituellement la méthode B-Rep pour décrire les modèles volumiques et utilisent des opérations booléennes qui conduisent à des modèles trimmés. Ainsi, la génération du modèle volumique à partir des frontières décrites par des surfaces NURBS est nécessaire puisque la plupart des logiciels commerciaux ne savent pas représenter un volume mathématique ; ceci est encore plus vrai pour les modèles volumiques utilisables directement pour l'IGA.

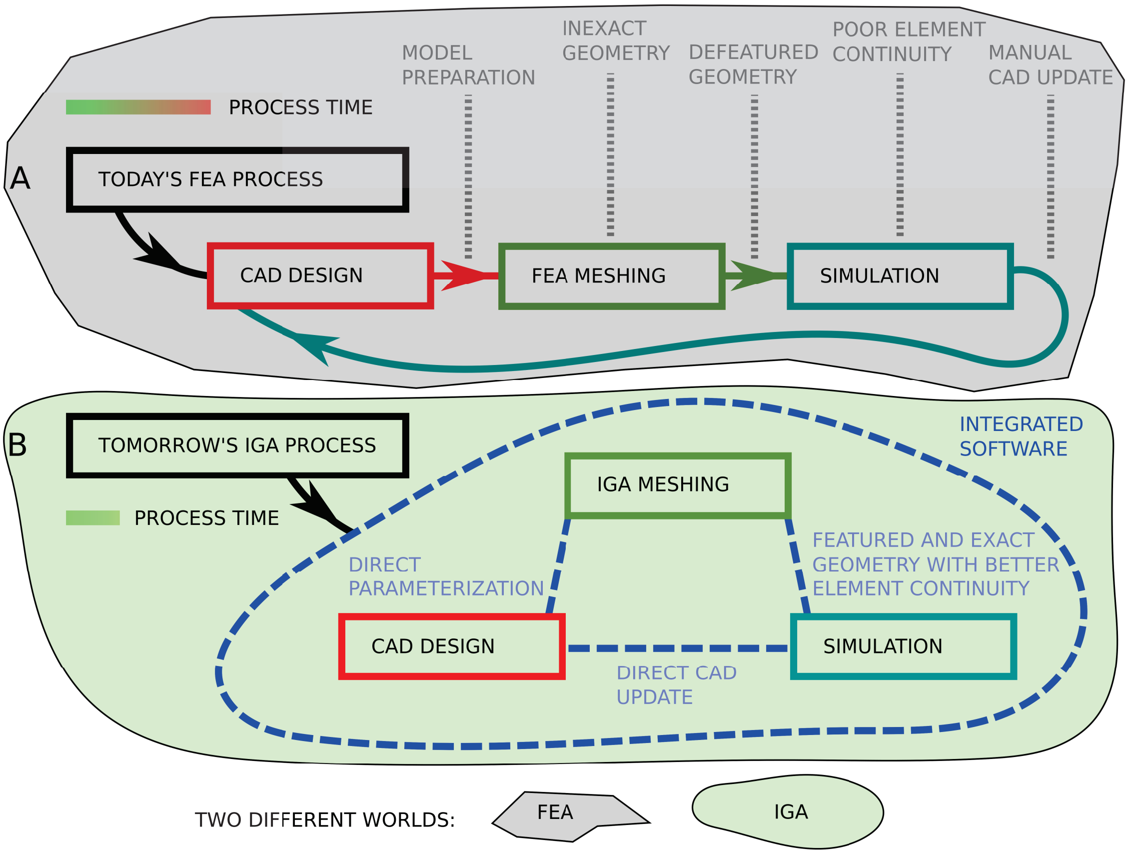

Figure 3: Comment promouvoir l'IGA à la place de la FEA de nos jours. (A) Le processus de FEA est linéaire : chaque étape est indépendante. (B) Le processus de l'IGA imaginé pour demain. Un des arguments pour l'IGA est le suivant : une meilleure géométrie pour une meilleure simulation. Un logiciel où toutes les étapes d'un processus sont intégrées dans un même environnement semble être adapté à l'IGA. Nous remarquerons que l'étape de conception peut être foncièrement différente de la CAO classique.

L'étape de discrétisation en FEA est équivalente à paramétrer la géométrie en IGA puisque les fonctions de base utilisées pour le calcul décrivent aussi la géométrie. Le paramétrage volumique implique le paramétrage des surfaces qui le compose mais aussi de l'intérieur du volume. Ce paramétrage volumique est toujours considéré comme un grand défi [Cottrell, Hughes et Bazilevs 2009]. Pour le paramétrage des surfaces nous utiliserons les coordonnées à valeurs moyennes dans le cas d'une surface topologiquement équivalente à un disque [Floater 2003]. Pour des surfaces à topologie plus complexe, des graphes de découpage nous permettrons de produire une surface topologiquement égale à un disque. A l'aide de champs de croix (cross fields) définis sur notre maillage triangulé issu de la CAO, une paramétrisation globale alignée avec le champ de croix est calculée et optimisée [Bommes, Zimmer et

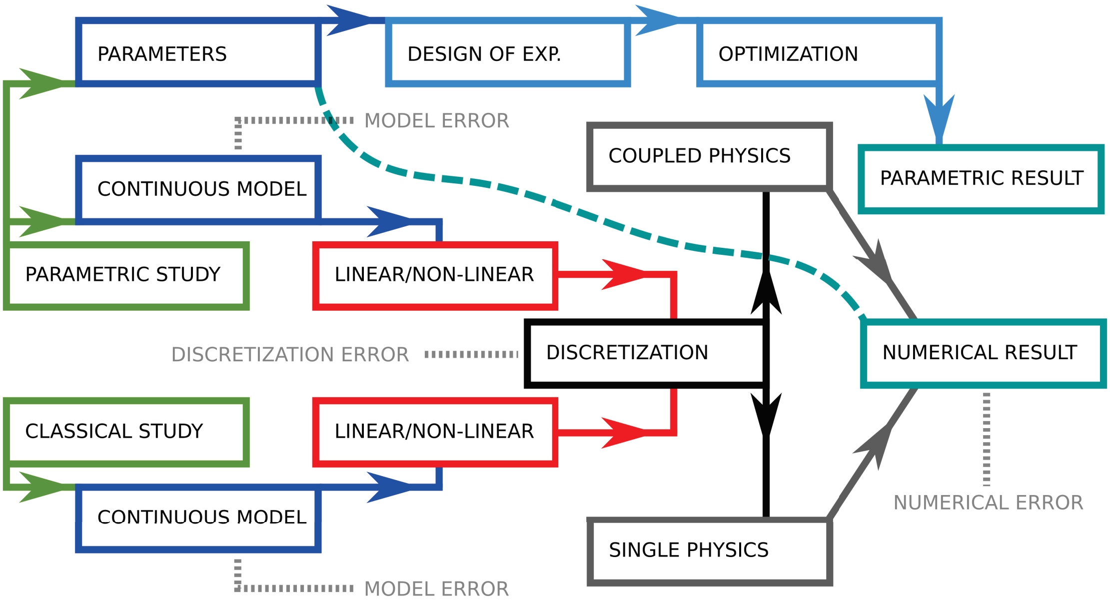

Figure 4: La complexité des modèles augmente. Ceci est essentiellement expliqué par le besoin de précision des simulations mais aussi par les avancées en terme de puissance de calcul impliquant des méthodes numériques innovantes. Plusieurs erreurs sont rencontrées au fil du processus.

Kobbelt 2009 ; Myles et al. 2010 ; Myles et Zorin 2012 ; Campen et Kobbelt 2014].

Le travail suivant est basé en partie sur les travaux effectués sur la disposition en quadrilatères intégrée aux maillages triangulaires [Campen et Kobbelt 2014] mais aussi sur les champs de croix [Crane 2010 ; Crane, Desbrun et Schröder 2010]. Nous utiliserons aussi le travail effectué dans la thèse précédente regroupant quelques techniques présentées ci-dessus comme une base pour nos développements [Al-Akhras 2016].

Ce travail se construit dans un premier temps à travers une segmentation judicieuse des surfaces triangulées représentant la géométrie. Nous segmenterons en pantalons [Li, Gu et Qin 2009 ; Hajij, K. Dey et Li 2016], puis en cuboïdes ou polycubes généralisés [Li et al. 2013]. Un champ de croix est ensuite calculé et une paramétrisation optimisée en est déduite. Le champ de croix est astucieusement généré grâce à la compréhension de théorèmes et des propriétés des surfaces. Pour finir, des volumes B-Spline sont interpolés utilisant les domaines paramétriques cubiques des cuboïdes. Tout au long de ce processus, les propriétés et attributs d'une conversion de surface à volume sont rigoureusement analysés. Ces approches mathématiques sont soigneusement expliquées. Grâce à la paramétrisation interne des B-Splines, chaque volume isogéométrique d'une pièce donnée peut être contraint pour obtenir des maillages isotopologiques entre différentes instances géométriques pour une application à la réduction de modèle, et ceci sans étapes de projection. Des applications à la réduction de modèle utilisant l'IGA avec des paramètres géométriques seront présentées dans ce travail.

0.2 Pré-requis de topologie simplifiés

On introduit ici très brièvement la topologie, c'est à dire l'étude des propriétés d'entités géométriques soumises à des transformations continues. On étudie donc les propriétés de continuité, connexité lors de déformations continues incluant le pliage et l'étirement mais pas le collage et le déchirement. Un espace topologique décrit ces propriétés communes. Nous référons les lecteurs à la Définition 0.1 pour plus de détails.

Définition 0.1. Espace topologique. Un espace topologique est espace constitué d'ensembles munis d'une notion de voisinage autour de chaque point. Ces voisinages satisfont des axiomes spécifiques entre eux.

Nous nous concentrons en particulier sur des espaces topologiques dits variétés géométriques (la Figure 5 nous renseigne sur le type d'espaces utilisés dans ces travaux de thèse). Pour une compréhension rapide, nous donnons des illustrations en Figure 6 pour comprendre les notions de déformations continues entre deux espaces topologiques. Nous appelons un homéomorphisme une transformation possédant une fonction continue et préservant les propriétés topologiques tout au long de la conversion géométrique. Un homéomorphisme est aussi appelé un isomorphisme topologique.

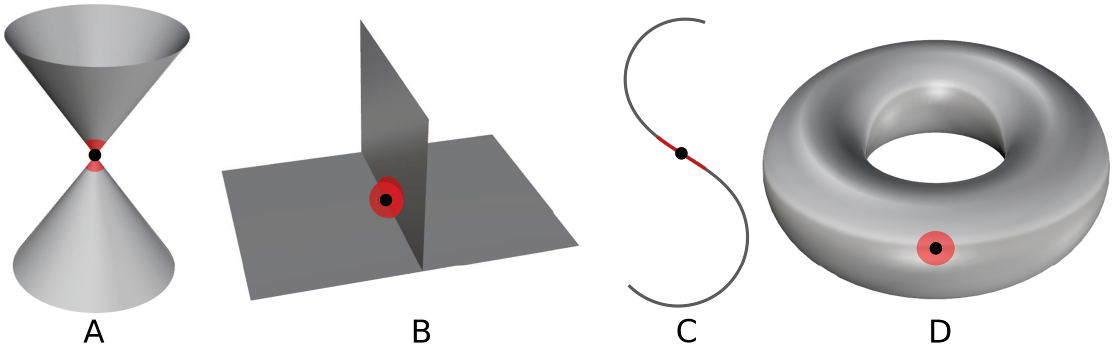

Figure 5: Espaces topologiques étudiés. (A) Un double cone ne possède pas les propriétés requises pour être une variété géométrique. (B) Mêmes conclusions que (A). (C) Une courbe est une variété géométrique de dimension 1. (D) Un tore surfacique est une variété géométrique de dimension 2.

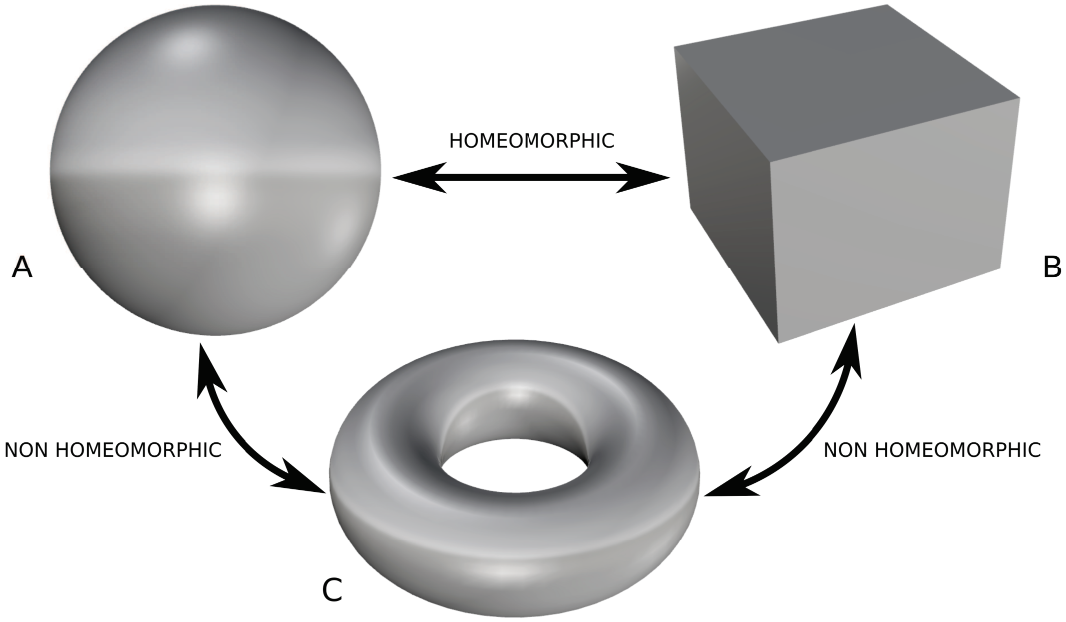

Figure 6: Homéomorphisme entre surfaces. (A) Une sphère est homéomorphique à un cube (B). (C) Le tore possède des propriétés topologiques différentes de (A) et (B).

0.3 Stratégie de décomposition de surface

0.3.1 Décomposition en pantalons

La décomposition en pantalons a été introduite par [Hatcher, Lochak et Schneps 2000 ; Hatcher 2001] et de nombreux travaux ont été effectués pour trouver la segmentation optimale en pantalons [Verdière et Lazarus 2007]. D'autres méthodes plus récentes existent [Hajij, K. Dey et Li 2016]. Un pantalon est une surface de genre 0 avec 3 frontières. Nous référons les lecteurs au Chapitre 2 pour comprendre les notions de genre, frontière et caractéristique d'Euler. Autrement dit un pantalon est topologiquement équivalent à une sphère à 3 trous, à un disque à deux trous ou encore à un tuyau à trois voies. Plusieurs critères peuvent guider une décomposition en pantalon comme le chemin le plus court, la règle de courbure minimum et la symétrie. Rappelons que notre maillage d'entrée avant segmentation est un maillage triangulé surfacique (surface combinatoire de triangles). Une notion élémentaire de topologie est nécessaire pour définir un pantalon. Pour une surface M de genre-g avec b frontières, la décomposition en pantalons est possible si et seulement si l'Équation (1) est satisfaite. De plus, selon la caractéristique d'Euler $\chi(M)$ de la surface M considérée, le nombre de patchs de pantalons est défini en Équation (2).

$$\chi(M) = 2 - 2g - b \leq -1, \tag{1}$$

$$N_{Patches} = 2g + b - 2 = -\chi(M) \ \ (\text{Si} - \chi(M) \geq 1). \tag{2}$$

Notre algorithme de décomposition en pantalons (surface M avec $-\chi(M) \geq 1$ et un critère géométrique) est très robuste et fonctionne très bien sur un maillage de basse qualité et bruité. L'Algorithme 0.1 en est la composante principale. La donnée de sortie est un ensemble globalement optimisé de patchs de pantalons. Un aperçu rapide de la décomposition en pantalon sur une plaque à deux trous est illustré en Figure 7. A noter deux importantes caractéristiques :

- Les boucles géométriques (handle et tunnel loops) sont optimales.
- L'espace topologique entier des décompositions en pantalons possibles est énuméré et la meilleure décomposition est choisie à l'aide d'un critère géométrique.

Algorithme 0.1. Main geometry-aware pants decomposition algorithm.

```
Input 1 : Triangulated genus-$g$ surface $M$ with $b$ boundary components.
Input 2 : $g$ geometrically relevant handle loops of $M$.
Input 3 : Global geometric criterion for $L$.
Output : Set of $-\chi(M)$ pants patches $T = \{T_1, ..., T_{-\chi(M)}\}$, with $M = \cup T_i$.

k = 1.
Slice $M$ along all its handle loops and get a surface $M_k$ with $2g+b$ boundaries.
Put all boundaries of $M_k$ in a set $W = \{w_1, ..., w_{2g+b}\}$.
While $|W| > 3$ do
    Build or reset an empty set of loops $L = \{0\}$.
    Compute $N_c$ combinations : $\dim(N_c) = \frac{Size(W)!}{2!(Size(W)-2)!}$.
    For all couples $[w_i, w_j]$ in $N_c$ :
        Compute a cycle $w_{ij}$ homotopic to $w_i \circ w_j$ (Algorithms 3.2 and 3.3).
        Add loop to $L$.
    End For
    Sort relevant loops in $L = \{l_1, ..., l_{\dim(N_c)}\}$ using a global geometric criterion.
    The optimal $w_{ij}$ cycle is classified in $L$.
    $\{w_1, w_j, w_{ij}\}$ bound a pants patch $T_k$. Remove $T_k$ from $M_k$ : $M_k \leftarrow M_k \setminus T_k$.
    Remove $w_i$ and $w_j$ from $W$, and add $w_{ij}$ into $W$.
    $k \leftarrow k + 1$.
End While
```

0.3.2 Décomposition en cuboïdes

Chaque pantalon est ensuite décomposé en 4 cuboïdes minimum. Un cuboïde est une sphère topologique composée de 6 surfaces homéomorphes à un disque. On remarquera qu'en fonction de la géométrie (angles, arrêtes vives, frontières) il existe

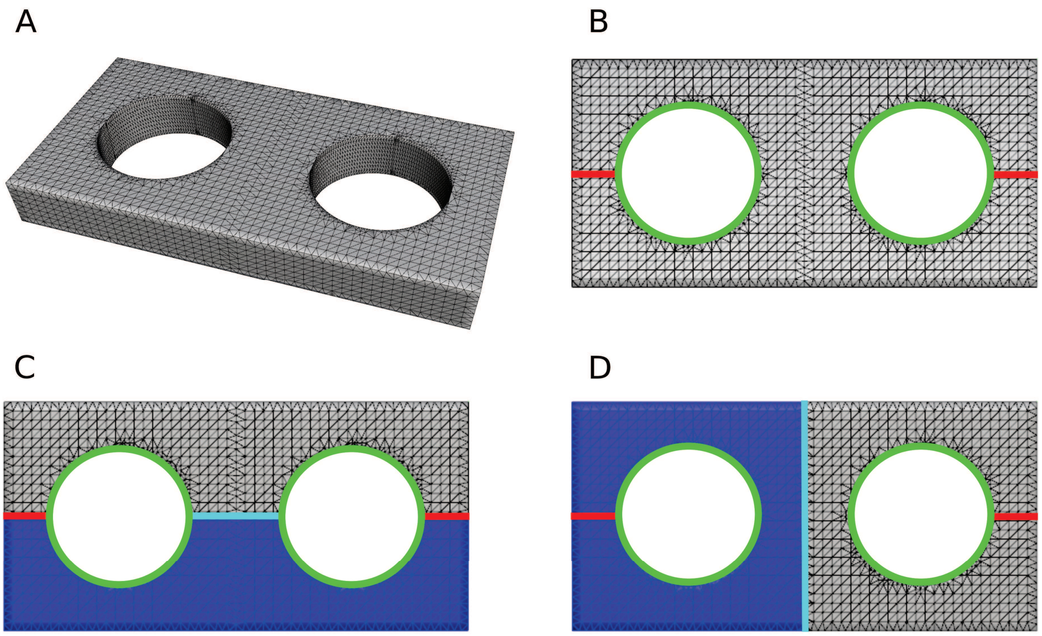

Figure 7: Décomposition en pantalons. (A) Maillage triangulé issu de la CAO. (B) Handle et tunnel loops calculées en utilisant des critères géométriques (les handle loops en rouge, les tunnel loops en vert). (C) Segmentation en pantalon utilisant le critère géométrique de la boucle de découpage la plus courte. (D) Segmentation en pantalon utilisant un critère de symétrie.

en général une configuration en cuboïdes qui permet de respecter la géométrie d'un pantalon donné. La Figure 8 nous montre trois exemples de configuration de cuboïdes pour 3 différentes géométries de pantalons. Nous verrons par la suite qu'il est important de bien choisir la configuration en cuboïdes car elle affecte significativement la paramétrisation volumique B-Spline. Il nous faut donc trouver des descripteurs géométriques et topologiques de chaque pantalon afin de pouvoir déterminer la bonne configuration possible. Une bonne configuration respecte la géométrie d'entrée avec ses arrêtes vives et ses angles.

0.4 Paramétrisation de surface et optimisation

Les surfaces NURBS ou B-Spline ont besoin d'un domaine paramétrique rectangulaire donc par conséquent homéomorphe à un disque dans l'espace physique. De plus, un maillage de contrôle de quadrilatères est essentiel. Afin de pouvoir au mieux construire ce maillage de contrôle, il nous est nécessaire de construire des champs de directions. Par exemple un champ de lignes (2-symétrie) est utilisé pour placer une texture, un champ de croix (4-symétrie) peut être utilisé pour remailler en quadrilatères [Bommes, Zimmer et Kobbelt 2009]. Nous devons donc concevoir

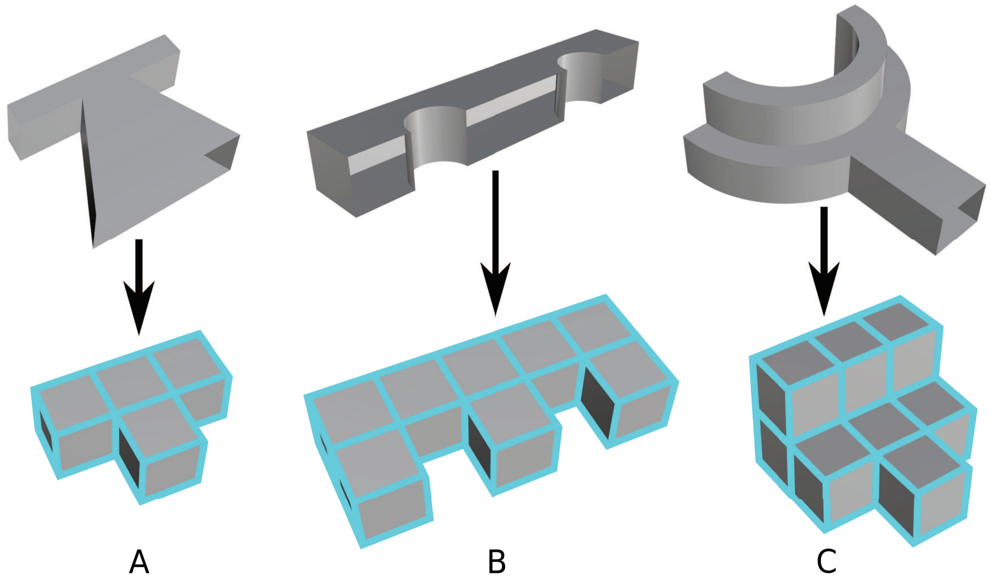

Figure 8: Décomposition en cuboïdes. Pour chaque géométrie de pantalon, une configuration en cuboïdes est optimale pour comprendre ces caractéristiques géométriques. (A) La plus simple des configurations en cuboïdes pour un pantalon. (B) Une configuration avec 8 cuboïdes. (C) Une configuration avec 10 cuboïdes.

un champ de croix topologiquement conforme avec la décomposition en cuboïdes et correspondant aux directions principales et aux caractéristiques géométriques. Une fois ce champ calculé, il est utilisé pour en déduire un maillage en quadrilatères issu d'une paramétrisation globale surfacique alignée avec celui-ci. A noter que la configuration en cuboïdes est une segmentation de surface et donc reste une entité surfacique. L'intégration surfacique de cette décomposition est optimisée afin de réduire la distorsion des éléments quadrilatèraux en utilisant l'approche de [Campen et Kobbelt 2014]. La Figure 9 image très simplement le processus de paramétrage.

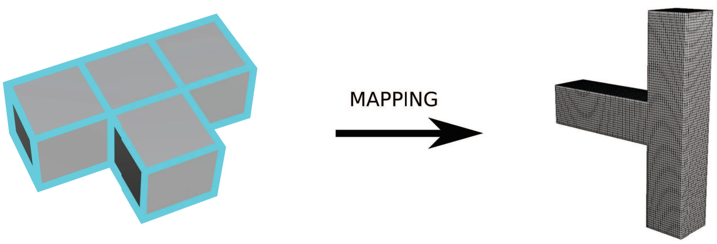

Figure 9: Mapping de configuration de cuboïdes. En utilisant les données topologiques et géométriques de la configuration en cuboïdes ainsi que la paramétrisation globale, un maillage en quadrilatères est calculé.

0.5 Conversion de maillages surfaciques en maillages volumiques structurés pour des applications de réduction de modèles

Cette section vise à résumer rapidement comment les structures volumiques servant à la définition des volumes isogéométriques sont construites. Nous nous servons de la décomposition optimisée en cuboïdes ainsi que du maillage en quadrilatères résultant de la paramétrisation de surface. Tout au long de ce processus, nous analysons les attributs topologiques de cette conversion afin de déterminer la structure volumique adéquate. En effet, lors de la conversion d'une surface à un volume, des propriétés topologiques sont héritées d'une dimension à une autre. Par contre, comme l'intérieur du volume n'est pas clairement défini et segmenté, il est important de connaitre certaines prérogatives à la construction volumique. Nous conseillons vivement aux lecteurs de lire le Chapitre 6 pour de plus amples détails. Ce chapitre concernant la conversion volumique est un des développements majeur de ce travail de thèse.

Dans un objectif de réduction de modèles incluant des simulations avec des paramètres géométriques, nous donnons notre stratégie en Figure 10 pour les B-Splines volumiques. Une structure volumétrique commune aux différentes instances géométriques à étudier est déduite et un membre-α est choisi. Les contraintes de maillages isotopologiques sont appliquées sur la population entière ; ceci résultant en un ensemble de maillages ayant la même connectivité. La contrainte homologue nous permet quant à elle de définir la comparaison point par point de maillage. Elle traduit donc plus un aspect de géométrie que de topologie.

0.6 Application à la réduction de modèles avec des paramètres géométriques utilisant l'analyse isogéométrique

La réduction de modèles est une tache fastidieuse surtout quand il s'agit d'y introduire des paramètres géométriques [Lu, Blal et Gravouil 2018 ; Maquart et al. 2019a ; Maquart et al. 2019b]. En effet on souhaite conserver la même structure de données (c'est à dire le maillage) pour chaque instance géométrique de notre population. Avec notre processus, chaque volume isogéométrique d'une pièce donnée peut être contraint pour obtenir des maillages isotopologiques entre différentes instances géométriques.

Nous montrons dans ce résumé deux exemples de modèles réduits. On utilise l'analyse isogéométrique sur des modèles formés de B-Splines volumiques. Le premier exemple en Figure 11 montre l'évaluation du modèle réduit de joint en temps réel pour un jeu de paramètres arbitraires. Le second est donné en Figure 12.

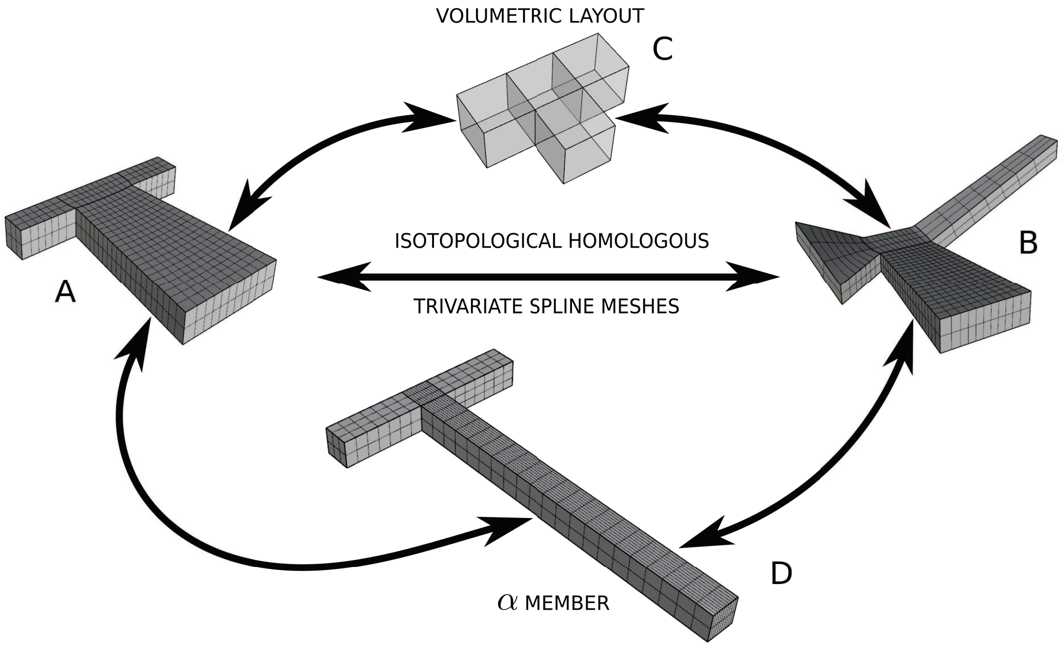

Figure 10: Construction de maillages isotopologiques pour des applications de modèles réduits à paramètres géométriques. (A) Géométrie A d'un volume formé de B-Splines. (B) Géométrie B d'un volume formé de B-Splines. (C) Structure volumique de référence. (D) Membre-α choisi pour représenter la population de géométries à étudier.

Seal part range	Min	Max
Radius 1	11	15
Radius 2	20	30
Radius 3	35	45
Height 1	28	35
Height 2	10	16
Length 1	50	80
Load intensity	100 N	175 N
Poisson's ratio	0.28	0.34

Table 1: Plage de paramètres utilisée pour le modèle réduit de joint.

0.7 Conclusion

Nous avons introduit dans cet article une méthode de génération de maillages volumétriques et isotopologiques entre eux. Ceci est réalisé à partir de la B-Rep issue de la CAO. Nous avons montré que notre stratégie de maillage est bien adaptée à la modélisation d'ordre réduit avec des paramètres géométriques. La comparaison

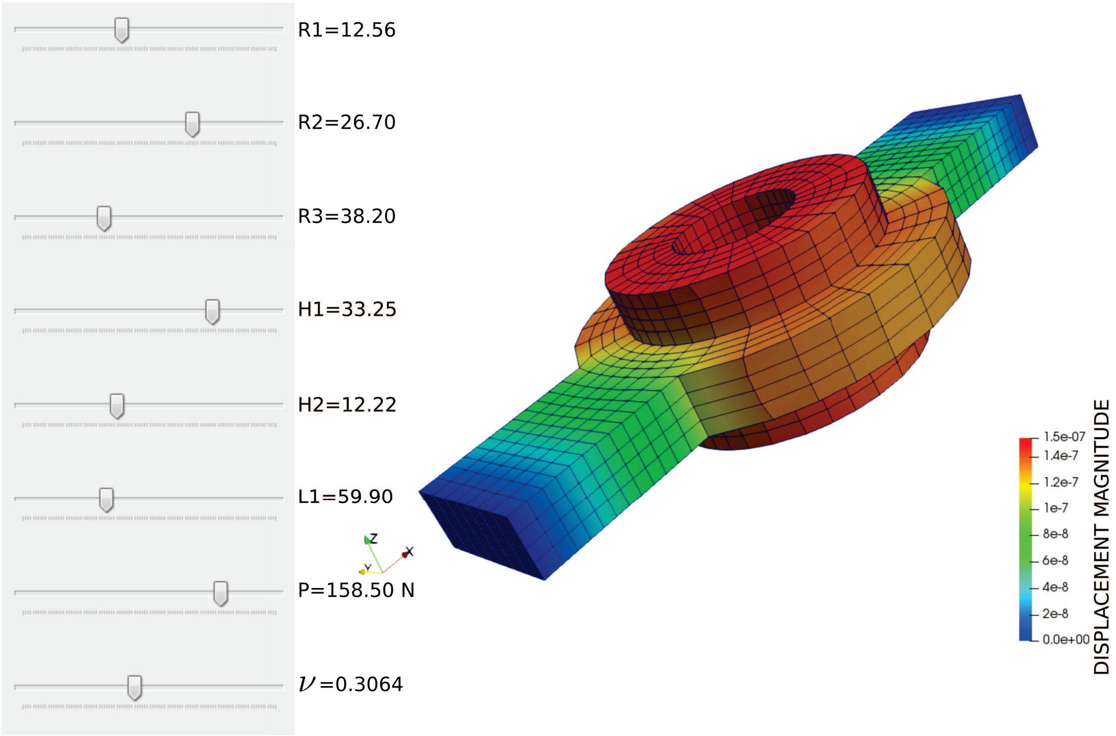

Figure 11: Évaluation du modèle réduit de joint. La base réduite est constituée des 50 premiers modes. 400 snapshots ont été nécessaires pour construire ce modèle réduit. La plage des paramètres utilisée est donnée en Tableau 1.

Wheel part range	Min	Max
Radius 1	7.8	9.75
Radius 2	13.65	16.25
Radius 3	25.35	29.9
Radius 4	62.725	67.275
Radius 5	73.775	80.275
Radius 6	86.625	91.975
Height 1	26	32.5
Height 2	8.125	9.75
Length 1	39	43.875
Load intensity	100 N	175 N
Young's modulus	200 GPa	230 GPa

Table 2: Plage de paramètres utilisée pour le modèle réduit de roue.

efficace des champs mécaniques se fait en prenant en compte le même paramétrage pour toutes les instances géométriques de la population à étudier. L'introduction de

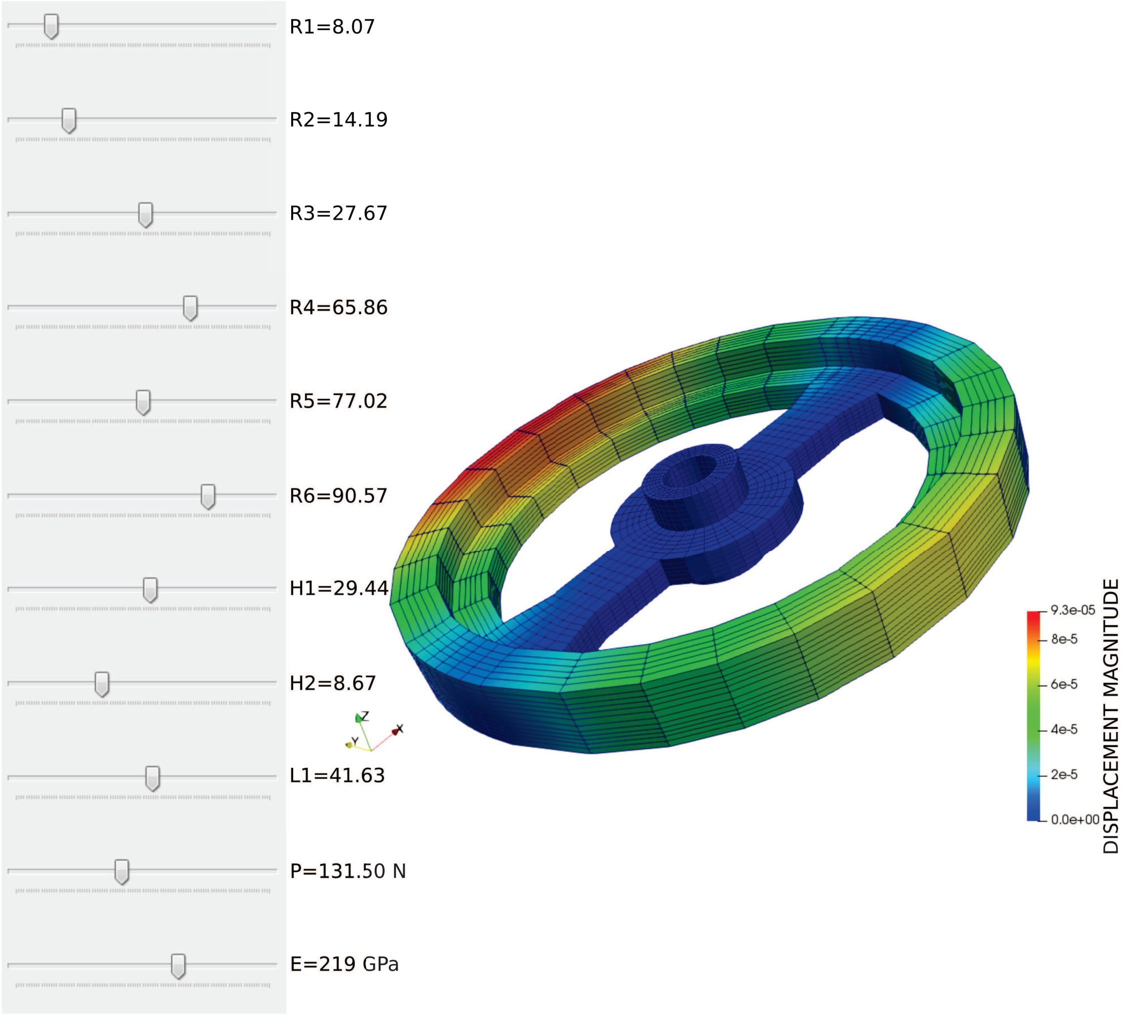

Figure 12: Évaluation du modèle réduit de roue. La base réduite est constituée des 50 premiers modes. 592 snapshots ont été nécessaires pour construire ce modèle réduit. La plage des paramètres utilisée est donnée en Tableau 2.

paramètres géométriques dans un modèle d'ordre réduit permet par exemple d'optimiser la forme, ce qui est utile aujourd'hui dans un objectif de réduction du poids d'une pièce. Un réel avantage a été déployé en définissant une méthode générique pour surmonter la difficulté de génération fiable et automatique de maillages isotopologiques. Les évaluations en temps réel présentées démontrent la robustesse et la fiabilité de la méthode développée.

Une contribution clé est amenée pendant la segmentation de la surface d'entrée fournie par la CAO. La théorie de la décomposition de surface est un outil essentiel pour atteindre nos objectifs. Nous nous efforçons de comprendre à la fois la géométrie et la topologie au cours de cette étape. Pour d'autres propriétés telles que les indices des singularité des champs de croix et la paramétrisation globale de surface, nous avons utilisé le travail de [Campen et Kobbelt 2014] associé à nos améliorations précédentes.

Nous avons montré de nouveaux outils mathématiques pour comprendre les propriétés topologiques invariantes lors de la conversion de surface en volume formant une autre avancée significative. Cette problématique continue de susciter un certain intérêt dans les communautés du traitement de la géométrie, de la mécanique et de la physique. Le contrôle des propriétés topologiques au cours du processus de conversion est fondamental. En effet, les informations invariantes transmises de la surface au volume sont essentielles pour construire les maillages volumétriques nécessaires à notre méthode.

Malgré les capacités de nos algorithmes et outils présentés dans cette thèse, traiter automatiquement toute géométrie complexe issue de la CAO reste un défi majeur. Pour les cas complexes avec une géométrie arbitraire, la décomposition en pantalons peut ne pas être cohérente. Nous pouvons résoudre ce problème en ajoutant des entrées utilisateur au processus automatique. La décomposition en cuboïdes générée est adaptée à la définition de la surface, ce qui donne une définition arbitraire du volume intérieur. Toutefois, il est possible de s'y attaquer en adressant à la méthode des entrées spécifiques.

Introduction

Isogeometric representations for a better continuity and geometry

Since its introduction in 2005, IsoGeometric Analysis has demonstrated several abilities in terms of efficiency, accuracy and quality in analysis. By using the same mathematical representation for both geometry and analysis, isogeometric elements are geometrically better than traditional finite elements. B-Spline and NURBS (Non-Uniform Rational B-Splines) were initially introduced to construct complex parts for graphical purposes but also for design softwares in the automotive industry. Indeed, a coarse level of discretization suffice to represent complicated shapes. It has the potential to reduce the numerical error related to the geometry discretization compared to classical methods encountered in computational mechanics.

A particularly highlighted capability of IGA is to have the power to reunify the worlds of Computer Aided Design and Computer Aided Engineering. Very recent trends are to design a geometry while parameterizing its analysis model. With such workflow, we avoid numerous time consuming back and forth between CAD and CAE softwares currently used.

IGA possesses additional properties than the standard Finite Element Analysis. Continuity is achieved thanks to high-order B-Spline basis functions. This is the same functions which are used for model discretization and analysis. Such approach has been successfully applied in many fields. Fluid mechanics, contact interfaces, shape optimization, Fluid Structure Interaction are a non-exhaustive list of examples. For some applications, exhibited results with this method have been greatly improved and accuracy goals have been reached.

Nevertheless, a specific need for IGA is the disponibility of mathematical models which are analysis suitable. Not all geometries hold these requirements. To deal with this problematic, various implementations of isogeometric analysis exists. Commercial softwares, e.g. Abaqus, LS-Dyna and also RADIOSS have implemented or have planned to use IGA. Obtaining analysis suitable geometries remains nonetheless a current challenging problematic: numerous analyzed parts are computed from manual modeling or with prototype research codes. This thesis aims to give a contribution in this field.

Reduced order modeling with geometric parameters

Recent progresses in the computer industry, enable very large scale computations. In fact, super computers and high performance computing solutions are able to treat ever bigger complex problems. Fifteen years earlier, such computations would not have been possible. However, we wish nowadays to better exploit disponible resources. Mostly if onboard simulations are required, e.g. for immediate decision making systems. Moreover, intense arithmetic tasks are energy consuming and are not economically sustainable.

Reduced Order Models (ROMs) are known by their very low computational cost. Real-time evaluations of complex solutions are thus made possible. The construction of a reduced order model requires prior computations. These precomputations are called snapshots. Into a shape optimization process, standard procedures are running parametric studies, in the way to find the best set of geometrical parameters. Despite the current capacity of the actual computational power, accumulating thousands of numerical simulations is not reasonable. That is why, some industries prefer to over-size mechanical parts in order to avoid years of computations. Mass reduction objectives are common in the aeronautical industry. Indeed, increasing mass of a structure lead to increase its fuel consumption.

Modeling with geometric parameters is a problematic we want to tackle in this thesis work. Changing the geometry meaning to deal with a different mesh, and thus with a different structuration of the data between shapes. Nonetheless, ROMs require solutions vectors with the same dimension, i.e., to avoid an inacurrate projection step between different instances.

Topology

Polygonal meshes are widely used discretizations with numerous applications in computational mechanics, numerical simulation, computer graphics and so on. The idea is to discretize the geometry into cells or simple geometrical entities. Triangles and quadrilaterals are the most used polygonal entities for surface definition. Quadrilateral meshes are well-suited for many tasks involving graphics and texture mapping. Triangle meshes are easier to generate, because they present unstructured properties. For instance, in CAD softwares, it is nowadays very easy to generate triangle meshes from a NURBS design. However, discretized combinatorial arrangements of triangles do not hold relevant topological attributes while geometry is well replicated.

Since years, most researches have focused on converting unstructured meshes to structured ones, whether it is applied for surface of volume entities. Indeed, tetrahedral meshes are by far the most employed in numerical simulation. But, for various reasons in different fields, current researches are trying to convert geometries in order to obtain a superior structuration of the geometry. Isogeometric analysis is based on smooth spline representations that are structured. Such geometrical transformations are closely related to mathematics, and in particular in topology. This thesis focuses on properties and theorems governing these reconstruction processes.

Followed strategies in this thesis

We give a method to compute quality 3D hexahedral or trivariate B-Spline meshes with specific properties needed in parametric analysis. We strive to build isotopological meshes from triangulated surface provided by B-Rep CAD. Such meshes are generated using objects with complex geometry and arbitrary topology. This work is based on smart geometry-comprehensive algorithms which interact together. Programming is an essential tool widely used throughout proposed approaches.

To do this, we present an integrated pipeline partitioning the input from triangulated surface in relevant domains useful to compute comparable 3D hexahedral meshes. Hexahedral meshes are degree-1 B-Spline meshes. Firstly, we seek to understand the geometry while decomposing the mesh. This is the first proposed enhancement involving geometry-aware pants decomposition and feature-aware-cuboid decomposition algorithms. We treat input surfaces with pants decomposition approaches [Verdière and Lazarus 2007; Li, Gu, and Qin 2009; Zhang and Li 2014; Hajij, K. Dey, and Li 2016]. Thereafter, we perform cuboid decomposition [Lin et al. 2008; Li et al. 2013; Liu et al. 2015] splitting each pants patch into a coarse quadrilateral mesh lying on triangulated mesh features as possible: the quadrilateral layout.

Second novelty is brought by locating properly high valence nodes of the quadrilateral layout. A surface optimized global parameterization helps us to define a high quality quadrilateral mesh. Based on the approach introduced by [Campen and Kobbelt 2014], quadrilateral patches embedded on the studied surface are optimized in a way to minimize the surface parameterization distortion. We design cross fields to guide the parameterization [Ray et al. 2008; Bommes, Zimmer, and Kobbelt 2009; Crane, Desbrun, and Schröder 2010]. Topological properties of such direction fields are entirely provided from the coarse quadrilateral layout.

The third main significant contribution is topology based. We use topology concepts throughout the pipeline to design volumetric layouts from unstructured CAD geometry. From the beginning to the end, decomposed topologies are constrained and analyzed in order to build structured volumetric meshes using unstructured surface ones. We present properties of $2, 3$-dimensional manifolds embedded in $\mathbb{R}^3$ for 2-dimensional manifolds to 3-dimensional manifolds conversion. Close links between quadrilateral layouts and volumetric layouts are then determined. Suitable volumetric layouts are then an essential scheme to build required trivariate isogeometric and pure hexahedral meshes.

Finally, the problem of generating isogeometric analysis suitable models for

ROMs is tackled. The fourth novelty is given by adressing the same parameterization to different shapes. Mechanical fields are computed with isogeometric analysis onto isotopological snapshots meshes. The snapshots are sampled in the way to cover large parameters spaces involving many geometrical parameters.

Manuscript organization

This thesis work is organized in 7 chapters:

- Chapter 1 presents a state of the art concerning isogeometric analysis and reduced order modeling. Methods followed to fulfill our objectives will be detailed.
- Chapter 2 introduces topology prerequisites which are fundamental for the next developments.
- In Chapter 3, the decomposition pipeline is revisited to understand the geometry.
- Chapter 4 explains the used aligned global parameterization technique computed from a geometrically relevant cross field. We then extract a suitable quadrilateral mesh of the triangulated surface.
- Chapter 5 presents applications to statistical shape analysis and virtual charts results based on quadrilateral meshes.
- Chapter 6 deal with topological properties and constraints during surface to volume conversion.
- Chapter 7 presents results on reduced order models with geometric parameters. Several illustrations demonstrate the efficiency of the method.

Used algebraic operators and notations are detailed in Appendix A.

Chapter 1

Isogeometric analysis based reduced order modeling

This chapter presents current main challenges concerning computational mechanics. State of the art related on isogeometric analysis and reduced order modeling is reviewed.

Contents

1.1 Computational mechanics

1.1.1 Global motivations for numerical simulation

Simulation softwares are nowadays powerful and robust to be exploited into an industrial objective. Such processes and tools have become indispensable in the actual industry. They serve to design, optimize and validate products. Physics phenomena must be understood as well as possible in order to provide and simulate behavior of structures, fluids and so on. CAD seems to be an essential approach to describe the geometry of the studied objects. For decades, it has been used as the first step of an engineering process: the geometrical design. Physics are solved by defining partial derivative equations on an approximated geometry provided from CAD. This is the main task of a CAE software.

Despite today's ability of CAD and CAE to lead increasing complex computations, one of our main motivation in this thesis is to better represent the geometry. Indeed, the link between CAD and CAE worlds is brought by a discretization step. Numerical analysis can not be performed directly through the CAD geometry. We point out two different approaches: the FEA and IGA as depicted in Figure 1.1. FEA represented in Figure 1.1 (A) is based on a mesh generation step while IGA in Figure 1.1 (B) is already parameterized and can describe an exact geometry as well as the CAD design process does. Although CAD can use same geometrical objects as IGA, the geometry is not directly analysis-suitable due to boolean operations widely prescribed in these designing pipelines.

Due to the increasing complexity of executed simulations and precision needs, importance to hold a powerful discretization method is an actual problematic. The principal motivation of IGA users, is to fill the gap between the worlds of CAD and CAE by using a comprehensive geometry representation and parameterization. Shape optimization purposes are thus straightforwardly adapted with the isogeometric discretization.

1.1.2 Better simulation through better geometry using IGA

IGA is a recent numerical analysis method that is very promising for design and analysis by replacing traditional finite elements with B-Splines and Non-Uniform Rational B-Splines elements (NURBS). This method finds its origin in the work of [Hughes, Cottrell, and Bazilevs 2005] and is detailed few years later by [Cottrell, Hughes, and Bazilevs 2009]. B-Splines and NURBS functions (see e.g. [Rogers 2000; Farin 2002; Piegl and Tiller 2012]) were initially chosen for their free form and deformation capacities in CAD softwares. IGA represents the geometry better than standard FEA meshes and has better continuity properties between elements. Indeed, this method uses the same type of mathematical representation for both geometry and computation of solution fields. That is why this computational approach offers the possibility to fill the gap between design and analysis. Low degree

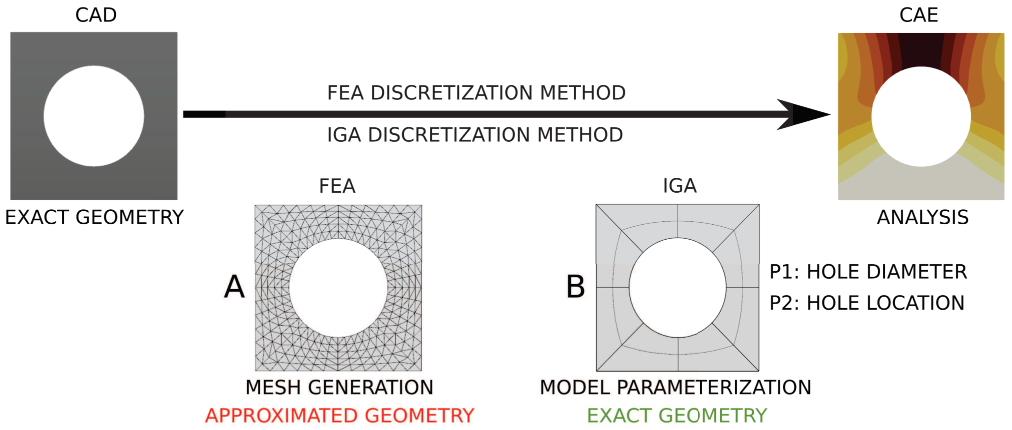

Figure 1.1: Quick comparison between two discretization methods for numerical analysis. (A) FEA discretization method passing by a mesh generation step yielding an approximated geometry. FEA and CAD use different description for the geometry. (B) IGA discretization method represents the exact B-Rep CAD geometry and the whole model is parameterized: IGA and CAD use the same description for the geometry of the surface. Geometry can be changed using parameters $P1$ and $P2$ without modifying the parameterization. IGA allows parametric computations.

B-Splines and NURBS, i.e., quadratic or cubic, are particularly interesting for analysis. Indeed, their calculation cost is not much higher compared to conventional finite elements and they allow a significant improvement for the solution quality [Occelli 2018]. This is in particular due to the geometry description: as pointed before, IGA gives the possibility to treat design and numerical simulation with the same geometrical model. One of the most interesting aspects of classical B-splines is that different kind of refinement strategies are possible while leaving the underlying geometry and its parameterization intact [Cottrell, Hughes, and Bazilevs 2009].

Today's challenges are to bring the IGA from the concept stage to a real tool for industry. A contribution of this problematic is delivered in this work, see e.g. Appendix B. The issues of an industrial finite element code are directly related to the world of industry. Solutions must be effective, general and lead to quality results while being as robust as possible. This is the main idea behind Figure 1.2. Figure 1.2 (A) shows the classical FEA workflow that is almost linear: the different stages are done in different softwares. From design to simulation, communication between numerical entities are not optimized. On the contrary, Figure 1.2 (B) depicts the aim of the IGA process of tomorrow. Researchers are trying to incorporate design and analysis in the same software [Coreform 2019]. But complexity of such hard task is particularly related to geometry and topology problematics. This thesis aims to understand them. Scientists usually insist on 5 main differences to sell or to prove that IGA must be the future tool for numerical analysis that reunifies the worlds of CAD and CAE [Derek et al. 2019]:

- Accuracy of IGA.
  Smooth basis functions improve the accuracy of the entire simulation process.
- Efficiency of IGA with better geometry.
  Geometry can be understood with few degrees of freedom yielding to an improved accuracy per degree of freedom.
- Robustness of IGA.
  Larger mesh deformations are acceptable compared to traditional FEA: other mechanical problems can be tackled.
- Adaptative refinement of IGA.
  Depending on the type of used splines, local refinement is available for specific simulation purposes.
- IGA is well-suited for all mechanical applications.
  IGA capacities are larger than FEA: from design to parametric shape optimization, IGA is successful.

Despite all mentionned benefits and capabilities of IGA, today's problems are the availability of solid models. B-Rep geometry from CAD offers trimmed surfaces and poor topological information. These geometries coming from design can not be used directly for analysis. Generating IGA models for analysis while designing remains a hard task.

1.1.3 Real-time computations: the need for ROM

Since few years, numerous applications in computational physics are dedicated to reduced order modeling, i.e., the construction of Reduced Order Models (ROMs). Indeed, a real benefit is brought by determining complex solutions in real-time. For example, onboard sophisticated computations in fighter aircrafts becomes possible. Nowadays problems are multiparametric models, see e.g. [Chinesta, Ammar, and Cueto 2010; Chinesta, Ladeveze, and Cueto 2011]. Figure 1.3 gives a quick approach on the current problematics involving increased complexity of numerical simulations. Many modern models of real-life physical computations pose challenges when used in numerical simulations, due to time complexity and large size. In fact, calculations infrastructures are limited in terms of operations per second. In case of complex studies, a issue exists between memory space and required simulation time. Today problems in science and engineering remain intractable, in spite of the recent progresses in the physics field. For the last decade, dealing with high numerical complexity leads us to adopt learning approaches. As a consequence, novel methods are required in order to tackle not only non-linear problems but also large scale and parametric problems, mostly if onboard simulations are required. Domains of applications are changing and new emerging issues in the physics world require reliable fast resolution. For example, [Niroomandi et al. 2008] have used an offline step

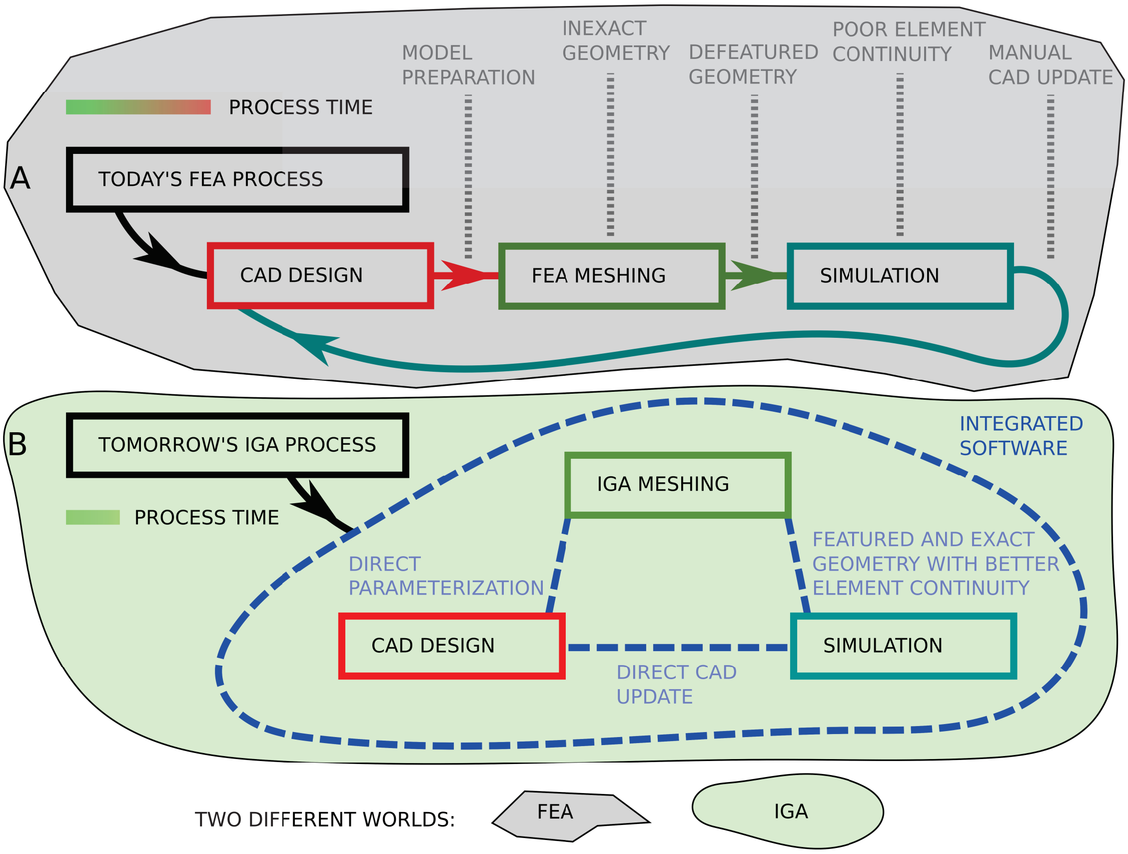

Figure 1.2: How to sell IGA instead of FEA. Showdown is imminent between FEA (A) and IGA (B). (A) Classical FEA process is linear: from design to simulation, each step is independent yielding to a time consuming approach. Moreover, geometrical aspects and features are not necessarily conserved until simulation. (B) Tomorrow's IGA process. An integrated software controlling the design, the meshing and numerical simulation seems to be the required efficient solution for today's problematics. Note that designing methods in (B) could be very different than current processes. One of the main argument for IGA is the following: better geometry for a better simulation.

to reduce non-linear responses of living tissues. The principal motivation behind reduced order modeling is to enable real-time analysis. This is realized thanks to its very low computational cost during solution evaluation.

Clusters and others supercomputers used for expensive computations, e.g. fluid mechanics, are in constant evolution. Parallel progresses of numerical methods implies an overall computational improvement [Glotzer et al. 2009]. ROMs aim to lower the computational complexity of dedicated problems. Such reduced order model techniques can be applied for numerous non-linear and linear problems. In addition, parametric studies are then easily understood and large sets of data can be analyzed. These learning methods consist in solving a problem into a reduced

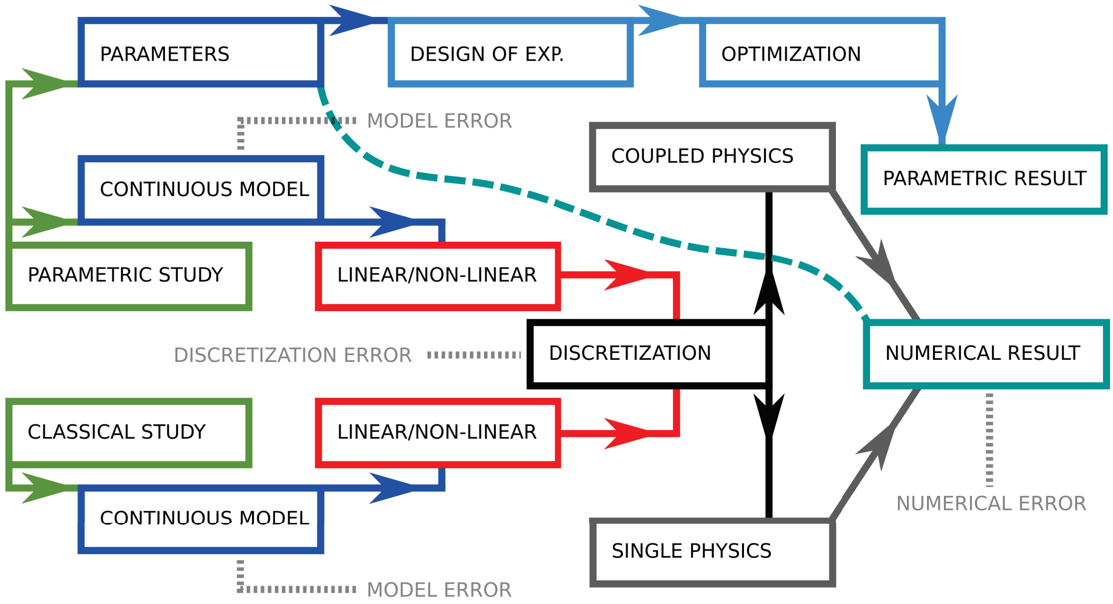

Figure 1.3: Increasing model complexity for more realistic simulations. Starting from a classical study or a parametric one, numerous additional stages with expensive computational costs can be added depending on the physics. Numerical result is obtained after a few minutes for simple problems or months for FSI (Fluid Structure Interactions) studies. Such nested steps are subject to several errors: modeling, discretization and numerical errors.

subspace which is trying to capture the most dominant trends of the studied fields. The main important variations are embedded into modes. Thus, the goal is to evaluate a solution with few modes that best describe the main tendencies of the physics phenomenon.

1.2 Isogeometric analysis

1.2.1 Introduction and state of the art

One of the major strengths of NURBS or other isogeometric representations are the easy manipulation of the geometry by moving control points. Thus, the shape of the underlying surface can be smoothly modified while preserving the continuity between elements. The choice of NURBS functions is certainly due to their native presence in CAD and graphics softwares. These functions can represent exactly a wide range of common shapes, i.e., conical sections, spheres, cylinders, ellipsoids and so on. But, notice that this is not the case for helical surfaces. Classical NURBS and B-Splines functions possess an intrinsic structured aspect, thus local refinement is not possible. However, B-Splines provide refinement possibilities and therefore refinement does not require any interaction with the original geometry provided from CAD while FEA does. NURBS detain other useful properties for numerical simulation and geometric modeling. Knot insertion, C^{p-1} continuity for NURBS of degree p and convex hull properties are profitable as pointed in [Cottrell, Hughes, and Bazilevs 2009]. This is a non-exhaustive list. The differential quantities associated to such functions are mathematically defined, thus avoiding approximations. A benefit is brought for shape optimization purposes. Indeed, shape and sizing optimization can be performed in an identical manner [Hirschler et al. 2018].

Understanding both limitations and potentials of classical NURBS or splines objects [Piegl and Tiller 2012], nowadays isogeometric analysis community is growing. Some researchers employ the so-called T-Splines for volumetric reconstruction [Zhang, Wang, and Hughes 2012; Wang et al. 2013; Harmel, Sauer, and Bommes 2016], for mesh optimization [Escobar et al. 2011] or for volumetric construction using boolean operations [Liu, Zhang, and Hughes 2014]. Others are denominated hierarchical B-Splines and allow local refinement [Occelli 2018]. Very recent trends, are to use U-Splines [Coreform 2019; Derek et al. 2019] that unlock the full potential of IGA for industrial purposes. U stands for unstructured; inventors are promising local adaptivity, refinement at extraordinary points, integration of triangles and backwards compatibility with older splines technologies.

Nevertheless, the native tensor product problematic of splines restricts the conversion possiblity of standard spline models to IGA. In particular for volumetric studies. Hence, geometries provided from CAD can not be used directly. The reason is because CAD softwares use boolean operations yielding to trimmed geometries for surface entities. The method is called the B-Rep (Boundary Representation) for volumetric models. Moreover, design processes are often leading to connection problems between patches or a non-conform welding. [Lai et al. 2016; Lai et al. 2017] tried to integrate the design directly into a CAE software, but it remains a hard task to be efficient and time-preserving compared to classical FEA. Although generation of volumetric spline models is difficult to obtain in an automatic manner, powerful solutions will appear in the next years due to the craze in this field. [Cohen et al. 2010] showed that the quality of the volumetric parameterization has an important impact on the analysis.

1.2.2 Basic mathematical aspects

1.2.2.1 B-Spline basis functions

A knot vector Ξ is a set of non-decreasing real numbers, defined in the parametric space. It is composed of $n+p+1$ values. n being the number of univariate B-Spline basis functions of order p as given in Equation (1.1). Where $\xi_i \in \mathbb{R}$ is i^{th} knot, i is the knot index and $i = \{1, 2, \dots, n+p+1\}$. Knots divide the parametric space in knot spans $[\xi_i, \xi_{i+1}]$ and the global interval $[\xi_1, \dots, \xi_{n+p+1}]$ defines a patch. A knot vector is called uniform if its knots are uniformly spaced. Otherwise, it is called a non-uniform knot vector. It is also called non-periodic or open if its first and last knots are repeated $p+1$ times as pointed in Table 1.1 for quadratic splines. In this thesis, for isogeometric analysis, only uniform and open knot vectors will be used.

$$\Xi = \{\xi_1, \ldots, \xi_{n+p+1}\}. \tag{1.1}$$

	Open or non-periodic
Uniform	$\{0,0,0,1,2,3,4,4,4\}$
Non-uniform	$\{0,0,0,1,3,4,4,4\}$

Table 1.1: Non-exhaustive list of different knot vectors for quadratic B-Splines.

B-Splines are defined from a knot vector Ξ. They are constructed recursively in the parametric space from linear combinations of B-Spline functions, beginning with piecewise constants. Equation (1.2) gives the basis functions for $p = 0$. For $p \geq 1$, the basis is defined by the Cox-de Boor recursion formula [Piegl and Tiller 2012] as written in Equation (1.3). The constructed basis functions for a uniform knot vector $\{0, 1, 2, 3, 4, \ldots\}$ are given in Figure 1.4.

$$N_{i,0}(\xi) = \begin{cases} 1 \text{ if } \xi_i \leq \xi < \xi_{i+1}, \\ 0 \text{ otherwise}, \end{cases} \tag{1.2}$$

$$N_{i,p}(\xi) = \frac{\xi - \xi_i}{\xi_{i+p} - \xi_i} N_{i,p-1}(\xi) + \frac{\xi_{i+p+1} - \xi}{\xi_{i+p+1} - \xi_{i+1}} N_{i+1,p-1}(\xi). \tag{1.3}$$

B-Spline basis functions defined by the global knot vector can be seen with a local point of view. A knot vector of size $n{+}p{+}1$ will generate n linearly independent basis functions of degree p on $p+2$ knots for support. Each basis function support is a part of the knot vector, where the corresponding function is non-zero. Reciprocally, a knot span $[\xi_i, \xi_{i+1}]$ is covered by $p+1$ B-Spline basis functions. According to these considerations, a given open uniform knot vector $\Xi = \{0, 0, 0, 1, 2, 3, 4, 5, 6, 7, 8, 8, 8\}$ will define 10 quadratic B-Spline functions with 10 so-called local knots and 8 knot intervals, see Figure 1.5. We then list some of the fundamental properties of B-Spline basis functions:

- Continuity.
  Across knots, basis functions will be C^{p-m} where p is the polynomial degree or order and m is the multiplicity of the knot. B-Spline basis functions constructed from an open uniform knot vector are interpolatory, i.e., they are C^0 at the extremities of the knot interval $[\xi_1, \ldots, \xi_{n+p+1}]$, but are not in general at the interior knots. In the case of the basis constructed from the knot vector $\Xi = \{0, 0, 0, 1, 2, 3, 4, 5, 6, 7, 8, 8, 8\}$, none of the middle knots is repeated. Their multiplicity is then minimum, i.e., $m = 1$.

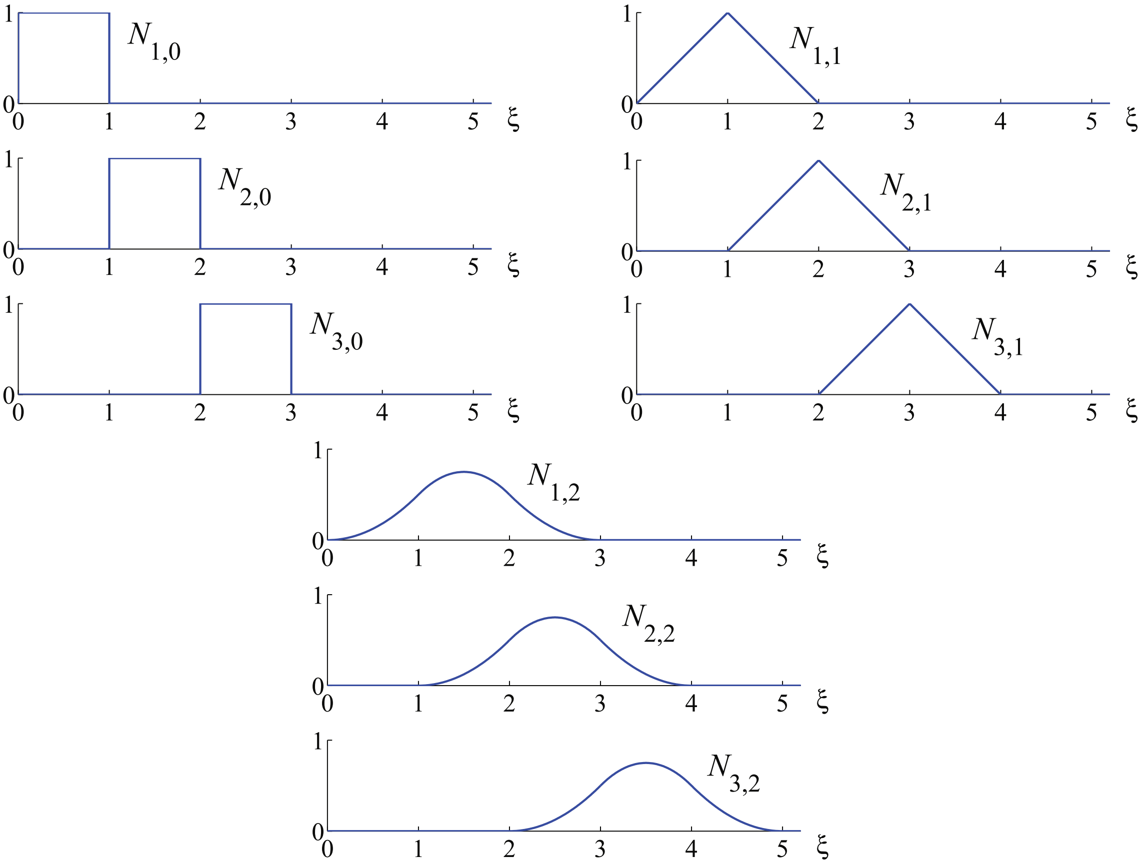

Figure 1.4: B-spline basis functions of order $p = 0, 1$ or 2 for a uniform knot vector $\{0, 1, 2, 3, 4, \ldots\}$. Picture from [Cottrell, Hughes, and Bazilevs 2009].

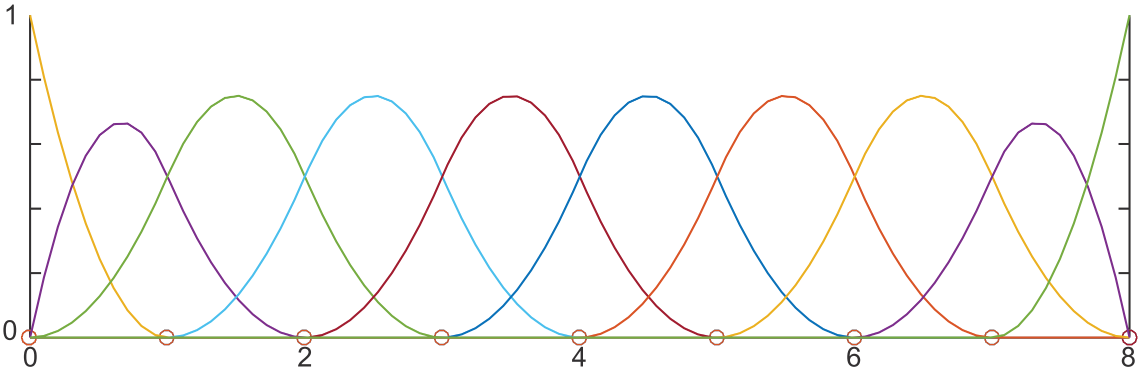

Figure 1.5: Quadratic basis functions generated by the knot vector Ξ. All quadratic basis functions generated by the knot vector $\Xi = \{0, 0, 0, 1, 2, 3, 4, 5, 6, 7, 8, 8, 8\}$. Each individual basis function can be described using a local knot vector of $p + 2$ knots each. Picture from [Occelli 2018].

- Partition of the unity.
  A B-Spline basis constructed from an open knot vector has the partition of

unity property:

$$\sum_{i=1}^{n} N_{i,p}(\xi) = 1, \ \forall \xi. \tag{1.4}$$

- Linear independence.
  A B-Spline basis is linearly independent:

$$\sum_{i=1}^{n} c_i N_{i,p}(\xi) = 0 \Leftrightarrow c_i = 0, \ \forall i \in \{1, \ldots, n\}, \ \forall \xi. \tag{1.5}$$

- Compact supports of B-Spline basis functions.
  A B-Spline basis function has a compact support, i.e., the support of $N_{i,p}$ is included in $[\xi_i, \ldots, \xi_{i+p+1}]$.

1.2.2.2 B-Spline objects

B-Spline curves can be built in $\mathbb{R}^d$ by linear combination of B-Spline basis functions, where $d \geq 1$. Coefficients $\mathbf{B}_i \in \mathbb{R}^d$, $\forall i = \{1, 2, \ldots, n\}$ are called control points. They are analogous to nodes for finite element analysis and define the control polygon. Given n functions $N_{i,p}$, $\forall i = \{1, 2, \ldots, n\}$ of degree p and a knot vector $\Xi = \{\xi_1, \ldots, \xi_{n+p+1}\}$, a B-Spline curve is defined in Equation (1.6). An example of a cubic B-Spline curve is given in Figure 1.6 (A).

$$\mathbf{C}(\xi) = \sum_{i=1}^{n} N_{i,p}(\xi) \mathbf{B}_i. \tag{1.6}$$

Given a control polygon $\mathbf{B}_{i,j} \in \mathbb{R}^d$, $\forall i = \{1, 2, \ldots, n\}$, $\forall j = \{1, 2, \ldots, m\}$ and knot vectors for each parametric direction $\Xi = \{\xi_1, \ldots, \xi_{n+p+1}\}$ and $\mathcal{H} = \{\eta_1, \ldots, \eta_{m+q+1}\}$ respectively of degree p and q, a B-Spline surface can be constructed using the global tensor product generalization of univariate B-Spline functions as formulated in Equation (1.7). An example of a cubic B-Spline surface is given in Figure 1.6 (B).

$$\mathbf{S}(\xi, \eta) = \sum_{i=1}^{n} \sum_{j=1}^{m} N_{i,p}(\xi) M_{j,q}(\eta) \mathbf{B}_{i,j}. \tag{1.7}$$

Given a control polygon $\mathbf{B}_{i,j,k} \in \mathbb{R}^d$, $\forall i = \{1, 2, \ldots, n\}$, $\forall j = \{1, 2, \ldots, m\}$, $\forall k = \{1, 2, \ldots, l\}$ and knots vectors $\Xi = \{\xi_1, \ldots, \xi_{n+p+1}\}$, $\mathcal{H} = \{\eta_1, \ldots, \eta_{m+q+1}\}$ and $\mathcal{Z} = \{\zeta_1, \ldots, \zeta_{l+r+1}\}$, respectively of degree p, q and r, a B-Spline volume can be constructed in a similar way in Equation (1.8). Notice that 2D and 3D basis functions have the same fundamental properties of 1D basis functions.

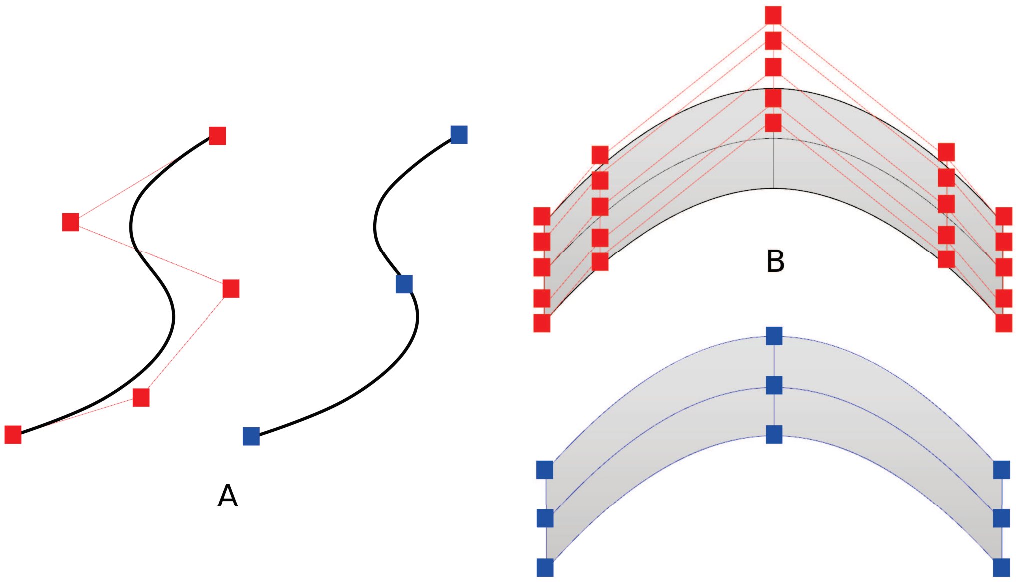

Figure 1.6: Cubic B-spline curve and surface. (A) A B-Spline curve with knot vector $\Xi = \{0, 0, 0, 0, 1, 2, 2, 2, 2\}$. (B) A B-Spline surface with knot vector $\Xi = \{0, 0, 0, 0, 1, 2, 2, 2, 2\}$ and $\mathcal{H} = \{0, 0, 0, 0, 1, 2, 2, 2, 2\}$. Control points are depicted in red, whereas physcial knot locations are in blue.

$$\mathbf{V}(\xi, \eta, \zeta) = \sum_{i=1}^{n} \sum_{j=1}^{m} \sum_{k=1}^{l} N_{i,p}(\xi) M_{j,q}(\eta) L_{k,r}(\zeta) \mathbf{B}_{i,j,k}. \tag{1.8}$$

NURBS are constructed from B-Splines. They can be obtained by weighting the B-Spline functions, assigning a weight to each of the control points. More specifically, NURBS functions in $\mathbb{R}^d$ are built from projective transformations of B-Splines in $\mathbb{R}^{d+1}$. The main advantage of NURBS compared to B-Splines is their ability to represent more geometric entities. NURBS can precisely represent conic sections, such as circles and ellipses. We refer the readers to the books of [Cottrell, Hughes, and Bazilevs 2009; Piegl and Tiller 2012] for more details. We recall that, in the following, only uniform and open knot vectors will be used for B-Spline objects.

1.2.3 Analysis-suitable parameterization

One of the most challenging problematic in IGA, is to generate required suitable meshes from an initial standard B-Rep CAD design. Given a solid model from CAD, i.e., possibly trimmed NURBS surfaces defining the boundary of the volume, generating an IGA mesh remains a hard task. Same issue exists when converting a triangulated mesh or tetrahedral one into a structured pure hexahedral mesh. Indeed, when designing in CAD softwares or using automatic meshing algorithms, the initial geometry is hidden or defeatured. Important information is lost. Nowadays tasks in the geometry community is concentrated to recover these lost topological aspects. In this work, we seek to understand all mathematics needed to retrieve these properties.

There exists many different techniques to build analysis-suitable parameterizations for IGA. Recall that the problematic of generating a pure hexahedral mesh from a B-Rep CAD is the same of designing an IGA mesh from a triangulated surface geometry. [Martin, Cohen, and M. Kirby 2009] proposed a method that generates generalized cylinders used to construct a volumetric isogeometric representation. [Wang et al. 2008; Li et al. 2013] use generalized polycubes to fulfill the same objective of reparameterization. However, in terms of spline construction, cylinders produce degenerated points along their axis. Polycubes are themselves more dedicated to this parameterization approach. For genus-zero solids, other methods exist [Zhang, Wang, and Hughes 2012; Wang et al. 2013].

In the biomedical field, geometries are obtained using scanning techniques. It is nowadays reasonable to obtain meshes from various organs with powerful instruments. Encountered procedures are mainly automatic. Scanners create a point cloud that is triangulated by a specific reconstruction software [Hornung and Kobbelt 2006]. Technically speaking, delaunay triangulation in $\mathbb{R}^3$ is a starting point for these meshing pipelines.

Our work investigates objects with complex geometry and arbitrary topology given by a B-Rep model. We seek to generate a trivariate parameterization which respects a given solid model defined by its B-Rep CAD or triangulated mesh of the volume's boundary. Figure 1.7 gives the two main studied workflows, i.e., the CAD and biological ones.

1.3 Reduced order modeling

1.3.1 Introduction to reduced order modeling

ROMs are usually presented as computationally efficient mathematical representations that can offer the potential for near real-time analysis. Reduction means finding an appropriate basis composed by less vectors than the number required to define a snapshot. A snapshot is defined as a solution for a given set of parameters that may include time, mechanical properties or shape parameters. Large amount of time is saved when interrogating an appropriate basis that represents the major trends of the physics phenomenon: the so-called reduced basis. Nevertheless, finding a reduced basis providing both an attractive dimensional reduction and a relevant solution is still challenging. Figure 1.8 shows today's problematics concerning parametric studies for industry where model reduction methods can be useful.

Two different approaches of reduction methods exist. Roughly speaking, the ROM world is divided between a posteriori and a priori approaches. The first one consists in determining a reduced space before performing reduced order model computations. Snapshots are obtained from mechanical experiments or simulations. The

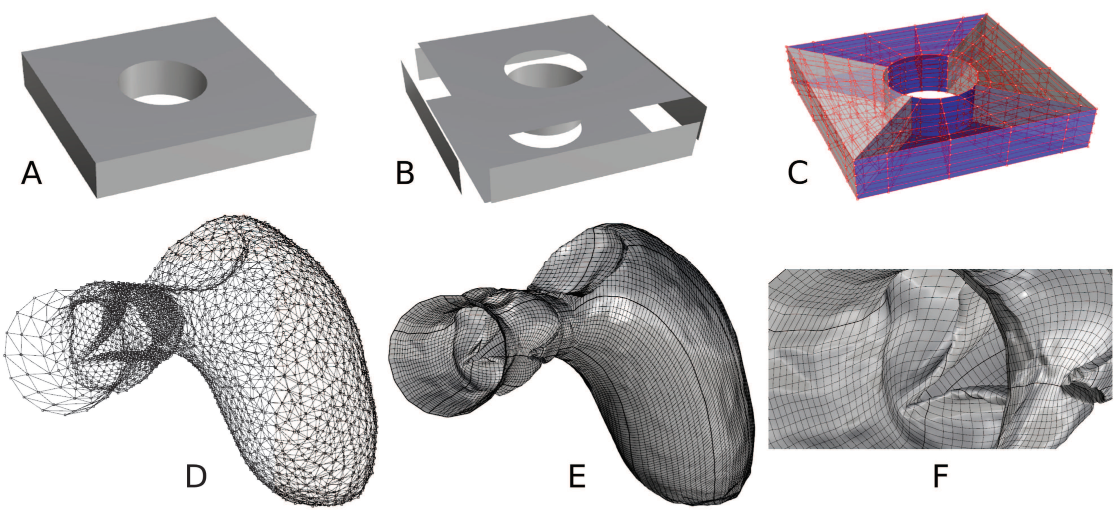

Figure 1.7: Analysis-suitable parameterization examples. (A) B-Rep from CAD. (B) Solid is considered by the computer as a combination of NURBS trimmed surfaces. (C) Smart segmentation and parameterization are mandatory to obtain a trivariate isogeometric parameterization that conserves the features of (A). (D) Point cloud and reconstructed triangulated mesh. (E) Surface isogeometric mesh and its detail in (F). Heart surface parameterization has been computed by our IGA_ROM PlugIn (see Appendix B).

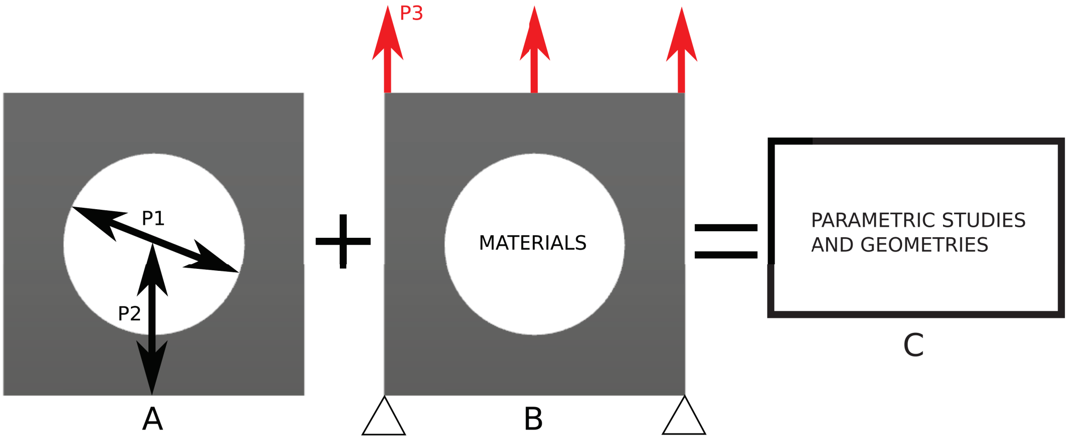

Figure 1.8: Parametric models generation. Reduced order modeling is a well-suited tool for these designing pipelines. (A) A feature based parametric design done in industries. (B) Applying loading parameters, boundary conditions and material properties. (C) Parametric studies and geometries resulted from (A) and (B).

Proper Orthogonal Decomposition is computed from snapshots in order to obtain the needed reduced basis. POD is based on the Singular Value Decomposition of a matrix. As earlier said, reduced order model evaluation or computation generally require a low computational effort and thus it is particularly adapted for on-board computations for large parametric problems. Numerous types of problems can be resolved [Kunisch and Volkwein 2001; Ryckelynck et al. 2006; Kerfriden et al. 2011; Amsallem, Zahr, and Farhat 2012]. Foremost introduced in fluid dynamics, a posteriori methods have been then exploited in structural mechanics.

The second one, does not require prior knowledge about the solution. The reduced basis is determined and sized on-the-fly during the resolution process. We name the Proper Generalized Decomposition a well-known kind of a priori approach [Chinesta, Ammar, and Cueto 2010; Chinesta, Ladeveze, and Cueto 2011; Boucinha, Gravouil, and Ammar 2013]. PGD was introduced to resolve non-linear problems in mechanics involving large time increments.

More generally, efficient reductions use mixed approaches between a priori and a posteriori ones. For example, given a reduced basis, some evaluations are computed from a ROM and if the level of accuracy is not reached, the reduced basis is enriched. This is the technique behind adaptive sparse grids [Lu 2017; Lu, Blal, and Gravouil 2018]. At the inverse, for a priori methods, previous calculations could be used as a starting point. Relevant and reliable strategies rely on both methods, e.g. for 3D crack propagation [Galland 2011; Galland et al. 2011] or for frictional contact [Giacoma 2014].

1.3.2 Singular value decomposition and statistical shape analysis

Singular value decomposition is a powerful matrix factorization technique. It was introduced in the 1870's. It is a factorization for real and complex matrices and generalizes the eigen decomposition of positive semi-definite normal matrices. In the following, we focus only on real numbers. Computing the SVD of a matrix $\mathbf{U}$ of dimensions $n \times m$ consists in computing its factorization under the form given in Equation (1.9). For more technical details we refer the readers to [Giacoma 2014] or [Galland 2011].

$$\mathbf{U} = \mathbf{\Psi}\mathbf{\Sigma}\mathbf{\Phi}^t. \tag{1.9}$$

Now, let $\mathbf{U}$ be a snapshot matrix, i.e., a matrix filled with ordered snapshots. For instance, in dynamics, matrix dimension n represents the degrees of freedom and dimension m the time steps as formulated in Equation (1.10).

$$\mathbf{U} = [\mathbf{u}(t_1), \dots, \mathbf{u}(t_m)] = \begin{bmatrix} u_1(t_1) & u_1(t_2) & u_1(t_3) & \dots & u_1(t_m) \\ u_2(t_1) & u_2(t_2) & u_2(t_3) & \dots & u_2(t_m) \\ \vdots & \vdots & \vdots & \ddots & \vdots \\ u_n(t_1) & u_n(t_2) & u_n(t_3) & \dots & u_n(t_m) \end{bmatrix}. \tag{1.10}$$

$\mathbf{U} \in \mathbb{R}^{n \times m}$ is a real rectangular matrix and $\mathbf{u}(t_j)$ are the snapshots of the studied field throughout the time variable t at step j. According to the singular value theorem [Eckart and Young 1936], $\mathbf{U}$ can be factorized using SVD as explained in Equation (1.11).

$$\mathbf{U} = \mathbf{\Psi}\mathbf{\Sigma}\mathbf{\Phi}^t = [\mathbf{\Psi}_1\mathbf{\Psi}_2\dots\mathbf{\Psi}_n] \begin{bmatrix} \sigma_1 & 0 & 0 & \dots & 0 \\ 0 & \sigma_2 & 0 & \dots & 0 \\ \vdots & \vdots & \vdots & \ddots & \vdots \\ 0 & 0 & 0 & \dots & \sigma_r \\ \mathbf{0} & \mathbf{0} & \mathbf{0} & \dots & \mathbf{0} \end{bmatrix} \begin{bmatrix} \mathbf{\Phi}_1^t \\ \mathbf{\Phi}_2^t \\ \mathbf{\Phi}_3^t \\ \vdots \\ \mathbf{\Phi}_m^t \end{bmatrix}, \tag{1.11}$$

where $r = min(n, m)$ and $\mathbf{\Psi} \in \mathbb{R}^{n\times n}$ is an unitary matrix containing left-singular vectors (also called modes). $\mathbf{\Phi} \in \mathbb{R}^{m\times m}$ is also an unitary matrix containing right-singular vectors. $\mathbf{\Sigma} \in \mathbb{R}^{n\times m}$ contains positive singular values σ_k in decreasing amplitudes. This decomposition is unique up to an arbitrary sign for the pair $(\mathbf{\Psi}_k, \mathbf{\Phi}_k)$. The SVD factorization in Equation (1.9) can be rewritten into the following rank one expansion as given in Equation (1.12).

$$\mathbf{U} = \sum_{k=1}^{r} \sigma_k \mathbf{\Psi}_k \mathbf{\Phi}_k^t. \tag{1.12}$$

Taking into account only the $rom \leq r$ first singular values of the SVD of $\mathbf{U}$ allow to define a low rank approximation of $\mathbf{U}$ denoted by $\bar{\mathbf{U}}$ as written in Equation (1.13).

$$\bar{\mathbf{U}} = \sum_{k=1}^{rom} \sigma_k \mathbf{\Psi}_k \mathbf{\Phi}_k^t. \tag{1.13}$$

According to the Eckart-Young's low rank approximation theorem [Eckart and Young 1936], $\bar{\mathbf{U}}$ is the best approximation of rank rom of $\mathbf{U}$ with respect to the Frobenius' norm. Moreover, if $rom = r$ then $\bar{\mathbf{U}} = \mathbf{U}$. The relative error can be measured analytically between the snapshot matrix $\mathbf{U}$ and its SVD approximation of lower rank rom as reported in Equation (1.14).

$$\varepsilon(\mathbf{U}) = \sqrt{\frac{\sum_{i=rom+1}^{r} \sigma_i^2}{\sum_{i=1}^{r} \sigma_i^2}}. \tag{1.14}$$

We remark that the smaller the rank approximation rom, the faster the reduced order model computations. However, rom is generally chosen in the way that $\varepsilon(\mathbf{U})$ is lower than 0.1. For reducible problems, i.e., problems with highly energetic first trends, few modes ($rom \ll r$) are then sufficient to arrive to an accurate goal. Having introduced basics of SVD, we now seek to apply this technique to statistical shape analysis. Consider a set of m shapes, i.e., snapshots that have a mesh structure holding a connectivity. Connectivity is the same applied to all studied shapes, thus n points are sufficient to define required snapshots $\mathbf{M}_j$ as formulated in Equation (1.15). Geometries are included in the $\mathbb{R}^{3n}$ space.

$$\mathbf{M}_j = [x_1 y_1 z_1 \dots x_n y_n z_n]^t. \tag{1.15}$$

An existing snapshot $\mathbf{M}_j$ can be written exactly as a linear combination of left-singular vectors $\mathbf{\Psi}$ augmented by coefficients. Remark that left-singular vectors are orthogonal. Coefficients are computed from singular values contained in $\mathbf{\Sigma}$ and right-singular vectors in $\mathbf{\Phi}$. Equation (1.16) shows the coefficients computation whereas Equation (1.17) formulates the linear combination of a specific snapshot $\mathbf{M}_j$. α_k^j refers to the coefficient for the mode $\mathbf{\Psi}_k$ of the snapshot j.

$$\alpha_k^j = \sigma_k \phi_k(j), \tag{1.16}$$

$$\mathbf{M}_j = \sum_{k=1}^{r} \sigma_k \mathbf{\Psi}_k \phi_k(j) = \sum_{k=1}^{r} \alpha_k^j \mathbf{\Psi}_k. \tag{1.17}$$

Modes captures the principal shape variations among all geometrical instances given in the snapshot matrix $\mathbf{U}$. First modes are the most energetic ones because they are weighted by singular values σ_k sorted by a decreasing amplitude manner. Similarly to previous equations, a snapshot $\mathbf{M}_j$ can be expressed into a low rank approximation, see e.g. Equation (1.18).

$$\bar{\mathbf{M}}_j = \sum_{k=1}^{rom} \alpha_k^j \mathbf{\Psi}_k. \tag{1.18}$$

An arbitrary snapshot $\mathbf{M}_j$ can be projected in such truncated basis rom or r, and its coefficients are evaluated in Equation (1.19). The process consisting in finding the most energetic modes for a set of shapes is called Principal Component Analysis. On the contrary, given a well-known and suitable basis, a new shape (not a used snapshot in the SVD) can be projected onto the basis rom or r. This is the idea behind Equation (1.20). Statistical shape analysis aims to recover shape coefficients of an unknown geometry $\mathbf{M}_s$ in order to extract main parameters defining the shape. These main parameters are relative to the previously computed reduced basis. Notice that $\mathbf{M}_s$ must detain the same mesh connectivity to avoid a projection step. Virtual meshes that statistically represent members of a population of snapshots can be thus generated.

$$\alpha_k^j = \mathbf{M}_j . \mathbf{\Psi}_k, \tag{1.19}$$

$$\alpha_k^s(\mathbf{M}_s) = \mathbf{M}_s . \mathbf{\Psi}_k. \tag{1.20}$$

1.3.3 Snapshots and parametric studies

Parametric studies focus on a parametric model for which parameters are well chosen in order to fulfill the desired designing goal. For an input parameter or set of parameters P_1, the solution field $\mathbf{u}(P_1)$ is computed using numerical simulation for example. This is done with several sets of parameters in the way that the parameter space is sufficiently covered. However, it strongly depends on the physics phenomenon and as we already said, large parameter spaces are difficult to sample. Remember that sparse grid techniques are a possible answer [Bungartz and Griebel 2004; Lu, Blal, and Gravouil 2018]. In solid mechanics, the solution field $\mathbf{u}$ could be the displacement field for example. P_1 could be a single shape parameter or a set of mechanical parameters. Figure 1.9 (A) shows the field solutions $\mathbf{u}$ for discrete sets of parameters.

In physics, we are expecting that the solution fields do not vary randomly with input parameters P. But in some cases, small variations of P can lead to big variations of the solution field. That is why physics regularity properties have to be understood before computing these fields with arbitrary parameters P. The solution field $\mathbf{u} \in \mathbb{R}^m$ is embedded in the space $\mathbb{R}^n > \mathbb{R}^m$. It is assumed that all possible solutions taking into account the range of parameters P do not cover the entire space $\mathbb{R}^m$. Figure 1.9 (B) explains this idea. Thankfully, with reduced order modeling tools, a lower dimensional subspace $\mathbb{B}$ can describe the field variation with reliability.

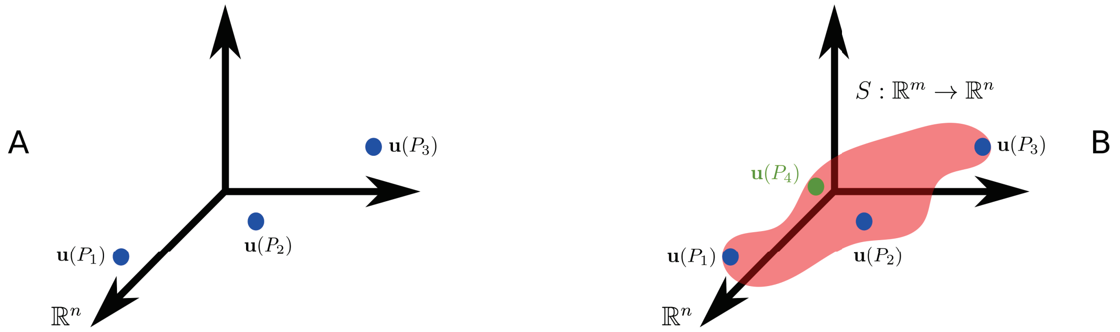

Figure 1.9: Parametric studies and associated dimensional manifolds. (A) $\mathbf{u}(P_1)$, $\mathbf{u}(P_2)$ and $\mathbf{u}(P_3)$ are precomputed solution fields involving sets of parameters P_1, P_2 and P_3. These solutions reside in the $\mathbb{R}^n$ space. (B) Assuming that the physics has not a random behavior, a lower dimensional manifold of dimension m in red can be determined: $S : \mathbb{R}^m \to \mathbb{R}^n$. New green solution $\mathbf{u}(P_4)$ is directly evaluated and computation time is saved.

Nevertheless, some prerequisites are mandatory for ROM construction. ROM computations can not handle large geometrical variations of parameters and topology issues. This work focuses on topological properties of meshes and other geometrical attributes. We aim to build snapshots using morphing techniques between different geometrical instances. This is done in order to compare isotopological information, i.e., same connectivity for meshes and hence same number of nodes. Indeed, in the matrix $\mathbf{U}$, snapshots must have the same dimension. Figure 1.10 illustrates interesting possible morphings.

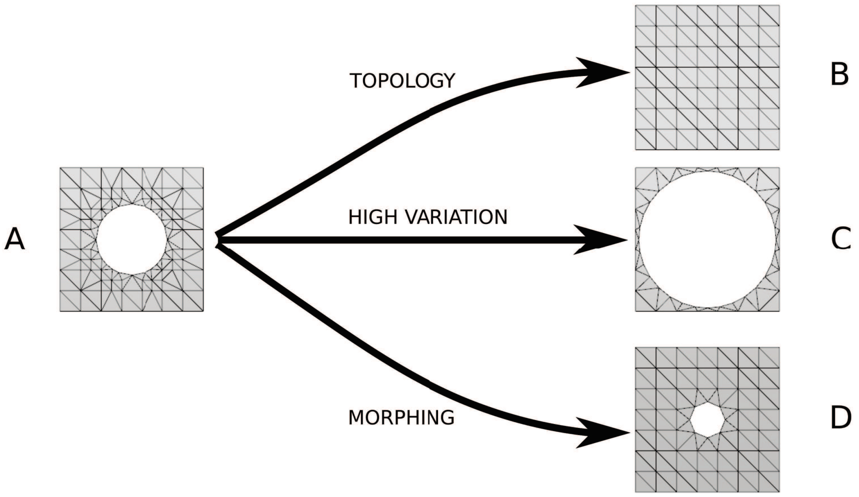

Figure 1.10: Geometrical snapshots morphing issues. (A) Reference mesh shape of studied geometries. (B) Meshes that don't have the same topology can not be morphed and hence, same connectivity between meshes can not be achieved: (A) and (B) can not be snapshots in the same matrix $\mathbf{U}$. (C) High geometrical variation produces high distorted elements. (D) Mesh can be morphed in (A) and inversely. Same snapshot dimension and mesh connectivity can be determined even if depicted meshes do not hold the same mesh discretization for (D). Morphing properties, i.e., homeomorphism properties between topological spaces are not related to mesh discretization, see e.g. Chapter 2.

1.3.4 Isotopological snapshots problematic for ROMs

The construction of parametric studies holding geometrical parameters requires a set of geometries with strong regularity properties. Snapshots are then different shape instances coupled with mechanical parameters, and geometrical ones. Isotopological meshes are required for reduced order modeling with geometrical parameters to avoid an inaccurate projection step. The presented methods in the following are used to obtain such properties of meshes. A first method is presented for quadrilateral meshes (the MEG-IsoQuad strategy), and a second one for volumetric meshes including pure hexahedral and trivariate isogeometric representations (the MEG-IsoHex strategy). Due to the consistent structure of isogeometric meshes and their intrinsic parameterization properties, generating isotopological meshes is more natural.

1.3.4.1 Quadrilateral meshes for mechanical and biomechanical applications

Problem 1.1. (Quadrilateral meshes problematic for ROMs) We want to compute quadrilateral meshes embedded in the topological space $\mathbb{R}^3$ whose properties belong to a very restricted class. The goal is to be able to compare different shapes, i.e., different geometries of the same topology class. These geometries could be used for reduced order modeling objectives. The problematic is illustrated with abdominal aortas in Figure 1.11. We seek to differenciate meshes that have the following desirable properties:

- Minimum number of singularities that are defined to be the nodes with a valency different from 4.
- Alignement with features, curvature directions and boundaries.
- High quality elements, close to a square.
- Constrain the number of elements, connectivity and features locations to enable relevant comparison between studied shapes: homologous comparison with isotopological meshes.

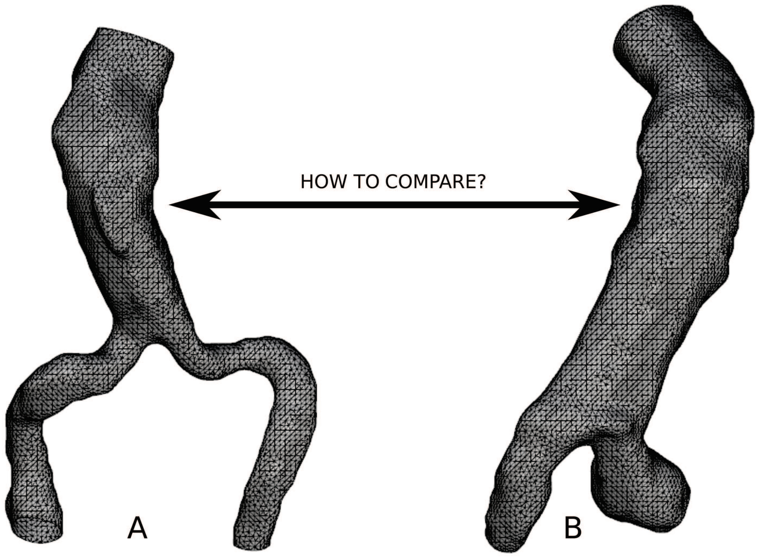

Figure 1.11: Quadrilateral meshes problematic for ROMs of different meshes with the same topology. Problematic is illustrated with abdominal aortas. To overcome this issue, a proposed strategy is given in Strategy 1.1.

Strategy 1.1. (The MEG-IsoQuad strategy)

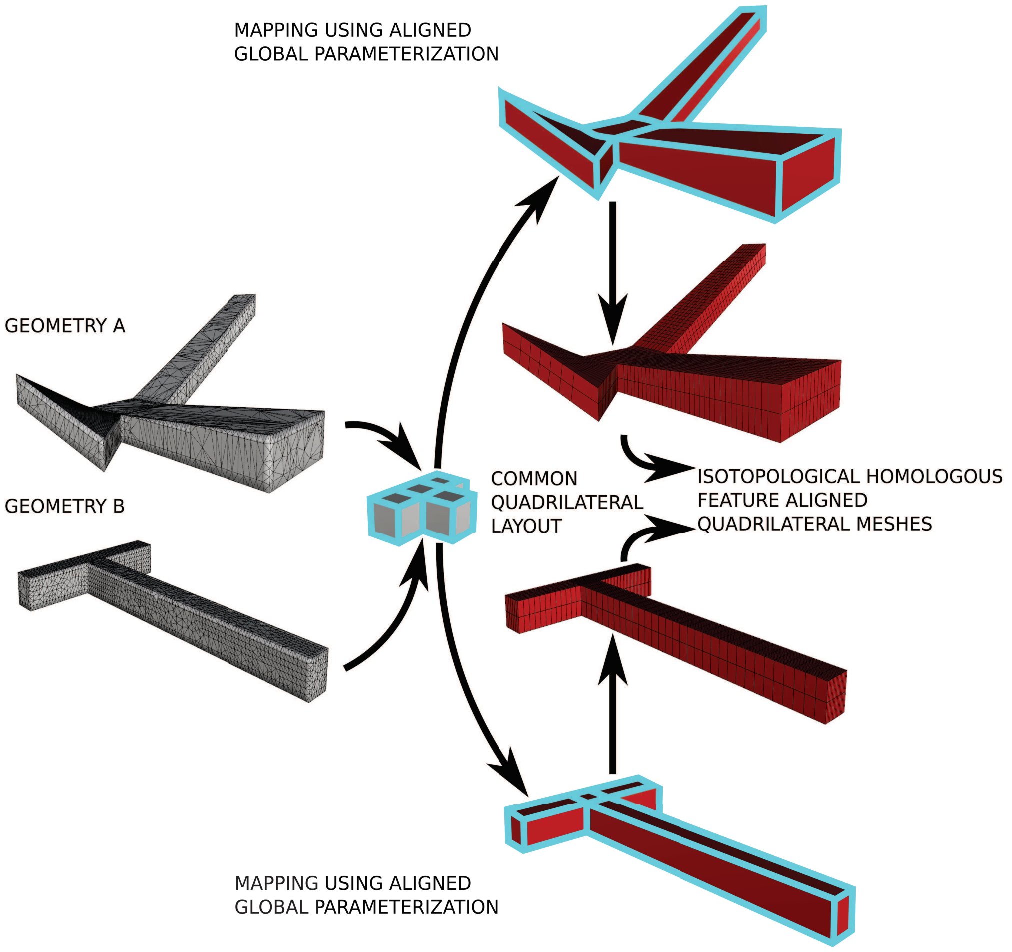

Figure 1.12: The **MEG-IsoQuad strategy**. Building isotopological homologous feature-aligned quadrilateral meshes from triangulated meshes with the same topology. Resulting isotopological meshes have non-uniform isotropy. Quadrilateral meshes have been computed by our IGA_ROM PlugIn (see Appendix B).

1.3.4.2 Isogeometric and hexahedral meshes for computational mechanics

Problem 1.2. (Isogeometric and hexahedral meshes problematic for ROMs) We seek to build volumetric meshes whose properties are specific to reduced order modeling applications. The aim is to be able to compare different shapes with different geometries but with the same structure, i.e., with the same topology. In other words, we want to analyze field differences between distinctives meshes of a population. Since spline meshes need to be structured, relevant hexahedron extraction is straightforward. The most desirable mesh properties usually are:

- Minimum number of high valence nodes.
- Alignement with features, curvature directions and boundaries.
- High quality elements, close to a hexahedron.
- Constrain the number of elements, connectivity and features locations to enable relevant comparison between studied shapes: homologous comparison with isotopological meshes.

Figure 1.13: Isogeometric and hexahedral meshes problematic for ROMs of different meshes with the same topology. Problematic is given as an answer using trivariate splines. To overcome this issue, a proposed strategy is given in Strategy 1.2. Trivariate spline meshes have been computed by our IGA_ROM PlugIn (see Appendix B).

Strategy 1.2. (The MEG-IsoHex strategy)

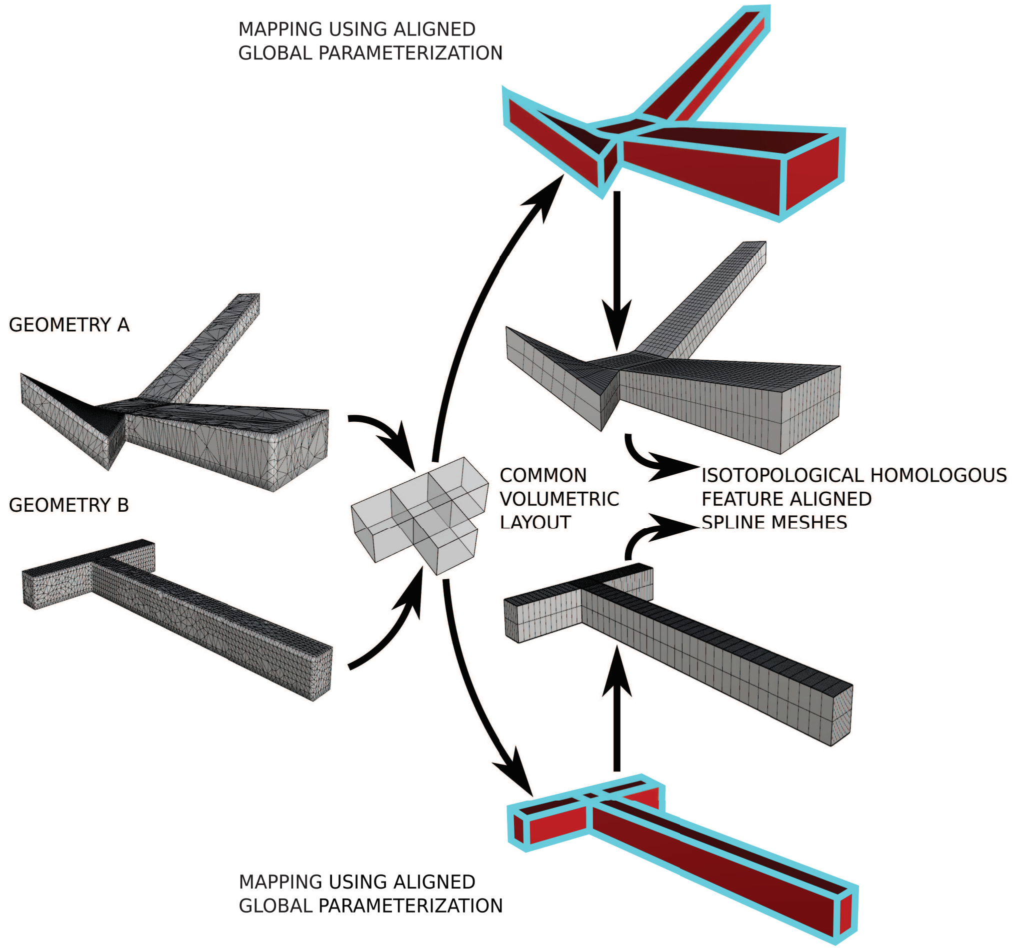

Figure 1.14: The **MEG-IsoHex strategy**. Building isotopological homologous feature-aligned hexahedral or spline meshes from triangulated meshes with the same topology. Resulting isotopological meshes have non-uniform isotropy. Trivariate spline meshes have been computed by our IGA_ROM PlugIn (see Appendix B).

1.4 Conclusion

IGA is a powerful recent analysis technique that uses the same basis functions for solving partial derivate equations and for shape representation. However, automatic generation of trivariate isogeometric meshes remains challenging. CAD models use B-Rep of solids, but in general these geometries are not directly suitable for analysis due to their trimmed nature. The parameterization property of splines objects are greatly appreciated to generate volumetric meshes that have controlled number of elements.

ROMs are mathematical objects used to solve complex physics in near real-time. Construction of such objects requires to accumulate snapshots. Snapshots are precomputed solutions obtained from accurate numerical simulations or experiments. Parametric studies are nowadays more and more used in the industry, e.g. for shape optimization. Thus, these studies must include geometrical aspects. In order to build a ROM with geometrical parameters, studied shapes of the population, i.e., meshes that compose the study have to be isotopological. By isotopological we mean, meshes holding the same connectivity and hence the same number of elements. SVD techniques require snapshots with the same dimension: precomputations have to be performed on isotopological meshes.

This work aims to overcome the issue of having isotopological description of a set of geometries needed for snapshots. IGA is naturally chosen because of the structured properties that holds. Moreover, geometrical aspects are also useful: splines were introduced to describe a geometry. In this spirit and to fulfill our goals, strategies are proposed. Strategy 1.1 is introduced for quadrilateral meshes. Strategy 1.2 is suggested for volumetric isogeometric or hexahedral meshes.

Chapter 2

Topology and parameterization prerequisites

This chapter presents a state of the art in geometry and topology. Surface decomposition methods, parameterization techniques and related theorems for continuous and discrete surfaces will be explained.

Contents

2.1 Topology for geometry processing

2.1.1 Introduction to topology

We briefly introduce needed background in topology for the next developments. Topology is the study of properties like continuity, connectedness and boundaries of a space that are preserved under continuous deformations, such as bending and stretching, but not tearing and gluing. A topological space describes these common properties (see Definition 2.1 for a simplified topological space definition).

Definition 2.1. Topological space. Topological space can be viewed as a set of points and related neighborhoods of these points satisfying specific axioms between them.

A homeomorphism is an isomorphism that admits a continuous function between two topological equivalent spaces that has a continous inverse function as written in Equation (2.1) contained in Definition 2.2. Homeomorphic spaces admit a homeomorphism between them, thus topological spaces are equivalent. Figure 2.1 gives an example of homeomorphic properties. We are interested in transformations that preserve all the topological properties of a given space. In other words, our study focuses on properties of different geometries with same topological attributes. We refer the readers to the books of [Hatcher, Lochak, and Schneps 2000; Hatcher 2001] for more details.

Definition 2.2. Homeomorphism. Homeomorphism is a topological isomorphism, i.e., a continuous deformation function f between two topological spaces with different geometries G_1 and G_2, a mapping that preserves all the the topological properties of the space:

$$f : G_1 \Rightarrow G_2. \tag{2.1}$$

Where f is continuous and bijective. f^{-1} is continuous.

2.1.2 Surface manifolds properties and topological decomposition

2.1.2.1 2-manifold definition and examples

We focus on surfaces, i.e., 2-dimensional topological manifolds as defined in Definition 2.3. For the sake of simplicity, surfaces will be abbreviated 2-manifolds or

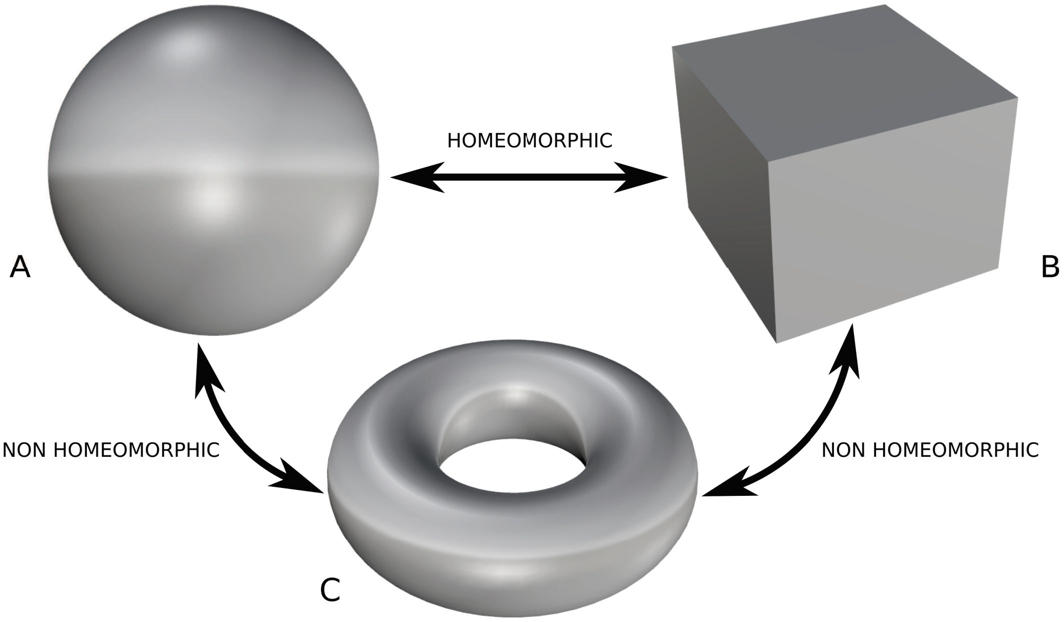

Figure 2.1: Homeomorphic properties of surfaces. (A) A sphere is homeomorphic to the cube (B). Sharp edges are only geometrical aspects not to consider in topological properties. (C) A torus possesses different topological properties than (A) and (B), thus (A) and (C) are non-homeomorphic.

2-dimensional manifolds in the following. Surface manifolds evolve in an euclidean topological space. Euclidean spaces are spaces where each point belongs to a neighborhood homeomorphic to the same euclidean space. 2-manifolds represent surfaces, thus they are embedded in $\mathbb{R}^2$ or $\mathbb{R}^3$. Points with closed half plane $\mathbb{R}^2_+$ neighborhood are defined to be on the boundary ∂M of the surface M. We give in particular the Definition 2.4 for surfaces with borders. Boundaries of surfaces are lower dimensional manifolds: they are 1-dimensional manifolds. In the Euclidean topological space $\mathbb{R}^2$, it is not possible to draw a finite surface without boundaries. For instance, the sphere or torus are embedded in $\mathbb{R}^3$ and have no boundaries. Figure 2.2 depicts some examples and counterexamples of manifolds.

Definition 2.3. **2-dimensional manifold**. A 2-dimensional manifold or 2-manifold M is a topological space in which each point has a neighborhood homeomorphic to the plane $\mathbb{R}^2$.

Definition 2.4. **2-dimensional manifold with boundaries**. A 2-dimensional manifold with boundaries or 2-manifold with boundaries M is a topological space in which each point has a neighborhood homeomorphic to either the plane $\mathbb{R}^2$ or the closed half plane $\mathbb{R}^2_+$.

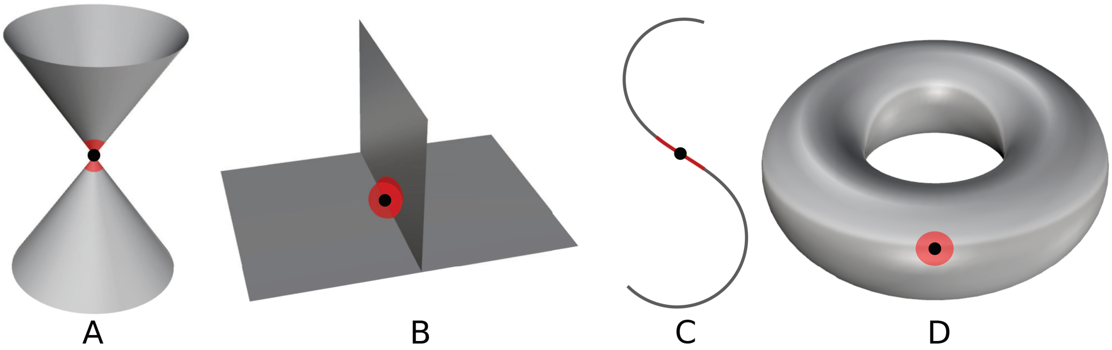

Figure 2.2: 1-manifolds and 2-manifolds. A 1-manifold is topological space that locally looks like to the Euclidean space $\mathbb{R}^1$. A 2-manifold is topological space that locally looks like to the Euclidean space $\mathbb{R}^2$. (A) Double cone is a 2-manifold with boundaries everywhere except in the depicted black point location: double cone is thus a pseudo-manifold with boundaries. (B) Black point neighborhood is not homeomorphic to $\mathbb{R}^2$. (C) 1-manifold. (D) 2-manifold or surface torus.

Connected surfaces are surfaces with only one connected component. In other words, we can walk on the surface without jumping to rejoin another region of the surface. It is a topological space which can not be represented as the disjoint union of non-empty surface subsets. Figure 2.3 (A) represents a disconnected surface whereas Figure 2.3 (B) is a connected one. Orientable surfaces are topological entities such that is possible to establish a difference between two sides. Onto a non-orientable surface, we can draw a connected path which bring us back to the starting point without span a boundary. For instance, the Klein bottle, Möbius underpants or Möbius strip are non-orientable geometric entities as represented in Figure 2.3 (C) for the strip. The cylinder in Figure 2.3 (D) is orientable: we distinguish two differents normals in the same point, the inside and outside ones. Compact surfaces are made with a finite number of triangles, they are composed of a finite number of elements. Surface entities without boundaries are denominated as closed surfaces. Closed surfaces are made compact. In the following we investigate only connected, orientable and compact surfaces possibly with boundaries. In addition, the differentiable property will be mandatory for specific needs.

2.1.2.2 Topological invariants

We now strive to study topological attributes of surfaces in order to estimate topological invariants for surface classification purposes. In this objective, genus of a

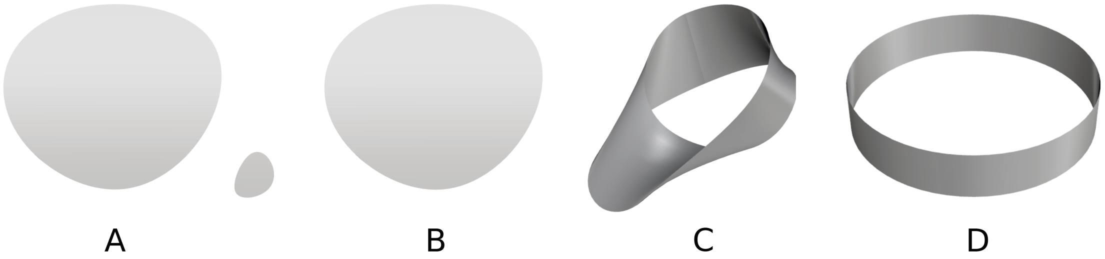

Figure 2.3: Surfaces or 2-dimensional manifolds additional attributes. (A) Disconnected surface. (B) Connected surface. (C) Non-orientable Möbius strip. (D) Orientable cylinder.

surface is given in Definition 2.5. Genus is an integer that states how the surface is self-connected. For instance, a n-torus is a genus-n surface. The genus of a connected, compact and orientable surface with borders corresponds to the genus of the same surface without boundaries. Indeed, adding a finite number of boundaries onto a surface will not change its genus. Figure 2.4 illustrates the two main topological attributes of surfaces: boundaries and genus.

Definition 2.5. Genus of a surface or a 2-dimensional manifold. Genus of a connected, compact and orientable surface M, i.e., a 2-manifold embedded in $\mathbb{R}^3$, is the maximum number of non-intersecting closed curves which can be drawn on it without disconnecting the surface, the complement of these curves staying connected. Genus-g surface will refer to the surface genus g.

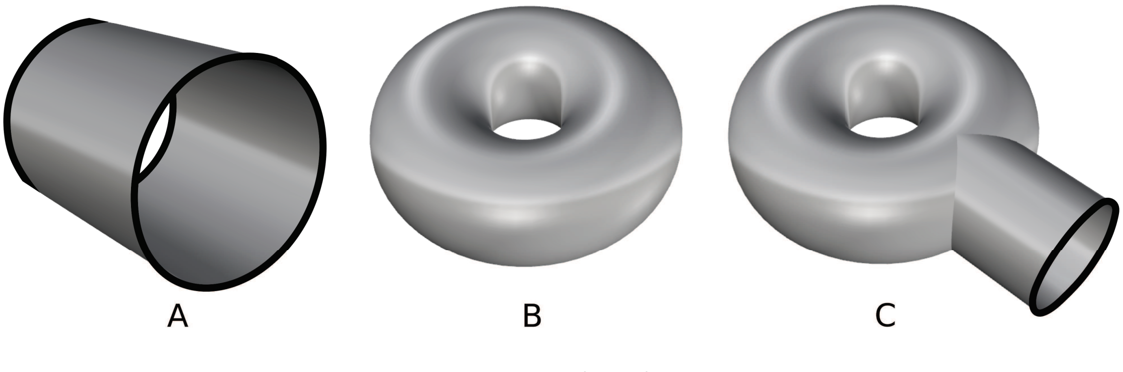

Figure 2.4: Main topological attributes of surfaces. Boundaries are highlighted in black. (A) A cylinder with 2 boundaries. (B) A torus is a genus-1 surface. (C) Genus-1 torus with 1 boundary component.

With this definition, taking into account a genus-g surface M possibly with b boundary components, we can now define a relevant topological invariant. This invariant used to classify surfaces is called the Euler characteristic $\chi(M)$ of a surface M given in Equation (2.2). Surfaces with different Euler characteristic can not be homeomorphic. Notice that the reciprocal is not always true. For instance, a torus and a cylinder have the same $\chi(M)$. Moreover, surfaces with different number of boundaries can not be mapped into each other by a continuous function f. To our best knowledge, genus g and number of boundaries b can not be directly related to homeomorphic properties between 2 arbitrary topological spaces, but for connected, closed surfaces the following Theorem 2.6 is explicit. Theorems 2.7 and 2.8 are also useful to evaluate the Euler characteristic knowing further explicited properties of surfaces.

$$\chi(M) = 2 - 2g - b. \tag{2.2}$$

If M is a triangulated surface with vertices V, edges E and faces F, we can define the characteristic as written in Equation (2.3). For this discrete purpose, 3 geometrically different meshes are computed in Figure 2.5. All depicted meshes M are homeomorphic if an associated continuous surface is considered.

$$\chi(M) = \dim(V) - \dim(E) + \dim(F). \tag{2.3}$$

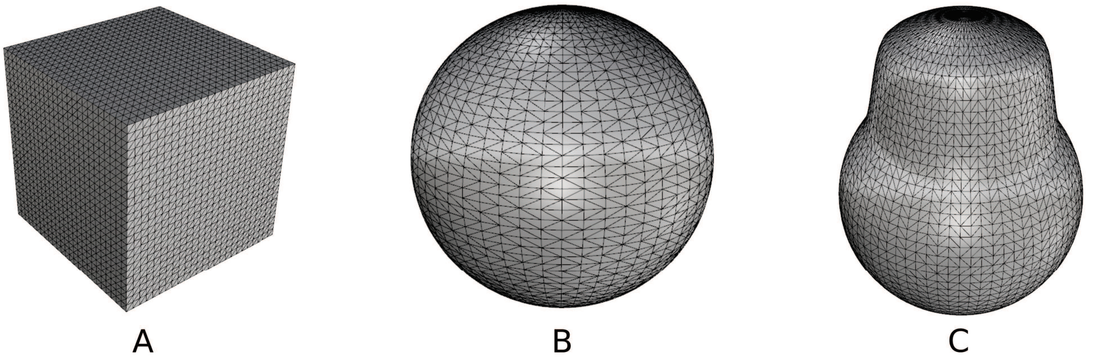

Figure 2.5: Different homeomorphic surfaces with the same Euler characteristic $\chi(M) = \dim(V) - \dim(E) + \dim(F) = 2$. (A) Cube triangulated mesh. (B) Sphere triangulated mesh. (C) Pear-shaped thorium 223 nucleus triangulated mesh [Maquart et al. 2017].

The Euler characteristic can be also obtained simply from Betti numbers. Betti numbers are used to differentiate topological spaces. Figure 2.6 shows some examples of common shapes and their associated Betti numbers. The first Betti number, b_0 counts the number of connect components. Thus, if a connected surface is being considered, $b_0 = 1$. b_1 is an integer value which tells us the maximum amount of cuts that must be made before separating the surface M in two parts. These cuts are executed by joining two boundaries or by making a closed curve. The integer b_2 examines the number of independent cavities. Betti numbers vanish above the dimension of a space, i.e., they equal 0 beyond the dimension of the considered topological space. Similarly to the discrete case, the Euler characteristic is expressed with Betti numbers in Equation (2.4).

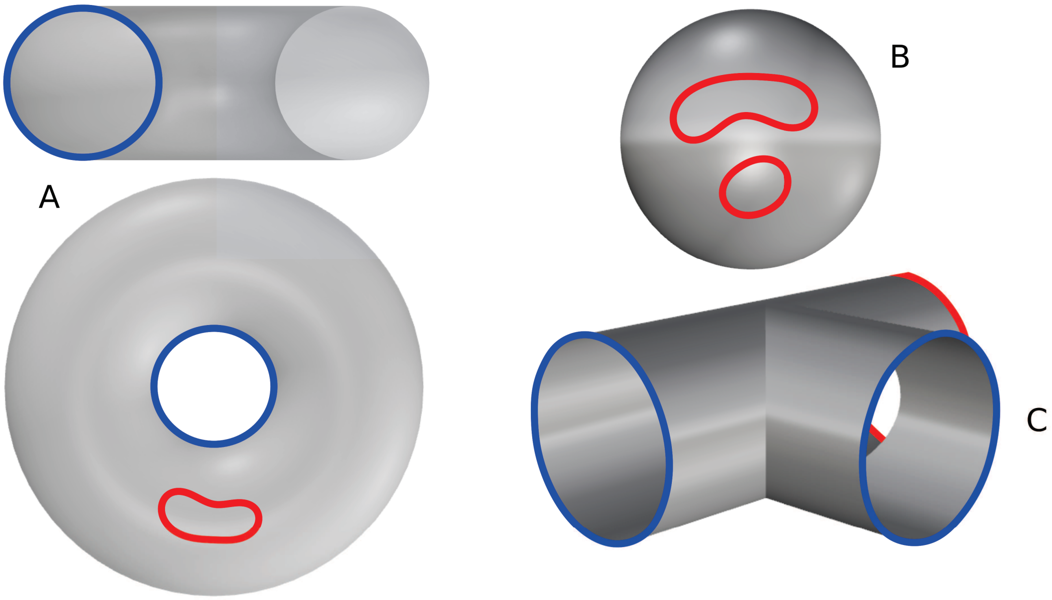

Figure 2.6: Betti numbers for surfaces. Blue curves represent independent 1-dimensional manifolds whereas red ones are dependent or can be continuously shrunk into a point. (A) A surface torus has $b_0 = 1, b_1 = 2$ and $b_2 = 1$. (B) A sphere has no independent 1-dimensional manifolds thus $b_0 = 1, b_1 = 0$ and $b_2 = 1$. Like the torus, the sphere possesses one independent cavity. (C) A 3-way pipe has 2 independent 1-manifolds since the third can be composed by the others blue curves, so $b_0 = 1, b_1 = 2$ and $b_2 = 0$.

$$\chi(M) = b_0 - b_1 + b_2. \tag{2.4}$$

2.1.2.3 Graph theory and cut graphs

A graph G is formed by edges and vertices. Let $G = (V, E)$ be a graph, with a set of vertices V and an edge set E. An embedding of the graph G in a surface mesh M is a mapping between some of vertices and edges of M and G. Graphs are useful 1-dimensional topological entities that are used for lot of applications on discrete surfaces. There exists many different types of graphs depending on certain properties they are holding. For instance, tree graphs are graphs where only one path is possible between two distinct vertices. They are undirected, so there is no privilegiate direction between two vertices. A spanning tree, is a special case of a tree graph that can be particularly embedded into a mesh M which includes all the vertices of M. Forest of trees are disjoint union of tree graphs. Other graphs are said to be complete, i.e., all vertices are connected with all others by edges. In Chapter 3 the well-known Dijkstra's algorithm [Dijkstra 1959] is used to compute shortest paths on meshes resulting in shortest-paths trees. Weighted graphs are used to determine such particular paths: edges are assuming a specific metric.

Among the large abundance of different graphs types, one is useful for futher developments: the cut graph. A cut graph G is an embedding of a graph G in a surface M whose compliment is a topological disk. In other words, when slicing a mesh along the edges of G, it allows to deal with a surface which is homeomorphic to a disk; a surface with only one boundary and Euler characteristic equal to $\chi(M) = 1$.

2.1.2.4 Homotopy and homology theories

First stage of homotopy comprehension objectives is to define the notion of homotopic paths on surfaces as defined in Equation (2.5) contained in Definition 2.6. A path p on a surface M is continuous map $m_p : [0, 1] \to M$. Homotopy is a topology branch that investigates continuous deformations between topological spaces, i.e., 1-dimensional or 2-dimensional manifolds and so on. Difference to homeomorphism is that topological properties are not necessarily conserved during the transformation. For instance, a disk can be continuously deformed into a point, but the topological spaces have different properties. In the following developments, genus-g surface M with b boundary components ∂M are studied. ∂M represents the set of b borders belonging to the surface. Loops are considered as closed paths. By closed we mean a path with the same endpoints. Paths or loops can be drawn on surfaces and hold specific properties. This is the idea depicted in Figure 2.7. Figure 2.7 (A) shows homotopic paths whereas Figure 2.7 (C) depicts non-homotopic loops.

Definition 2.6. Homotopic paths on a surface M. Two paths p_1 and p_2 are homotopic if and only if one path can be continuously deformed into the other by passing through a family of paths on the surface M. More formally, a homotopy between p_1 and p_2 with endpoints a and b, is a continuous map $h : [0, 1] \times [0, 1] \to M$ such that [Verdière and Lazarus 2007]:

$$h(0, q) = p_1, h(1, q) = p_2, h(r, 0) = a \ \& \ h(r, 1) = b \ \forall \ q, r \in [0, 1]. \tag{2.5}$$

We introduce a chain γ as an oriented 1-manifold embedded in M. Chains are not necessarily connected and can be composed of multiple components. A cycle is thus defined as a chain with no boundaries, i.e., without 0-dimensional manifold: $\partial\gamma = \emptyset$. Cycles can be viewed as loops for paths but with chains attributes. Properties of chains and cycles are defined in Property 2.1. Figure 2.7 (D) represents two chains;

the chain γ_1 that is composed by two connected components. Figure 2.7 (E) and (F) are showing different cases of homological cycles.

Property 2.1. Chains and cycles properties. These properties have been extracted from the papers of [Ray et al. 2008] and [Erickson and Whittlesey 2005]. Some definitions are slightly modified to suit the following developments.

- A chain γ is oriented, thus it as a unique tangent vector $\mathbf{t}_\gamma$. With this tangent vector and the surface normal $\mathbf{n}$, defining an orthonormal frame is straightforward. $(\mathbf{t}_\gamma, \mathbf{n}_\gamma, \mathbf{n})$ being the direct frame.
- The reversal of a chain $-\gamma$ is the chain with opposite orientation: $\mathbf{t}_{-\gamma} = -\mathbf{t}_\gamma$. $-\mathbf{n}_\gamma$ is associated to $\mathbf{t}_{-\gamma}$ in order to conserve the same surface normal.
- ∂ is called the boundary operator, such that ∂M is the subset of points of the surface M with a neighborhood homeomorphic to the half plane. This subset is a cycle γ composed by many connected components. We can choose an orientation for this cycle by requiring its conormal to point outwards the surface. In this case, we say that the cycle is a boundary.
- A chain is called exact if there exists a submanifold $Sub(M)$, i.e., a part of the surface M such that $Sub(\partial M) = \gamma$. An exact chain is a cycle which is also a boundary.
- If M is a sphere, all cycles which can be drawn on the surface are said to be contractibles cycles, i.e., they can be shrunk into a point. In other words, it is homotopic to the null loop or constant loop.
- Two cycles γ_1 and γ_2 are homological cycles if and only if $\gamma_1 - \gamma_2$ or $\gamma_1 \cup -\gamma_2$ is exact. The union $\cup$ is omitted in the following. Homological cycles can have different number of connected components. Homology is a more flexible concept than homotopy. We can compose cycles with the homology concept, with operations on cycles such as splitting or fusionning. Homotopy does not accept this kind of discontinuous transformations.

We briefly introduce the concept of homotopy basis. For that purpose, we refer the readers to the work of [Erickson and Whittlesey 2005] or [Verdière and Lazarus 2005] for visual elements. We define a system of loops as a cut graph G with only one node: the common node of all loops in the system. Here, we focus on continuous surfaces, a system of loop is thus a set of loops drawn on a surface, but they are intersecting into only one specific location: the only node of the system of loops without others self-intersections. A homotopy basis is a generalization of this

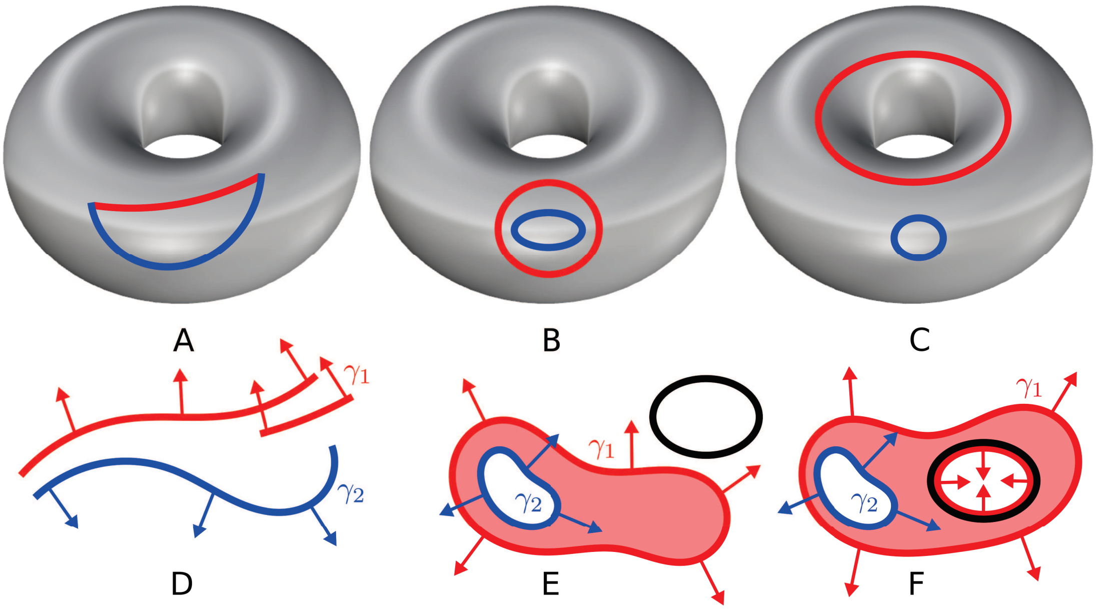

Figure 2.7: Homotopy and homology properties of paths, loops and chains. (A) Homotopic paths. (B) Homotopic loops. (C) Non-homotopic loops. (D) Two chains. (E) $\gamma_1 - \gamma_2$ or $\gamma_1 \cup -\gamma_2$ is exact, thus they are homologic. Black curve is an arbitrary surface boundary. (F) $\gamma_1 + (-\gamma_2)$ is also exact: they are boundaries of the red surface. Blue and red vectors represent $\mathbf{n}_\gamma$.

concept. It consists of a set of $2g$ loops for a closed genus-g surface M as shown in Figure 2.8 (A). Every system of loops is a homotopy basis, but the reciprocal is not true. Like we said before, homotopy basis is a less flexible concept than homology basis. Self-intersections or intersections generate additional nodes in the homotopy basis. These additional nodes can not be removed by continuous functions f, i.e., by homotopy processes.

Aiming to define a homology basis that requires less properties than homotopy because of the acceptance of discontinuous transformations with cycles, the definition is given in Definition 2.7. For a closed genus-g surface M, this homology basis is composed by a set of $2g$ loops as depicted in Figure 2.8 (B). An homotopy basis is also an homology basis, but the reciprocal is not true. We recall for readers that these considerations are made for compact, connected and orientable surfaces [Erickson and Whittlesey 2005]; to our best knowledge, it has to be studied carefully in the general case for arbitrary topological spaces. Indeed, cycles in a homology basis do not have a common point in the general case. The tunnel and handle loops are defined to be an homology basis for a closed genus-g surface M. [Dey et al. 2008] gives a formal definition of such relevant loops. Suppose a closed surface $M \subset \mathbb{R}^3$ which separates the topological space $\mathbb{R}^3$ into a bounded space $\mathbb{I}$ and an unbounded space $\mathbb{O}$. A loop l_1 is a tunnel if it spans a disk in the unbounded space $\mathbb{O}$. A loop l_2 is a handle if it spans a disk in the bounded space $\mathbb{I}$. These loops have been widely studied in the geometry community [Verdière and Lazarus 2005; K. Dey, Li, and Sun 2007; Verdière and Lazarus 2007; Dey et al. 2008; K. Dey, Fan, and Wang 2013]. In Figure 2.8 (B) handle and tunnel loops form a homology basis of the surface M.

Definition 2.7. Homology basis by [Ray et al. 2008]. The non-empty set of cycles $H^1(M) = \{\gamma_i^H\}_{i\in[1,n]}$ define a homology basis for a genus-g surface M with borders b if it satisfies:

- Linear independence condition: $\sum a_i\gamma_i^H \equiv_l \emptyset \Leftrightarrow a_1 = ... = a_n = 0$,
- Spanning condition: $\forall\gamma,\ \exists a \in \mathbb{Z}^n$ such that $\gamma \equiv_l \sum_{i=1}^n a_i\gamma_i^H$.

Any cycle embedded in M is homological to a formal sum of the basis cycles. n represents the number of cycles contained into the basis. $\equiv_l$ denotes the homological equivalence.

To be more precise, and for futher developments we define homology basis components as written in Proposition 2.1. Classes of homotopy and homology are explicted in Proposition 2.2. We are only interested on the first group of homotopy $\pi_1(M, x)$ and first group of homology $H^1(M)$. We refer the readers again to more formal topological developments in the books of [Stillwell 1993; Hatcher 2001] or papers of [Erickson and Har-Peled 2004; Erickson and Whittlesey 2005]. Homology groups are relevant information to evaluate the Euler characteristic of a surface M. Since homotopy basis is also an homology basis, homotopy groups are also important information for the topological invariant χ. Homology and homotopy groups are profound and useful topological invariants, but they are very far from sufficient to classify spaces up to homeomorphism in the general case. Important thing is that the Betti number b_n represents the rank or length of the homology group H^n, composed by n-dimensional objects.

Proposition 2.1. Homology basis components. For a compact, connected and orientable genus-g surface M with b boundary components, the number of cycles has length $\dim(\gamma_i^H) = n = 2g + b - 1$. This comes from the fact that the last boundary of a genus-0 surface can be composed by the others by homology theory. We name the $2g$ cycles as homology generators. $b - 1$ boundary cycles and homology generators form a homology basis. Notice that for the sphere, it is not applicable [Ray et al. 2008].

Proposition 2.2. Homotopy groups, homology groups and associated classes.

- A homotopy group $\pi_1(M, x)$ is a set of loops which are 1-dimensional entities with a basepoint x embedded on the surface M. Into the set $\pi_1(M, x)$, each loop can be continuously deformed into its influence zone on the surface. Thus a homotopy class defines all possibilities of homotopic tranformations on M for a given loop in π_1. We call this an homotopy class on the surface M.
- A homology group $H^1(M)$ is a set of cycles which are 1-dimensional entities without basepoint embedded on the surface M. $H^1(M)$ is composed by $2g$ and $b-1$ cycles. On M, each cycle contained in $H^1(M)$ belongs to its own homology class: two cycles of a same class are homologic. Two homology cycles are in the same homology class if one can be continuously deformed into the other via a deformation that may include splitting cycles at self-intersection points, merging intersecting pairs of cycles, or adding or deleting separating cycles [Erickson and Whittlesey 2005].

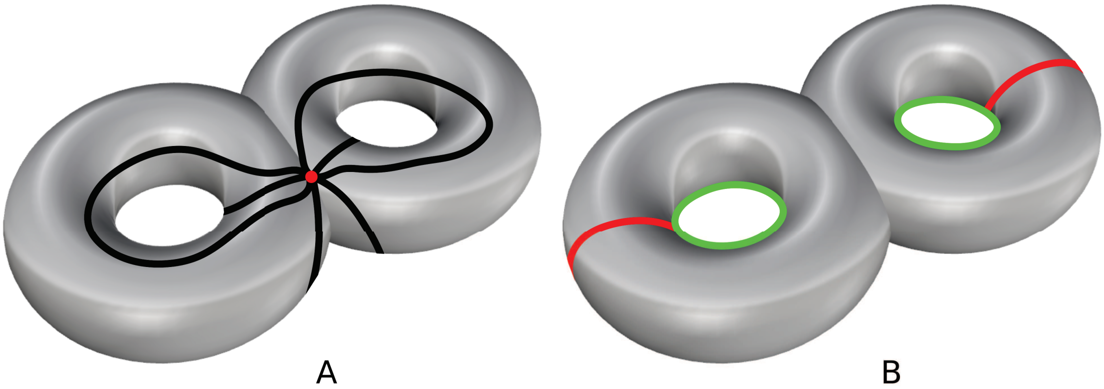

Figure 2.8: Homotopy basis and homology basis for a closed genus-g surface M: a double torus. (A) System of loops which is a homotopy basis with its red basepoint x. (B) Homology basis. Handle loops are depicted in red whereas green curves are tunnels loops. Tunnel loops are shortest as possible in terms of arc length in this example.

2.1.2.5 Basics of pants decomposition

A pant is a basic genus-0 topological object M with 3 boundaries and Euler characteristic $\chi(M) = -1$. It is a canonical domain like the sphere, the disk or the cylinder but a little bit more complicated from a topological point of view. For a complicated surface, with an arbitrary topology, work has been done for years to find such pants decompositions [Hatcher, Lochak, and Schneps 2000]. Finding the optimal segmentation of a given surface into relevant pants patches has been tackled by [Verdière and Lazarus 2007] using the shortest homology basis [K. Dey, Sun, and Wang 2010]. Geometry-aware pants decomposition has been also investigated by [Zhang and Li 2014]. [Li, Gu, and Qin 2009] developed a pants decomposition framework to compute maps between surfaces with arbitrary topologies. An example of pants decomposition using a homology basis is shown in Figure 2.9. More recently [Hajij, K. Dey, and Li 2016] tried to segment surfaces into pants using a morse function.

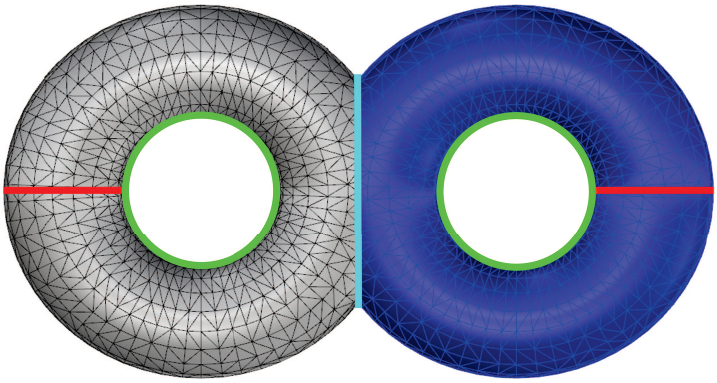

Figure 2.9: Pants decomposition of a double torus mesh computed from a CAD model by our IGA_ROM PlugIn (see Appendix B). A double torus is a genus-2 surface without boundary and has Euler characteristic $\chi = 2 - 2g - b = -2$. Pants decomposition provides two pants (gray and blue meshes) by cutting along handle loops and using symmetry (symmetry loop is depicted in cyan). Homology basis is composed by two handle loops and two tunnel loops respectively depicted in red and green.

Let $M_{g,b}$ be a surface of genus g with b boundary components. A pants decomposition of $M_{g,b}$ is a collection of pairwise disjoint simple cycles that splits the surface into pants patches. Each pants patch is a genus-0 surface with 3 boundaries. We assume that M is a surface with negative Euler characteristic, i.e., M is none of the surfaces $M_{0,0}$ (topological sphere), $M_{0,1}$ (topological disk), $M_{0,2}$ (topological cylinder) and $M_{1,0}$ (topological torus). In this case, pants decompositions of M do exist, and each pants decomposition consists of $3g + b - 3$ curves and divides M into $2g + b - 2 = -\chi(M)$ pants patches. For $M_{g,b}$, pants decomposition is possible if and only if Equation (2.6) is satisfied. Figure 2.10 illustrates a famous pant decomposition result working on a level-1 Sierpinski sponge.

$$\chi(M) = 2 - 2g - b \leq -1. \tag{2.6}$$

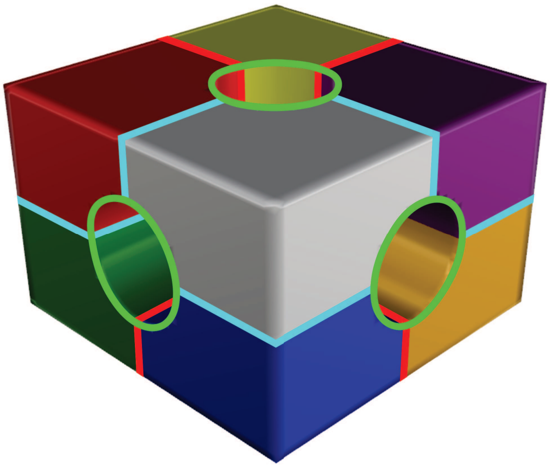

Figure 2.10: Pants decomposition of a level-1 Sierpinski sponge computed by our IGA_ROM PlugIn (see Appendix B). It is a genus-5 surface without boundaries. Red and green loops define the homology basis composed by $2g$ loops. Red ones are handle loops, green ones are tunnel loops. Some of loops are hidden by the volume. $\chi(M) = -8$, so 8 topological pants are depicted in different colors (7 are visible).

2.1.3 Geometric representations

2.1.3.1 Continuous case

Representing surfaces can be made by different techniques. In this work, we focus on mappings, i.e., parametric surfaces which are one of the three differents classes of surfaces types. We name implicit, explicit and parametric representations. The parametric one attracts our attention. The concept is to describe a surface through a mapping with two coordinates: $f(u,v) : \Omega \to \mathbb{R}^3$ as depicted in Figure 2.11 for a continuous surface. A relation is established between the parametric domain $\Omega \subset \mathbb{R}^2$ and the embedded surface in the topological space $\mathbb{R}^3$.

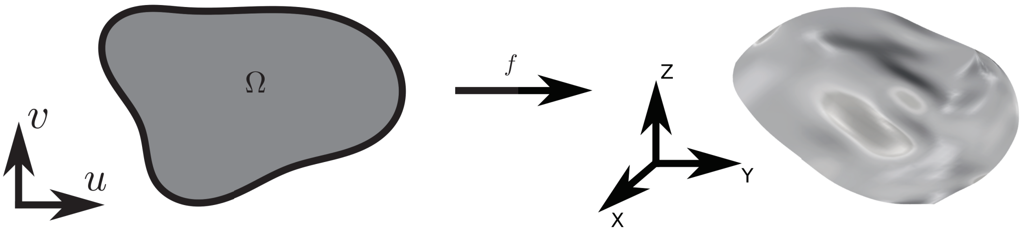

Figure 2.11: Continuous mapping of a surface. $\Omega \subset \mathbb{R}^2$ is the parametric domain. f is the mapping function which maps Ω to a surface embedded in $\mathbb{R}^3$.

2.1.3.2 Mesh representations

In computer graphics and numerical methods communities, the most used discrete representation is the triangle mesh for surfaces or tetrahedral mesh for volumes. Surface meshes are the classical representation of surfaces in $\mathbb{R}^3$. A surface mesh $M = (V, E, F)$ is a composition of three sets: the vertices V, the edges E and the faces F. Each vertex $v_i \in V$ is a vector in $\mathbb{R}^3$. Each edge $e_i \in E$ is a pair of two vertices: $e_i = (v_j, v_k)$. Each face $f_i \in F$ is composed by vertices and edges which are connected respecting a specific connectivity to form a suitable topological polygon.

We introduce some useful vocabulary for meshes. Two elements are said to be incident if the vertices of one are a subset of the vertices of the other. In other words, faces can be incident at a common vertex. Incidence describes the neighborhood relation between elements of different dimensions, adjacency is a similar concept for entities of equal dimension. Adjacent vertices are incident to a common edge, adjacent edges are incident to a common vertex and adjacent faces overlap at a common edge [Al-Akhras 2016].

The valence of a vertex is the number of edges incident to him. An edge of a given mesh M is on a boundary, i.e., is a boundary and a 1-dimensional manifold of M if it is incident to a single face. We call an interior edge an edge incident to two different faces. If an edge is incident to more than two faces, thus the discrete surface mesh M is considered to be non-manifold.

Dual mesh is characterized by $M^* = (V^*, E^*, F^*)$ constructed from the primal one $M = (V, E, F)$. This dual entity is an isomorphism which is a one-to-one mapping between the primal n-dimensional entities of the structure to the $(2-n)$-dimensional entities. The process can be inversed. 0-dimensional entities are known for vertices V, 1-dimensional entities for edges E and 2-dimensional for faces F. More formally, each vertex v_i is mapped to a dual face f_i^*, each edge e_i is mapped to a dual edge e_i^* and each face f_i is mapped to a dual vertex v_i^*. Remark that the connectivity of the dual mesh is inherited from the primal mesh.

A simplicial complex is a union of discrete n-dimensional counterparts. Into such simplicial complexes, we can find a 0-simplex which is a point, a 1-simplex which is a line, a 2-simplex which is a face and so on. The term simplices designates a set constituted by many simplex. A simplicial complex is then denominated as a simplicial n-complex depending on the higher n-dimensional counterpart in his composition.

Triangles possess an intrinsic parameterization. Each triangle with points p_i, p_j and p_k can be parameterized by the barycentric linear mapping $\mathbf{B}(u, v) = u \times p_i + v \times p_j + (1 - u - v) \times p_k$ with $u, v > 0$ and $u + v \leq 1$. In practice, all these individual triangle mappings are often combined into one piecewise linear mapping. That is why triangles are useful to compute inverse mappings.

Nowadays, quadrilateral meshes are widely studied. They are preferred because of their superior structure, regular shape and level of accuracy for numerical methods. Quadrilateral meshes are often used over triangle meshes especially in animation and mostly for texture rendering purposes [Dischler et al. 2002]. However, it is important to notice that in general, a quadrilateral mesh is not a geometry representation comparable to a triangle mesh. In contrast to a triangle, a quadrilateral might be non-planar and possibly non-convex.

2.1.4 Useful theorems

Useful theorems for following developments will be detailed here. They are adapted to suit the further explanations linked with our problematic. Theorems concerning geometry, topology and parameterization are explicited. Some of them are fundamental tools used to fulfill mathematical needs. Others are given for a general comprehension throughout the next chapters. Explicited form of Theorem 2.1 serves to analyze fields (or n-symmetry direction fields which are developed in the succeeding part) behavior on surfaces M and more particularly the properties of singularities. Theorem 2.2 is an equivalent formulation which introduces the notion of boundary. A famous corollary of the Poincaré-Hopf theorem is also formulated in Corollary 2.1. The Gauss-Bonnet theorem is an important result in the topology field that states the link between topology and geometry in an integral manner (see Theorem 2.3). The Radó-Kneser-Choquet theorem is defined in Theorem 2.4 and informs on bijective mappings for parameterization goals. Indeed, bijective mappings avoid fold-overs. The formulation in Theorem 2.5 evaluates some properties of mappings. To close the list of useful theorems, Theorems 2.6, 2.7 and 2.8 are closely related with the Euler characteristic.

2.1.4.1 Poincaré-Hopf theorem and corollary

Theorem 2.1. Poincaré-Hopf theorem. Let M be a compact differentiable manifold and $\mathbf{d}$ be a 4-symmetry direction field with n_s isolated singularities of indices $I^i_{\mathbf{d}}$ embedded in vertices v or points P in the surface M. If M has some boundaries, the field must be pointed outward the normal direction along them, i.e., relative to the following boundary number theorem in Theorem 2.2:

$$\sum_{i=1}^{n_s} I^i_{\mathbf{d}} = \chi(M). \tag{2.7}$$

Where $\chi(M)$ is the Euler characteristic of the surface M. In the context of this thesis, we are interested only on connected, compact and oriented differentiable manifolds possibly with boundaries.

Corollary 2.1. Poincaré-Hopf corollary. Every surface homeomorphic to a sphere must have at least one singularity: every horse must have at least one mane.

2.1.4.2 Boundary number theorem

Theorem 2.2. Boundary number theorem. Let M be a compact differentiable 2-manifold embedded in $\mathbb{R}^3$ with boundaries ∂M and $\mathbf{d}$ be a n-symmetry direction field, then:

$$T_{\mathbf{d}}(\partial M) = -\chi(M). \tag{2.8}$$

Where $\chi(M)$ is the Euler characteristic of the surface M and ∂M is the set of boundaries. We can demonstrate that the boundary turning number theorem is equivalent to the Poincaré-Hopf theorem (see Theorem 2.1) with a proper definition of the index of singularity [Ray et al. 2008]. For that purpose, we refer the readers to a personal recent work [Maquart 2018]. We recall that, in this thesis, interesting surfaces are only connected, compact and oriented differentiable manifolds possibly with boundaries.

2.1.4.3 Gauss-Bonnet theorem

Theorem 2.3. Gauss-Bonnet theorem. This theorem links the total Gaussian curvature and total geodesic curvature to a topological invariant. In other words, this theorem states the connection between topology and geometry:

$$\int_M K dS + \int_{\partial M} kg \; ds = 2\pi\chi(M). \tag{2.9}$$

Where K is the Gaussian curvature on the surface of area S and kg the geodesic curvature along boundary cycles $\gamma(s) \in \partial M$. s is an arc length parameter, which parameterizes the cycle $\gamma(s)$. More formally, this theorem investigates compact 2-dimensional Riemannian manifolds with boundaries. For connected, compact and oriented differentiable 2-manifolds M, Equation (2.9) remains valid.

2.1.4.4 Radó-Kneser-Choquet theorem

Theorem 2.4. Simplified Radó-Kneser-Choquet theorem. Suppose f as a harmonic function of a mapping process. The parametric space S_m of the mapping is convex, $S_m \subset \mathbb{R}^2$ and the boundary ∂M of a topological disk M is mapped homeomorphically to ∂S_m, thus f is bijective. With these conditions and positive vertices weights for discrete maps, f has to be bijective.

2.1.4.5 Isometric theorem

Theorem 2.5. Simplified isometric theorem. Any mapping with a function f is said to be isometric if angles and surfaces are conserved. In other words, an isometric mapping preserves length if this mapping is conformal (angle preserving) and equiareal (area preserving). Developable surfaces admit this kind of isometric map.

2.1.4.6 Euler characteristic related theorems

Theorem 2.6. Classification theorem. Two connected, closed and orientable surfaces M_1 and M_2, i.e., 2-manifolds, are homeomorphic if they have the same Euler characteristic:

$$\chi(M_1) = \chi(M_2). \tag{2.10}$$

This theorem is applicable to surfaces which are also non-orientable; but we consider only compact, connected and orientable surfaces in this development: this theorem holds.

Theorem 2.7. Topological invariance theorem. The Euler characteristic is a topological invariant. For two topological spaces X and Y, if X is homeomorphic to Y, then:

$$\chi(X) = \chi(Y). \tag{2.11}$$

Theorem 2.8. Homotopy invariance theorem. The Euler characteristic is a homotopy invariant. For two topological spaces X and Y, if X is homotopic to Y, then:

$$\chi(X) = \chi(Y). \tag{2.12}$$

2.1.5 Continuous fields on surfaces

Many algorithms in computer graphics and geometry processing are based on smooth direction fields, i.e., unit tangent vector fields defined on a surface M. For instance, such direction fields were used to steer the orientation of features in texture synthesis [Praun, Finkelstein, and Hoppe 2000; Turk 2001], or to remesh a surface with cells aligned with the principal curvature directions [Alliez et al. 2003; Marinov and Kobbelt 2004]. Encountered recent applications use objects of higher symmetry than simple unit vector fields. Using objects invariant by rotation of π or $\pi/2$ around the surface normal allow us to increase the symmetry properties of the field. These objects are called n-symmetry direction fields. N being the symmetry of the field. At every point of the surface M we associate N unit vectors forming equal angles between radially consecutive directions. For instance, 2-symmetry direction fields are lines, 4-symmetry direction fields are cross fields. Cross fields are used for quadrilateral meshing purposes [Bommes, Zimmer, and Kobbelt 2009; Bommes 2012; Campen and Kobbelt 2014] and 6-symmetry fields helped to remesh with hexagons.

Direction fields hold different properties than classical vector fields. They have been introduced to better understand the topology of the studied surface M. because they have a unit norm, their singularities can not be defined as zeroes. Holes solve the problem. In quadrilateral meshing processes, the singularities are important information not to neglect. Indeed, they guide the mesh irregular connectivity. Reseachers have proposed a large set of methods to compute a suitable 4-symmetry direction field with prescribed properties. [Ray et al. 2008] were the first to present a robust pipeline mathematically and firmly anchored to design such n-symmetry fields for arbitrary surfaces. Different approaches exist to compute the field behavior which is partially based on related singularities. A number of methods tackle user-defined locations of singularities [Ray et al. 2008; Crane 2010; Crane, Desbrun, and Schröder 2010; Lai et al. 2010] and other methods solve singularity positions automatically [Bommes, Zimmer, and Kobbelt 2009; Ray et al. 2009; Knöppel et al. 2013]. Such fields are subject to the Poincaré-Hopf theorem and boundary number theorem [Ray et al. 2008] (see Theorem 2.1 and Theorem 2.2 respectively). Illustrated singularities can be found in [Li et al. 2006], for 2-symmetry direction fields able to hold indices of 1/2.

2.1.5.1 Continuous n-symmetry direction field representation

A direction field defined on a surface M is a tangent unit vector field: at each point of the surface, there exists a direction $\mathbf{u}$ such that $\|\mathbf{u}\| = 1$ and $\mathbf{u}.\mathbf{n} = 0$, where $\mathbf{n}$ is the normal of M. A n-symmetry direction field $\mathbf{d}$ is a multivalued direction field: at each point of the surface M, there exists a n-symmetry direction $\mathcal{U}$ which is a set of N directions $\{\mathcal{U}_1,\mathcal{U}_2,...,\mathcal{U}_{N-1},\mathcal{U}_N\}$ preserved by rotations of $2\pi/N$ around the normal $\mathbf{n}$ of M. We introduce in particular a 4-symmetry direction field $\mathcal{C}$, i.e., a set of 4 directions $\{\mathcal{U}_c, \mathcal{V}_c, -\mathcal{U}_c, -\mathcal{V}_c\}$ preserved by rotations of $\frac{2\pi}{4}$ around the normal $\mathbf{n}$. 4-symmetry direction fields are named cross fields $\mathcal{C}$ due to their 4-symmetry properties. These cross fields are used later in Chapter 4.

2.1.5.2 Field singularities and turning numbers

The singularities of a vector field or a n-symmetry direction field embedded on a surface are commonly a set of a finite dimension. If we define a vector field on a surface M such as $\mathbf{d} : \mathbb{R}^2 \to \mathbb{R}^2$, the set of zeroes are the singularities, i.e., the set of $\mathbf{d}$ that respect: $\{\mathbf{d}(x, y) = \mathbf{0}\}$ for each singularity placed at (x, y). Depending on the n-symmetry of the field, the singularities can be classified by their index $I_{\mathbf{d}}(P_i)$ around a neighborhood Ω of points P_i in place of singularities as written in Equation (2.13).

$$I_{\mathbf{d}}(P_i) = \frac{1}{2\pi} \int_{\partial\Omega(P_i)} d\theta. \tag{2.13}$$

In addition, if we design a cycle $\gamma(s)$ to be equal to the boundary of the neighborhood Ω, we can express the field singularities as in Equation (2.14). Recalling that s is an arc length parameter, which parameterizes the cycle $\gamma(s)$.

$$I_{\mathbf{d}}(P_i) = \frac{1}{2\pi} \int_{\gamma(s)=\partial\Omega(P_i)} \kappa_{\mathbf{d}} ds. \tag{2.14}$$

Where $\kappa_{\mathbf{d}}$ is the field curvature. With the previous correct definitions of field singularities, we now describe the number of turns a field $\mathbf{d}$ can make along a given cycle $\gamma(s)$. Turns of the field are accomplished in a specific frame [Ray et al. 2008]. This amount of turns is called the turning number $T_{\mathbf{d}}(\gamma)$ of $\mathbf{d}$ along the cycle $\gamma(s)$ as formulated in Equation (2.15).

$$T_{\mathbf{d}}(\gamma) = \frac{1}{2\pi} \int_{\gamma(s)} (\kappa_{\mathbf{d}} - \kappa_{\gamma}) ds. \tag{2.15}$$

Where κ_{γ} is the cycle γ geodesic curvature. We can reasonably show that the turning number in $\mathbb{R}^2$ can be also expressed in Equation (2.16) with the index of singularity.

$$T_{\mathbf{d}}(\partial\Omega(P_i)) = I_{\mathbf{d}}(P_i) - 1. \tag{2.16}$$

Fields embedded on surfaces can contain relevant invariant information. Turning numbers have fundamental properties which make them useful to compare fields topologies. These information are straightforward to study fields on 2-manifolds. Topology of a field is related by its turning numbers along boundary cycles, homology generators and around singularities [Ray et al. 2008; Campen and Kobbelt 2014] as defined in Equation (2.17) contained in Definition 2.8. Field topological degrees of freedom are explained in Property 2.2.

Definition 2.8. Field or n-symmetry direction field topological equivalence. Two n-symmetry direction fields $\mathbf{d}_1$ and $\mathbf{d}_2$ defined over a surface M are homotopic if and only if they have the same turning numbers along the cycles of their homology basis $H^1(M)$ and around singularities minus one, which depends on the others via the Poincaré-Hopf theorem (see Theorem 2.1). This yields to the following statement:

$$\mathbf{d}_1 \equiv_t \mathbf{d}_2 \Leftrightarrow \forall \gamma_i^H \in H^1(M), T_{\mathbf{d}_1}(\gamma) = T_{\mathbf{d}_2}(\gamma) \tag{2.17}$$

Where $H^1(M)$ is the homology basis of the surface M. Singularities are omitted in this formulation: we deal with a continuous field without singularities. Hence, at least one border b must exist to place singularities (see the boundary number theorem in Theorem 2.2) in the case of $\chi(M) \neq 0$. Notice that $\equiv_t$ denotes the topological equivalence of the studied surface M.

Property 2.2. Field or n-symmetry direction field topological degrees of freedom. Topological degrees of freedom of a n-symmetry direction field are:

- Turning numbers $T_{\mathbf{d}}(\gamma)$ around $2g$ homology generators.
- Turning numbers $T_{\mathbf{d}}(\gamma)$ around b boundary cycles.
- Turning numbers $T_{\mathbf{d}}(\gamma)$ around $s-1$ singularities.

Since the Poincaré-Hopf theorem establishes that the sum of indices of singularity depends on the Euler characteristic of M, the total number of degrees of freedom is: $2g + b + s - 1$, if the surface has at least one boundary b or singularity s. For a torus, $\chi(M) = 0$, $b = 0$ and $g = 1$. Thus, we can design a field without singularities and also without borders to place them. This design process yields 2 degrees of freedom for the torus.

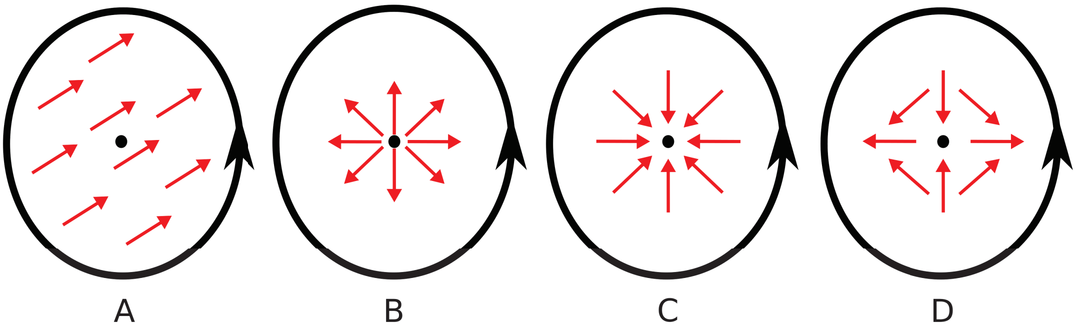

Figure 2.12: Singularity indices and associated turning numbers examples of different vector fields. We use black points P_i for singularities and black cycles $\gamma(s)$ for turning numbers. The indice of singularity is the number of counter-clockwise rotations that the vector make as we travel counter-clockwise around P_i. The turning number is the number of counter-clockwise rotations that the vector make as we travel counter-clockwise around $\gamma(s)$ minus the geodesic curvature of $\gamma(s)$, i.e., in $\mathbb{R}^2$ minus $2\pi/2\pi$. (A) $I_{\mathbf{d}}(P_i) = 0$ and $T_{\mathbf{d}}(\gamma) = -1$. (B) $I_{\mathbf{d}}(P_i) = +1$ and $T_{\mathbf{d}}(\gamma) = 0$. (C) $I_{\mathbf{d}}(P_i) = +1$ and $T_{\mathbf{d}}(\gamma) = 0$. (D) $I_{\mathbf{d}}(P_i) = -1$ and $T_{\mathbf{d}}(\gamma) = -2$.

2.1.6 Advanced topology prerequisites

2.1.6.1 Gaussian curvature distribution

While having defined discrete geometry with triangulated meshes, we can now adapt into a discreet manner some topological quantities used in above theorems. The Gaussian curvature of an embedded vertex v on a triangulated mesh can be expressed like formulated in Equation (2.18). N_v is the number of edges incident to v, and θ_i the angle in $\mathbb{R}^3$ between successive pairs of edges.

$$K_v = 2\pi - \sum_{i=1}^{N_v} \theta_i. \tag{2.18}$$

The geodesic curvature kg along boundary cycles $\gamma(s)$ catches the topological information embedded in boundaries. In discrete geometry at a vertex v, on a triangulated mesh, Equation (2.19) gives the formulation. α_r is one of the two discrete curve angles at v, on the right or left side of the discrete oriented cycle $\gamma(s)$. Changing the α_r side modifies the sign of kg_v. With both discrete equations, namely the discrete Gaussian curvature and discrete geodesic one, we are now able to resolve the Gauss-Bonnet theorem on triangulated meshes (see Theorem 2.3). Resolved curvatures are depicted in Figure 2.13.

$$kg_v = \frac{2\pi}{\sum_{i=1}^{N_v} \theta_i}\left(\frac{\sum_{i=1}^{N_v} \theta_i}{2} - \alpha_r\right) = \pi\left(1 - \frac{2\alpha_r}{\sum_{i=1}^{N_v} \theta_i}\right). \tag{2.19}$$

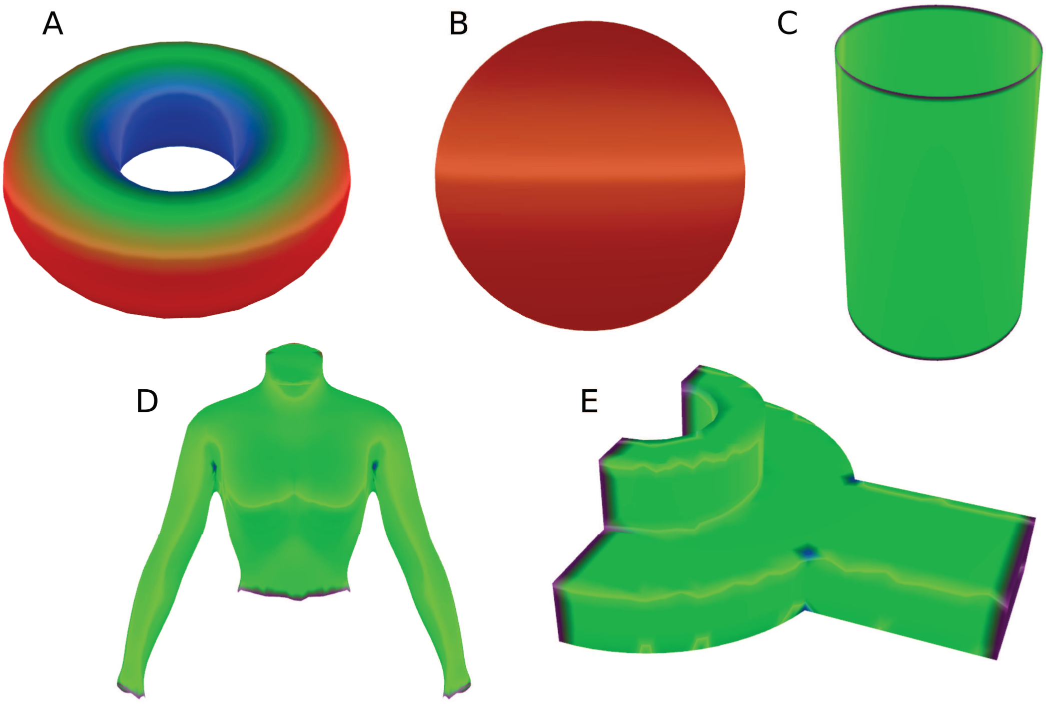

Figure 2.13: Gaussian curvature color mapping on discrete triangulated meshes computed by our IGA_ROM PlugIn (see Appendix B). For each shape, the color scale is different: scale is inflated or shrunk between examples to better show the curvature distribution. Purple areas are subjected to geodesic curvature. Blue color represents negative Gaussian curvature whereas red areas hold a positive curvature. Green zones have mostly zero curvature. All examples are a direct application of the Gauss-Bonnet theorem in Equation (2.9). (A) A torus with positive and negative curvature, $\chi(M) = 0$. (B) Sphere has a constant positive curvature, $\chi(M) = 2$. (C) Cylinder has zero Gaussian curvature everywhere, $\chi(M) = 0$. (D) Female bust, $\chi(M) = -1$. Remark the negative curvature observed under the arms. (E) Half-seal mechanical part with localized negative curvature, $\chi(M) = -1$.

After some necessarily formulated discrete quantities, the following is dedicated to the Gaussian curvature distribution. Gaussian curvature distribution stands for sampling the singularities on a mesh M where the topology is locally concentrated on the geometry [Maquart et al. 2019c]. Technically speaking, the goal is to find links between the Poincaré-Hopf and Gauss-Bonnet theorem. We seek for a new formulation helping us to understand the properties between geometry and topology and hence giving us valuable information on indices, number and locations of singularities. For that purpose, we proceed on triangulated meshes. We store at each vertex v a value of the discrete Gaussian curvature. Depending on the computed value, we classify each vertex in one of the six following cases as explained in Equation (2.20).

$$2\pi - \sum_{i=1}^{N_v} \theta_i = \begin{cases} K_v & \simeq 2\pi \text{ Sharp}, \\ K_v & \simeq \frac{\pi}{2} \text{ Spherical}, \\ K_v & \simeq 0 \text{ Euclidean}, \\ K_v & \simeq \frac{-\pi}{2} \text{ Hyperbolic}, \\ K_v & \simeq -\pi \text{ Ultrahyperbolic}, \\ K_v & \simeq -2\pi \text{ Solid angle}. \end{cases} \tag{2.20}$$

Afterwards, we deal with an associated closed mesh M_c without boundaries which is in fact related to an open mesh M with boundaries. Closing boundaries b of triangulated meshes is straightforward. Aiming to cut the mesh in a smart manner, for n_s singularities of a 4-symmetry direction field embedded on the closed mesh M_c of M, we define an associated ring. A 1-ring neighborhood is a surface composed by faces incident to the vertex v in place of the singularity. It allows us to express the Gauss-Bonnet theorem for each ring. n_s rings are homemorphic to a disk yielding $\chi(R_{v_n}) = 1$ for each singularities as explicited in Equation (2.21). Please note that the geodesic curvature is signed depending on the way we turn.

$$\begin{cases} R_{v_1} & \int_{M_{R_{v_1}}} K_1 dS + \int_{\partial M_{R_{v_1}}} kg_1 \; ds = 2\pi\chi(R_{v_1}), \\ R_{v_1} & = 2\pi - \sum_{i=1}^{N_{v_1}} \theta_i + kg_{v_1} = 2\pi, \\ ... & ..., \\ R_{v_n} & \int_{M_{R_{v_n}}} K_n dS + \int_{\partial M_{R_{v_n}}} kg_n \; ds = 2\pi\chi(R_{v_n}), \\ R_{v_n} & = 2\pi - \sum_{i=1}^{N_{v_n}} \theta_i + kg_{v_n} = 2\pi. \end{cases} \tag{2.21}$$

Extraction of the n_s rings to the closed mesh gives us a mesh denoted M_{n_s} with n_s boundaries and discrete geodesic curvatures kg_{v_i}. Euler characteristic of M_{n_s} now equals to $\chi(M_{n_s}) = 2 - 2g - n_s$. Recall that g is the genus of the considered surface. Let us define the Gauss-Bonnet theorem for M_{n_s} in the following Equation (2.22). Taking into account geodesic curvatures of all rings, we can define the new form written in Equation (2.23).

$$\int_{M_{n_s}} K dS + \int_{\partial M_{n_s}} k_g \; ds = 2\pi\chi(M_{n_s}) = 2\pi(2 - 2g - n_s), \tag{2.22}$$

$$\int_{M_{n_s}} K dS - \sum_{i=1}^{n_s} \int_{\partial M_{R_{v_i}}} kg_i \; ds = 2\pi\chi(M_{n_s}). \tag{2.23}$$

Therefore we can make geodesic curvature abstraction, i.e., boundary abstraction. More formally, this means that geodesic curvature is substituted by the Gauss-Bonnet theorem. This idea in then described in Equation (2.24) and has for discrete form the Equation (2.25). n_t is defined as the total number of vertices of M_{n_s} excepting boundary vertices. N_{v_j} is the number of edges incident to v_j. K_{v_i} is the discrete Gaussian curvature at v_i in place of singularities. Finally, we introduce singularity indices $I_{\mathbf{d}}^i$ of a potential n-symmetry direction field $\mathbf{d}$ in order to obtain a global form which links strong mathematical notions between topological and geometrical aspects in Equation (2.26a) and Equation (2.26b).

$$\int_{M_{n_s}} K dS - \sum_{i=1}^{n_s} \Big[2\pi - \int_{M_{R v_i}} K_i dS \Big] = 2\pi\chi(M_{n_s}), \tag{2.24}$$

$$\sum_{j=1, j \ni \partial M_{n_s}}^{n_t} \Big[2\pi - \sum_{i=1}^{N_{v_j}} \theta_i \Big] - \sum_{i=1}^{n_s} \Big[2\pi - K_{v_i} \Big] = 2\pi\chi(M_{n_s}), \tag{2.25}$$

$$\sum_{j=1, j \ni \partial M_{n_s}}^{n_t} \Big[2\pi - \sum_{i=1}^{N_{v_j}} \theta_i \Big] = \sum_{i=1}^{n_s} \Big[2\pi - K_{v_i} \Big] + 2\pi\chi(M_{n_s}), \tag{2.26a}$$

$$\sum_{j=1, j \ni \partial M_{n_s}}^{n_t} \Big[2\pi - \sum_{i=1}^{N_{v_j}} \theta_i \Big] = \sum_{i=1}^{n_s} \Big[2\pi - K_{v_i} \Big] + 2\pi \Big[\sum_{i=1}^{n_s} I_{\mathbf{d}}^i - \sum_{i=1}^{n_s} 1 \Big]. \tag{2.26b}$$

Hence Equation (2.26) can be minimized to locate properly a specific amount n_s of desired singularity indices. In this thesis, only the mathematical concept is kept, Equation (2.26) is not directly minimized but shows where the singularities must go. This equation can be named Gauss-Bonnet-Euler-Poincaré-Hopf due to its formulation. It is clearly noticed that there are nested properties between Gaussian curvature, Euler characteristic and singularity indices in this new expression. Since the Gauss-Bonnet theorem establishes a relation between geometry and topology, it is better to locate field singularities $I_{\mathbf{d}}^i$ near non-Euclidean areas. On surface M_c, indices can be estimated using Equation (2.27) if a 4-symmetry direction field is being considered: values have been determined by the symmetry n of the field and above topological considerations.

$$I_{\mathbf{d}}^i = \begin{cases} \text{Sharp} & \text{Non-defined}, \\ \text{Spherical} & +\frac{1}{4}, \\ \text{Euclidean} & 0, \\ \text{Hyperbolic} & -\frac{1}{4}, \\ \text{Ultrahyperbolic} & -\frac{1}{2}, \\ \text{Solid angle} & \text{Non-defined}. \end{cases} \tag{2.27}$$

2.1.6.2 Disk-sphere field duality theorem

This part treats useful personal work [Maquart 2018]. The reformulated theorem extracted from the related paper is given in Theorem 2.9. This theorem shows that it is possible to define a field without indices of singularity if at least one boundary exists. This example states the trade between the boundary number theorem and the Poincaré-Hopf theorem. In the same spirit of the previous formulated Poincaré-Hopf theorem corollary, a disk-sphere field duality theorem corollary is proposed in Corollary 2.2.

Theorem 2.9. Disk-sphere field duality theorem. For two singularities on a sphere, one embedded in a vertex v and one located at P_i, they have opposite turning numbers corresponding to the following duality:

$$T_{\mathbf{d}}(\partial v) = I_{\mathbf{d}}(v) - 1 = -(I^1_{\mathbf{d}}(P_i)_c - 1) = -T_{\mathbf{d}}(\partial\Omega(P_i)). \tag{2.28}$$

Where ∂v is the cycle around the vertex v, $I_{\mathbf{d}}(v)$ the index of singularity at v and $\partial\Omega(P_i)$ the cycle around the point P_i. $I^1_{\mathbf{d}}(P_i)_c$ refers to the index of singularity at P_i on the closed surface S of the associated disk D used to show this formulation in [Maquart 2018].

Corollary 2.2. Disk-sphere field duality theorem corollary. Hair implantation problematic for the hairdresser is to understand body hair behavior.

2.2 Parameterization techniques

2.2.1 Related work on parameterization

Quadrilateral remeshing is a long time interest, especially in the graphics community. Indeed, surveys exist [Floater and Hormann 2005; Alliez et al. 2008; Bommes et al. 2013b; Campen and Zorin 2017]. A particular work for simulation and animation is proposed by [Bommes 2012]. Previous decade tried to determine quadrilateral elements orientation with the understanding of principal curvature directions [Alliez et al. 2003; Marinov and Kobbelt 2004]. Most recent parameterization based techniques are very powerful to compute oriented quadrilateral meshes. [Ray et al. 2006; Huang et al. 2008; Zhang et al. 2010] present pipelines in order to find the cross field singularities automatically. Others are solving a mixed integer problem [Bommes, Zimmer, and Kobbelt 2009] to elucidate such properties of embedded fields on surfaces. Mixed integer problems have been also studied by [Bommes, Zimmer, and Kobbelt 2010; Bommes et al. 2013a]. These methods give good results, but they are not in communication, i.e., they are not aware of the placement of the others singularities. The optimization of quad meshes is an inherently global problem since local changes affect the whole mesh quality. [Bommes, Lempfer, and Kobbelt 2011] developed an algorithm to optimize quadrilateral meshes and improve its global structure. Last year, [Huang et al. 2018] produces structured meshes with many fewer singularities based on an existing algorithm.

To overcome this potential issue for complicated surfaces, papers exploit topological information derived from a patch layout. Such patches decompose the surface into a coarse quadrilateral mesh which has the same topology of the input triangulated one. A quadrilateral layout is an embedded graph on the triangulated surface which partitions the surface into a set of non-overlapping quadrilateral patches. Each patch has 4 nodes and 4 polyline edges, i.e., a polyline is a set of multiple lines. If all patches of the layout are topogical quadrilaterals, thus we call this a quadrilateral layout of the surface. [Dong et al. 2006; Bommes, Vossemer, and Kobbelt 2008] construct patches manually whereas automatic methods exist [Campen, Bommes, and Kobbelt 2012; Bommes et al. 2013a; Campen and Kobbelt 2014; Razafindrazaka, Reitebuch, and Polthier 2015] and a recent survey can be found here [Campen 2017]. This task induces cutting charts, i.e., a cut graph due to the non-trivial topology of the surface [Campen, Bommes, and Kobbelt 2015] to parameterize the whole mesh. In the context of this thesis, we will use our method explained in the next Chapter 3 to compute such relevant layouts. The novelty is to add other properties in order to construct a further volumetric parameterization and to fit features of the mesh.

Recent advances in quadrilateral meshing are abundant. Very recent work are very different. Geometrical theories help to convert a triangulated mesh into a quadrilateral one, e.g. by foliation theory [Lei et al. 2017]. Others solve partial differential equations on a surface mesh so as to arrive to a quadrilateral meshing goal [Kowalski, Ledoux, and Frey 2013; Beaufort et al. 2017]. Singularities are determined automatically and global quadrilateral structure is determined by tracing streamlines from singularity positions.

In the following, we consider two different parts. The first is based for its majority on classical harmonic parameterization. The second aims to parameterize the whole surface in one shot, namely the global parameterization.

2.2.2 Weights based disk-like surface parameterization and other similar methods

Many different techniques of mapping exist. In our case, we are interested in mappings or parameterizations which map a surface M embedded in $\mathbb{R}^3$ to a canonical domain D in $\mathbb{R}^2$. Mapping serves to define a new distribution of the geometry and hence permits to remesh with quadrilaterals. Nice surveys exist, see e.g. [Li and Iyengar 2014]. The ideal parameterization is isometric, i.e., it fully preserves areas and angles as previously formulated in Theorem 2.5. For surfaces, an isometric parameterization is not possible in the general case due to Gaussian curvature. In particular cases, an appropriate cut graph G permits such parameterization without face overlapping. But it strongly depends on the embedded curvature. Therefore, approaches to 2-dimensional manifold attempt to find a mapping which is either conformal with no angular distortion, or equiareal with no area distortion. Conformal mappings always exist into one of the three following canonical domains: the sphere, the plane, and the hyperbolic space. As already said, the isometric theorem guarantees that a conformal equiareal mapping is isometric. In the following we consider a triangulated surface M with vertices V, edges E and faces F, and only disk-like surfaces for parameterization. We note that some techniques to map a multiply connected surface, i.e., a genus-0 surface with multiple boundaries exist [Zeng et al. 2009a]. Attempts consist in finding quasi-conformal mapping between surfaces by solving Beltrami equations [Zeng et al. 2009b]. Parameterization based quadrilateral meshing methods are abundant [Marinov and Kobbelt 2004; Dong et al. 2006; Tong et al. 2006; Huang et al. 2008; Zhang et al. 2010]. We use discrete harmonic mapping to solve such parameterizations. Harmonic mappings have attributes derived from conformal parameterization, but there is no guarantee on angles. Such mappings are trying to minimize a given defined energy. To proceed, we construct a harmonic function $f : M \longrightarrow \mathbb{R}$ such that $\Delta f = 0$. Harmonic maps minimize Dirichlet energy $E_D(f)$ as formulated in Equation (2.29).

$$E_D(f) = \frac{1}{2}\int_M \|\nabla f\|^2 dS. \tag{2.29}$$

The surface boundary ∂M is first mapped to the boundary of the parametric domain and then the parameterization for the interior vertices is obtained by solving the linear system written in Equation (2.30).

$$\Delta_w f(v_i) = \sum_{j \in N_i} w_{ij}(f(v_j) - f(v_i)) = 0. \tag{2.30}$$

Where v_i, $v_j \in V$, N_i is the neigborhood of v_i, and w_{ij} is the scalar weight assigned to the oriented edge $e_{ij}(v_i, v_j)$. Different parameterization methods assign different weights w_{ij}. The first definition of weight was introduced by [Tutte 1963]. In the parameter space, each vertex is placed at the barycenter of its neighbors. Recently [Saboret, Alliez, and Lévy 2016] have implemented a CGAL package handling some of the state-of-the-art surface parameterization methods such as the least squares conformal maps, discrete conformal map, discrete authalic parameterization, Floater mean value coordinates or Tutte barycentric mapping. To the best of our knowledge, the most used weights are the mean value coordinates weights introduced by [Floater 2003]. These weights are formulated in Equation (2.31). γ_{ij} and δ_{ij} are the two incident angles to the edge $e_{ij}(v_i, v_j)$. These angles are defined at v_i. Normalized weights λ_{ij} are expressed in Equation (2.32).

$$w_{ij} = \frac{tan(\gamma_{ij}/2) + tan(\delta_{ij}/2)}{\|v_j - v_i\|}, \tag{2.31}$$

$$\lambda_{ij} = \frac{w_{ij}}{\sum_{k \in N_i} w_{ik}}. \tag{2.32}$$

To finalize the introduction on parameterization, we summarize discrete bijective mapping by the Radó-Kneser-Choquet theorem previously developed in Theorem 2.4. Indeed, our needs is a mapping where f is harmonic, the parametric space $\subset \mathbb{R}^2$ is convex and the boundary ∂M is mapped homeomorphically in the parametric space. With these conditions and positive vertices weights for discrete maps, f has to be bijective. Mean value weights are always positive, thus they are taken for the next harmonic parameterizations. To show the ability of the presented harmonic parameterization tools and weights to produce mappings, a first example is depicted in Figure 2.14. Due to the constrained border of the parametric space, calculated quadrilaterals have different sizes. A second is given for an aortic valve [Morganti et al. 2015; Vy et al. 2016]. To do this specific parameterization and understand features of the valve, we segment the mesh into different square domains in Figure 2.15 (A). Afterwards, with the harmonic mapping per patch and treating connectivity, a pure quadrilateral mesh is extracted in Figure 2.15 (C). However, this kind of mapping induces high distortion between computed patches and does not take into account the global properties of the shape.

2.2.3 Aligned global parameterization

We develop here the concept of aligned global parameterization but only as introduction purposes. We invite the readers to Chapter 4 for more specific details. An aligned global parameterization is based on a guidance field, i.e., in general a cross field. The cross field is generated while respecting some prescribed features of the mesh. The global parameterization consists in finding a global coordinate system of the shape aligned with the cross field. In this case, a global parameterization is a piecewise linear map from the mesh $M \in \mathbb{R}^3$ to a topological disk domain $\Omega \in \mathbb{R}^2$. Disk domain is achieved by computing an appropriate cut graph G (see Section 2.1). Since the parameterization should be piecewise linear, assigning a couple of parameters (u, v) to each face vertex of the triangulated mesh is sufficient. Previous idea is depicted in Figure 2.16.

Quadrilateral remeshing techniques strive to generate an integer grid map [Bommes et al. 2013a]. In other words, it is a parameterization of the input surface into $\mathbb{R}^2$ such that the canonical grid of integer isolines forms a quadrilateral mesh when mapped back onto the surface integrated in $\mathbb{R}^3$. They seek to minimize an alignement energy with the computed cross field [Bommes, Zimmer, and Kobbelt 2009; Bommes, Zimmer, and Kobbelt 2010; Myles et al. 2010; Myles and Zorin 2012; Ebke et al. 2013; Myles and Zorin 2013; Campen and Kobbelt 2014].

2.3 Conclusion

Above developed topological formulations and theorems are fundamental tools for the next chapters. By doing such investigation process onto the topology field and

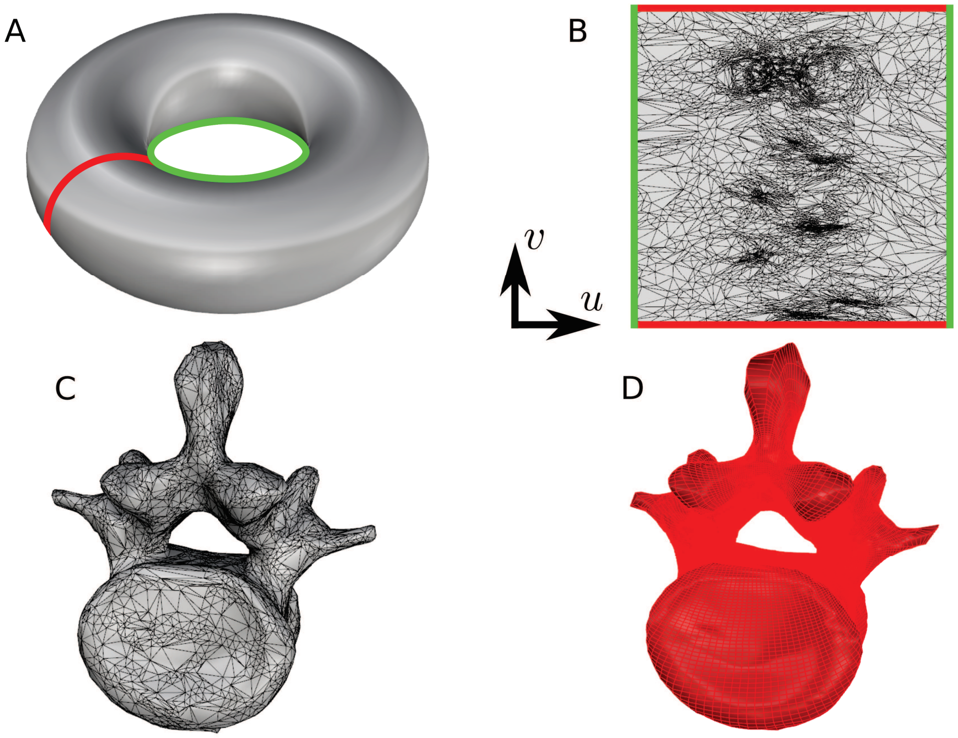

Figure 2.14: Harmonic parameterization using mean value weights computed by our IGA_ROM PlugIn (see Appendix B). (A) A CAD torus and its homology basis. (B) Such depicted homology basis is a homotopy basis and even a system of loops. The cut graph is then straightforward. Using the cut graph, we parameterize the mesh into a square. (C) Real vertebrae from medical imaging which is homeomorphic to a torus. (D) Produced inverse mapping and pure quadrilateral mesh. Workflows of (A) and (B) have been followed.

parameterization techniques, a strong mathematical basis is built. Complicated surfaces with an arbitrary topology and geometry are now understood.

Surface smart decomposition requires to evaluate topological invariants such as the well-known Euler characteristic. Comprehension of the homotopy and homology theories is also a way to sort surfaces understanding loops and cycles, but mainly remain serious ones for manifold segmentation: Chapter 3 is devoted to the surface partitioning. These theories are closely related to χ, and hence they hold invariant properties too. Since the Poincaré-Hopf theorem states a tight relation between singularity indices and Euler characteristic, designing fields on surfaces is related with the topological invariant χ. Chapter 4 is dedicated to discrete n-symmetry direction field computation; related theorems are compulsorily used. Nested properties have been elucidated from the previous explanations coming from the literature or from this thesis's work. Such intricated relations between some of described above theorems are essential when considering a surface with borders. Moreover,

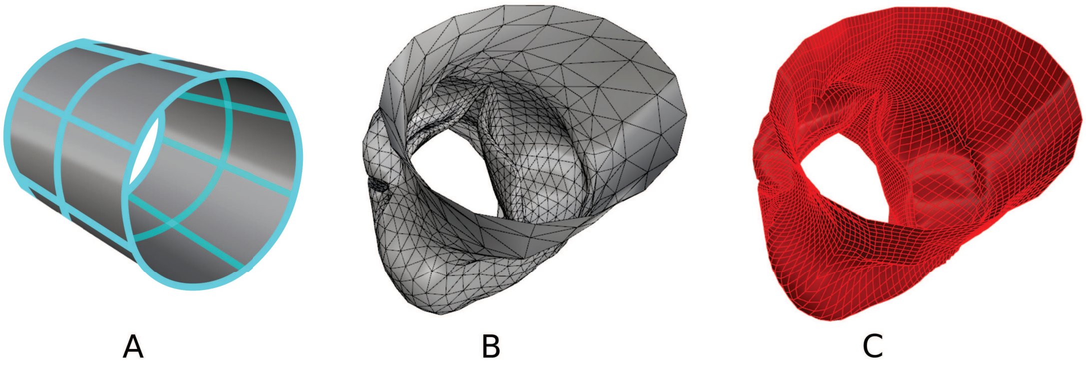

Figure 2.15: Aortic valve harmonic parameterization using mean value weights computed by our IGA_ROM PlugIn (see Appendix B). (A) The quadrilateral layout. (B) Scanned mesh obtained via medical imaging techniques. (C) Extracted pure quadrilateral mesh from parameterization.

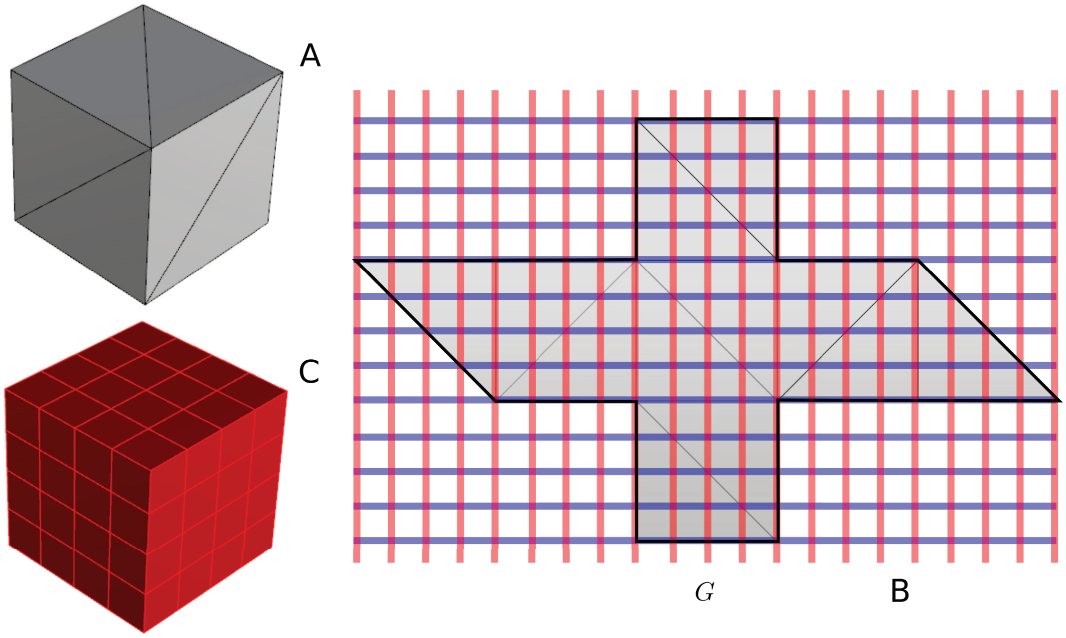

Figure 2.16: Basic approach of the global parameterization. (A) Input triangulated mesh. (B) Grid and parameterized domain in $\mathbb{R}^2$. Cross field is undepicted but brought to these red and blue transparent integer isolines. A cut graph G is computed and drawn in black. As early explained, non-overlapping faces in $\mathbb{R}^2$ can't be achieved due to Gaussian curvature in the general case. (C) Resulting quadrilateral mesh is obtained by inverse mapping, i.e., mapping from the parameterized domain $\mathbb{R}^2$ to the physical space in $\mathbb{R}^3$. Specific conditions are required along edges of G in order to obtain a conform structured mesh.

the comprehensive study of the Gauss-Bonnet theorem gives us an integral formulation between geometry and topology which will be very useful in the following to place singularities on a mesh. Chapter 6 is strongly based on presented topological prerequisites and thence will permit to go even further.

Methods relying on parameterization have been introduced in the way to follow the next Chapter 3. Harmonic method is particularly highlighted: the method is applicated in our quadrilateral layout partitioning algorithm. Chapter 4 uses the aligned global parameterization in order to compute quality quadrilateral meshes. With all of these essentials, the next steps will be straightforward. As a summary and for assimilation purposes, Figure 2.17 gives an overview of theorems and their application fields.

THEOREMS	RELATED ON	DIRECTLY USEFUL FOR
POINCARE-HOPF THEOREM [THEOREM 2.1]	FIELDS ON SURFACES WITHOUT BOUNDARIES	FIELD DESIGN [CHAPTERS 4 AND 6]
BOUND. NUMBER THEOREM [THEOREM 2.2]	FIELDS ON SURFACES WITH BOUNDARIES	FIELD DESIGN [CHAPTERS 4 AND 6]
DISK-SPHERE FIELD THEOREM [THEOREM 2.9]	TRADE BETWEEN [THEOREMS 2.1 AND 2.2]	ADDITIONAL COMPREHENSION [CHAPTER 6]
GAUSS-BONNET THEOREM [THEOREM 2.3]	SURFACE CURVATURE AND GEODESIC CURVATURE	FIELD DESIGN AND GEOMETRY [CHAPTER 4 AND APPENDIX C]
RADO-KNESER-CHO. THEOREM [THEOREM 2.4]	BIJECTIVE MAPPINGS OR PARAMETERIZATIONS	CUBOID DECOMPOSITION [CHAPTER 3]
ISOMETRIC THEOREM [THEOREM 2.5]	PROPERTIES OF MAPPINGS OR PARAMETERIZATIONS	CUBOID DEC. AND GLOBAL PAR. [CHAPTER 3 AND 4]
CLASSIFICATION THEOREM [THEOREM 2.6]	HOMEOMORPHISM RELATED ON A TOPOLOGICAL INVARIANT	MORPHISM PROPERTIES [ALL CHAPTERS]
TOPO. INVARIANCE THEOREM [THEOREM 2.7]	TOPOLOGICAL INVARIANT AND HOMEOMORPHISM	MORPHISM PROPERTIES [ALL CHAPTERS]
HOMO. INVARIANCE THEOREM [THEOREM 2.8]	TOPOLOGICAL INVARIANT AND HOMOTOPY	CONTINUOUS DEFORMATIONS [ALL CHAPTERS]

Figure 2.17: Theorems overview and application fields.

Chapter 3

Smart model decomposition

This chapter presents a surface decomposition approach in two steps: pants (in Section 3.1) and cuboid decomposition (in Section 3.2). We seek to segment the input surface in order to obtain a cuboid decomposition of a complex geometry with an arbitrary topology. From this chapter to the end, all computations are made with our IGA_ROM PlugIn (see Appendix B).

Contents

3.1 Geometry-aware pants decomposition

First step of surface decomposition is done by dividing a triangulated surface into a set of pants patches. Pants decomposition provides a canonical decomposition scheme for common surfaces. As already explained in the previous Chapter 2, $\chi = -1$ for a pants patch, therefore a pant is the simplest topology after the sphere, disk, cylinder and torus. Many algorithms take as input handle loops for genus-g surfaces to segment into pants patches [Li, Gu, and Qin 2009]. Handle loops required for automatic pants decomposition are computed using a technique introduced by [K. Dey, Li, and Sun 2007]. In this algorithm, loops are lying on the triangulated geometry and topologically compatible entities are sorted with a geometric criterion. In other words, the set of handle and tunnel loops are geometrically small in terms of length for the considered geometry. An improvement of this process was also developed by [Dey et al. 2008]. More recently, [K. Dey, Fan, and Wang 2013] exposed another method using reeb graphs; this technique is used in our developments.

3.1.1 Improved algorithm: geometry comprehensive

We explain our improved pants decomposition algorithm mainly based on the work of [Al-Akhras 2016; Al-Akhras et al. 2016] to decompose an arbitrary surface M into geometry-aware pants patches. We deal with homology generators, i.e., basis with entities formed by handle and tunnel loops.

First stage is done by taking a subset H composed of g simple pairwise disjoint handle loops $\{h_1, ..., h_g\}$. Slicing the surface M with b boundary components along its g handle loops will lead to a genus-0 surface with $2g + b$ boundary components denoted as $W = \{w_1, ..., w_{2g+b}\}$. We then iteratively pick two boundaries w_i and w_j among all non-repeating and commutative combinations in W and compute a new cycle w_{ij} to bound them, i.e., w_{ij} is homotopic to $w_i \circ w_j$. New improvement is brought by analyzing all possible conbinations among a given set of boundary components in W when picking the two current boundaries w_i and w_j in order to determine all cycles $w_i \circ w_j$. Optimal cycle w_{ij} is then found by sorting loops in L handling a global geometric criterion. The three cycles w_i, w_j and w_{ij} bound a pants patch T_k. We remove this pants patch T_k from M. The remaining patch is still genus-0 but its boundary number reduces by 1: the two cycles w_i and w_j are removed, and one new cycle w_{ij} is inserted. This is iteratively performed until $|W| = 3$.

The main process is formulated in Algorithm 3.1, and the operation that traces a cycle w_{ij} homotopic to cycle $w_i \circ w_j$ is formulated in Algorithm 3.2. Remark that, for geometry-aware decompositions needs, we have proposed a new enhanced algorithm which computes a cycle $w_i \circ w_j$ passing through user-defined relevant mesh points in Algorithm 3.3. Algorithm time complexity is expressed in Algorithm 3.4 thinking with one arbitrary pant patch decomposition as elementary operation. We refer the readers again to [Al-Akhras 2016] for more visual details.

Algorithm 3.1. Main geometry-aware pants decomposition algorithm.

Input 1: Triangulated genus-g surface M with b boundary components.
Input 2: g geometrically relevant handle loops of M.
Input 3: Global geometric criterion for L.
Output: Set of $-\chi(M)$ pants patches $T = \{T_1, ..., T_{-\chi(M)}\}$, with $M = \cup T_i$.

```
$k = 1$.
Slice $M$ along all its handle loops and get a surface $M_k$ with $2g+b$ boundaries.
Put all boundaries of $M_k$ in a set $W = \{w_1, ..., w_{2g+b}\}$.
While $|W| > 3$ do
    Build or reset an empty set of loops $L = \{0\}$.
    Compute $N_c$ combinations: $\dim(N_c) = \frac{Size(W)!}{2!(Size(W)-2)!}$.
    For all couples $[w_i, w_j]$ in $N_c$:
        Compute a cycle $w_{ij}$ homotopic to $w_i \circ w_j$ (Algorithms 3.2 and 3.3).
        Add loop to $L$.
    End For
    Sort relevant loops in $L = \{l_1, ..., l_{\dim(N_c)}\}$ using a global geometric criterion.
    The optimal $w_{ij}$ cycle is classified in $L$.
    $\{w_1, w_j, w_{ij}\}$ bound a pants patch $T_k$. Remove $T_k$ from $M_k$: $M_k \leftarrow M_k \setminus T_k$.
    Remove $w_i$ and $w_j$ from $W$, and add $w_{ij}$ into $W$.
    $k \leftarrow k + 1$.
End While
```

Algorithm 3.2. Homotopic cycle computation.

Input 1: Genus-0 surface M with b boundary components $\{w_1, ..., w_b\}$.
Input 2: Geometric criterion.
Output: A cycle w_{ij} homotopic to cycle $w_i \circ w_j$.

```
Compute the shortest path connecting $w_i$ to $w_j$.
Slice $M$ along this path to get one new large boudary $c_{ij}$.
Connect all other boundaries together using shortest paths.
Slice $M$ along these paths to get one new large boundary $c_k$.
$M$ becomes a topological cylinder.
Compute the shortest path $\gamma$ connecting $c_{ij}$ and $c_k$.
Slice $M$ along the path $\gamma$.
Every point $p_i \in \gamma$ ($n + 1$ points) is splitted into a pair $(p_i, \overline{p_i})$.
Trace all shortest paths connecting points pairs $(p_i, \overline{p_i})$.
Among these paths, the cycle $w_{ij}$ satisfies the geometric criterion.
```

Algorithm 3.3. Sharp homotopic cycle computation.

Input 1: Genus-0 surface M with b boundary components $\{w_1, ..., w_b\}$.
Input 2: Set of n_p sharp points $S = \{s_0, ..., s_{n_p}\}$.
Output: A cycle w_{ij} homotopic to cycle $w_i \circ w_j$.

```
Compute the shortest path connecting $w_i$ to $w_j$.
Slice $M$ along this path to get one new large boudary $c_{ij}$.
Connect all other boundaries together using shortest paths.
Slice $M$ along these paths to get one new large boundary $c_k$.
$M$ becomes a topological cylinder.
Compute the shortest path $\gamma$ connecting $c_{ij}$ and $c_k$.
Slice $M$ along the path $\gamma$.
Every point $p_i \in \gamma$ $(n+1$ points) is splitted into a pair $(p_i, \overline{p_i})$.
$\{p_0, \overline{p_0}, p_n, \overline{p_n}\}$ are setted to be the corners of a square harmonic mapping.
Partial line inverse mapping passing through $n_p$ points in $S$ is performed.
The cycle $w_{ij}$ is reconstructed using line segments.
```

Algorithm 3.4. Pants decomposition algorithm time complexity.

Input: A pant patch decomposition is used as elementary operation.
Output: Time complexity $C_T(\chi(M))$.
Note 1: We denote $C_T(\chi(M))$ as time complexity related to the surface M.
Note 2: $B = \{b_0 = 4, b_1 = 5, ..., b_i = -\chi(M) + 2\}$ and $\dim(B) = -\chi(M) - 1$.

```
$C_T(\chi(M)) = \sum_{i=0}^{-\chi(M)-2} \frac{b_i(\chi(M))!}{2!(b_i(\chi(M))-2)!}$.
```

All shortest paths computations on triangulated meshes have been realized by an adaptation of the well-known Dijkstra's algorithm [Dijkstra 1959] for weighted tree graphs. A CGAL package exists to compute these paths which was developed by [Kiazyk, Loriot, and Verdière 2016]. Different geometric criteria can be used to guide the pants decomposition. Geometric criterion can be adapted to M, i.e., for meshes provided from medical imaging or meshes for mechanical applications. In Algorithm 3.1, the specified geometric criterion can be different of the one used in Algorithm 3.2. For instance, we can sort loops in L with loops passing through areas of minimum curvature [Lee et al. 2005], symmetry or shortest length.

In Figure 3.1 (C) pants decomposition is performed using loops with minimum length, whereas in Figure 3.1 (D) decomposition is made by symmetry. In Figure 3.2, user selectionned sharp points are given to guide the pants decomposition. This guiding yields a geometry-aware decomposition. A common surface admits infinitely many pants decompositions. In general, not all pants decomposition results are suitable for the next step of our algorithm. However, if the pants decomposition is guided by the different geometric criteria presented above, we obtain satisfying results for all our test cases.

3.1.2 Pants decomposition examples

As example, we give few computed results in pictures in Figure 3.3. Another example is depicted in Chapter 2 for a level-1 Sierpinski sponge. With above developments, shortest length and symmetry criteria have been used to state depicted decompositions. In the following, some of presented pants segmentations will be used for the

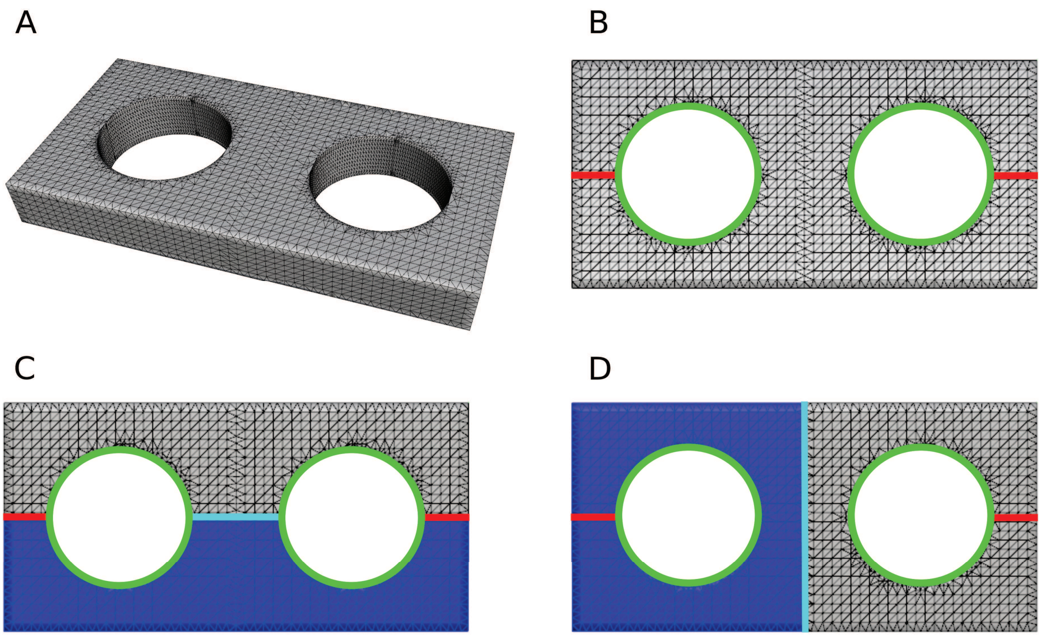

Figure 3.1: Genus-2 plate pants decomposition. (A) Input triangulated surface. (B) Surface with its handle and tunnel loops, depicted in red and green respectively. Pants decomposition using loops with shortest distance (C) and with symmetry (D).

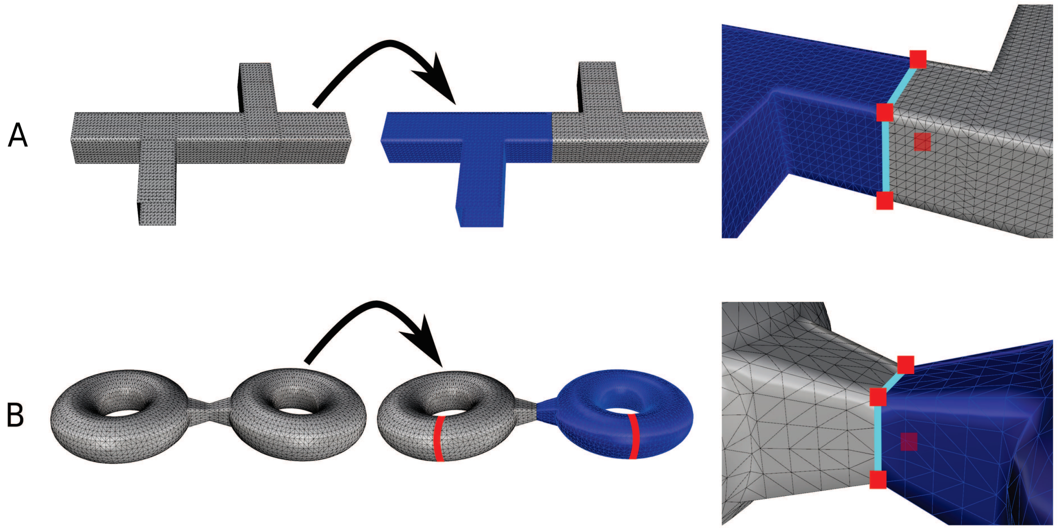

Figure 3.2: Geometry-aware pants decomposition with sharp points. (A) Double T is decomposed into pants using 4 sharp points given by the user or determined automatically. (B) A 2-torus pants decomposition passing through sharp points. Notice that using shortest length loops, the result will be the same for (B).

next step consisting in finding a suitable decomposition of a pant into feature-aware cuboids.

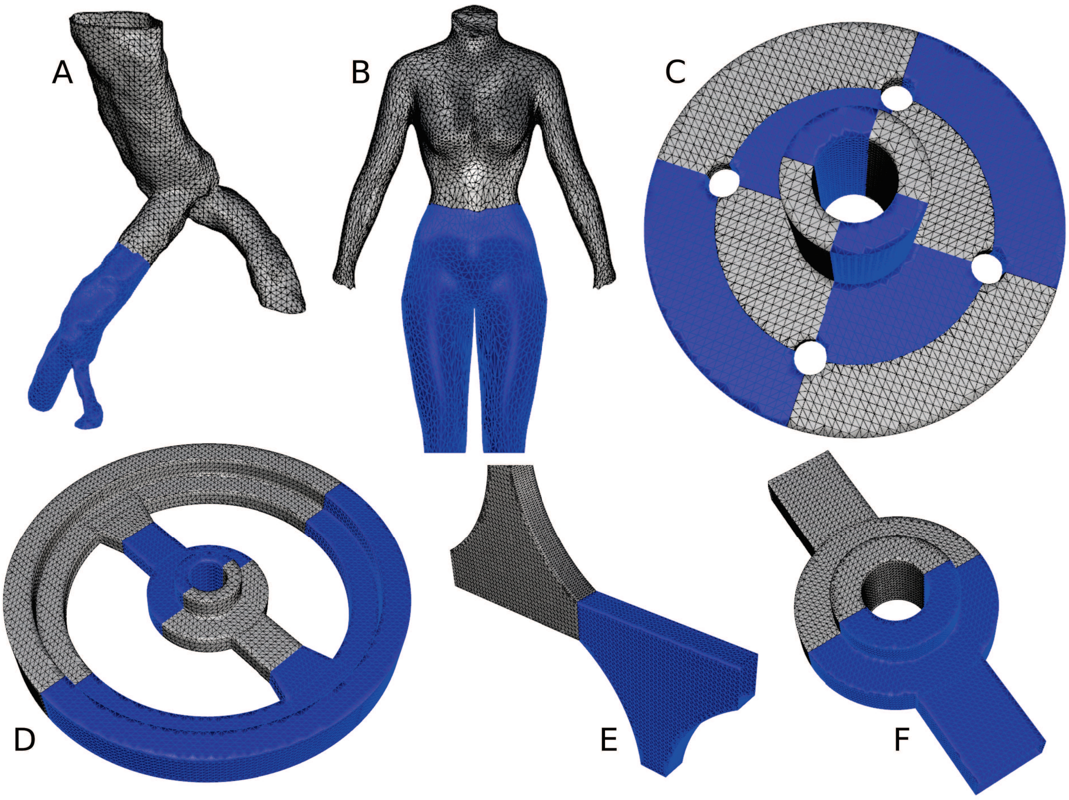

Figure 3.3: Pants decomposition examples. All blue and gray parts are both genus-0 surfaces with 3 boundaries. (A) Abdominal aorta with 4 boundaries. $\chi(M) = -2$. Decomposition was made with a prescribed set of points S. (B) Female body with 4 boundaries. $\chi(M) = -2$. Shortest length criterion allows this decomposition. (C) Casting part. $\chi(M) = -8$, yielding to 8 pants calculated using symmetry properties. (D) Wheel part. $\chi(M) = -3$. Symmetry properties were used to segment this mesh. (E) Double curved T part. $\chi(M) = -2$. (F) Seal part. $\chi(M) = -2$.

3.2 Feature-aware cuboid decomposition

This section aims to decompose each pant patch into a set of cuboids that understands the input geometry. Pants patches provide a very simple topology, and each pant patch can be treated separately. [Li et al. 2013] presented a method that generates the same quadrilateral patches number per pants patch with a given user data input. [Al-Akhras 2016] improves this method to perform the decomposition in a way that it does not require any input from the user. The last idea is to generate corners and polyedges on each pants patch and decompose it into a set of 4 cuboids, each having 8 corners and 12 polyedges in order to construct a volumetric parameterization; but it is not a suitable segmentation in the general case.

In our work we present an extended algorithm to handle more complicated geometry especially with sharp features. On each pant patch the number of quadrilateral patches is set to respect sharp vertices and sharp edges. Feature-aware cuboid decomposition is made to respect the topology of the input triangulated surface and consider sharp features. Of course, optimal number of cuboids depends on the features embedded into the considered pant patch. This decomposition approximates very roughly the geometry while faithfully replicating its topology taking into account sharp features. That is why we talk about feature-aware cuboid decomposition. Due to the patch regular structure of the quadrilateral layout, it can serve as parametric domain needed for pure 3D surface quadrilateral mesh computation. To go further, we will see in the following the useful properties of cuboid decomposition for building volumetric meshes.

3.2.1 Quadrilateral layout and cuboid decomposition definition

Quadrilateral layouting strive to decompose a surface into a set of quadrilateral patches, see e.g. [Campen, Bommes, and Kobbelt 2012; Campen, Bommes, and Kobbelt 2015]. Indeed, thanks to square domains, it is easier to parameterize. We name $\mathbb{Q}$ a quadrilateral layout decomposing the input triangulated surface into patches with 4 corners and 4 polylines or polyedges composed by many segments embedded in the unstructured mesh M. We call $\mathbb{C}$ the cuboid configuration that is a specific quadrilateral layout $\mathbb{Q}$ that authorize further volumetric parameterizations. Both $\mathbb{C}$ and $\mathbb{Q}$ are surface topological entities, i.e., 2-dimensional manifolds. In addition, because $\mathbb{C}$ and $\mathbb{Q}$ are surfaces, they can have boundaries. We insist on the fact that $\mathbb{C}$ is a surface, not a volume. Pertinence of pictured boundaries to illustrate $\mathbb{C}$ in figures will be determined case by case. We strive to conserve the cuboid aspect throughout the studied method. Above given definitions are sufficient to move to the next developments, they will be redefined in Chapter 6 in order to better characterize their topological properties. Figure 3.4 shows the mapping of a quadrilateral layout that is a cuboid configuration onto a triangulated geometry.

3.2.2 Improved algorithm: feature comprehensive

3.2.2.1 Algorithms steps

The following is dedicated to the feature-aware cuboid decomposition algorithm. As input, we have a set of pants patches. The 3 boundaries of a given pant patch will be arbitrary denoted by B_1, B_2 and B_3. We process these pants patches one by one in an arbitrary order. To guarantee cuboid corner alignment, when we determine one pant patch's result, we transfer its corners on the boundaries of the adjacent

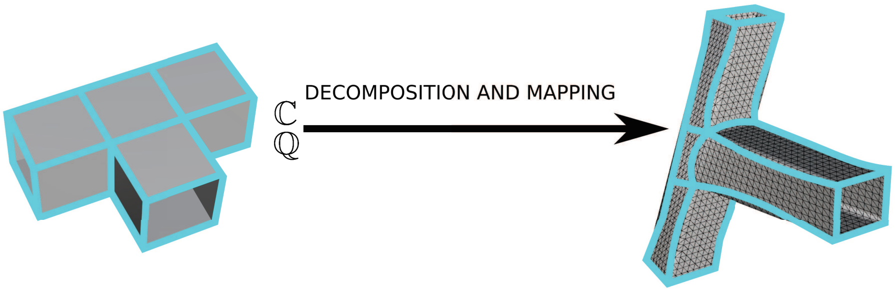

Figure 3.4: Cuboid configuration mapping onto a triangulated geometry yielding to a cuboid decomposition of the mesh. $\mathbb{C}$ and $\mathbb{Q}$ are both surface entities possibly with boundaries. $\mathbb{C}$ holds additional properties to build a volume due to its cuboid structure.

pants patches if they are not processed yet. This algorithm is robust even for low-quality and noisy meshes. Step 1 to step 3 are dedicated to the feature-aware cuboid decomposition procedure.

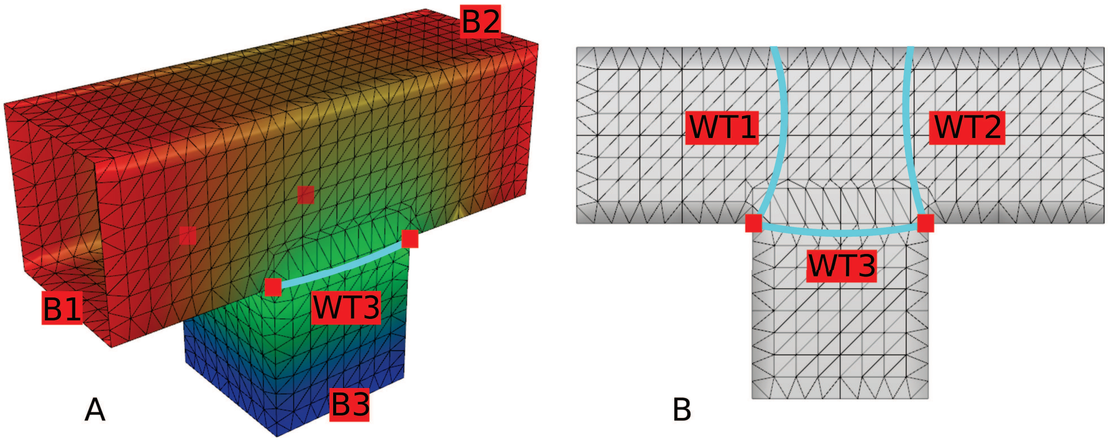

Figure 3.5: Temporary cutting curves generation. (A) Discrete harmonic function f_3. Blue color represents parametric values close to 0, red ones are close to 1. Using a set C of n_c sharp cutting points, f_2 and f_1, the three temporary cutting curves are computed in (B).

Step 1. We generate 3 sharp cutting curves W_{S1}, W_{S2} and W_{S3}:

[**A**] We compute 3 discrete harmonic functions: f_1, f_2 and f_3. To compute f_i, we set $f_i = 0$ for vertices on the boundary B_i and $f_i = 1$ for vertices on the remaining two boundaries B_j and B_k . Then we solve $\Delta f_i = 0$ using mean value coordinates. Figure 3.5 (A) for f_3.

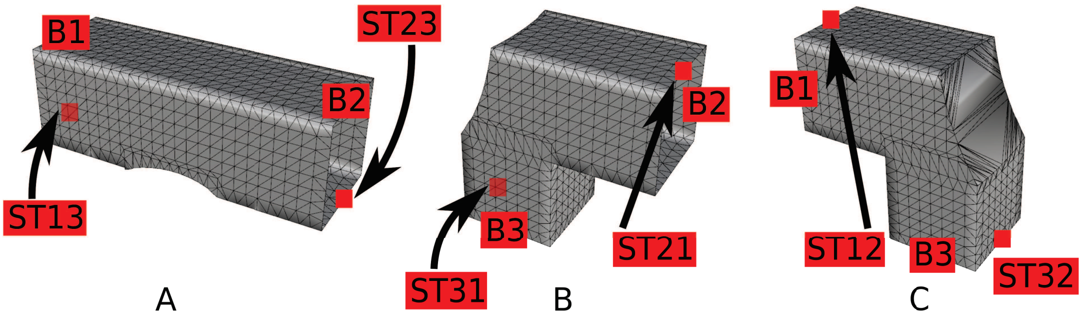

Figure 3.6: Boundary seed points computation. Temporary patches P_{T3}, P_{T1} and P_{T2} respectively in (A), (B) and (C). Using an approach close to circular conformal mapping of [Zeng et al. 2009a], temporary seed points s_{Tk} are determined into each respective patch P_{Tk}.

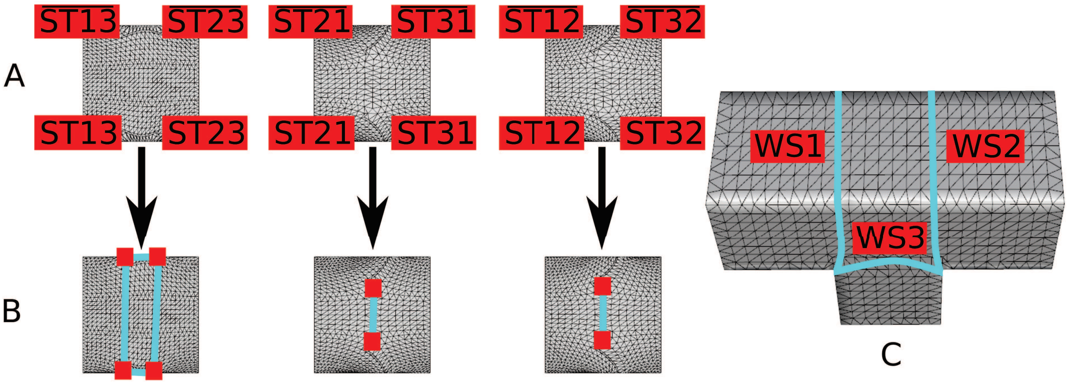

Figure 3.7: Sharp cutting curves generation. (A) The three temporary unit square maps U_{T3}, U_{T1} and U_{T2} (left to right). (B) Partial line inverse mapping using sharp cutting points in C performed in U_{T3}, U_{T1} and U_{T2} (left to right). (C) Computed sharp cutting curves W_{S1}, W_{S2} and W_{S3}.

[B] Each harmonic function f_i has one minimum component and two maximum components. Among a set C of n_c sharp cutting points $C = \{c_0, ..., c_{n_c}\}$, let $\overline{f_i} = min[f_i(c_j)], \forall c_j \in C$. Then a temporary non-sharp cutting curve W_{Ti} is defined as the isoparametric curve of the function f_i for the value $\overline{f_i}$. Figure 3.5 (B).

[C] We remove a long branch, i.e., by cutting along its temporary cutting curve W_{Tk}. After filling the cutting hole, the resulting patch is a topological cylinder with 2 boundaries B_i and B_j. We denote this temporary patch by P_{Tk}. Figure 3.6 (A), (B) and (C).

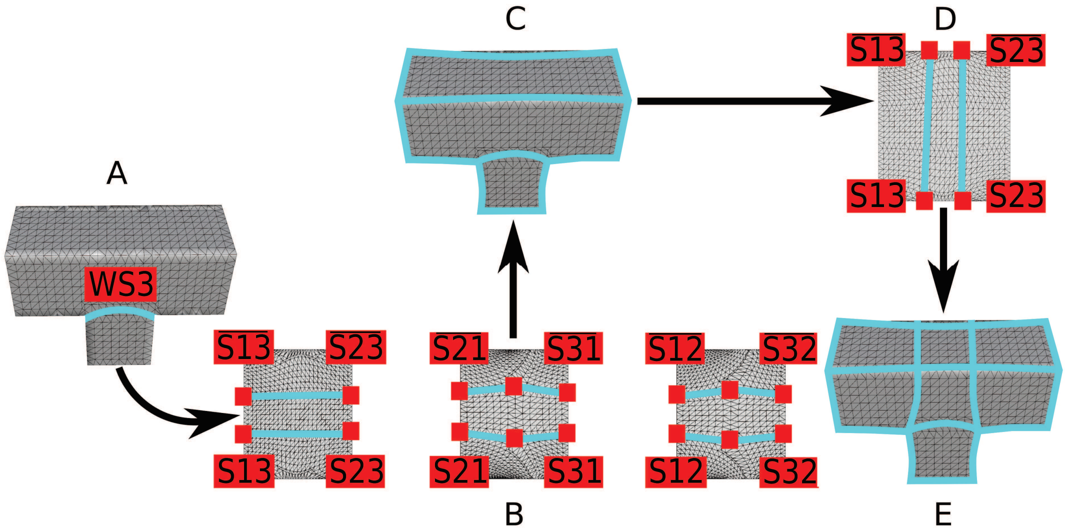

Figure 3.8: Quadrilateral layout arcs generation. (A) We keep W_{S3} passing through all cutting sharp points. Into each relevant U_k, partial line inverse mapping is performed using points in C and D as depicted in (B). Notice that we can use points in O, but this set is not pictured. (C) Shows curves in the physical space with supplementary traced boundary curves. Other arcs are determined to have a valid quadrilateral layout or cuboid decomposition, in the parametric space (D) and in the physical one (E).

[**D**] Using previously computed temporary patches P_{Tk}, we first set $u = 0$ for vertices on B_i and $u = 1$ for vertices on B_j, then solve $\Delta u = 0$. Using an approach close to [Zeng et al. 2009a], among all iso-v curves along ∇u starting from B_i and B_j, we automatically select two relevant curves which are intersecting the filled boundary B_k, one starting from temporary seed point s_{Tik} on B_i and one starting from temporary seed point s_{Tjk} on B_j. Figure 3.6 (A), (B) and (C).

[**E**] By performing this previous task on each temporary patch P_{Tk}, we obtain 6 temporary seed points s_{Tij}, s_{Tik}, s_{Tji}, s_{Tjk}, s_{Tki} and s_{Tkj}. Working on all patches P_{Tk}, we plot an iso-v curve along ∇u from the seed vertex s_{Tik} on the boundary B_i to the seed vertex s_{Tjk} on boundary B_j. We slice P_{Tk} along this iso-curve and get two duplicated boundary paths. We finally set $v = 0$ and $v = 1$ on them respectively and solve $\Delta v = 0$ to obtain the 3 oriented temporary unit-square maps denoted U_{Tk} with corners $\{s_{Tik}, s_{Tjk}, \overline{s_{Tik}}, \overline{s_{Tjk}}\}$. $\overline{s_{Tik}}$ and $\overline{s_{Tjk}}$ are duplicated points of s_{Tik} and s_{Tjk} respectively. Notice that triangles from filling are removed during U_{Tk} computation. Figure 3.7 row (A).

[**F**] Points in C are mapped into each unit-square map U_{Tk} and automatically classified using parametric coordinates u and v. Then we perform partial line inverse mapping between each classified cutting points c_j related to associated relevant U_{Tk} and merge computed lines to obtain valid sharp cutting curves W_{S1}, W_{S2} and W_{S3}. Figure 3.7 row (B) and (C).

Step 2. We generate 3 feature-aware oriented unit-square maps denoted U_k:

[**A**] We remove a long branch by cutting along its sharp cutting curve W_{Sk}. We proceed like **Step 1** [**C**] to obtain a feature-aware cutting patch P_k.

[**B**] Using the same workflow of **Step 1** [**D**] sharp seed points s_{ik} and s_{jk} are determined.

[**C**] Using the same workflow of **Step 1** [**E**], we obtain 6 sharp seed points s_{ij}, s_{ik}, s_{ji}, s_{jk}, s_{ki} and s_{kj}. Then 3 feature-aware oriented unit-square maps U_k are extracted.

Step 3. We generate all arcs of $\mathbb{Q}$:

[**A**] According to **Step 1** [**F**] sharp cutting arcs W_{Sk} have already been computed. We keep W_{S3} passing through all cutting sharp points. Figure 3.8 (A).

[**B**] Among a set D of n_d sharp boundary points $D = \{d_0, ..., d_{n_d}\}$, we map these points into corresponding maps U_k. Using automatic classification with parametric coordinates u and v, we pair on each relevant U_k points in D with sharp cutting points in C. We perform partial line inverse mapping to obtain arcs of the quadrilateral layout. Boundary arcs are determined directly in the physical space. Figure 3.8 (B) and (C).

[**C**] Consider a non-empty set O of n_o common sharp points $O = \{o_0, ..., o_{n_o}\}$. We proceed like **Step 3** [**B**] by pairing on each relevant U_k points in O possibly with C or D.

[**D**] Remaining arcs of the quadrilateral layout or cuboid decomposition are computed using partial line inverse mapping into relevant U_k with points in D, O or in C. Other arcs and points are then obtained by line-line intersection analysis. Figure 3.8 (D) and (E).

The proposed algorithm steps are given for a simple case of 4 cuboids per pant patch. We can easily add other sharp features to handle more complex geometry cases. With sharp points in C or other sharp points in D or O used in **Step 3** [**C**], a huge variety of shapes can be decomposed into feature-aware cuboids. Note that these sharp points or features can be integrated into a specific automatic algorithm to avoid manual selection.

3.2.2.2 Workflow overview

We split our geometry-feature-aware pants-to-cuboids decomposition approach in two main parts: the mechanical and biological workflows respectively in Figure 3.9 and in Figure 3.10. These illustrations provide keys points of the proposed method demonstrated with simple cuboid templates composed by 4 cuboids. Indeed, depending on the studied application, we can generate quadrilateral layout arcs in a different manner. [Al-Akhras 2016] has used specific quadrilateral layouts for biological purposes without prescribed sharp points.

In order to summarize, given a consistent pants decomposition, our algorithm is capable to decompose a triangulated surface into quadrilateral patches suitable for further volumetric parameterizations. This previous task is done by specifying relevant sharp points relative to a given quadrilateral layout $\mathbb{Q}$ or cuboid configuration $\mathbb{C}$ template. In addition, computed relevant parametric spaces U_k are important aspects not to neglect. To compute line inverse mapping on constrained square parametric spaces, more complex is the geometry, better has to be the square parameterization. Besides in Figure 3.9, remark that curves and 4-valency nodes of $\mathbb{Q}$ are not particularly lying and sitting on features. In fact, due to the harmonic parameterization and geometry of considered parametric spaces, arcs of $\mathbb{C}$ have not been constrained onto sharp edges.

3.2.3 Cuboid decomposition templates

Depending on the geometry provided by a specific pant patch, we need a precise cuboid configuration template to be mapped into the surface. This idea is illustrated in Figure 3.11 and configurations properties are examined in Chapter 6. Like we developed before, all features of the input triangulated geometry, i.e., sharp vertices, corners and edges must be replicated in the chosen cuboid configuration. For example, a set of sharp edges of a specific region may have an associated cuboid arc. This process, similar to a coarse one-to-one mapping for features is fundamental in order to obtain a suitable surface segmentation.

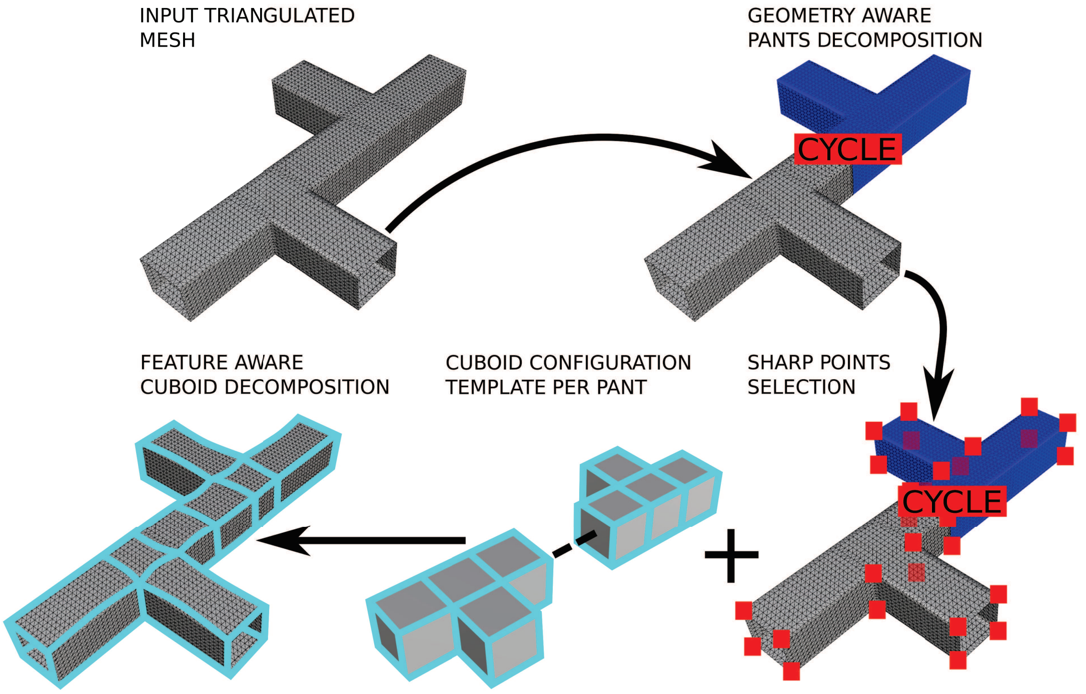

Figure 3.9: Smart model decomposition overview for mechanical applications. Starting with a triangulated surface, we decompose into a set of topological pants understanding the geometry. Afterwards, depending on the features embedded in the input mesh, cuboid configuration templates per pant are chosen. These templates are then mapped back into the surface mesh yielding to a feature-aware cuboid decomposition.

3.3 Towards hybrid n-pant topology surface decomposition

3.3.1 n-pant topology definition

Decomposing a surface can be done by really differents approaches. We have chosen to segment surface M into pants because of the topological characteristic equal to $\chi(M) = 1$. Moreover, the pants decomposition method allows to treat T-junctions because of three 1-manifolds, i.e., boundaries of the pant surface. But in general, in encountered mechanical parts, segmenting only with classical pants is not an optimal method. Aiming to map a cuboid configuration into a pant geometry, it is more suitable to consider n-pant divisions of the input surface. In Definition 3.1, we give properties of n-pant topologies in Equation (3.1). 1-pant topology is known as the classical pant with 3 boundaries.

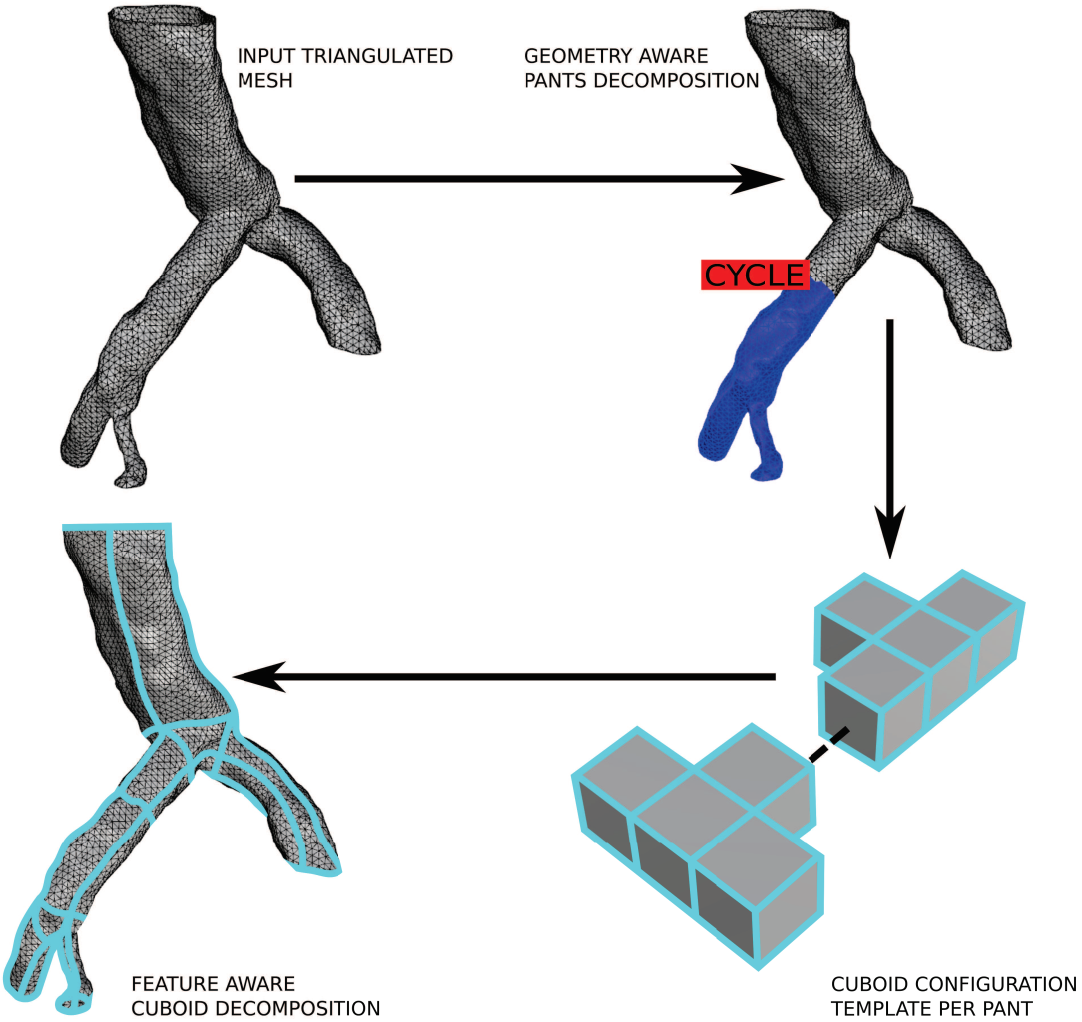

Figure 3.10: Smart model decomposition overview for biological applications. Starting with a triangulated surface from medical imaging, we decompose into a set of topological pants understanding the geometry. Cuboid configuration templates per pant are chosen. These templates are then mapped back into the surface mesh yielding to a feature-aware cuboid decomposition.

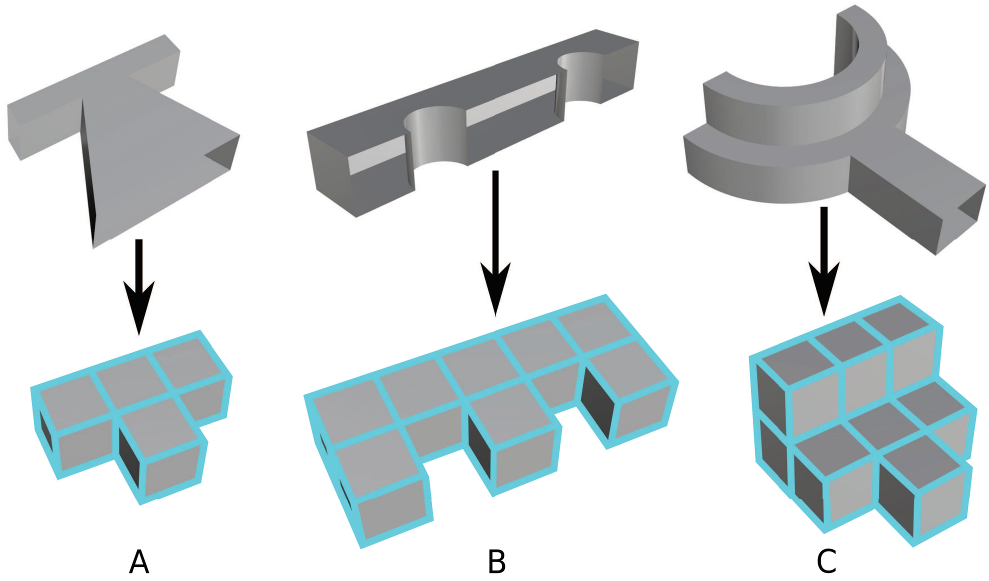

Figure 3.11: Cuboid configuration templates $\mathbb{C}$. To understand all the features of a CAD model, a specific cuboid configuration has to be applied for mapping purposes. (A) Represents the simplest cuboid configuration $\mathbb{C}$ for a pant. (B) Configuration $\mathbb{C}$ with 8 cuboids. (C) Configuration $\mathbb{C}$ with 10 cuboids.

Definition 3.1. ***n*-pant topology**. n-pant topology is a genus-0 connected, compact and oriented 2-manifold M with a number of boundaries $b \in [3, 4, 5, 6]$:

$$\begin{cases} \text{1-pant} : \chi(M_{1p}) = -1 \ \& \ b = 3, \\ \text{2-pant} : \chi(M_{2p}) = -2 \ \& \ b = 4 : \chi(M_{1p} \sqcup M_{1p}) = \chi(M_{1p}) + \chi(M_{1p}), \\ \text{3-pant} : \chi(M_{3p}) = -3 \ \& \ b = 5 : \chi(M_{2p} \sqcup M_{1p}) = \chi(M_{2p}) + \chi(M_{1p}), \\ \text{4-pant} : \chi(M_{4p}) = -4 \ \& \ b = 6 : \chi(M_{3p} \sqcup M_{1p}) = \chi(M_{3p}) + \chi(M_{1p}). \end{cases} \tag{3.1}$$

Where $\sqcup$ is the disjoint union operator for 2-manifolds. The Euler characteristic of the disjoint union is the sum of Euler characteristics. For instance, a 2-pant is composed by two distinct 1-pants. By merging these 1-pants along one of their boundaries, this process reduces the number of boundaries by 2. Disjoint union is achieved and true because of the exclusion-inclusion principle due to the topological nature of $\chi(M_{1p} \cap M_{1p})$. Indeed, $\chi(M_{1p} \cap M_{1p})$ is a circle composed by vertices and edges in the same quantity without faces: $\chi(M_{1p} \cap M_{1p}) = V - E + F = 0$. Figure 3.12 illustrates topological shapes of all possible n-pant topologies. For the sake of comprehension, 2-pants are called shirts, 3-pants are denominated suits and 4-pants are spacesuits due to the air inlet hole.

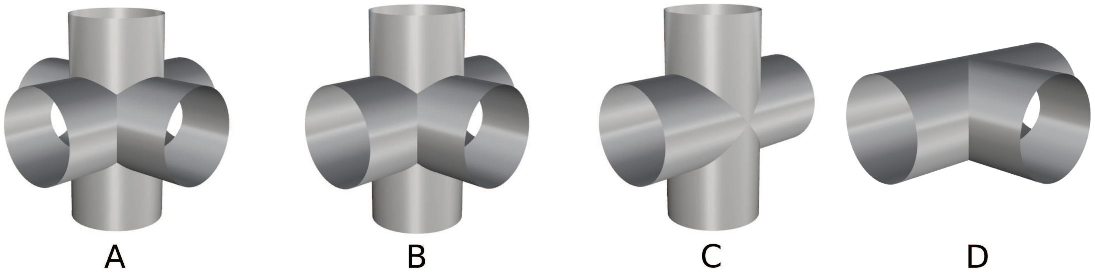

Figure 3.12: n-pant topological shapes. (A) 4-pant or spacesuit. (B) 3-pant or suit. (C) 2-pant or shirt. (D) 1-pant or classical pant.

3.3.2 n-pant cuboids library

Building a library which classifies admissible cuboid configurations per n-pant topologies is legitimate. Our approach is to first decompose the unstructured surface M into geometry-aware n-pants. Each pant of dimension n is chosen to respect the embedded features of the geometry in an optimal cuboid decomposition goal. By optimal we mean a cuboid configuration that can be mapped into the triangulated geometry and replicate sharp edges, corners and other relevant geometrical features. We seek to have less cuboids as possible while doing appearing of the geometry characteristics into the cuboid configurations $\mathbb{C}$.

Once we have decomposed the mesh M into pants, shirts, suits or spacesuits, a cuboid configuration is associated per n-pant. We construct the library in the way that the number of volumes is increasing from the simplest $\mathbb{C}$ admissible for a given n-pant topology. This draft idea is depicted in Figure 3.13. Figure 3.13 (A) is composed by a pant and a suit, Figure 3.13 (B) and Figure 3.13 (C) are adopted to be mapped onto the physical space, i.e., onto the mesh M to replicate the features.

3.4 Conclusion

We have greatly enhanced existing methods consisting in pants-to-cuboids decomposition [Li et al. 2013; Al-Akhras 2016] to geometry-feature-aware pants-to-cuboids decomposition. The first step toward this objective is the segmentation-aware pants decomposition. Such division decomposes a complicated surface into shapes with a trivial topology. We seek in addition to understand both topology and geometry while segmenting. Improvements were done by analyzing all topologically admissible pants decompositions by coupling all combinations of boundaries. Thus, homotopic cycles w_{ij} have a better shape according to a given global geometric criterion. In addition, sharp considerations were made to segment into pants along relevant edges or regions. The second step is done by associating a cuboid configuration to each pant and map it into the physical space. Such mapping is performed by solving harmonic functions on meshes, i.e., dealing with linear matrix systems. The novelty

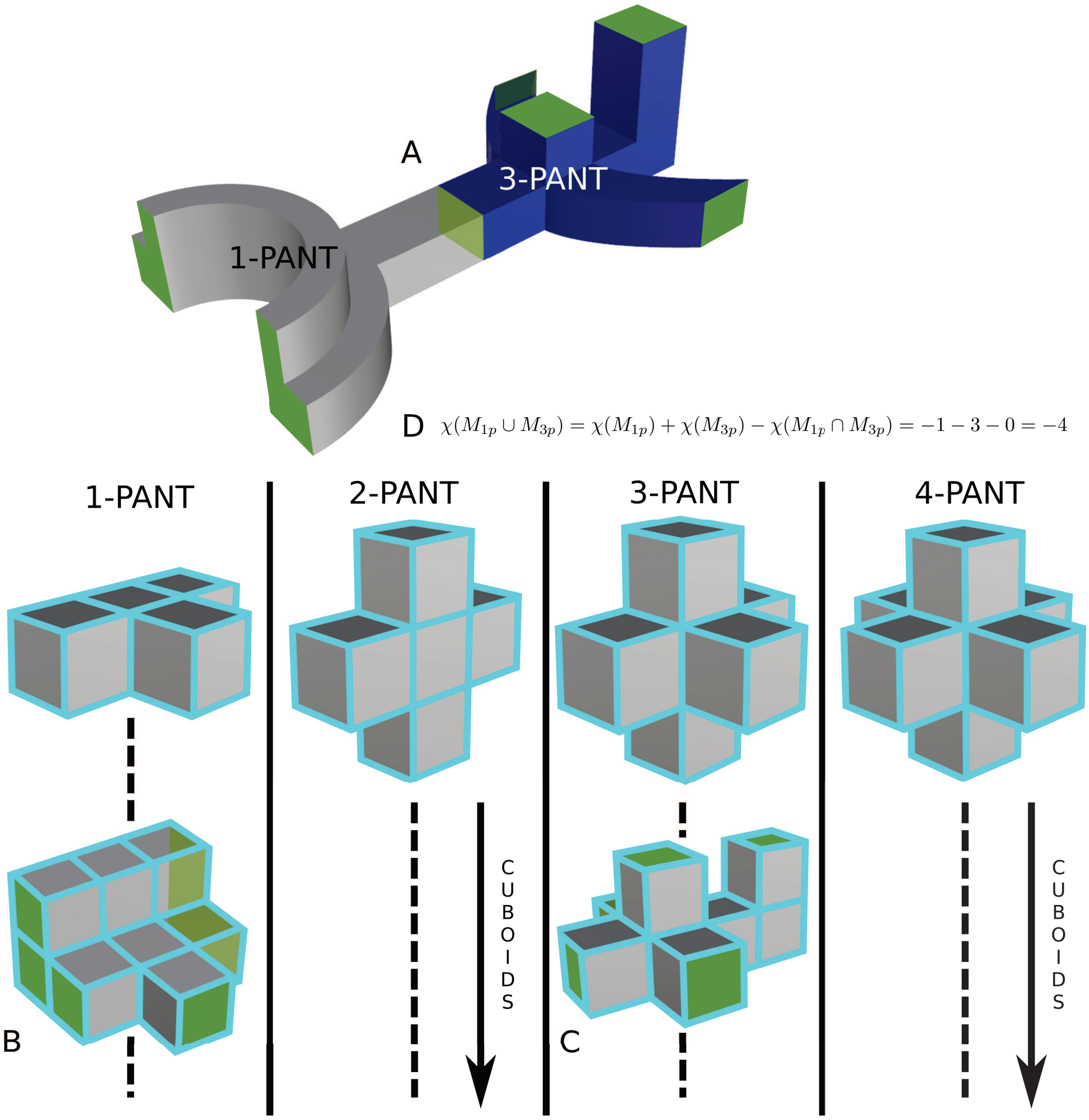

Figure 3.13: n-pant cuboids library. (A) A n-pant decomposition of an arbitrary B-Rep mesh M provided from CAD. (B) Adopted cuboid configuration $\mathbb{C}$ chosen in the 1-pant column for the left part of (A). (C) Adopted cuboid configuration $\mathbb{C}$ chosen in the 3-pant column for the right part of (A). Green surfaces represent cuboid faces which are mapped onto the boundaries of the M n-pant decomposition. (D) Euler characteristic of the n-pant topological decomposition (A) using union operator $\cup$.

is brought by constraining some of irregular nodes of the cuboid configuration $\mathbb{C}$ onto sharp corners. Moreover, the process has been designed in the way to be a geometrical feature one-to-one mapping between cuboid configuration and the real decomposition on the mesh M.

To go further, other decompositions types have been analyzed. n-pant topologies provide topological tools to expand the geometry comprehension of M during segmentation. n-pant approach bridge the gap for the notion of optimal cuboid decomposition of an arbitrary surface with a complex topology. Surface T-junctions, i.e., 3-way directions inside a volume enclosed by a surface are understood by 1-pants; but 4-way surface junctions are not. 4-pant or spacesuit handles 6 directions and permit to map suitable cuboid configurations.

Remembering that cuboid configurations are considered as surfaces or 2-manifolds, the next Chapter 4 will treat the triangulated surface parameterization in a global manner. This parameterization must conform with the cuboid structure and follow the features of the input CAD model.

Chapter 4

Model surface aligned global parameterization

This chapter presents surface global parameterization tools essential to build quadrilateral meshes from triangulated geometry.

Contents

4.1 n-symmetry direction field generation

Introduced in Section 2.1, 4-symmetry directions fields (i.e., cross fields $\mathcal{C}$) are widely used to determine an aligned global parameterization [Bommes, Zimmer, and Kobbelt 2009; Bommes et al. 2013a; Myles and Zorin 2013; Campen and Kobbelt 2014]. Designing a smooth cross field $\mathcal{C}$ on a surface is done with a given set of constraints. We categorize these constraints in two groups: topological and geometrical constraints. Topological constraints are imposed singularities and numbers induced by the surface topology with its homology generators or boundaries. Geometrical constraints are intrinsically embedded on the surface and depends on the local geometry behavior. Thus, we seek a cross field $\mathcal{C}$ which is smooth, aligned with local geometry and topologically compatible, i.e., defined by the surface properties. The quadrilateral layout $\mathbb{Q}$ or cuboid configuration $\mathbb{C}$ from Chapter 3 contains topological properties whereas the surface M holds the geometrical information. In the following, we study discrete cross fields embedded on triangulated surfaces. Important notions such as connection angles and period jumps are explicited and lead us to correctly define properties of these discrete fields.

4.1.1 Discretization on triangulated meshes

In order to represent discrete 4-symmetry direction fields, we consider a triangulation of the surface M, assumed to be a 2-dimensional manifold of genus-g with b boundary components. Directions will be stored at faces F to avoid definition of supplementary tangent planes. Hence, in the following, direction fields will be represented at faces F of the mesh M, or equivalently at vertices V^* of the dual mesh M^*. M is consistently oriented: normals are coherent, edges E are oriented and allow to define a unique orientation of dual edges E^*.

The first step of the discretization consists in finding a reference direction in each triangle. This is done by choosing a local orthonormal frame $(\mathbf{x}, \mathbf{y})$ attached on each face f. $\mathbf{x}$ is a unit vector along one of the oriented edges of face f, and $\mathbf{y} = \mathbf{n} \times \mathbf{x}$, $\mathbf{n}$ being the normal of f. A direction $\mathcal{U}_c$ on f can be formulated in terms of polar coordinates. Due to the unit norm of such directions, it is completely parameterized by the polar angle α it forms with $\mathbf{x}$. Thus, we denote α the direction angle. We deal with a 4-symmetry direction field, i.e., a set of 4 directions $\{\mathcal{U}_c, \mathcal{V}_c, -\mathcal{U}_c, -\mathcal{V}_c\}$ preserved by rotations of $\frac{\pi}{2}$ around the normal $\mathbf{n}$. This is the idea depicted in Figure 4.1 (A).

By unfolding adjacent triangles isometrically to a plane along their common edge, angles can be expressed in a common coordinate frame. In other words, we can formulate an angle on face f_i in f_i's adjacent faces. However, by calculating the direction field only at a set of points, it remains an infinite number of interpolation possibilities. This ambiguity can be solved between two points by specifying an integer $p_{ij} \in \mathbb{Z}$ called the period jump [Li et al. 2006; Ray et al. 2008] between face f_i and face f_j with references $\mathbf{x}_i$ and $\mathbf{x}_j$. The period jump specifies the number of

$\frac{\pi}{2}$ turns the direction $\mathcal{U}_c^i$ undergoes to be compared with $\mathcal{U}_c^j$ when walking along a dual edge e_{ij}^*. Other works introduce an angle w_{ij} named connection angle to solve the ambiguity [Crane 2010; Crane, Desbrun, and Schröder 2010]. Figure 4.1 (B) shows the used discretizations. $\kappa_{ij} \in]-\pi, \pi]$ represents the angle between a reference direction $\mathbf{x}_i$ on face f_i and $\mathbf{x}_j$ on face f_j. α_i^i and α_j^j are respectively angles expressed on their native faces.

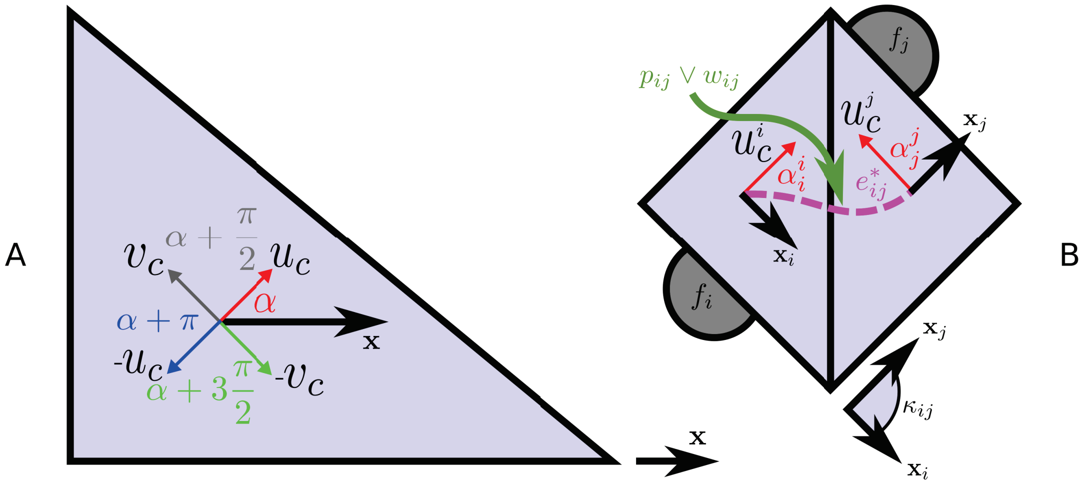

Figure 4.1: Cross field discretization on triangulated meshes. (A) A 4-symmetry direction field is a set of 4 directions $\{\mathcal{U}_c, \mathcal{V}_c, -\mathcal{U}_c, -\mathcal{V}_c\}$ preserved by rotations of $\frac{\pi}{2}$ around the face normal $\mathbf{n}$. (B) To interpolate a field between two discrete points and manage possibilities, the problem can be solved by introducing a period jump p_{ij} or a connection angle w_{ij}. Angles in adjacent faces can be expressed in a common coordinate frame using κ_{ij} and p_{ij} or w_{ij}.

In the following we consider two different discretizations: period jump based discretization and connection angle based discretization as summarized in [Al Akhras et al. 2017]. The first discretization computes an angle ${}^p\alpha_i^j$ from face f_i expressed in adjacent face f_j which is in general different from α_j^j as given in Equation (4.1). The attached cross field curvature ${}^p\kappa_{\mathcal{C}}(e_{ij}^*)$ of the period jump based discretization along oriented dual edge e_{ij}^* is computed as the difference between native angle α_j^j expressed on face f_j and ${}^p\alpha_i^j$, see Equation (4.2).

$$ {}^p\alpha_i^j = \alpha_i^i + \kappa_{ij} + \frac{2\pi}{4} p_{ij} \neq \alpha_j^j, \tag{4.1} $$

$$ {}^p\kappa_{\mathcal{C}}(e_{ij}^*) = \alpha_j^j - {}^p\alpha_i^j = \alpha_j^j - [\alpha_i^i + \kappa_{ij} + \frac{2\pi}{4} p_{ij}]. \tag{4.2} $$

The second discretization computes an angle ${}^c\alpha_i^j$ from face f_i expressed in adjacent face f_j which is in general equal to α_j^j as given in Equation (4.3). w_{ij} is the connection angle when walking on the dual edge linking face f_i to face f_j. ${}^c\kappa_{\mathcal{C}}(e_{ij}^*)$

is the cross field curvature for the connection angle based discretization along the oriented dual edge e^*_{ij} as expressed in Equation (4.4).

$$
\begin{aligned}
{}^{c}\alpha_i^j &= \alpha_i^i + \kappa_{ij} + w_{ij}, && (4.3)\\
{}^{c}\kappa_{\mathcal{C}}(e^*_{ij}) &= w_{ij}. && (4.4)
\end{aligned}
$$

In the following we will use connection angle based discretization for topological design and period jump based discretization for geometrical design of the cross field. Notice that we need a direction angle and all connection angles to completely define the direction field with discretization in Equation (4.3). For Equation (4.1) all direction angles and all period jumps are required.

4.1.2 Field smoothness

An important requirement for a cross field is smoothness. Measuring smoothness of a cross field reduces to measuring the smoothness of one of the four directions if the topology is fixed. In case of a field without prescribed topology, the smoothness is closely related to connection angles w_{ij}. This smoothness energy can be simply calculated as its integrated squared curvature $\kappa_{\mathcal{C}}(e^*_{ij})$ [Ray et al. 2008]. This is typically the sum of all curvatures endorsed along all oriented dual edges e^*_{ij} of the mesh M. We minimize the first energy ${}^{c}E(\mathcal{C})$ in Equation (4.5) to determine the field topology and the second energy ${}^{p}E(\mathcal{C})$ to compute the field geometry in Equation (4.6).

$$
\begin{aligned}
{}^{c}E(\mathcal{C}) &= \sum_{e^*_{ij}\in E^*} \|{}^{c}\kappa_{\mathcal{C}}(e^*_{ij})\|^2, && (4.5)\\
{}^{p}E(\mathcal{C}) &= \sum_{e^*_{ij}\in E^*} \|{}^{p}\kappa_{\mathcal{C}}(e^*_{ij})\|^2. && (4.6)
\end{aligned}
$$

4.1.3 Geometrical field generation

4.1.3.1 Topological design

Aiming to compute the cross field topology, we wish a smooth cross field $\mathcal{C}$ that is singular only at specified vertices: the position of irregular nodes of $\mathbb{Q}$. By irregular we mean a valence different than 4. Technically speaking, we want to restrict the field to a given topology, i.e., to fix all its degrees of freedom as explained in Chapter 2. We first focus on the method to set the topology understanding properties and theorems making it admissible on a given surface. Then, interesting topological degrees of freedom will be detailed.

For the topological step, we use parallel transport to map a direction between to distinct tangent planes [Crane 2010]. Generally, two adjacent mesh faces do not have the same tangent planes as reference. For a mesh M, the connection angle w_{ij} can be integrated on the oriented dual edge e^*_{ij} when passing from one face f_i to face f_j. If connection angles are set to zero, this gives us the usual Levi-Civita connection. Figure 4.2 shows the Levi-Civita connection between two adjacent triangles of gravity centers G_i and G_j having two different tangent planes.

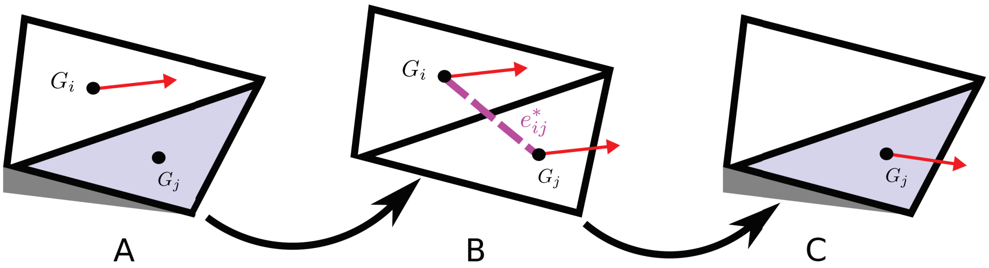

Figure 4.2: Levi-Civita connection using triangulated mesh faces. (A) Transporting a vector from face f_i to f_j of gravity centers G_i and G_j can be done as follows: (B) unfold the faces isometrically to a plane, parallel transport the vector along the oriented dual edge e^*_{ij} and then (C) fold back the face in its original configuration.

For a curved mesh M in the topological space $\mathbb{R}^3$, a direction parallel transported around a loop $l(s)$ by a connection will not return to its original orientation. This angle difference is called the holonomy δ along a loop $l(s)$. Holonomy is explicited in Definition 4.1 with Equation (4.7) to Equation (4.9). This angle defect is related to the Gaussian curvature of the surface and geodesic curvature of $l(s)$. For instance, for contractible cycles, i.e., cycles or loops $l(s)$ which can be reduced into a point, the holonomy of the connection is equal to the Gaussian curvature over the region. Readers are advised to see Equation (4.10) as demonstrated in Figure 4.3 contained in Proof 4.1. Indeed, for a sphere with a constant non-zero Gaussian curvature, an initial vector $\mathcal{V}_s$ is not mapped back to itself. This vector is mapped to $\mathcal{V}_e$ because of the holonomy.

Definition 4.1. Holonomy along a cycle or a loop $l(s)$. Holonomy is equal to zero when zero Gaussian curvature is present into the whole the mesh, i.e., it can be a surface integrated into the $\mathbb{R}^2$ topological space. So, for a disk in $\mathbb{R}^2$, holonomy should be equal to zero:

$$\int_M K dS + \int_{l(s)} k_g ds + \delta = 2\pi, \tag{4.7}$$

$$0 + \int_{l(s)} k_g ds + \delta = 2\pi, \tag{4.8}$$

$$\int_{l(s)} k_g ds = -\delta + 2\pi. \tag{4.9}$$

We notice that in $\mathbb{R}^2$, all loops $l(s)$ have a geodesic curvature equal to 2π. Holonomy is set as the angle defect between 2π and the classical geodesic curvature in the topological space $\mathbb{R}^2$.

Proof 4.1. Holonomy of a contractible cycle or a loop $l(s)$. In case of contractible cycles or loops $l(s)$, the holonomy around the loop is equal to the total Gaussian curvature over the region englobed by $l(s)$:

$$\int_M K dS = \delta. \tag{4.10}$$

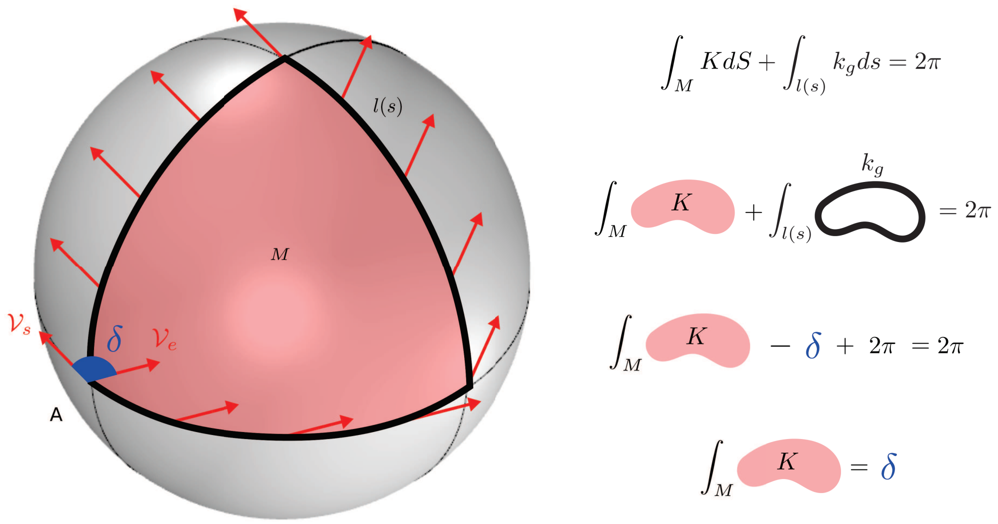

Figure 4.3: Holonomy of a contractible loop $l(s)$ demonstrated by the Gauss-Bonnet theorem. For a disk, $\chi(M) = 1$. Thus, the total geodesic and Gaussian curvature of the black loop and pink surface is equal to 2π.

The holonomy [Ray et al. 2008; Myles and Zorin 2012; Myles and Zorin 2013] of a Levi-Civita connection is defined in Figure 4.4 in Example 4.1 for used discrete cases. Around a vertex v, the holonomy of a cycle γ is equal to the discrete Gaussian curvature at this vertex. Since Gaussian curvature measures angle defects, holonomy can be viewed as the angle defect for geodesic curvature.

Example 4.1. (Discrete holonomy of a loop or cycle γ) For discrete meshes embedded in $\mathbb{R}^3$, a direction parallel tranported along a cycle γ is in general not mapped back to itself. Path of transport is formed by dual edges e^*_{ij} when passing from face f_i to face f_j. The discrete holonomy measures this quantity along γ. s_i are the signs associated to angles k_i depending on the direction of rotation and triangles connectivity. There are typically n_t triangles crossed by the cycle γ.

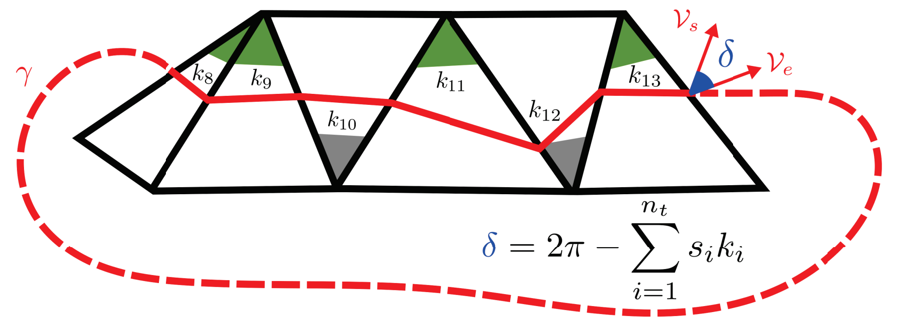

Figure 4.4: Discrete holonomy on triangulated meshes for a cycle γ. We observe an angle defect δ between $\mathcal{V}_s$ and $\mathcal{V}_e$ using the classical Levi-Civita connection along a cycle γ to transport a vector $\mathcal{V}_s$.

The issue of holonomy for fields embedded on surfaces has been tackled for example by [Crane 2010]. Such work gives an algorithm for the computation of connection angles w_{ij} needed for topological design. To respect theorems such as the Gauss-Bonnet theorem, we have to distribute smartly the Gaussian curvature. Zero holonomy for all possible cycles stands for zero Gaussian curvature everywhere. To overcome this major issue in order to map back transported vectors, [Crane, Desbrun, and Schröder 2010] presented a connection with globally vanishing holonomy yielding to path independent mappings. Total curvature is distributed on the mesh in a way that does not interfere with parallel transport. If a surface must have Gaussian curvature somewhere, curvature is concentrated at boundaries or singularities in increments of $\frac{\pi}{2}$. According to [Ray et al. 2008], the turning number $T_{\mathbf{d}}(\gamma)$ associated to a cycle γ formed by dual edges e^* is the number of turns a direction makes before coming back to its starting point as written in Equation (4.11). For the sake of simplicity, the field notation is now omitted: $T_{\mathbf{d}}(\gamma) = T_\gamma$.

$$T_\gamma = \frac{1}{2\pi}[\sum_{e^* \in E^*} {}^c\kappa_{\mathcal{C}}(e^*) - \sum_{i=1}^{n_t} s_i k_i]. \tag{4.11}$$

With this definition, the cross field curvature using connection angle discretization can be expressed in Equation (4.12) for an holonomy δ_γ associated to a considered cycle γ. This allows us to add curvature along cycles γ to cancel the holonomy found by the Levi-Civita connection. In terms of connections, we can add some curvature that cancels the holonomy in order to respect the Gauss-Bonnet theorem.

$$\sum_{e^* \in E^*} {}^{c}\kappa_{\mathcal{C}}(e^*) = 2\pi T_\gamma + 2\pi - \delta_\gamma. \tag{4.12}$$

Once we know the topological behavior of fields understanding holonomy aspects to compute a globally consistent cross field, we want to fix all these topological degrees of freedom. We wish to restrict the 4-symmetry direction field with desired properties inherited from the quadrilateral layout $\mathbb{Q}$. These topological degrees of freedom are identified to be turning numbers along $2g$ homology generators, b boundary cycles and $s-1$ singularities [Ray et al. 2008; Campen and Kobbelt 2014] as already detailed in Chapter 2. Typically, for a sphere which has no homology generators and boundaries, we add at least one singularity in order to respect the Poincaré-Hopf theorem. We use the approach of [Campen and Kobbelt 2014] to determine interesting turning numbers from the input quadrilateral layout. For that purpose, we use turning numbers referenced in Table 4.1. v_i refers to the valence of node i belonging to $\mathbb{Q}$. n_n is the number of nodes in the closest homotopic cycle γ_c whereas n_a is associated to the number of arcs crossed by γ. The sign is determined by the relative orientation between γ_c and γ.

Turning numbers	Location
$T_\gamma = -v_i/4$	Around nodes v_i of $\mathbb{Q}$
$T_\gamma = \pm 1/4(n_n - n_a)$	Around homology generators of $\mathbb{Q}$
$T_\gamma = \pm 1/4(n_n - n_a)$	Around boundary cycles $\mathbb{Q}$

Table 4.1: Turning numbers of the field determined by the quadrilateral layout $\mathbb{Q}$.

[Crane, Desbrun, and Schröder 2010] introduced an algorithm that, given these turning numbers, determines the appropriate connection angles w_{ij} only by solving a sparse linear system based on the minimization of Equation (4.5). We still need one direction angle to completely define the required direction field, thus we choose an arbitrary initial angle α_0. Figure 4.5 shows a topological field computation pipeline result on a 3-way pipe. $\chi(M) = -1$, so it is a topological pant as depicted in Figure 4.5 (A). We then use the quadrilateral layout $\mathbb{Q}$ computed from Chapter 3 to determine turning numbers around interesting cycles γ previously defined in Table 4.1 in Figure 4.5 (B). Figure 4.5 (C) gives the resulting cross field with topological constraints. In the detail of Figure 4.5 (D), we can notice that the field does not spin around the boundary cycle in red, resulting in a turning number $T_\gamma = \pm\frac{1}{4}(n_n - n_a) = \pm\frac{1}{4}(4-4) = 0$. Same process is done around singularities, i.e., irregular nodes of $\mathbb{Q}$, where in Figure 4.5 (E), $T_\gamma = -\frac{v_i}{4} = -\frac{5}{4}$. Remember the behavior of turning numbers near a singularity embedded in point P previously explained in Chapter 2, $T(\partial\Omega(P)) + 1 = T_\gamma + 1 = I(P) = -\frac{1}{4}$. Same analogy for boundary cycles can be done with homology generators if considering a genus-g surface.

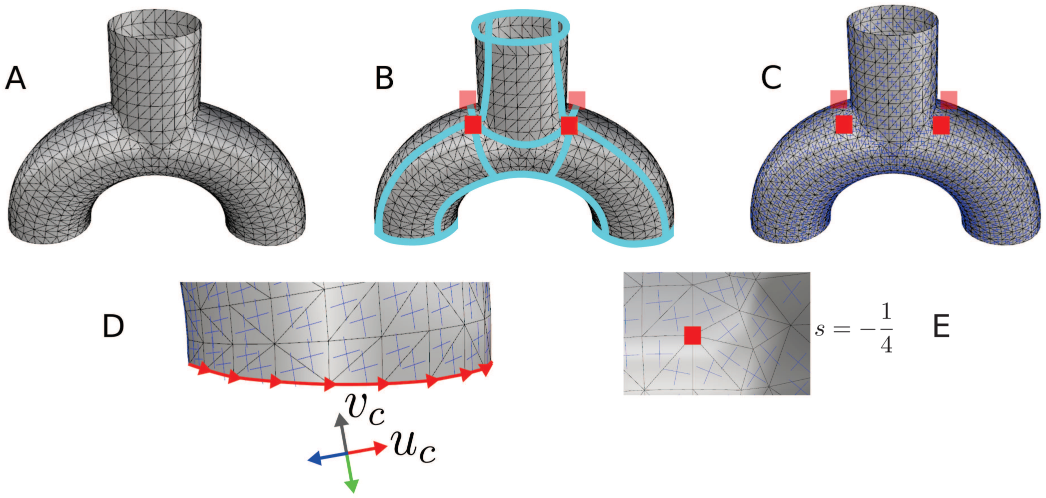

Figure 4.5: Cross field topological design. (A) Input triangulated surface. (B) Generated quadrilateral layout $\mathbb{Q}$ that define the cross field topological properties. (C) Generated topologically compatible cross field. (D) Detail of (C) near one of its 3 boundaries. The cross field has a turning number of $T_\gamma = 0$ along this boundary cycle, but it does not satisfy red boundary constraints. (E) Detail of (C) around one of its 4 singularities. The associated turning number near this singular zone is equal to $T_\gamma = -\frac{5}{4}$.

Going back to topological field generation using properties of $\mathbb{Q}$, another example of topological field generation is provided in Figure 4.6 (A) for a pant topology with sharp features. Because the field is topological, it does not respect sharp edges geometry and expected behavior near boundaries as shown in Figure 4.6 (B). Indeed, we need in addition a smooth cross field perfectly aligned to features we want to replicate in the new parameterization.

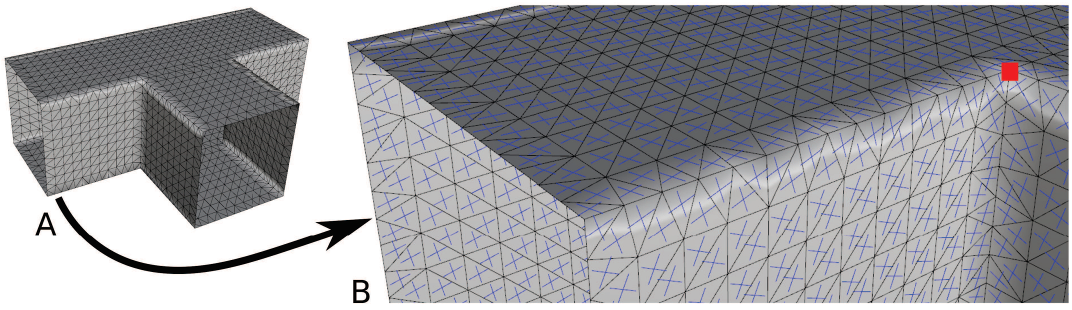

Figure 4.6: Cross field topological design with sharp features. (A) Input triangulated surface. (B) Generated cross field which does not understanding the geometrical features of the mesh. The turning number around the red singularity remains consistent.

In a topological designing process additional comprehension, properties of singularities can be estimated. Gaussian curvature distribution explained before in Section 2.1 is a method to locate and determine attributes of such singularities. This task can be done without quadrilateral layout $\mathbb{Q}$. Indeed, these fields can be generated with user specifications as long as the field properties are admissible with the surface topology.

4.1.3.2 Geometrical design

For a given topological cross field, we wish now to compute a smooth field that interpolates relevant principal curvature directions, sharp features and boundaries restricted to a given topology. In other words, geometrically, $\mathcal{C}$ must follow these geometrical features as depicted in Figure 4.7. Sharp features and boundaries constraints are obvious whereas principal curvature directions are not. In fact, for an arbitrary embedded point on the surface, we define the principal curvature directions as the product between 2 scalar quantities. They are calculated in 2 distinct perpendicular planes. We name k_1 and k_2 the minimum and maximum principal curvature such as $K = k_1 k_2$. Where K is the Gaussian curvature at a point surface. Directions are then defined by intersecting reference planes with the surface.

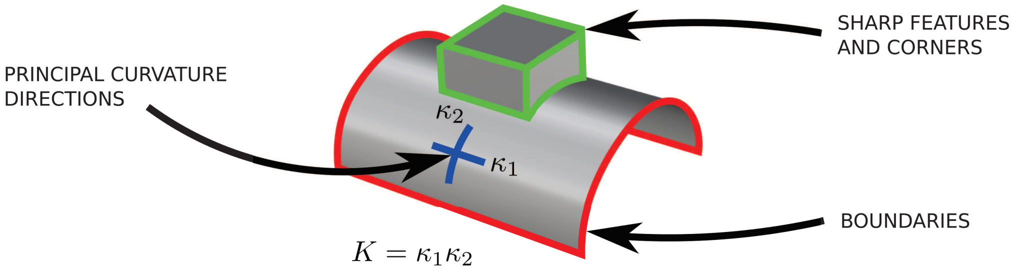

Figure 4.7: Relevant geometrical features which could be used for cross field interpolation. Sharp corners, boundaries and principal curvature directions refer to a certain global topological information embedded on the geometry. The Gauss-Bonnet theorem states the link between geometry and topology.

We search the smoothest field taking into account constrained directions α_c contained in a subset of faces $F_c \subset F$. Because the field topology is restricted, the period jumps of the field are fixed. The direction angles α are the only remaining variables used for the constrained minimization problem of the energy in Equation (4.6). For further comprehension, [Ray et al. 2008] showed that the topology of a cross field is entirely defined by its periods jumps. Using a technique presented by [Bommes, Zimmer, and Kobbelt 2009] and later exploited by [Al Akhras et al. 2017], we strive to minimize the constrained Equation (4.13). The geometrical field is a solution of a linear system obtained by setting the gradient of Equation (4.13) to zero. We refer the readers to the work of [Bommes, Zimmer, and Kobbelt 2009] for futher details.

$$\min_{\alpha\in\mathbb{R}^{|F|}} \sum_{e^*_{ij}\in E^*} \|{}^{p}\kappa_{\mathcal{C}}(e^*_{ij})\|^2 = \min_{\alpha\in\mathbb{R}^{|F|}} \|\mathbf{A}\boldsymbol{\alpha}-\mathbf{b}\|^2 \text{ s.t. } \alpha_i=\alpha_c,\ \forall f_i\in F_c. \tag{4.13}$$

With $\mathbf{A}\in\mathbb{R}^{|E|\times|F|}$, $\mathbf{b}\in\mathbb{R}^{|E|}$, and $\boldsymbol{\alpha}\in\mathbb{R}^{|F|}$. Remark that $\boldsymbol{\alpha}\in\mathbb{R}^{|F|}$ is the vector of unknown direction angles embedded on each face of the mesh M. For more details in matrix construction we refer the readers again to [Bommes, Zimmer, and Kobbelt 2009; Al-Akhras 2016]. This previous minimization can be also modified to integrate soft constraints. Figure 4.8 (B) shows the process using cross fields. Figure 4.8 (A) gives an interpolation using standard vector fields that do not yield a suitable result for a quadrilateral mesh purpose.

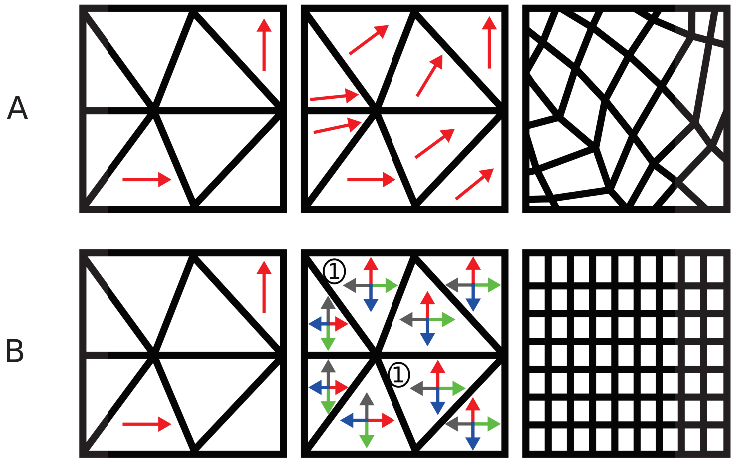

Figure 4.8: Cross field interpolation. (A) Sparse directions interpolation with a standard vector field. Parameterized mesh is not a suitable result for our objectives. (B) By using a cross field, i.e., a set of 4 directions, the resulting parameterized quadrilateral mesh as a natural expected geometry. Notice the period jump of 1, ensuring that the first red direction of the cross field match with given constrained directions.

To illustrate the geometrical interpolation, Figure 4.9 (A) shows the field alignement result with the boundary constraints. We observe that, the field behavior near the boundary cycle is perfectly aligned on each face. Figure 4.9 (A) is related to sharp edges constraints. With this particular mesh with sharp features, we compute a field aligned to edges belonging to faces with a certain normal vector angle threshold difference. Geometrical designing is done while respecting the imposed field topology. Consistent geometrical fields results then serve as reference to compute a suitable parameterization. This is done understanding surface topology and features of the input discrete triangulated mesh.

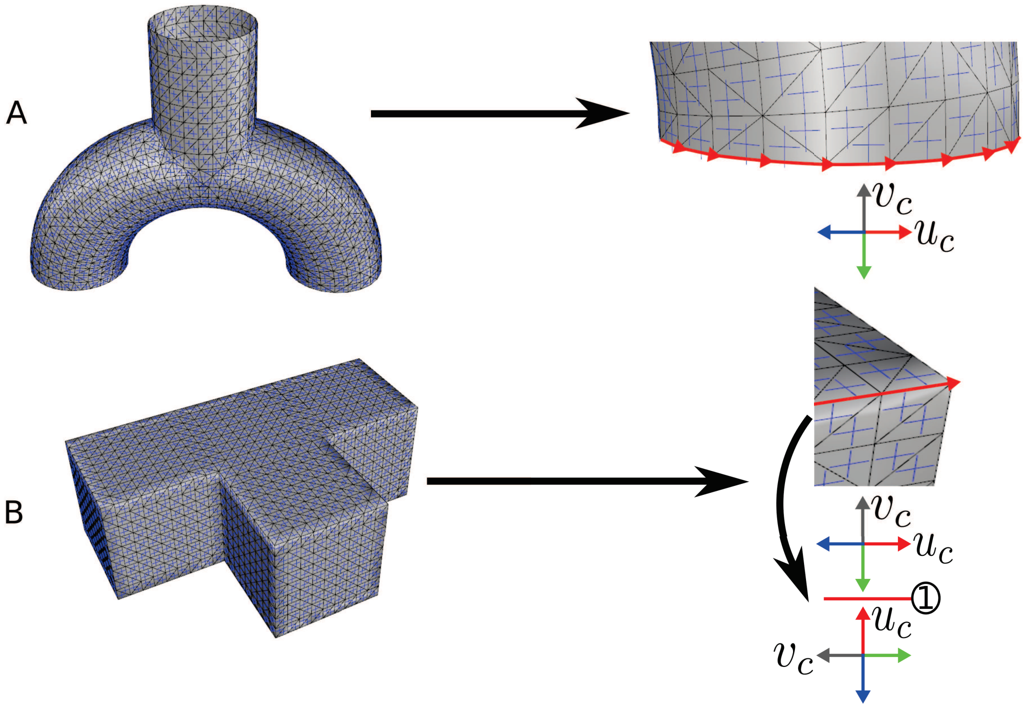

Figure 4.9: Cross field geometrical design. (A) Boundary red constraints interpolation. (B) Sharp edges red constraints interpolation. Across these sharp edges, the period jump is equal to 1, because of the $s = \frac{1}{4}$ singularity holded by the corner.

4.2 Aligned global parameterization from geometrical direction field

We now compute an aligned global parameterization, i.e., a map from the mesh M to a disk-like surface parameter domain $\Omega \in \mathbb{R}^2$ as already explicited in Chapter 2. We have to assign a couple (u, v) of parameters values on each vertex of M. The parameterization should be locally aligned with the features of the mesh, thus, this is done using the guiding geometrical cross field previously computed. In fact, replicating sharp features, sharp edges, boundaries and reliable principal curvature directions captured by the suitable geometrical cross field is our parameterization goal. Such parameterization implies that the gradients ∇u and ∇v of the discrete scalar field must follow the cross field directions on each face. This is the idea depicted in Figure 4.10.

4.2.1 Seamless parameterization

A planar parameterization of a mesh M embedded in $\mathbb{R}^3$ into a parametric domain Ω embedded in $\mathbb{R}^2$ is in general done by computing a cut graph G. Indeed, a planar isometric parameterization is in general impossible due to Gaussian curvature in the

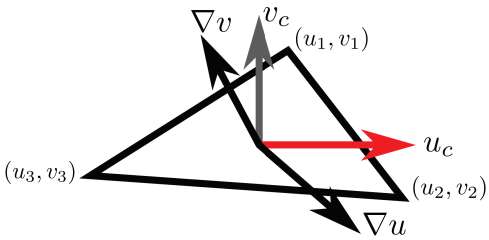

Figure 4.10: Global parameterization strategy using a geometrical cross field. We strive to find gradients ∇u and ∇v aligned to the first two parametric directions $\mathcal{U}_c$ and $\mathcal{V}_c$ of the cross field, by modifying parametric values (u, v) embedded in mesh vertices.

topological space $\mathbb{R}^3$. A cut graph G is a connected graph formed by edges of M that splits the mesh into a disk-like surface mesh M_d. Seams are then defined as duplicated paths of G. Transitions across seams need to belong to a very restricted class. We search for rigid transformations with a rotation angle multiple of $\frac{\pi}{2}$ because of the symmetry of cross fields. Moreover, across each seam edge or vertex, the corresponding transition must be integral, i.e., relative to an integer. Thus we talk about integral seamless parameterization [Kälberer, Nieser, and Polthier 2007; Bommes, Zimmer, and Kobbelt 2009; Myles and Zorin 2012; Myles, Pietroni, and Zorin 2014]. We target the cross field first and second directions $\mathcal{U}_c$ and $\mathcal{V}_c$ for the gradients of the parametric coordinates ∇u and ∇v. The parameterization is then computed as the solution of a constrained minimization problem written in Equation (4.14) subject to constraints referenced in Equation (4.15).

$$\min_{u,v} \sum_{f \in F} [\|\nabla u - \mathbf{u}^{\mathcal{C}}\|^2 + \|\nabla v - \mathbf{v}^{\mathcal{C}}\|^2] A_f \text{ s.t. Equation (4.15)}, \tag{4.14}$$

$$v_1^{'} = R_{\frac{\pi}{2}}^{m_{ij}} v_1 + t_{ij} \;\&\; v_2^{'} = R_{\frac{\pi}{2}}^{m_{ij}} v_2 + t_{ij}. \tag{4.15}$$

Where A_f is the area of the considered face $f \in F$. $v_1^{'}$ and $v_2^{'}$ are the corresponding final positions for a cut edge e_{ij} from face i to face j with endpoints vertices $v_1 \in \mathbb{R}^2$ and $v_2 \in \mathbb{R}^2$ in the parametric domain. Given a side of the cut by picking v_1 and v_2, the parameterization on the other side is determined by these previous transitions. $m_{ij} \in \mathbb{Z}$ is defined as the matching between the two local charts which specify the rotation operator R. Rotations are made by angles multiple of $\frac{\pi}{2}$. $t_{ij} \in \mathbb{Z}^2$ is an integer translation across a cut edge e_{ij}.

Aligned global parameterization can also integrate sharp edges and boundary constraints to ensure that a connected relevant set of sharp edges are mapped to an isoparametric curve [Bommes, Zimmer, and Kobbelt 2009]. This integration add constraints in the global parameterization in Equation (4.14).

4.2.2 Quadrilateral layout and nodes embedding optimization

4.2.2.1 Arcs embedding optimization

Once a valid quadrilateral layout and consistent geometrical cross field are provided, we wish to restrict each arc. Each arc is restricted in a way that the two incident nodes are lying on a common isoparametric curve. With isoparametric we mean that either the u or v parameter is constant along the curve when taking transitions in M_d into account. The minimization problem in Equation (4.14) is then constrained using nodes connection constraints. These constraints are derived from the quadrilateral layout $\mathbb{Q}$. Typically, each arc with endpoints n_1 and n_2 must lie on a common isoparametric curve taking seams transitions into account. Thus, the complete constraint has the form written in Equation (4.16) and in Equation (4.17) for the u and v parametric directions respectively [Myles et al. 2010]. Developments leading to these two equations are detailed in Appendix C.

$$n_{2u} = [(\prod_{i=0}^{m} R_{(m-i)+1})n_{1u} + (\sum_{i=0}^{m-1}(\prod_{j=0}^{m-1-i} R_{(m-j)+1})t_u^{i+1}) + t_u^{m+1}], \tag{4.16}$$

$$n_{2v} = [(\prod_{i=0}^{m} R_{(m-i)+1})n_{1v} + (\sum_{i=0}^{m-1}(\prod_{j=0}^{m-1-i} R_{(m-j)+1})t_v^{i+1}) + t_v^{m+1}]. \tag{4.17}$$

In this formulation, we consider a path crossing cut edges e_i, $\forall i \in \{0, 1, ..., m-1, m\}$ and rotation operators $|R| = |t| = m+1$ linking node n_1 and n_2. n_{2u} is defined as the linked u parametric value for n_{1u}. Thus, we are able to compute a suitable global parameterization of the mesh M, handling connection constraints provided by the quadrilateral layout $\mathbb{Q}$.

4.2.2.2 Nodes embedding optimization

Depending on geometry and position of $\mathbb{Q}$'s nodes, a better parameterization can be found using node relocation. Depending on the nature of the quadrilateral layout, fixed nodes rise to large distortions or even local non-injectivities. Mathematically speaking we are going to optimize Equation (4.14). The nodes are re-positionned based on the gradient of the parameterization's objective functional with respect to their positions. This is done iteratively until a global embedding quality is reached. Selective optimization of nodes can be also performed with given user specifications. We follow the method developed by [Campen and Kobbelt 2014] and exploited by [Campen, Bommes, and Kobbelt 2015; Al-Akhras 2016] to perform such optimization. These researchers use a geodesic polar map of the node's 1-ring [Welch and Witkin 1994]. Details of the process can be found in the appendix of [Campen and Kobbelt 2014]. Moreover, we give mathematical specific aspects in Appendix C to characterize the needed moving direction of nodes in order to decrease the energy given in Equation (4.14).

Figure 4.11 (A) shows an abdominal aorta scanned mesh retrieved from medical imaging. Figure 4.11 (B) illustrate the global parameterization optimization after 1 iteration using an arbitrary valid quadrilateral layout $\mathbb{Q}$. In Figure 4.11 (C), we observe the final global parameterization quality and nodes relocation after 25 iterations. The obtained aligned global parameterization is greatly improved. Thus, feature-aligned quadrilateral meshes are then constructed based on the optimized embedding of parametric values. Due to patch structure of the quadrilateral layout, such quadrilateral meshes can be computed patch by patch according to connectivity constraints.

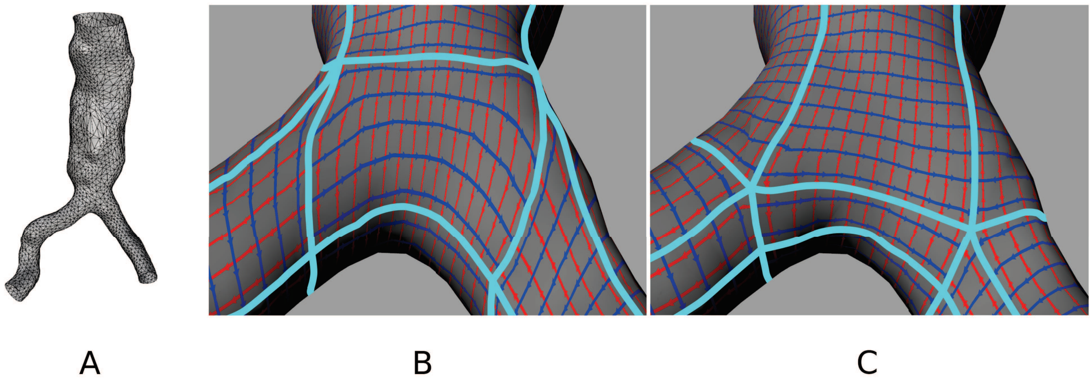

Figure 4.11: Abdominal aorta global parameterization optimization by $\mathbb{Q}$'s nodes relocation. (A) Input triangulated mesh from medical imaging. (B) Global parameterization and quadrilateral layout after 1 iteration. (C) Global parameterization and quadrilateral layout after 25 iterations.

4.2.2.3 Aligned global parameterization workflow summary

To summarize all used tools to compute a suitable global parameterization, the important steps are outlined in Figure 4.12. We start with a feature-aware cuboid decomposition per pant topology in Figure 4.12 (A) (see Chapter 3). We then determine turning numbers of a topologically compatible cross field using $\mathbb{Q}$'s properties. Remember that Table 4.1 gives the relevant needed turning numbers. Then, a geometrical cross field is built interpolating sharp features as depicted in Figure 4.12 (B). Global parameterization computation is achieved with the guiding field. Constraints formulated in Equation (4.15) and also sharp edges constraints are integrated to Equation (4.14) and yield results in Figure 4.12 (D). For instance, in Figure 4.12 (C) no constraints are provided to the parameterization. Thereafter, arcs constraints inherited from the quadrilateral layout are incorporated in Equation (4.15) as shown in Figure 4.12 (E). Arcs of the layout are belong to common isoparametric curves lying on relevant sharp edges. Global quality of the parameterization could be improved if needed, using node embedding optimization. For the sake of simplicity, this example is given without nodes relocation process. Finally, the parametric values u and v attached to each node of the triangulated mesh and the patch structure of the layout yields to a quadrilateral mesh in Figure 4.12 (F).

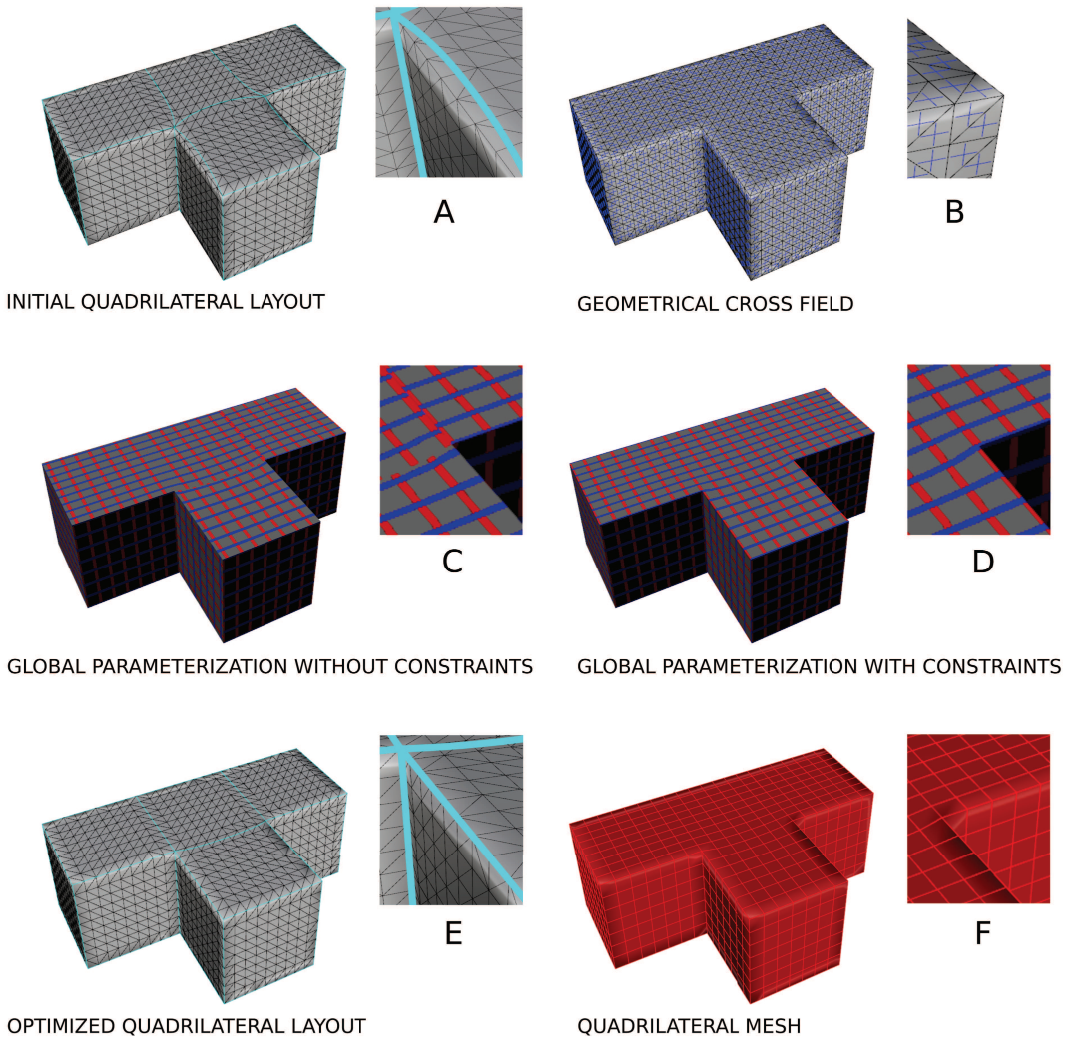

Figure 4.12: Aligned global parameterization worflow summary from geometry-feature-aware pants-to-cuboid decomposition. (A) Initial quadrilateral layout $\mathbb{Q}$. (B) Geometrical cross field. (C) Aligned global parameterization without constraints. (D) Aligned global parameterization with constraints. (E) Optimized quadrilateral layout embedding. (F) Extracted quadrilateral mesh.

4.3 Pure quadrilateral meshes from aligned global parameterization

4.3.1 Quality fundamentals

The issue of generating such 4-sided elements quality into the whole mesh has received a lot of attention recently [Bommes, Lempfer, and Kobbelt 2011; Bommes 2012; Kowalski, Ledoux, and Frey 2013; Campen 2017]. The reason why this problem is widely tackled in the geometry processing field, is that quadrilateral meshes are structured in way that they support texturing and other shape modification. As underlined before, quadrilateral meshing from unstructured geometry is a tedious task that requires to understand the entire shape and its topology. Quality criteria to differenciate them and state needed mesh properties are diverse. The most encountered quality aspects are:

- Element quality.
  The quadrilateral element should be as close to a parametric quadrilateral as possible, i.e., edges with the same length and angles between them.

- Alignement.
  Sharp edges, corners and boundaries must be correctly replicated in order to minimize the distance between triangulated mesh and sampled quadrilateral elements on the parameterized mesh.

- Orientation.
  Into the whole mesh, quadrilateral edges should be oriented to principal curvature directions, this yields to a more natural behavior.

- Global consistency from theorems.
  Achieving global structure is done by sampling singularities properly in areas with a high angle deviation compared to the topological space $\mathbb{R}^2$. Theorems of the topology field state that the singularities need to capture high Gaussian curvature zones to be consistently located.

- Computational mechanics.
  In applications such as FEA, and other computational mechanics purposes, elements close to a square are often preferred. These meshes support high deformations better than triangulated ones and lead to accurate simulations.

4.3.2 Results examples on quadrilateral meshes

This section presents some of non-exhaustive quadrilateral meshes results involving our global parameterization workflow and previously described quality criteria. We illustrate 3 major examples to give an overview of the meshing possibilities. Figure

4.13 (A) shows a feature-aware cuboid decomposition of a topological pant and its associated quadrilateral mesh. Figure 4.13 (B) is a symmetric wheel with a more complicated shape, and we notice that the high valence nodes of the quadrilateral layout $\mathbb{Q}$ are mainly located in curved areas. To sweep all kind of possible shapes, we give a particular exemple on a biological shape, e.g. a female body in Figure 4.14. In this application, the quadrilateral layout's nodes are re-positionned to achieve a global quadrilateral elements quality. Other optimized meshes satisfying items explained in Section 4.3 are depicted in Figure 4.15.

4.4 Conclusion

Aligned global parameterization adapts the parameterization, i.e., the (u, v) couple to the geometry because of its gradient alignement with the geometrical cross field. Indeed, the parameters u and v attached to the nodes of the triangulated mesh are computed taking into account a guiding geometrical cross field. This field serves as geometry reference and interpolates boundary behavior, sharp features and principal curvature directions. With this understanding, we strive to compute the so-desired parameterization based on the geometrical field. Thus, the task of adressing a good parameterization reduces to the computation of a good cross field.

First we determined a topologically compatible cross field whose turning numbers properties were derived from the quadrilateral layout $\mathbb{Q}$. The topological cross field is singular only at the positions of irregular vertices of the layout. Afterwards, we calculated a field interpolating features of the mesh. Interpolation was realized thanks to the symmetry of the cross field. Topological and geometrical constraints are designed only by solving two sparse linear systems.

The parameterization was locally oriented to the guiding geometrical field as much as possible. Thus, the gradients ∇u and ∇v of the piecewise linear scalar fields u and v should follow the cross field first and second directions $\mathcal{U}_c$ and $\mathcal{V}_c$. In addition, we optimize the parameterization using nodes relocation process based on the gradient of the parameterization objective functional. This is done so as to obtain a local optimum of global embedding quadrilateral mesh quality.

Presented quadrilateral mesh examples states the reliability of the followed method. Such quadrilatral meshes fully satisfy needed quality criteria explicited in Section 4.3. Extraction of structured grid of points is now straightforward in order to fit B-Spline surfaces. Reduced order modeling and statistical shape analysis are based on such structured geometries in the next Chapter 5.

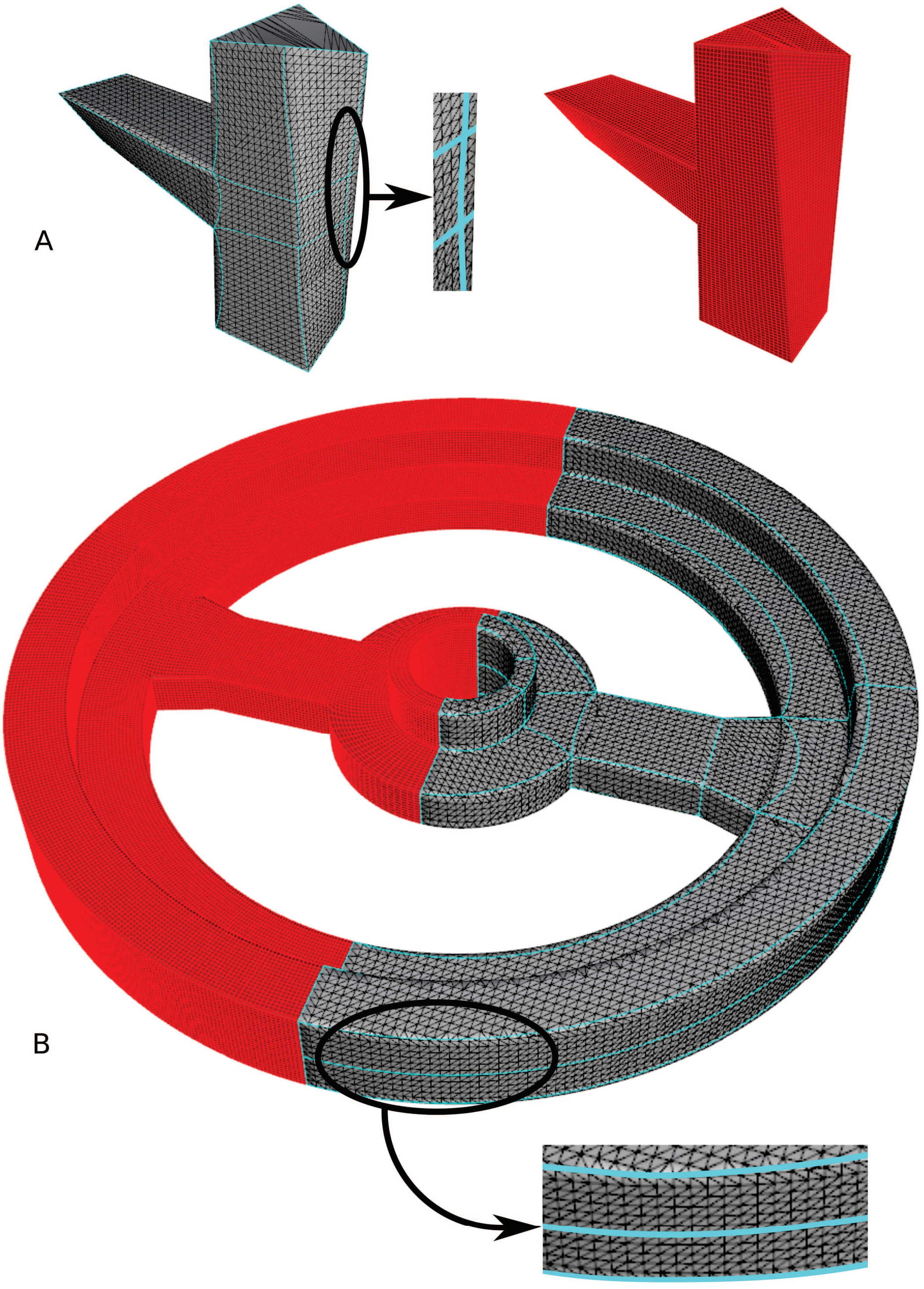

Figure 4.13: Mechanical quadrilateral mesh examples. (A) A pant part quadrilateral mesh with its feature-aware cuboid decomposition. (B) Symmetric wheel part quadrilateral mesh obtained by locating high valence nodes on curved areas.

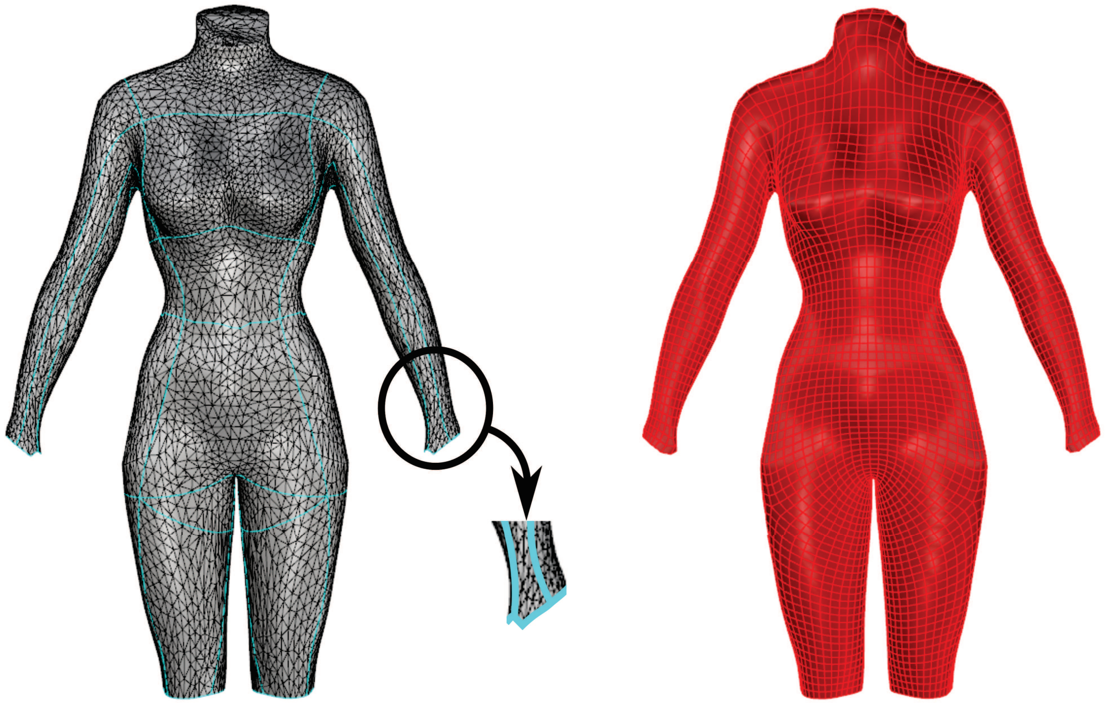

Figure 4.14: Biological quadrilateral mesh example on a female body.

Figure 4.15: Optimized quadrilateral meshes computed from an aligned global parameterization and a geometry-feature-aware pants-to-cuboid decomposition.

Chapter 5

Quadrilateral meshes for statistical shape analysis and geometrical reduced order modeling

This chapter presents reduced order modeling and statistical shape analysis applications using quadrilateral meshes. These reduced order models hold only geometrical parameters for most of them. Some of used meshes are coming from a global parameterization previously introduced in Chapter 4.

Contents

5.1 Isotopological homologous quadrilateral meshes

This section introduces mesh properties and geometrical notions recommended to compare meshes with different geometries. Some of following mesh characteristics are well-suitable for reduced order modeling calculations due to a certain data structuration.

5.1.1 Isotopological and homologous concept definitions

Isotopological properties of a set of meshes and the homologous concept are tackled here. The problematic exposed in Chapter 1 for quadrilateral meshes will be detailed for specific needs of this chapter. Given a set of input triangulated meshes, we strive to find 3D surface quadrilateral meshes which respect the four following properties:

- Pure quadrilaterals with low distortion.
  With the definition of a quadrilateral layout replicating perfectly the topology of the input triangulated surface mesh, it is possible to define a pure quadrilateral mesh. Low distortion is achieved by minimizing the alignement of the global parameterization with the guiding field.

- Feature aligned.
  Sharp edges, vertices and principal curvature directions are important features of meshes. Alignement to these features is required on all instances to fully conserve significant features. Thus the input quadrilateral layout must contain all the sharp edges and vertices to ensure right feature alignement into all input meshes.

- Isotopological with homologous points into other geometric instances.
  A sufficient condition to have isotopological meshes is to hold the same connectivity. But it is not a sufficient condition to compare meshes because of orientation. That is why we want each point of the computed mesh to have a homologous point into all other geometric instances of the considered set. It is achieved globally by patch connectivity, locally by classifying sharp features and by applying patch parameterization.

- Non-uniform isotropy.
  Mesh non-uniform isotropy provides the freedom between isotopological meshes from different geometrical instances. Non-uniform isotropy is intrinsically set because of patch connectivity and discretization.

We then follow the Strategy 1.1 to compute the required meshes. The same concepts are adapted to volumetric meshes in Section 6.3.

5.1.2 Population constraints

To respect above definitions on 3D isotopological homologous quadrilateral meshes, we first set the discretization sampling. This is done by choosing one ideal member of the population. We call him the α-*member*. This member is ideally chosen as the most representative member of the population, e.g. the representative patient for heart geometries. For instance, Principal Component Analysis is a serious way to evaluate this geometry from biological scanned ones. For mechanical applications with geometrical parameters, the α-*member* is given as the barycenter of all designing parameters. The quadrilateral discretization is then based on this particular geometry. Taking into consideration features and geometry of the representative mesh, we set for all members of the studied population the isotopological property and homologous constraints.

The homologous concept is illustrated in Figure 5.1 taking a specific quadrilateral layout in Figure 5.1 (A) constructed to capture some of the geometrically relevant mesh features aspects. Isotopological meshes are not necessarily suitable for a point per point comparison. Figure 5.1 (B) shows a linear interpolation between two isotopological meshes. If meshes hold the same connectivity, the interpolated quadrilateral structure remains globally consistent as depicted in Figure 5.1 (C). But the suitable result is found with homologous constraints in Figure 5.1 (D). Once correct wishes on mesh properties are fixed, all snapshots can be calculated involving a mapped quadrilateral layout, see Figure 5.2 (A). For instance, we illustrate 10 steps of a heart ventricle contraction cycle in Figure 5.2 (B). It is stressed that for statistical shape analysis and reduced order modeling applications given in Section 5.2, meshes must not differ by a rigid body transformation.

5.2 Applications on quadrilateral meshes

This section presents applications for the statistical shape analysis procedure using biological scanned meshes, but also virtual charts of 3D quadrilateral meshes. Firstly, we introduce the statistical method consisting in finding major trends of shape variation. Secondly, we will focus on mechanical parts. To finish, a draft project lead by the ANSYS research team using reduced order model techniques is presented. Reduced order models are built with an ANSYS proprietary software, the ROM builder.

5.2.1 Biological main features extraction

Statistical shape analysis is an investigation of the geometrical attributes of some set of shapes by statistical methods. Medical surgery is one of the application field. In fact, this tool is useful to determine normal and pathological aortas or blood vessels just by analyzing shapes differences. A related work has been done on the human femur to retrieve a given patient shape using PCA and morphing methods

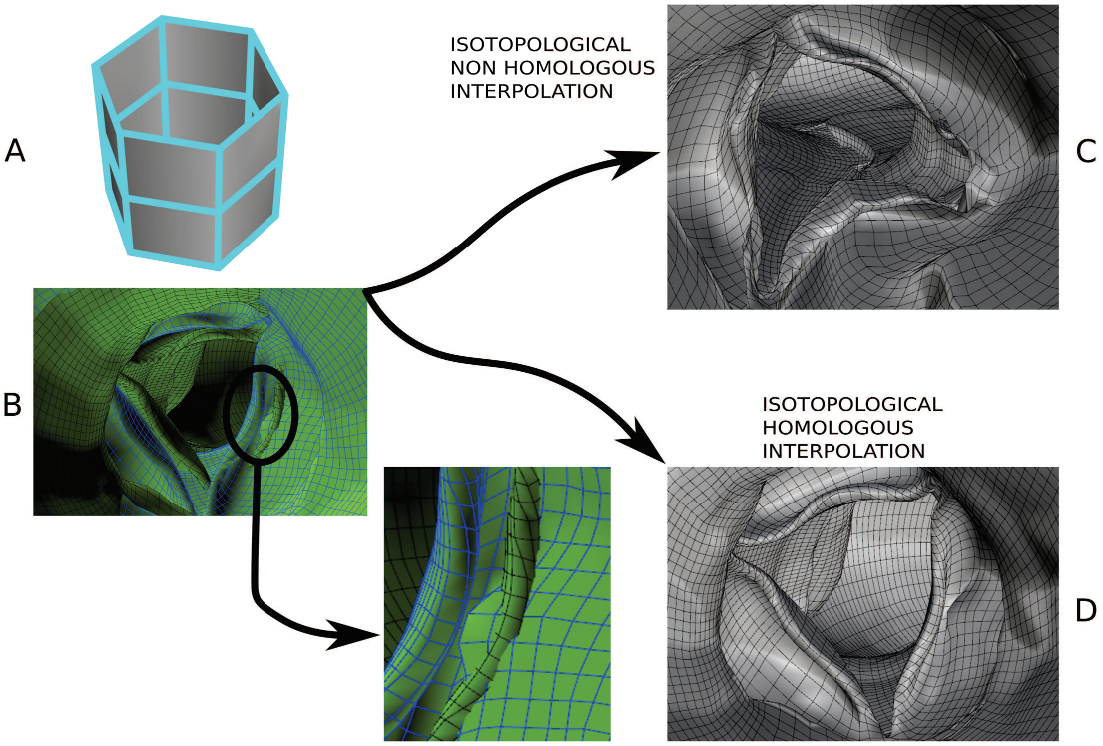

Figure 5.1: Isotopological homologous concept between heart ventricle meshes. (A) Quadrilateral layout used to obtain the quadrilateral mesh. (B) 2 heart ventricle meshes with different geometries (depicted in blue and black wireframe) and their details. (C) Isotopological non homologous linear mesh interpolation result. (D) Isotopological homologous linear mesh interpolation yielding consistent results: a real ventricle geometry.

[Hraiech 2010]. Estimating mean shapes that best represent the studied population is one of the abilities of shape analysis. For instance, in bones, shape and density distribution can vary a lot between individuals due to the human variability [Grassi et al. 2014]. One of the main used methods to tackle these issues is PCA. In addition, this approach allows to generate virtual meshes, virtual patients that respect the main distribution of the shape variation. Recently, [Alliez, Pion, and Gupta 2016] built a CGAL package to compute this particular analysis. Such techniques require morphing for all members of a given set, i.e., a possibly random set of meshes of a given population. Global surface parameterization and tools earlier presented can be really useful to represent all geometrical data in an isotopological manner.

To illustrate above discussed methods, we first focus our attention on abdominal aortas. AAA (Abdominal Aortic Aneurysm) is a pathology that affects abdominal aortas. It is a localized enlargement such that the diameter is greater than $3cm$ or more than 50% larger than normal diameter. Involving our worlflow to build isotopological homologous meshes from a scanned set of geometries obtained by

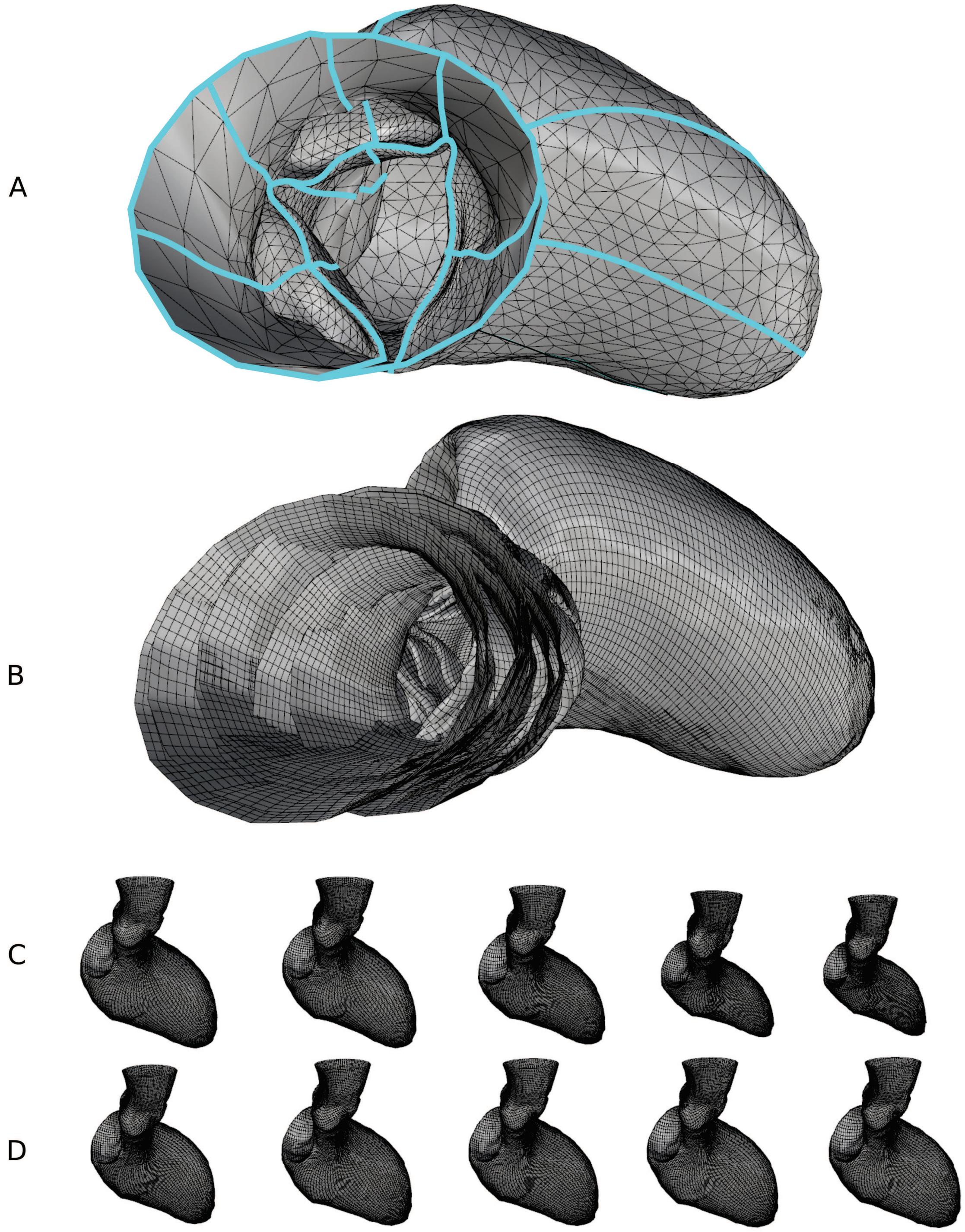

Figure 5.2: Heart ventricle snapshots computation respecting sharp features. (A) Optimized quadrilateral layout $\mathbb{Q}$ embedded in the triangular surface. (B) 10 produced isotopological homologous snapshots using adapted layouts $\mathbb{Q}$ for each shape. (C) Snapshots 1 to 5 (left to right, phase 0% to 40%). (D) Snapshots 6 to 10 (left to right, phase 50% to 90%). See Figure 5.6 for more details.

tomograhic processes, we plot some results in Figure 5.3. As previously introduced in Section 1.3, statistical shape analysis is working only on geometry. The goal is to find a new relevant subspace $\mathbb{B}$ that best describes the distribution of the input data. The computed subspace $\mathbb{B}$ contains less coordinates than the classic $\mathbb{R}^{3n}$ space. Indeed, each shape, i.e., each isotopological mesh is vector in $\mathbb{R}^{3n}$. n being the number of nodes of the discretized geometry. Needed subspace is computed with a PCA approach using SVD tools.

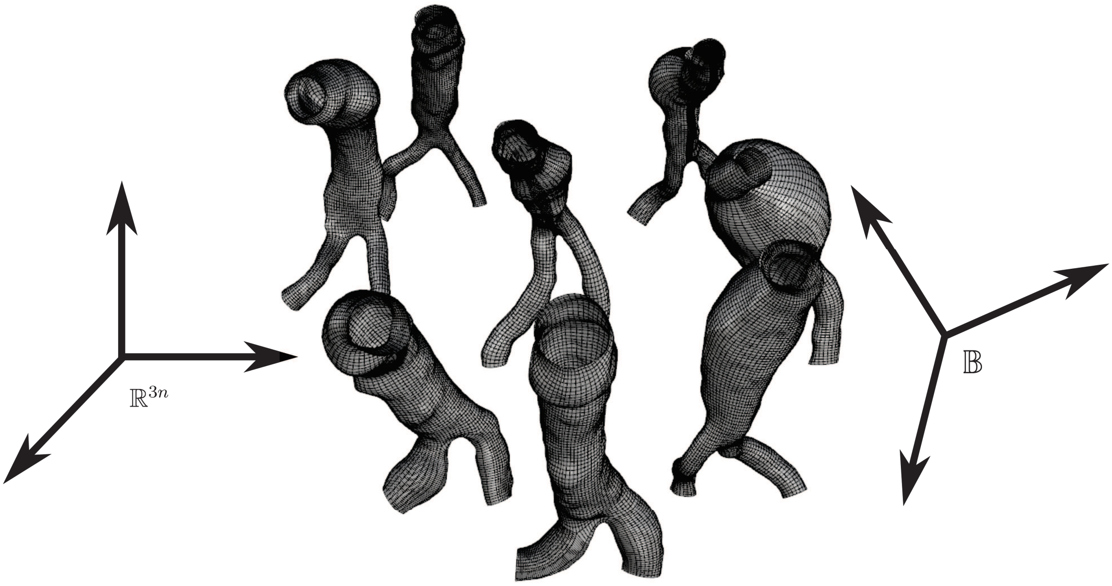

Figure 5.3: Abdominal aortas population suffering of an abdominal aortic aneurysm. Each geometry is a vector in $\mathbb{R}^{3n}$. $\mathbb{B}$ is the reduced basis with a better coordinate system which best reflects the shape variation. $\mathbb{B}$ has fewer coordinates than $\mathbb{R}^{3n}$.

Secondly, we give illustrations for the spatial basis of the singular value decomposition. In fact, modes capture the principal variations of the population and they are the new axis of the reduced basis $\mathbb{B}$. This is the idea showed in Figure 5.4 with a heart ventricle into a basis composed by the 3 first modes. Representing a snapshot in the reduced basis is done by linear combination between modes and coefficients. α_i are the coefficients relative to a given mode for a specific snapshot. They are obtained from singular values σ_i and right singular vectors $\phi_i(j)$ for a considered snapshot j. We refer the readers to Section 1.3 for mathematical details. We have used the quadrilateral layout $\mathbb{Q}$ from Figure 5.2 (A) to compute a snapshot at a given contraction time. We demonstrate that, taking only the first 3 modes and a learning of 10 snapshots (see Figure 5.2 (B)) during a cardiac cycle, the geometry approximation remains nonetheless consistent and reliable. Gray and red meshes illustrate the error comparison in Figure 5.4. We remark that the first mode represent a scaling whereas others are holding local effects and variations.

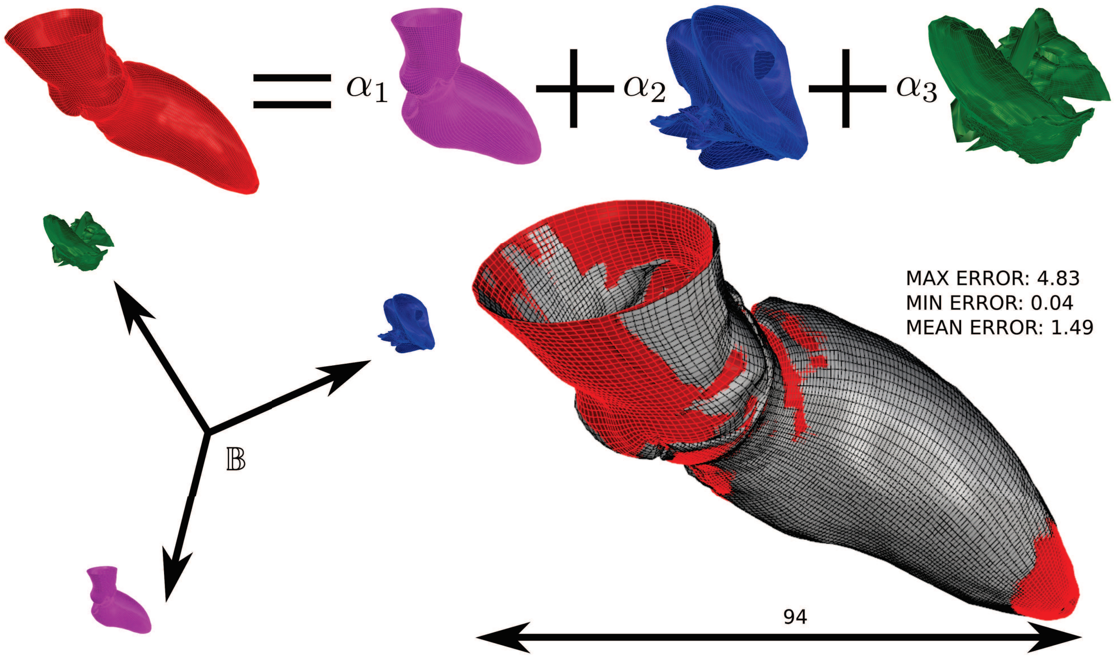

Figure 5.4: Principal component analysis on a heart ventricle during a cardiac cycle. A given snapshot is a linear combination of modes with associated coefficients α_i. In the new reduced basis $\mathbb{B}$, modes are its axis. 3 modes suffice to represent with a certain reliability the shape of a given snapshot. First mode is homogeneous to a shape, others are holding local effects.

5.2.2 Virtual quadrilateral meshes models

5.2.2.1 Snapshots sampling

Sampling of parameters have been done using a sparse grid technique, see [Bungartz and Griebel 2004; Lu 2017; Lu, Blal, and Gravouil 2018]. Adopting this method in a low level manner, i.e., by populating only axis of parameters, we are then able to fill large parameter spaces [Chinesta, Ammar, and Cueto 2010]. Many models encountered in science and engineering are defined in multidimensional spaces, as the ones involved in chemistry, mechanics or financial mathematics [Chinesta, Ladeveze, and Cueto 2011]. Indeed, sparse grids are especially more suitable for high-dimensional problems. In this development, a sparse grid method is used for sampling snapshots among a large parameter space and it will be an efficient solution for a fast a posteriori learning strategy. Sparse grids representations are shown in Figure 5.5. First refinement of the level 1 sparse grid is then adopted in the following, only for some specified mechanical examples.

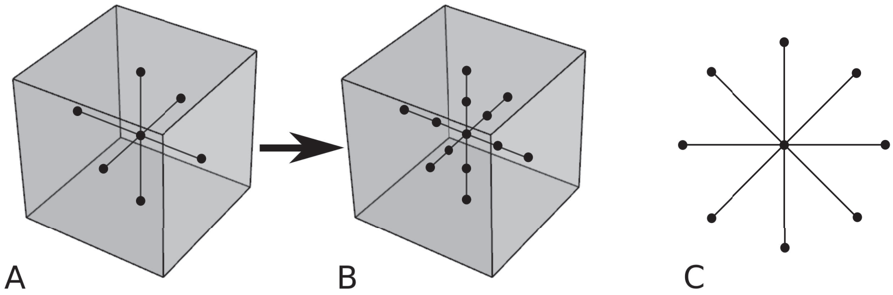

Figure 5.5: Snapshots sampling with a sparse grid technique. (A) Level 1 sparse grid of a 3-dimensional parameter space. (B) First refinement of the level 1 sparse grid. (C) 2D representation of a level 1 sparse grid of a 4-dimensional parameter space.

5.2.2.2 Heart ventricle

Heart ventricle geometrical reduction is dedicated to a specific biological application. Scanned data from medical imaging related to one patient is provided during one cardiac cycle uniformly sampled by 10 meshes. These scanned meshes are called phases. They start from 0 to 90 as depicted in Figure 5.6. The volumetric capacity during a cardiac cycle admit a large variation because of its well-known function.

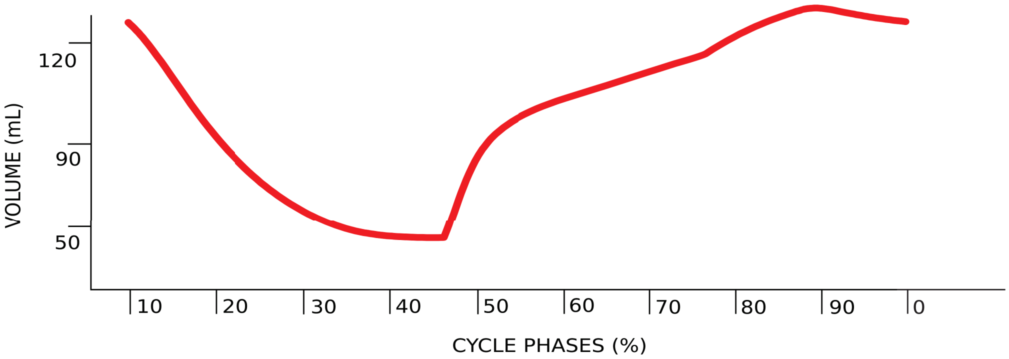

Figure 5.6: Heart ventricle volumetric capacity during a cycle.

Using a specific pipeline well-suited for these particular meshes, a quadrilateral layout is computed by modifying the scanned mesh topology from disk to cylinder. We add a little hole at the bottom of the ventricule (see Figure 5.2 (A) in Section 5.1) for that purpose. Afterwards, an optimized aligned global parameterization is extracted using leaflet, (i.e., the leaflet of the aortic valve) principal curvature direction interpolation for the geometrical cross field. Mapping of the layout to obtain snapshots is shown in Figure 5.7. A reduced order model is built using the phase parameter and previously computed isotopological homologous population of meshes. For instance, two geometries have been evaluated at phase 38.7% (systole, i.e., contraction phase) and 81% (diastole, i.e., expansion phase) in Figure 5.8 (A) and Figure 5.8 (B) respectively. This is done in real-time, less than 1 second is required to evaluate data with the depicted discretization.

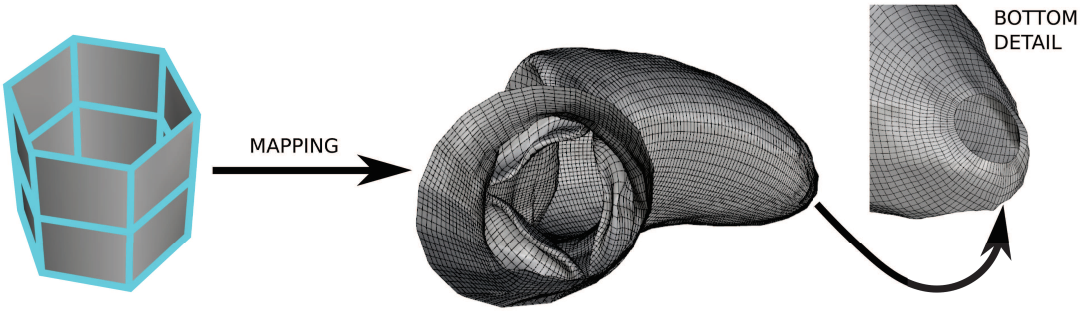

Figure 5.7: Quadrilateral mesh parameterization of the heart ventricle. We apply the same parameterization among all members of the population to obtain isotopological comparable quadrilateral meshes.

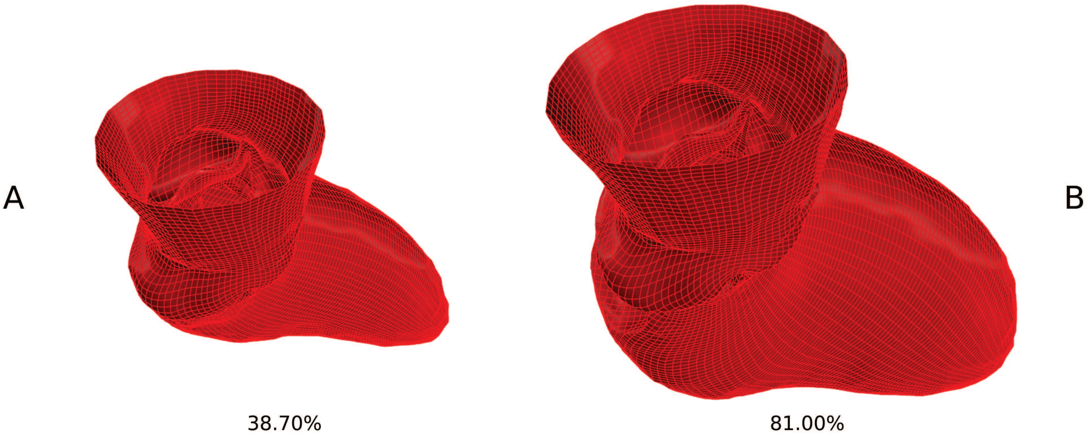

Figure 5.8: Heart ventricle reduced order model real-time geometry evaluation. (A) Evaluation at phase 38.70%. (B) Evaluation at phase 81.00%. Truncated basis is constructed with the first 3 modes.

For a given patient, we have built a virtual geometrical chart of its cardiac cycle. With only 10 tomographic snapshots, we are able to reconstruct with fidelity any geometry at a given intermediate phase. Reliability is mainly achieved thanks to the homologous concept and with the understanding of features. Structured meshes are also an important key. These results can be further exploited for isotopological hexahedral mesh generation in order to run Fluid Structure Interactions simulations to design aortic valves devices. This problem is currently tackled by the ANSYS research team.

5.2.2.3 Pant part

We introduce the pant part for a rapid understanding of our global approach explained in previous chapters. This pant part has a very simple topology: $\chi = 1$ because of its genus-0 and $b = 3$ properties. Thus pants decomposition is useless. For introductory purposes, we define the number and the range of geometrical parameters for an arbitrary study.

The input meshes come from a standard CAD software. Each input triangulated mesh has an attached set of 9 geometrical parameters based on the zero reference of 3 distinct local coordinate frames as illustrated in Figure 5.9 (A). Then a feature-aware cuboid decomposition is performed involving a pant mesh as topological input in Figure 5.9 (B) for the whole population. Thereafter, an optimized aligned global parameterization is computed with the quadrilateral layout. Hence, this gives us the desired quadrilateral mesh with required geometrical and connectivity properties. We proceed the workflow on all 37 input geometrical instances in order to generate all isotopological homologous meshes. Indeed, sampling is involving 37 meshes with a first refinement of the level 1 sparse grid. The mapping process is given in Figure 5.10.

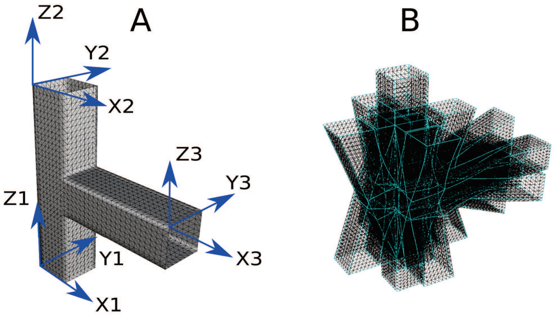

Figure 5.9: Geometrical snapshots generation of the pant part. (A) Zero reference of geometrical parameters in the attached local coordinate frames. (B) Feature-aware cuboid decomposition of all geometrical instances.

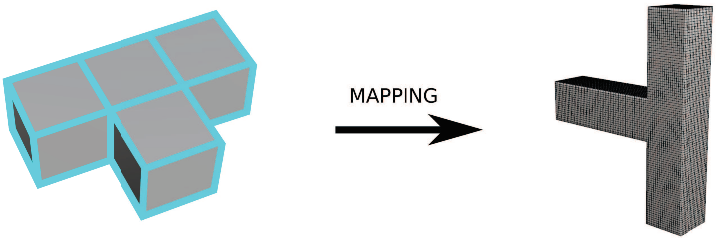

Figure 5.10: Quadrilateral mesh parameterization of the pant part. We apply the same parameterization among all members of the population to obtain isotopological comparable quadrilateral meshes.

Once the reduced order model is built, we can generate in real-time all desired geometries. Demonstration example is exhibited in Figure 5.11. The entire pipeline, i.e., pants-to-cuboid decomposition to quadrilateral mesh generation takes a certain amount of time. The set of needed quadrilateral meshes have been computed in less than a hour. Thus, our approach is still relevant since geometrical evaluations are done in less than 1 second.

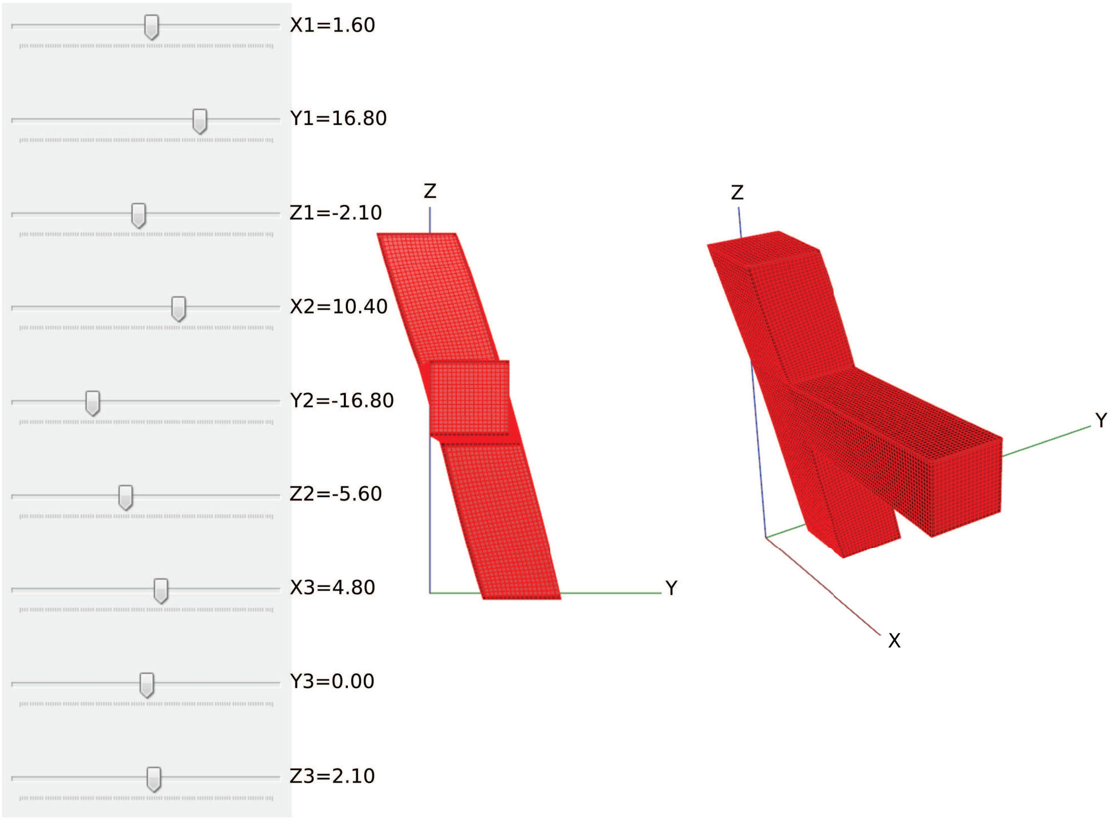

X1=1.60
Y1=16.80
Z1=-2.10
X2=10.40
Y2=-16.80
Z2=-5.60
X3=4.80
Y3=0.00
Z3=2.10

Figure 5.11: Pant part reduced order model real-time geometry evaluation. Truncated basis is constructed with the first 12 modes. Used range of parameters is detailed in Table 5.1.

5.2.2.4 Casting part

This casting part is a classical one that can be found in mechanical systems for coupling shafts together. This part remains more complex than the previous pant part. Genus-5 surface is considered involving many different possibilites of consistent and non-consistent pants decompositions. Starting with a given feature-aware pants decomposition, we apply a specific cuboid configuration and map it into each pant as shown in Figure 5.12 to capture features.

Then, the worflow is very similar to the pant part. The sampling of the 6

Pant part range	Min	Max
X1 boundary 1	-40	40
Y1 boundary 1	-40	40
Z1 boundary 1	-35	35
X2 boundary 2	-40	40
Y2 boundary 2	-40	40
Z2 boundary 2	-35	35
X3 boundary 3	-40	40
Y3 boundary 3	-40	40
Z3 boundary 3	-35	35

Table 5.1: Range of parameters used for the pant part geometrical reduced order model.

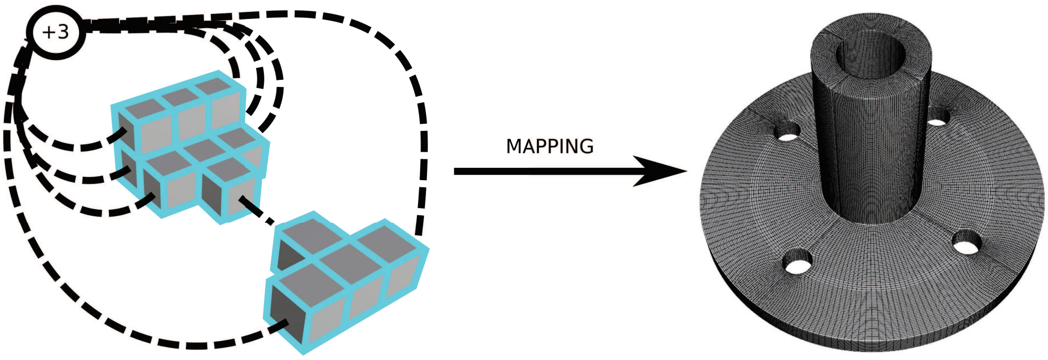

Figure 5.12: Quadrilateral mesh parameterization of the casting part. We apply the same parameterization among all members of the population to obtain isotopological comparable quadrilateral meshes.

input geometrical parameters (see Figure 5.13) was made in a random manner so as to generate 65 triangulated meshes covering as best as possible the $\mathbb{R}^6$ space. Parameters ranges have been defined like an industrial case with large and short variations.

We generate in real-time all desired geometries handling the same process already explicited. Due to the mesh size, evaluation of an arbitrary geometry takes around 3 seconds to be computed. Moreover, during the isotopological meshing process to produce snapshots, user intervention was mandatory to segment with suitable pants geometries. A total time of 4 hours was necessary to build this geometrical virtual chart. This time has to be compared with nowadays industrial techniques which requires days or weeks to obtain such quality meshes suitable for reduced order modeling.

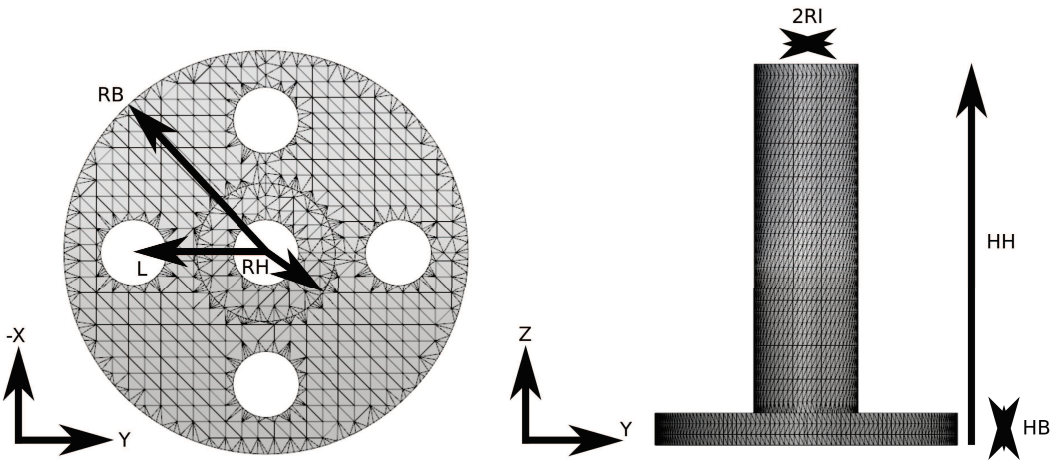

Figure 5.13: Casting part distribution of parameters. 6 geometrical parameters are settled.

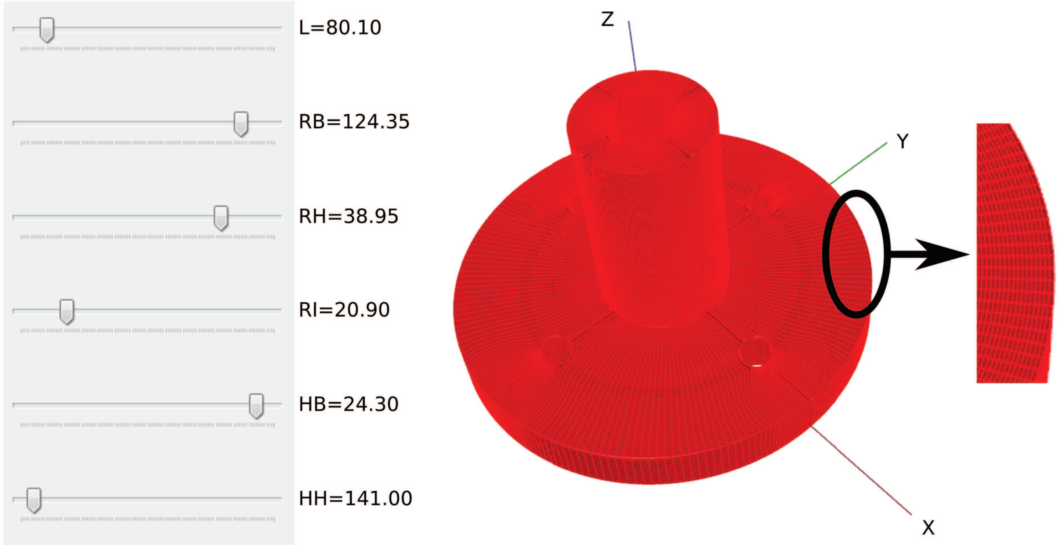
L=80.10
RB=124.35
RH=38.95
RI=20.90
HB=24.30
HH=141.00

Figure 5.14: Casting part reduced order model real-time geometry evaluation. Truncated basis is constructed with the first 15 modes. Used range of parameters is detailed in Table 5.2.

5.2.3 Statistical shape analysis based reduced order biological models

5.2.3.1 Medical devices problematic

Many modern surgery methods use medical devices to treat pathological diseases. A medical device can be seen as an apparatus, material or software used for treatment, prevention or diagnosis. We focus here on devices which are apparatus designed for

Casting part range	Min	Max
Length	80	81
Radius B	120	125
Radius H	35	40
Radius I	20	25
Height B	15	25
Height H	140	160

Table 5.2: Range of parameters used for the casting part geometrical reduced order model.

treatments. In particlar those used for endovascular applications. An endovascular surgery is used to treat a specific pathology by passing into vessels. In general it involves the placement of a medical material, e.g. an expandable stent or web. This kind of surgery is appreciated due to its opposition with open surgery which can have heavy health consequences. However, due to huge human variability, surgeons must have experience and great applied knowledge. They have to look after a given patient whose treatment have to be personalized. In fact, to reduce human decision parameters during the surgical act, a recent trend exists. Using computational physics solutions to guide professionals is nowadays widely possible. Human and machine are both the new surgeon couple of the next decade. Nonetheless, FSI or deformable mechanics have an high computational cost and time is important in such surgical operations. We illustrate this problematic into Figure 5.15 with cerebral aneurysm pathology. Statistical shape analysis and reduced order mdeling methods are well-suited for the medical problematic [Luboz et al. 2018], they have the following advantages:

- Metric of the human variability is quantified. For a new patient, the closest successfully treated patient can be found in the database by projection. Physicians can retrieve information and parameters of the previous operation. This task can decrease significantly the human error.
- Virtual patients can be generated to test other devices or surgical configurations.
- Population variability is computed and devices manufacturers can enlarge their product range until limits of this variability.

5.2.3.2 Web deployment reduced order model demonstrator

We aim to build a reduced order model in order to evaluate in near real-time stent or web deployment in cerebral aneurysms. Our objective is to determine contact

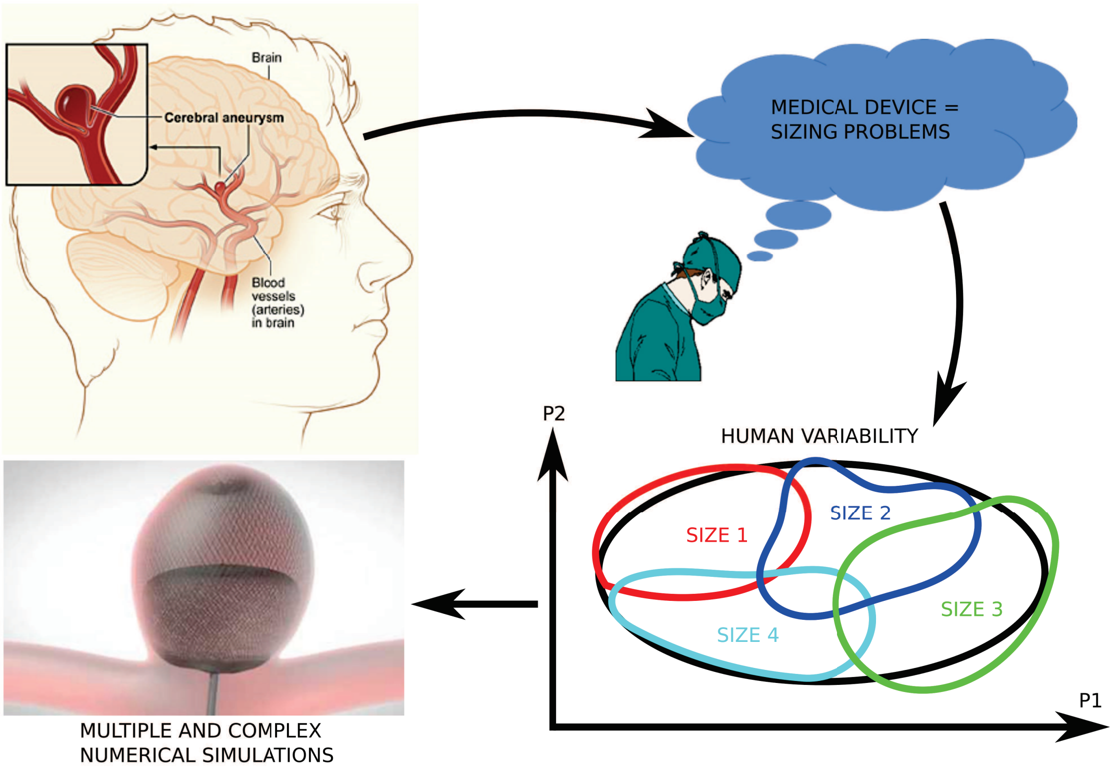

Figure 5.15: Medical devices implantation problematic with cerebral aneurysms. Due to the human variability, surgeons have to pick one of the available devices based on their knowledge and experience. If the human variablity of the considered pathology depends on two parameters $P1$ and $P2$, there is still many possibilities of numerical simulations.

pressure between the aneurysm (considered as an undeformable surface) and the deployed device. Then the pressure contact information is given to surgeons as key data to lead real surgery designing process.

We first decide to build a demonstrator, i.e., with emulated aneurysms geometries in the spirit of the true major geometrical variations of such diseases. For that purpose we use not real geometrical parameters but real surgical ones. One size of device is considered. Indeed, demonstrating with other sizes will be straightforward. Used parameters can be seen in Figure 5.16 taking into account a web size of $9mm \times 5mm$. For the sake of simplicity, the 3 most relevant parameters are variable, others are fixed (see Table 5.3 for details).

Once correct surgical and geometrical parameters have been settled, we build a Design Of Experiment of 50 snapshots. This DOE is then used to construct the reduced order model. Technically speaking, we take 50 differents sets of 3 parameters that best fill the $\mathbb{R}^3$ parameter space. A second DOE of 20 snapshots is independently determined for future ROM validation. We then perform mechanical computations with ANSYS to obtain web deformation and pressure contact results.

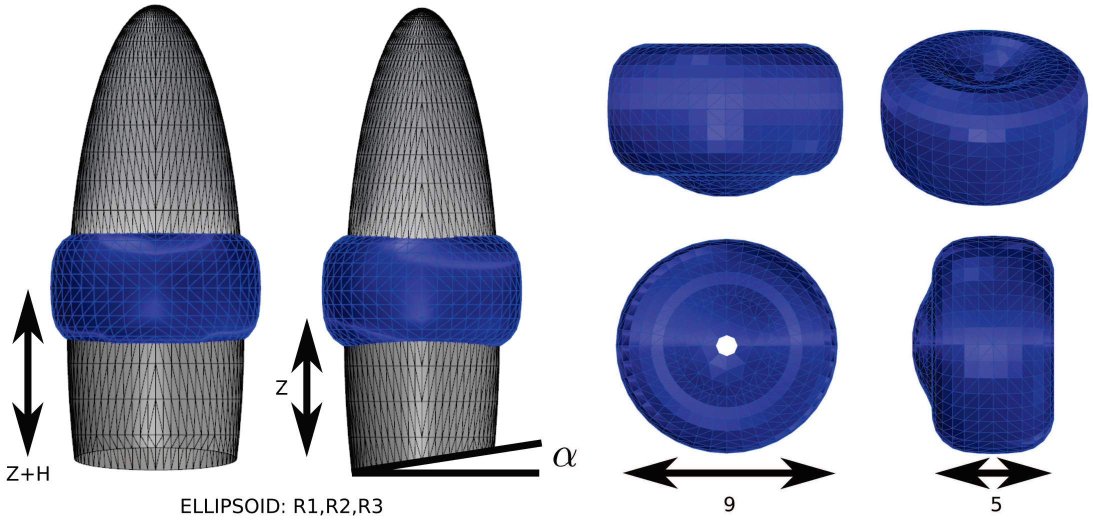

Figure 5.16: Parameters used for the web deployment reduced order model demonstrator. A web size of $9mm \times 5mm$ is considered. Z represent the lower height where the aneurysm is truncated along his height axis. H being the dropping height of the web. Aneurysm emulated geometry is defined by an ellipsoid with radius parameters $R1$, $R2$ and $R3$. $R3$ design the height of the aneurym whereas $R1$ and $R2$ are planar radius in the plane composed by the ellipsoid center and an arbitrary vector colinear to Z. Used range of parameters is detailed in Table 5.3.

Web and aneurysm range	Min	Max	Remark	Type
Radius 1	3.5	4	Variable	Geometrical
Radius 2	3.5	4	Variable	Geometrical
Radius 3	14	14	Constant	Geometrical
Dropping height H	0	2.8	Variable	Surgical
Height Z	5.6	5.6	Constant	Geometrical and surgical
Angle α	0.15	0.15	Constant	Geometrical and surgical

Table 5.3: Range of parameters used for the web deployment reduced order model demonstrator.

Reduced order model is built with the first 16 modes and gives relevant results. We compare the validation DOE with the reduced order model and find a contact pressure mean error of 1.25% over the 20 snapshots. The max error 2.15% is found for the couple presented in Figure 5.17. We analyze these two specific computations. Figure 5.17 (A) shows the evaluation result of $R1 = 3.5625$, $R2 = 3.6375$ and $H = 2.31$. Figure 5.17 (B) is the snapshot of the second DOE involving the same parameters. Error is given in Figure 5.17 (E) according to the scale in Figure 5.17 (F).

We have presented a concrete ROM example with applications in the medical

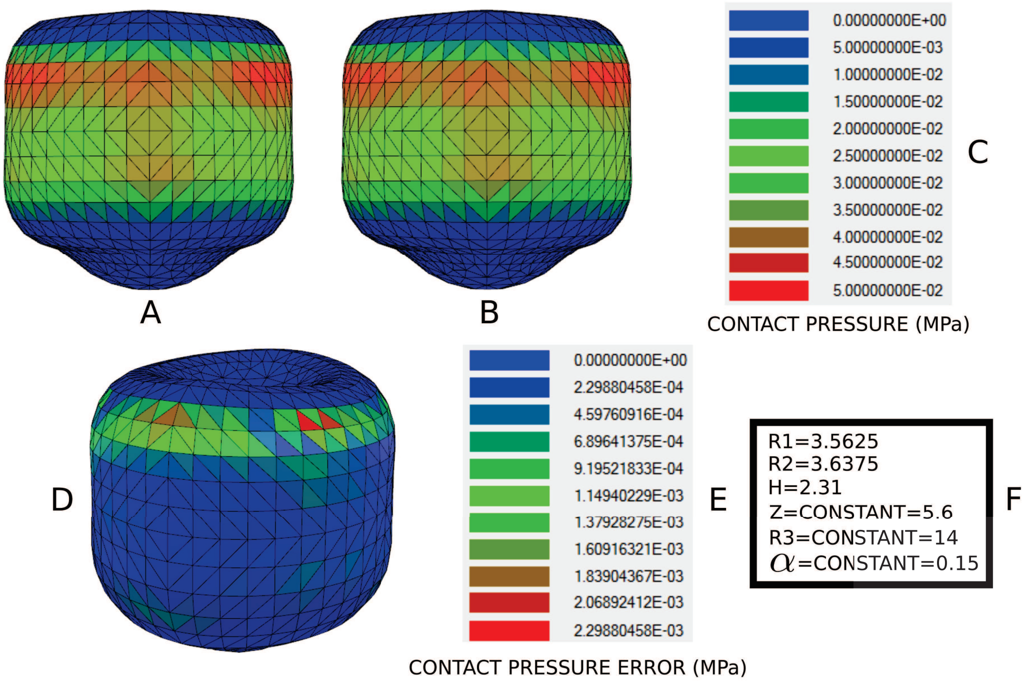

Figure 5.17: Web deployment reduced order model demonstrator validation. (A) Reduced order model evaluation constructed with a DOE of 50 snapshots, using parameters in (F). (B) Snapshot with parameters in (F) of the second DOE composed by 20 snapshots. (C) Pressure contact color scale for (A) and (B). (D) Pressure contact error between (A) and (B) using color scale (E).

field. Although aneurysm geometries are not real ones, surgical parameters and mechanical computations previously performed are. Moreover, followed simulations are consistent due to the experience feedback of surgeons with whom we talked. Mechanical properties of implied devices were given by manufacturers. Efficiency of the approach is demonstrated by the near real-time results. Around a second is necessary to evaluate the pressure contact, instead of 2 until 5 minutes for a standard snapshot calculation time. Due to the potential dangerous pathological patient situation, 2 minutes are too much to evaluate such contact pressure. In fact, medical professionals have to test several web deployments to find the best size deployed in the suitable configuration. That's why reduced order modeling is really adapted to the problematic. Observed errors are very acceptable according to the truncated basis size and number of computed snapshots in the $\mathbb{R}^3$ parameter space.

5.2.3.3 Towards biological cerebral aneurysm web contact pressure reduced order model

Aiming to build a real web deployment solution, we focus here on real aneursym geometries. Like we said before, we have to reduce the human variability parameters of pathological cerebral aneurysms in order to correctly adapt a future endovascular treatment. To do this, we develop a specific method suitable to deal with highly different meshes. By different, we mean geometrically and topologically different as depicted in Figure 5.18 (A). For example, number of boundaries and genus can be really different while treating the same pathology. Surface meshes which do not have the same Euler characteristic χ can not have the same connectivity. In fact, an isotopological population of meshes can not be found for the statistical shape analysis process. In addition, scanned meshes contain problems such as non-manifold zones and possibly redondant faces and vertices. Physicians are not trained to fix the mesh properties. It becomes not feasible to analyze and patch combinatorial geometries in near real-time during a surgery process.

To overcome this major issue, previous tools such as segmentation, global parameterization are not suitable. We decide to exploit a hand made topologically controlled method. We call it the GSM (Geometrical Strain Method) as explained in Figure 5.18 (B). A representative topology with a constant Gaussian curvature is used, i.e., a geometrical sphere to control the morphing topology. We drop the sphere at a relevant point into the aneurysm. Then, the spherical object is inflated step by step until geometrical contact is found or strain criterion is reached for all elements. Taking into account contact points, at each iteration i of the sphere radius R_i, an edge l_j is set to be converged if Equation (5.1) is satisfied. The morphed isotopological geometry is computed in few seconds. Different strain criteria can be adapted to suit the population variation or the disease intensity in order to determine the required isotopological population in Figure 5.18 (C).

$$\forall R_i,\ \varepsilon_j(R_i) \geq \frac{\Delta l_j(R_i)}{l_j(R_i)}. \tag{5.1}$$

A complete user-friendly software distributed in hospitals, available for surgeons and medical professionals remains a tedious task to execute. We give main steps of a complete surgical process, including an offline learning approach and a real-time treatment in Figure 5.19. Figure 5.19 (A) refers to the statistical shape analysis offline process done before the first patient's arrival in Figure 5.19 (B). Once accurate isotopological morphing of the studied population is computed and statistical methods are performed, we are ready to retrieve shape coefficients of the new patient. This is done by projecting the new shape into the statistical reduced basis. This basis is formed by the most energetic modes. Remark that, modes are composed by rigid body aspects due to the disease location into the brain. We follow the same mechanical computations as done before for the web deployment of the demonstrator presented above. The reduced order model based on the displacement field can be realized with real isotopological aneurysms shapes. Same task is done involving pressure contact field. Surgeons will give the remaining parameters, such as dropping height and web or stent size, in order to evaluate in near real-time the contact pressure solution mapped on the deformed geometry in Figure 5.19 (C).

5.3 Conclusion

We have shown many reduced order models constructed with 3D surface quadrilateral meshes. Most of determined isotopological structured meshes have been computed with the generalized process presented in previous chapters. Others have been determined especially for nowadays real problematics in the medical field.

Thanks to the mesh properties introduced in this chapter, we are able to perform various surface meshing of a given population with a certain accuracy. Accuracy means meshes that respect sharp features, principal curvature directions and boundary constraints for the whole studied population. The homologous concept was introduced to answer to this problematic not captured by topological properties of meshes.

The results we shown on reduced order models validate our approach for modeling with geometrical parameters. Indeed, including geometrical parameters in such studies is not straightforward. The isotopological process allows to map surface geometries with fidelity in order to perform a relevant comparison. For biological applications, the holomogous concept is even more important. In fact, point per point consistent analogy between different geometries is useful and accurate, e.g. for statistical shape or principal component analysis. For all these reasons, evaluations are trustworthy for a reasonable amount of snapshots depending on the parameter space dimension.

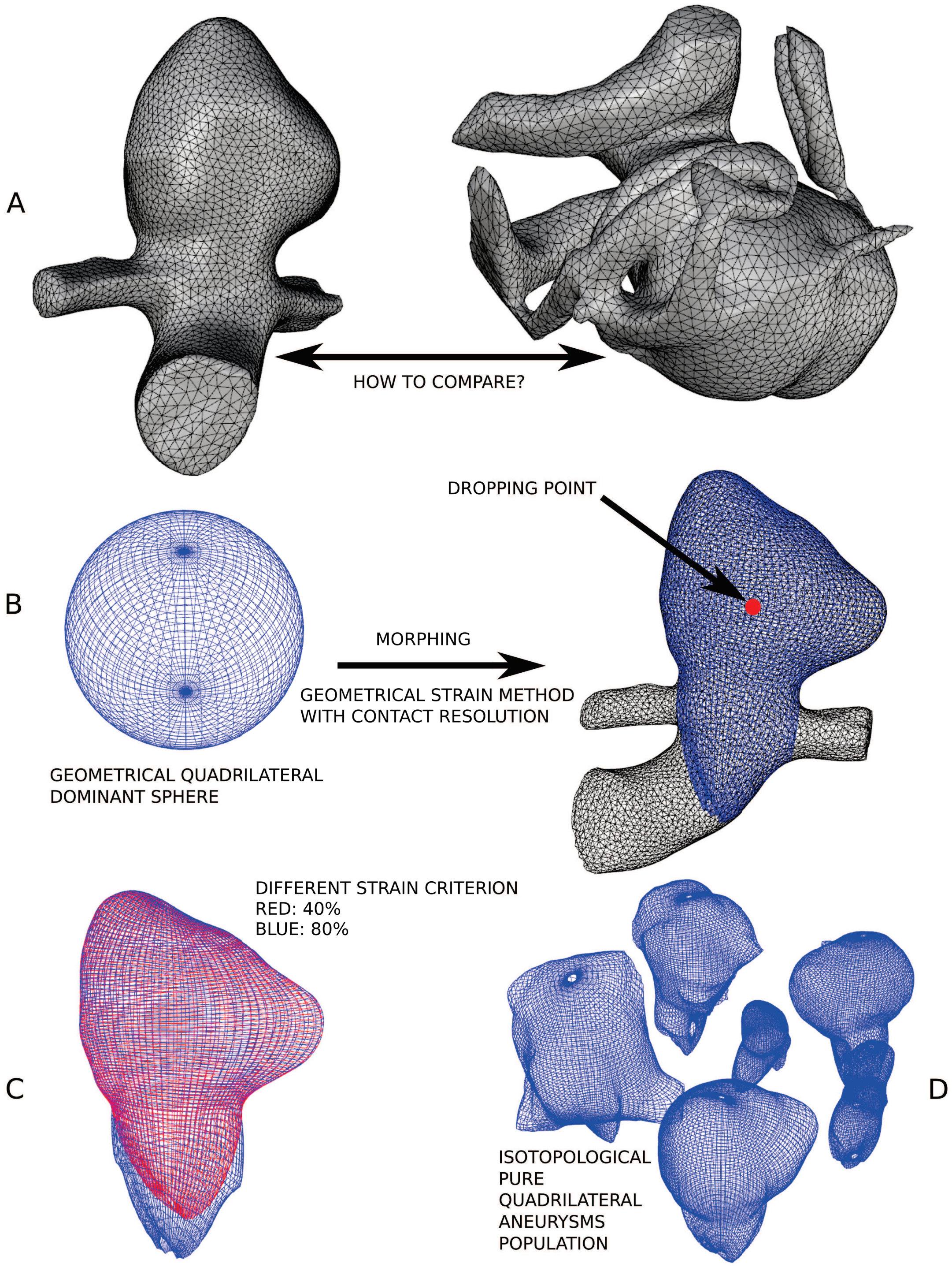

Figure 5.18: Aneurysm mesh properties problematic solved by the GSM (Geometrical Strain Method) method. (A) Comparison problematic between 2 topologically different aneurysms. (B) GSM method used to determine isotopological meshes of aneurysms. (C) Different strain criteria which can be used for computing an isotopological pure quadrilateral mesh population of aneurysms.

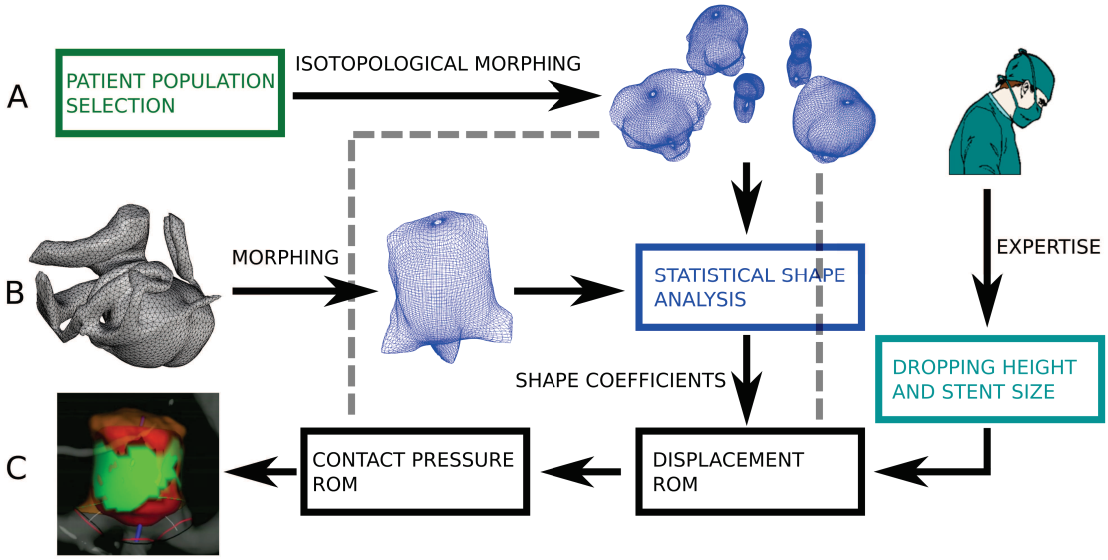

Figure 5.19: Aneurysm treatment approach by learning methods. (A) Offline reduction of the human variability. (B) Arrival of a new patient. (C) Near real-time web pressure contact result on a sick aneurysm geometry. Some of illustrations are coming from the IDsize® software module developed by Sim&Cure.

Chapter 6

Surface to volumetric manifolds using surface global parameterization for reduced order modeling

This chapter aims to build structured volumes from surface global parameterization. In addition, throughout this process, topological properties are analyzed in the way to build valid volumes of interest.

Contents

6.1 Poincaré-Hopf theorem and Euler characteristic for higher dimensional manifolds

In this section we present a generalization of needed topological theorems and properties for higher dimensional manifolds. In fact, converting 2-dimensional manifolds into 3-dimensional ones requires to understand invariant volume information. Such theorems govern fields on surfaces, on volumes and for n-dimensional manifolds. Generalized properties give structural information of surfaces, volumes and n-dimensional manifolds restricted to a given topology. In the following, theoretical background in surface topology is needed as earlier presented in Chapter 2. Moreover, for consistent needs, we use M to refer to a topological space that locally looks like an Euclidean space near each point, i.e., a n-dimensional topological manifold:

Definition 6.1. n-dimensional manifold with boundaries. A n-manifold M is a topological space such that for each point $p \in M$, there exists an open neighborhood U of p in M and a continuous bijective mapping $x : D \longrightarrow U$, where D is either an open set in $\mathbb{R}^n$ or an open set in the half space $\mathbb{R}^n_+$.

6.1.1 Generalized Poincaré-Hopf theorem

We would like to point out that the Poincaré-Hopf theorem can be generalized for higher dimensional manifolds. For instance, we give a formulation of the generalized Poincaré-Hopf theorem for compact oriented differentiable manifolds of higher dimensions. Such generalization will support our further developments and some results will be used to base the reasoning in the next mathematical needs. Work has been done recently to generalize this theorem [Jubin 2009]. In the mathematics field, older important researches exist. Efforts have been spent for decades to find formulation of the Poincaré-Hopf theorem for higher dimensional manifolds [Pugh 1968; Feßler 1995]. We first want to establish summation properties of singularities as given in Proposition 6.1.

Proposition 6.1. Sum of singularity indices. Let $\mathbf{d}$ be a vector field or a n-symmetry direction field with isolated zeros on the compact oriented n-dimensional manifold M. If M has boundaries ∂M, the total index of singularity is defined to be the sum of its indices on the interior and on the boundaries [Jubin 2009]:

$$\sum_{i=1}^{n_s=n_i+n_b} I^i_{\mathbf{d}} = \sum_{i=1}^{n_i} I^i_{\mathbf{d}} + \sum_{i=1}^{n_b} I^i_{\mathbf{d}}. \tag{6.1}$$

n_i represents the number of singularities embedded on surface whereas n_b represents the number of singularities on boundaries. Afterwards, we express the summation of indices involving the dimension of the considered manifolds $\dim(M)$, yielding to the following Proposition 6.2:

Proposition 6.2. Sum of singularity indices and dimension. Let $\mathbf{d}$ be a vector field or a n-symmetry direction field with isolated zeros on the compact oriented n-dimensional manifold M with boundaries ∂M, then [Jubin 2009]:

$$\sum_{i=1}^{n_s=n_i+n_b} I^i_{\textbf{-d}} = (-1)^{\dim(M)} \sum_{i=1}^{n_s=n_i+n_b} I^i_{\mathbf{d}}. \tag{6.2}$$

Note that Equation (6.1) and Equation (6.2) serve us to state the generalized Poincaré-Hopf theorem in Equation (6.3) contained in Theorem 6.1.

Theorem 6.1. Generalized Poincaré-Hopf theorem. Let $\mathbf{d}$ be a vector field or a n-symmetry direction field with n_s isolated zeros on the compact oriented n-dimensional manifold M with boundaries ∂M, then [Jubin 2009]:

$$\sum_{i=1}^{n_s} I^i_{\mathbf{d}} = \begin{cases} \chi(M) & \text{if } \dim(M) = \{2n | n \in \mathbb{N}\}, \\ 0 & \text{if } \dim(M) = \{2n+1 | n \in \mathbb{N}\}. \end{cases} \tag{6.3}$$

Using this generalized form, we wish to securely anchor developments on 3-dimensional manifolds using some of properties of lower dimensional manifolds, i.e., surface manifolds. Antecedent propositions and theorems are then used to achieve next improvements.

6.1.2 Generalized Euler characteristic

In this section we provide well-known results on the generalized Euler characteristic. Generalized Euler characteristic is introduced for the following purposes. Firstable, we define cohomology groups. They are invariant information attached to a specific group as expressed in Definition 6.2.

Definition 6.2. Cohomology groups. The cohomology group $\mathbf{H}^n$ looks at the group action between a group G in an associated $G - module\ M$. Elements of a n-dimensional group G^n representing n-simplices:

$$\mathbf{H}^n = \mathbf{H}(G^n, M). \tag{6.4}$$

Thus, we can characterize the general formulation of Euler characteristic using previous definition of cohomology groups. Characteristic is computed regarding the properties of the associated simplicial complex in cases of meshes, i.e., their n-dimensional counterparts. Simplicial complexes have a certain combinatorial nature and allow numerical computations. We want to define geometrical objects with both continous and combinatorial properties. CW-Complex (also known by Closure-finite Weak-topology) entities k_i have been introduced to answer the needs of homotopy theory in simplicial complexes. In other words, properties that allow continuous deformations for combinatorial structures are needed. Generalized Euler characteristic of a compact n-dimensional manifold M is the alternate sum of the lengths of the cohomology groups $\mathbf{H}^i$ as written in Equation (6.5). This characteristic can be also obtained simply from Betti numbers b_i. Betti numbers are used to differentiate topological spaces, it can be also used for simplicial complexes or CW-complexes.

$$\chi(M) = \sum_{i=0}^{n<\infty} (-1)^i |\mathbf{H}^i| = \sum_{i=0}^{n<\infty} (-1)^i k_i(M) = \sum_{i=0}^{n<\infty} (-1)^i b_i(M). \tag{6.5}$$

Such previous formulations help us to connect the gap between discrete and continuous cases. Indeed, we strive to work with meshes intrinsically having a combinatorial structure, but also with continuous concepts. Needed key topological aspects were elucidated by CW-Complexes. Furthermore, generalized Euler characteristic was given to found invariant properties of n-dimensional manifolds. Technically speaking, invariant information attached to a n-manifold, e.g. a 3-dimensional manifold. These important concepts previously explained will be used in Section 6.3.

6.1.3 Volumetric manifold examples

Into an illustration purpose, exhibition of volumetric manifolds will be given. For a classic visualization and understanding human eyes and brain limits, only volumes in the $\mathbb{R}^3$ topological space are depicted. Thus, a particular interest is accorded to 3-dimensional manifolds in $\mathbb{R}^3$. Volumes embedded in the $\mathbb{R}^3$ or $\mathbb{R}^n$, $n \geq 3$ topological spaces are defined in Definition 6.3. For higher-dimensional manifolds, we refer the readers to the previous definition already given in Definition 6.1.

Definition 6.3. **3-dimensional manifold**. A volume V is a 3-manifold, i.e., a topological space in which each point has a neighborhood homeomorphic to either the sphere $\mathbf{S}^3$ in $\mathbb{R}^3$ or the closed half sphere $\mathbf{S}^3_+$ in $\mathbb{R}^3_+$.

For instance, Euler characteristic of some familiar sets will be imaged to make the developments more visual [Simsek, Ozdaglar, and Acemoglu 2007]. $\mathbf{B^n}$ is the one-boundary n-dimensional manifold and $\mathbf{S^n}$ the sphere n-dimensional manifold. Examples are shown in Equation (6.6).

$$\begin{cases} \mathbf{B^n} & \Rightarrow \chi(\mathbf{B^n}) = 1, \\ \mathbf{S^n} & \Rightarrow \chi(\mathbf{S^n}) = 2 \text{ if } n = \{2n | n \in \mathbb{N}\}, \\ \mathbf{S^n} & \Rightarrow \chi(\mathbf{S^n}) = 0 \text{ if } n = \{2n+1 | n \in \mathbb{N}\}. \end{cases} \tag{6.6}$$

Examples are given considering a 3-dimensional manifold V in Equation (6.7). Geometrical view of a cylinder $\mathbf{C^3}$ and an associated volumetric manifold V of a surface torus $\mathbf{T^2}$ are provided in Figure 6.1. We use Betti numbers b_i for continuous manifolds and simplicial complex entities k_i for discrete ones as described in Table 6.1 and Table 6.2. Betti numbers b_i with $i > 2$ are equal to zero for a volume integrated in $\mathbb{R}^3$. Additional comprehension for Betti numbers is given in Figure 6.2.

$$\begin{cases} \text{Betti numbers} & \chi(V) = \sum_{i=0}^{3} (-1)^i b_i(M), \\ \text{CW-Complexes} & \chi(V) = \sum_{i=0}^{3} (-1)^i k_i(M), \\ \text{Figure 6.1 } (A) & \chi(V) = b_0 - b_1 + b_2 - b_3 = 1 - 0 + 1 - 0 = 2, \\ \text{Figure 6.1 } (B) & \chi(V) = k_0 - k_1 + k_2 - k_3 = 32 - 64 + 40 - 8 = 0, \\ \text{Figure 6.1 } (C) & \chi(V) = k_0 - k_1 + k_2 - k_3 = 28 - 70 + 60 - 16 = 2, \\ \text{Figure 6.1 } (D) & \chi(V) = b_0 - b_1 + b_2 - b_3 = 1 - 1 + 0 - 0 = 0. \end{cases} \tag{6.7}$$

Betti number	Description
b_0	Number of connected components (volumes are considered)
b_1	Number of holes or tunnels (1-dimensional independent entity)
b_2	Number of cavities (2-dimensional independent entity)
b_3	Number of 3D holes (3-dimensional independent entity)

Table 6.1: Betti numbers description adapted for 3-dimensional objects.

Simplicial complex entity	Description
k_0	Number of vertices
k_1	Number of edges
k_2	Number of faces
k_3	Number of volumes

Table 6.2: Simplicial complex entities description.

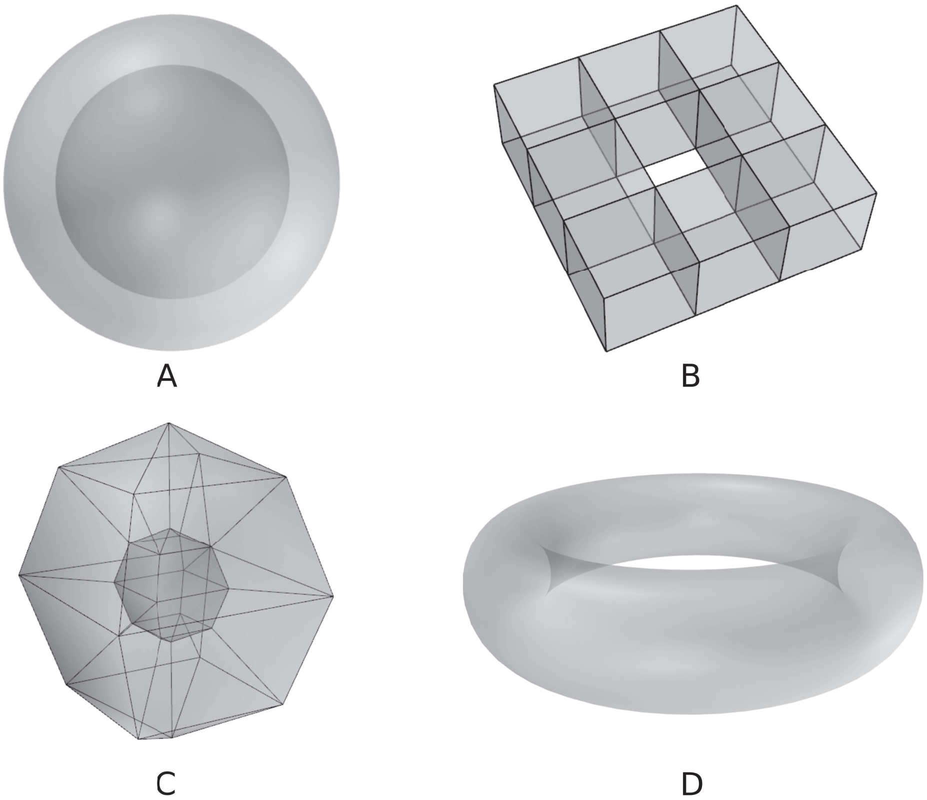

Figure 6.1: 3-dimensional manifold V examples. Represented objects are filled taking into account surfaces as boundaries. (A) Cylinder $\mathbf{C^3}$ can be obtained by performing volumetric boolean operation. These processes are widely used in CAD using surfaces boolean operations. This volume has one cavity. (B) Coarse hexahedral mesh defined from a surface torus $\mathbf{T^2}$. (C) Discrete case of (A). (D) Continuous case of (B). This volume has one connected object, one hole or tunnel but zero cavities.

6.2 Quadrilateral layout to cuboid configuration

As used in Chapter 3, Chapter 4 and Chapter 5, a quadrilateral layout $\mathbb{Q}$ is a coarse quadrilateral mesh. In this development, we will define correctly a quadrilateral layout and its properties. Moreover, we will show that additionnal properties are

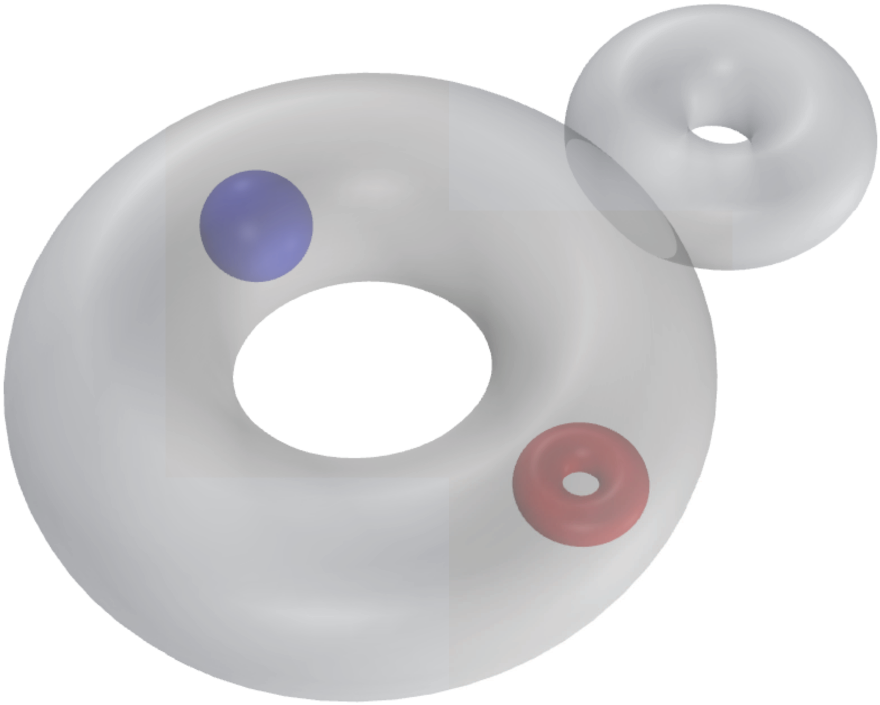

Figure 6.2: Betti numbers for a 3-dimensional manifold. Number of connected components is 1, so $b_0 = 1$. Number of tunnels, or holes is 3, taking into account the red torus embedded into the volume. There are 2 cavities in blue and red respectively, so: $\chi(V) = b_0 - b_1 + b_2 = 1 - 3 + 2 = 0$.

required to build a volume. In this particular case we call $\mathbb{C}$ a valid associated cuboid configuration of $\mathbb{Q}$. $\mathbb{C}$ is then used as a bridge to construct a volumetric layout.

6.2.1 Quadrilateral layout and cuboid configuration definition

A quadrilateral layout $\mathbb{Q}$ is formed by arcs and nodes embedded in the input triangulated surface. We refer the readers to our previous work to have more visual data about quadrilateral layouts [Al Akhras et al. 2017; Maquart et al. 2019a] and also to other papers in the field [Campen, Bommes, and Kobbelt 2012; Myles, Pietroni, and Zorin 2014; Razafindrazaka, Reitebuch, and Polthier 2015; Campen 2017]. To firmly anchor our further developments, we formulate more precisely the quadrilateral layout's definition in Definition 6.4.

Definition 6.4. Quadrilateral layout. A quadrilateral layout is a coarse quadrilateral mesh topologically equivalent to the input unstructured triangulated mesh. Arcs are not necessarily formed by only one simplex, they are combinations of simplices inherited from the input triangulated surface. Nodes are embedded on surface vertices.

Irregular vertices of the layout $\mathbb{Q}$ hold singularities of the associated 4-symmetry direction field. These irregular locations can be determined by Gaussian curvature distribution [Maquart et al. 2019c] or other methods suitable to locate them properly depending on the geometry. Indices and number of singularities can be also estimated. Aim is to characterize valid quadrilateral layout by its associated cuboid configuration, if it exists. Cuboid configurations decompose a surface into a set of quadrilateral patches which are ready for hexahedral meshing. They are special cases of $\mathbb{Q}$ with additional properties. To remove ambiguity between cuboid configuration and quadrilateral layout definition, valid quadrilateral layouts $\mathbb{Q}$ exist if Equation (6.8a) is satisfied for surfaces without boundaries ∂M. For surfaces with boundaries ∂M, Equation (6.8b) will be satisfied. Valence 2 nodes are not being considered. Additional quadrilateral layout constraints to build a valid cuboid configuration $\mathbb{C}$ are introduced in Equation (6.9).

$$\forall v_i \in \mathbb{Q}, \sum_{i=1}^{n_{\mathbb{Q}}} (1 - \frac{v_i}{4}) = \chi(M_c) = 2 - 2g, \tag{6.8a}$$

$$\forall v_i^m \in [\mathbb{Q} \setminus \partial M] \ \& \ \forall v_i^b \in \partial M, \sum_{i=1}^{n_{\mathbb{Q}}^m} (1 - \frac{v_i^m}{4}) + \sum_{i=1}^{n_{\mathbb{Q}}^b} (1 - \frac{v_i^b}{3}) = \chi(M). \tag{6.8b}$$

$$\forall \gamma_{\mathbb{Q}} \in \mathbb{C}, n_{\gamma_{\mathbb{Q}}} \geq 4 \ \& \ n_{\gamma_{\mathbb{Q}}} \in \{2n_{\gamma_{\mathbb{Q}}} | n_{\gamma_{\mathbb{Q}}} \in \mathbb{N}\}. \tag{6.9}$$

Where M_c is the associated closed mesh. We note that, for obvious purposes, only associated closed mesh is taken for computations. Topologically, our goal is to determine volumes, thus surface boundaries have to be closed. A quadrilateral layout is composed by arcs and $n_{\mathbb{Q}}$ nodes of valence v_i. v_i^m and v_i^b refer to the valence of interior and boundary quadrilateral layout's vertices respectively. Associated cuboid configuration of a quadrilateral layout $\mathbb{Q}$ exists by analyzing number of nodes $n_{\gamma_{\mathbb{Q}}}$ contained in cycles $\gamma_{\mathbb{Q}}$ formed by arcs. $\mathbb{C}$ can be viewed as a structured template to build a pure hexahedral mesh. Because this cuboid configuration comes from a surface quadrilateral layout embedded in $\mathbb{R}^3$, the interior volume is not clearly defined. Aiming to build a volumetric objects, we have to close boundaries of the 2-dimensional manifold, in order to have a surface enclosing a volume. This process is shown in Figure 6.3, yielding to closed cuboid configurations $\mathbb{C}_c$. In the following, $\mathbb{C}_c$ will be used for volumetric purposes.

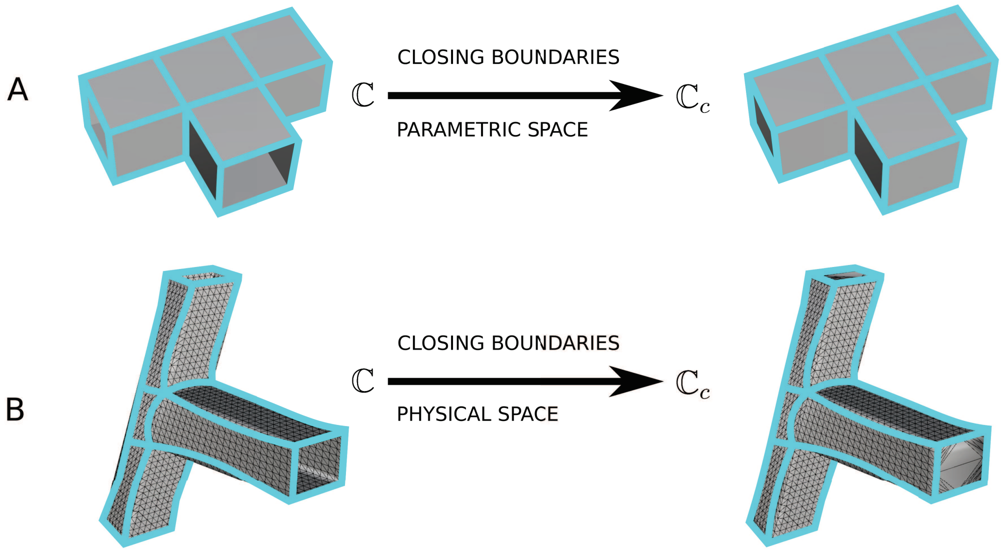

Figure 6.3: $\mathbb{C}$ to $\mathbb{C}_c$ conversion. (A) Closing boundaries in the parametric space. (B) Closing boundaries in the physical space.

6.2.2 Examples and limitations

Large variety of cuboid configurations exist. Depending on the features we want to replicate in the final structured mesh, configurations have to be well thought out. By features we mean sharp edges, corners and high curvature areas. Figure 6.4 shows us some of used closed cuboid configurations $\mathbb{C}_c$ in this manuscript. $\mathbb{C}_c$ are known for the closed configurations if no boundary exists. Indeed, no boundaries, i.e., 1-dimensional manifolds, have to remain to construct a volume. These particularly depicted cuboid arrangements are genus-0 (like surfaces ready to be mapped onto pants geometries). Mapping process considers pants boundaries and designates quadrilateral patches of the cuboid configuration which have to be on the boundary.

To illustrate some of valid quadrilateral layouts which are examined to be valid or invalid cuboid configurations, we draw 2 key examples. The first considers a triangular cylinder (genus-0 with 2 boundaries) whose topology is replicated with a valid quadrilateral layout in Figure 6.5 (A). Equation (6.8a) states that we are not in the presence of a suitable quadrilateral layout when closing its 2 boundaries. On the other hand, Equation (6.8b), which is boundary-aware, validates the quadrilateral layout. Topologically and geometrically, this layout is conform for a surface quadrilateral application. Expected closest valid cuboid configuration is represented in Figure 6.5 (D). The second example succeeds the first testing equations,

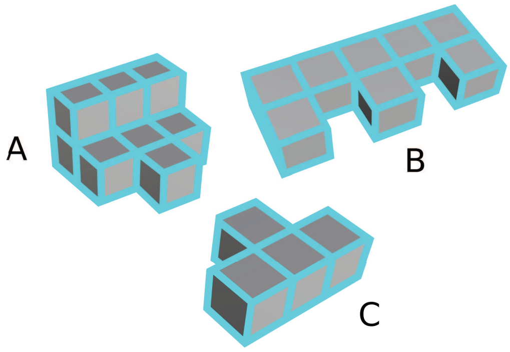

Figure 6.4: Genus-0 closed cuboid configuration $\mathbb{C}_c$ examples with Euler characteristic $\chi = 2$. (A) Configuration with 28 nodes. (B) Configuration with 36 nodes. (C) Configuration with 20 nodes. These configurations are coming from Chapter 3.

i.e., Equation (6.8) due to the torus topology. $\gamma_{\mathbb{Q}}$ cycle analysis shows us the lack of nodes. In this topological situation, this quadrilateral layout is rejected to be a cuboid configuration thanks to Equation (6.9).

Despite large improvements onto constraining topological properties during triangulated mesh to valid cuboid configuration generation, some particular geometry cases are determined taking into account some precautions. Effectively, previous tests are done topologically, meaning that no consideration is accorded to the physical space. It is typically the given demonstration behind the geometry of Figure 6.5 (C). Associated cuboid configuration in the parametric space is shown in Figure 6.5 (F). Physically, $\mathbb{Q}$ suits the geometry perfectly but we can not define all cuboids with a non-zero volume with this specific embedded quadrilateral layout.

We have defined properties and constraints required to a quadrilateral layout to become valid and if needed for volumetric purposes, to become a cuboid configuration. As well as thinking surface to volumetric conversion, further developments will use cuboid configurations to define a volumetric layout and its properties. Cuboid configurations can be seen as connected information between the surface and volumic worlds.

6.3 Cuboid configuration to volumetric layout

Once a valid cuboid configuration has been determined for a triangulated surface, we seek to turn it into a real volume, i.e., a 3-dimensional manifold. As we said before in Section 6.2, cuboid configurations are valid quadrilateral layouts with additional properties. These better properties make them ready to construct a volume. We will explain invariant properties of computed volumes relying on strong mathematical tools from the topology field. Precisely, we will expose in the following one of our most important contributions in this Chapter 6.

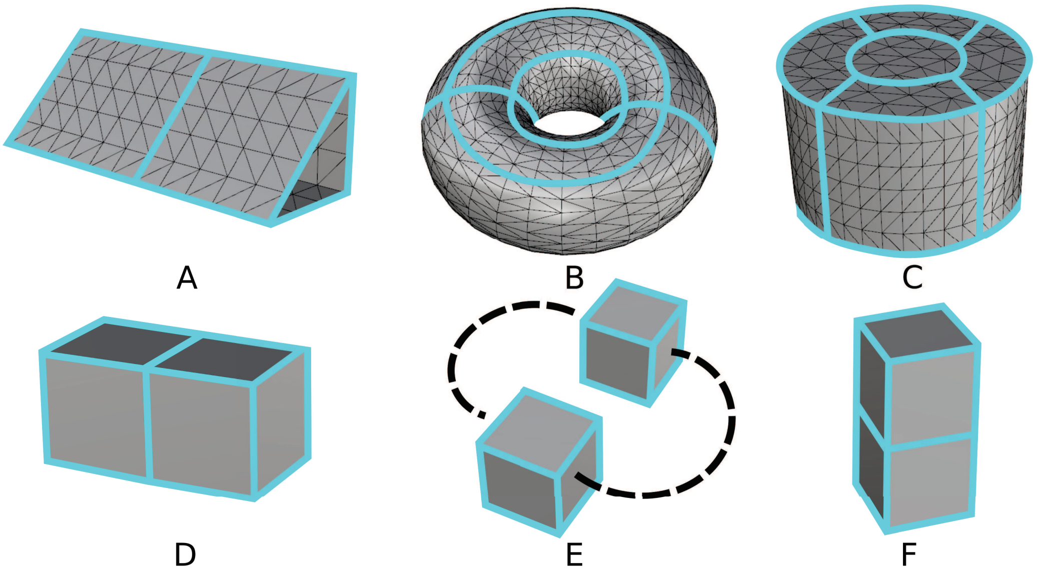

Figure 6.5: Invalid cuboid configurations and limitations. (A) A valid quadrilateral layout, but involving an invalid closed cuboid configuration. (B) Quadrilateral layout of a genus-1 geometry. $\mathbb{C}_c$ is invalid. (C) Quadrilateral layout with 12 nodes of a closed cylinder. $\mathbb{C}_c$ is valid but yielding to a flattened cuboid in the physical space. (D) Closest expected valid cuboid configuration for (A). (E) Closest expected cuboid configuration for (B). (F) Valid $\mathbb{C}_c$ of (C).

6.3.1 Volumetric layout definition

We introduce volumetric layout to serve as coarse hexahedral mesh whose boundary, i.e., a 2-dimenional manifold is topologically equivalent to the input unstructured closed triangulated mesh. Our volumetric layout vision is described in Definition 6.5. Volumetric layouts are particularly studied for their trivariate form, allowing tensor product. In the litterature many different definitions and uses of trivariate layouts exist. Some of them are trying to turn cuboids or polycubes [Tarini et al. 2004] from a surface representation [Li et al. 2013] into a volumetric map [Lin et al. 2008; Fu, Bai, and Liu 2016]. For instance, work has been done by [Yu et al. 2013] to optimize mapping of polycubes. Others are treating these structured trivariate objects to construct continuous mathematical volumes [Wang et al. 2008; Li et al. 2010; Massarwi and Elber 2016]. Various possibilities of such volumetric generations are currently explored, e.g. [Liu et al. 2015] determines polycubes from a skeleton curve capturing features of a triangulated mesh. Techniques coming from the geometrical processing and the topology fields are widely used to compute hexahedral meshes [Hu and Zhang 2016; Lyon, Bommes, and Kobbelt 2016; Lei et al. 2017]. Hexahedral dominant meshes are also currently tackled [Ray et al. 2017; Reberol 2018].

Definition 6.5. Volumetric layout. Volumetric layout is a coarse hexahedral mesh topologically equivalent to the input unstructured tetrahedral mesh embedded in the volume. If volumetric layout is constructed from a cuboid configuration, volumetric layout's boundary is topologically equivalent to the input unstructured closed triangulated mesh. Arcs are not necessarily formed by only one simplex, they are combinations of simplices inherited from the input triangulated surface in case of the volumetric layout's boundary. Otherwise they can be integrated inside the volume with or without a combinatorial form. Nodes are embedded on surface vertices or inside the volume.

6.3.2 Mathematical formulations and properties from generalized theorems

We strive to found cuboid configurations $\mathbb{C}$ with an associated 3-dimensional manifold $V_{\mathbb{C}}$ that respects some constraints inherited from topological and geometrical properties of a surface mesh M. We seek for constraints provided from the surface to be mapped into the volume manifold. We focus here on quadrilateral and hexahedral meshes, i.e., simplicial complexes. Into a volumetric layout $V_{\mathbb{C}}$ the number of volumes k_3 is defined by Equation (6.10a).

$$k_3 = -\chi(V_{\mathbb{C}}) + k_0 - k_1 + k_2, \tag{6.10a}$$

$$\text{s.t. } \{k_{0_{\mathbb{C}}} - k_{1_{\mathbb{C}}} + k_{2_{\mathbb{C}}} = \chi(\partial V_{\mathbb{C}}) = \chi(\mathbb{C}_c) \ \& \ |\partial V_{\mathbb{C}}| = 1\}. \tag{6.10b}$$

This equation yields more than one possibility in the general case. $k_{i_{\mathbb{C}}}$ are the CW-complex entities of the closed cuboid configuration $\mathbb{C}_c$. $\mathbb{C}_c$ is provided from a configuration $\mathbb{C}$ possibly with boundaries. Since Equation (6.10a) has overabundant unknown terms, and in general not enough constraints in Equation (6.10b), one closed cuboid configuration $\mathbb{C}_c$ can refer to many non-isomorphic associated volumetric layouts $V_{\mathbb{C}}$. The constraint $|\partial V_{\mathbb{C}}| = 1$ is trivial. We build volumetric manifolds only from one connected 2-dimensional manifold. Hence, for one given closed cuboid configuration $\mathbb{C}_c$, there exists different possible volumetric layouts satisfying above constraints. Depending on the surface or mesh features, we can choose the best volumetric layout by analyzing geometry. It leads us to the following statement in Proposition 6.3.

Proposition 6.3. Non-isomorphic associated volumetric layouts. Let $\mathbb{C}_c$ be a valid closed cuboid configuration of a compact oriented 2-dimensional manifold M. If we want to turn $\mathbb{C}_c$ into a volumetric manifold $V_{\mathbb{C}}$, there exists a set $U_{V_{\mathbb{C}}}$ with an infinite size of non-isomorphic volumetric structures that satisfies constraints provided in Equation (6.10b):

$$\mathbb{C}_c \Rightarrow V_{\mathbb{C}}^{i} \not\equiv_{iso} V_{\mathbb{C}}^{j}, \forall i, j < |U_{V_{\mathbb{C}}}| = \infty. \tag{6.11}$$

Where $\equiv_{iso}$ denotes the isomorphic equivalence.

Non-isomorphism between different volumetric layouts $V_{\mathbb{C}}$ differ just by number of volumes k_3, number of surfaces k_2 and number of edges k_1. In other words, two volumetric layouts are isomorphic if they have the same number of simplices of each dimension $n,\ n \in \{0, 1, 2, 3\}$, in allowing mapping with a discontinuous function. Homeomorphic configurations are isomorphic configurations holding exactly the same simplicial complex connectivity. The set $U_{V_{\mathbb{C}}}$ has an infinite size as clarified in Proof 6.1.

Proof 6.1. Infinite size of the set $U_{V_{\mathbb{C}}}$. The set of non-isomorphic associated volumetric layouts $U_{V_{\mathbb{C}}}$ of an associated closed cuboid configuration $\mathbb{C}_c$ has an infinite size because of the properties of the 3-simplex subdivision. It is always possible to subdivide a n-simplex in the way that $(n-1)$-simplices of the boundary remains topologically the same; and the created manifold is also embedded in the same n-dimensional topological space, so:

$$|U_{V_{\mathbb{C}}}| = \infty, \forall V_{\mathbb{C}}. \tag{6.12}$$

Taking into account previous definitions and constraints, we now seek to find which volumetric Euler characteristic $\chi(V_{\mathbb{C}})$ is interesting. In other words, we mean a 3-dimensional manifold embedded in $\mathbb{R}^3$ with specific properties inherited from the input surface and its associated closed cuboid configuration $\mathbb{C}_c$. Then, we want a volume which lies in $\mathbb{R}^3$ with only one $(n-1)$-dimensional compact, connected and orientable entity. However, we can not accept any 1-dimensional entity, i.e., boundaries of 2-dimensional manifolds. Finally, Equation (6.13) in Proposition 6.4 states our interesting volumetric Euler characteristics.

Proposition 6.4. Equation $2\chi(V_{\mathbb{C}}) = \chi(\mathbb{C}_c)$. In $\mathbb{R}^3$, a 3-dimensional manifold $V_{\mathbb{C}}$ constructed from compact oriented 2-dimensional manifolds $\mathbb{C}_c$ with at least one 2-dimensional compact, connected and orientable entity is restricted to the following volumetric Euler characteristic $\chi(V_{\mathbb{C}})$:

$$\chi(V_{\mathbb{C}}) = \frac{\chi(\mathbb{C}_c)}{2} = 1 - g. \tag{6.13}$$

Using g as the genus of the cuboid configuration $\mathbb{C}$ or $\mathbb{C}_c$, i.e., $g(\mathbb{C})$ or $g(\mathbb{C}_c)$. Indeed, adding 1-dimensional manifold entities to a 2-dimensional one does not change its genus g.

This result can be demonstrated using CW-complex properties and Betti numbers in a topological space $\mathbb{R}^3$ [Damiand 2010], see Equation (6.14) in Proof 6.2. Meshes are simplicial complexes due to their combinatorial form. Remember that CW-complexes are themselves both simplicial complexes and continuous entities on which homotopy theory is applicable.

Proof 6.2. Equation $2\chi(V_{\mathbb{C}}) = \chi(\mathbb{C}_c)$. To turn any 3-dimensional volumetric manifold $V_{\mathbb{C}}$ embedded in $\mathbb{R}^3$ into a topological object homeomorphic to $\mathbf{B^3}$, we have to add CW-complex objects to $V_{\mathbb{C}}$. We first create g surfaces k_2, i.e., for each tunnel or 1-dimensional independent manifold (see Figure 6.6 (A)). Secondly, we create two edges k_1 and one surface k_2 for each 2-dimensional cavity (see Figure 6.6 (B)):

$$\begin{aligned}
\chi(V_{\mathbb{C}}) &= k_0 - (k_1 + 2b_2) + (k_2 + b_1 + b_2) - k_3, && \text{(6.14a)}\\
&= k_{0_{\mathbb{C}}} - k_{1_{\mathbb{C}}} + k_{2_{\mathbb{C}}} - 2b_2 + b_1 + b_2 - k_3, && \text{(6.14b)}\\
&= \chi(\mathbb{C}_c) + b_1 - b_2 - 1, && \text{(6.14c)}\\
&= \chi(\mathbb{C}_c) - \chi(V_{\mathbb{C}}) \Rightarrow 2\chi(V_{\mathbb{C}}) = \chi(\mathbb{C}_c). && \text{(6.14d)}
\end{aligned}$$

Where $b_3 = 0$ (considering the topological space $\mathbb{R}^3$). $k_0 = k_{0_{\mathbb{C}}}$, $k_1 = k_{1_{\mathbb{C}}}$ and $k_2 = k_{2_{\mathbb{C}}}$ ($\mathbb{C}_c$ remains unchanged). $k_3 = 1$ (we consider only one connected volume).

This previous equation establishes the topological relation between associated volume $V_{\mathbb{C}}$ of a cuboid configuration $\mathbb{C}_c$. To go further we can express in Equation (6.15) the Betti numbers of $V_{\mathbb{C}}$ using the previous results.

$$\begin{cases} b_0 = 1, \\ b_1 = b_0 + b_2 - \frac{\chi(\mathbb{C}_c)}{2}, \\ b_2 = |M|. \end{cases} \tag{6.15}$$

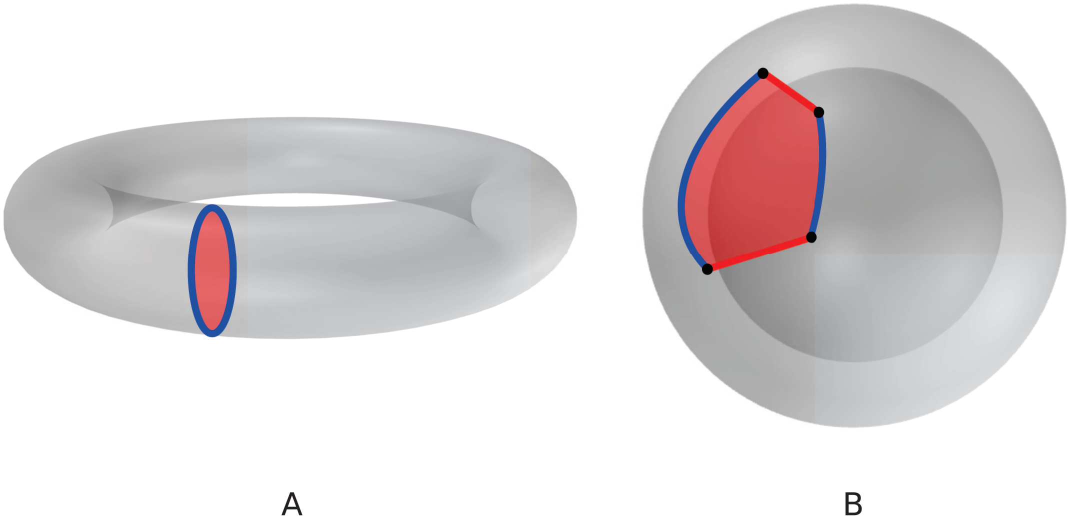

Figure 6.6: 3-dimensional volumetric manifold $V_{\mathbb{C}}$ to $\mathbf{B^3}$ conversion using CW-complexes. (A) g surfaces k_2 are created for a g-torus (red surface), i.e., for a tunnel. (B) Two edges k_1 and one surface k_2 are constructed (red curves and surface) for a cavity. Black and blue objects are not created beacause they are lying on a lower dimensional object than a volume.

With $|M|$ the number of connected 2-dimensional manifolds used to define $V_{\mathbb{C}}$ minus one. As we said before, only one surface manifold is used for our purposes, so $|M| = 0$. We now can re-write Equation (6.10) to include interesting volumetric characteristics and needed topological space constraints. This idea is formulated in Equation (6.16).

$$k_3 = g - 1 + k_0 - k_1 + k_2, \tag{6.16a}$$

$$\text{s.t. } \{k_{0_{\mathbb{C}}} - k_{1_{\mathbb{C}}} + k_{2_{\mathbb{C}}} = \chi(\partial V_{\mathbb{C}}) = \chi(\mathbb{C}_c)\} \text{ and} \tag{6.16b}$$

$$\{|\partial V_{\mathbb{C}}| = 1 \;\&\; V_{\mathbb{C}} \in \mathbb{R}^3 \;\&\; \partial V_{\mathbb{C}} \equiv \mathbb{C}_c\}. \tag{6.16c}$$

Where $\equiv$ denotes the classic geometric equivalence. $\partial V_{\mathbb{C}}$ and $\mathbb{C}_c$ are topologically and geometrically the same. $\partial V_{\mathbb{C}}$ replicates perfectly the associated closed cuboid configuration. This is a necessary condition to bound a volume. To be more precise, in Equation (6.16b) and Equation (6.16c), constraints are not independent. Since $\partial V_{\mathbb{C}}$ is provided from $\mathbb{C}_c$, $|\partial V_{\mathbb{C}}|$ and $\chi(\partial V_{\mathbb{C}})$ are already set.

With previous developments and theorems, we recall that the volumetric Euler charcateristic $\chi(V_{\mathbb{C}})$ can not be directly related to the n-symmetry direction field $\mathbf{d}$ embedded in the volume. This reminder is formulated in Remark 6.1 with Equation (6.17).

Remark 6.1. *3-dimensional manifold Euler characteristic is in general different of the singularity indices summation, see Equation (6.3):*

$$\chi(V_{\mathbb{C}}) = 1 - g(\mathbb{C}_c) \neq \sum_{i=1}^{n_s} I^i_{\mathbf{d}}, \;\; \mathbf{d} \in V_{\mathbb{C}}. \tag{6.17}$$

In addition, for the 3-dimensional sphere $\mathbf{S}^3$, whose reprentation is only possible in the $\mathbb{R}^4$ topological space, its Euler charcacteristic can be expressed in the same spirit of Equation (6.8a) using a volumetric layout V. Precedent idea is written in Conjecture 6.1 with Equation (6.18). This given equation has to be proved and demonstrated using topology concepts available in the litterature, e.g. [Hatcher, Lochak, and Schneps 2000; Hatcher 2001; Damiand 2010].

We finally remark that, according to [Huang et al. 2011], representing vector fields in 3D is not possible. [Huang et al. 2011] have proposed a method with a frame representation to overcome the issue. More recently, [Ray and Sokolov 2015] have introduced a method to compute a 3D frame field based on the previous representation. [Chemin et al. 2018] presented an approach with high order tensors. Over researches generalize the concept of octahedral fields embedded in volumes [Solomon, Vaxman, and Bommes 2017; Liu et al. 2018]. Such fields are subject to singularities which are lying on a 1-dimensional manifold. In other words, they are located on a singularity graph. In volumetric objects represented in the $\mathbb{R}^3$ topological space, the fourth dimension can help to characterize singularities, like the third dimension define the positive or negative rotation direction for vector fields integrated on surfaces.

Conjecture 6.1. We suppose that the Euler characteristic of the 3-dimensional sphere can be related directly to its nodes valencies v_i, n_V being the number of nodes in the corresponding simplicial complex or volumetric layout V:

$$\forall v_i \in V, \sum_{i=1}^{n_V} (1 - \frac{v_i}{6}) = \chi(\mathbf{S}^3). \tag{6.18}$$

6.3.3 Volumetric layout examples from standard CAD

To illustrate some of presented above mathematical formulations, we give two volumetric layout examples with a basic geometry in Figure 6.7. B-Rep triangulated meshes hold genus-0 and $\chi = 2$ properties. Thus they are topological spheres. Figure 6.7 (A) and (B) are the triangulated geometries whereas Figure 6.7 (C) and

(D) are the associated volumetric layouts that best describe and replicate the sharp features. Firstly, we inspect the couple (A) and (C). By analyzing number of n-simplices of each dimension n, this brought us to $\chi(V_{\mathbb{C}}) = k_0 - k_1 + k_2 - k_3 = 1$. In fact, $\mathbb{C}_c$ is also a genus-0 surface and $V_{\mathbb{C}}$ is homeomorphic to the 1-boundary 3-dimensional manifold $\mathbf{B}^3$ in $\mathbb{R}^3$. For the pair (B) and (D) it seems to be not as obvious as the previous couple was. However, we should have to evaluate directly Equation (6.13). Since volumetric characteristics $\chi(V_{\mathbb{C}})$ of interesting volumetric layouts in the $\mathbb{R}^3$ topological space are entirely defined by the genus of the associated closed cuboid configuration $\mathbb{C}_c$ with an additional integer, $\chi(V_{\mathbb{C}}) = 1$ while the number of 3-simplices were changed as depicted in Figure 6.7 (D).

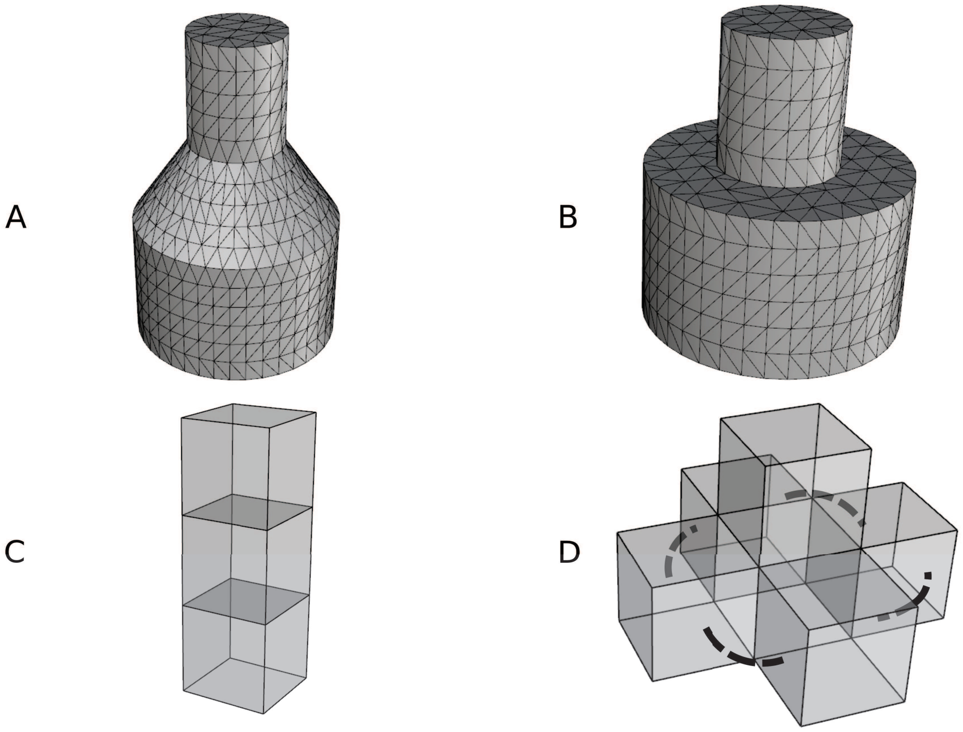

Figure 6.7: Volumetric layouts straightforward examples. (A) Triangulated mesh with sharp features. (B) Triangulated mesh with particularly marked sharp features. (C) Proposed volumetric layout for (A). (D) Proposed volumetric layout for (B).

6.3.4 Isotopological volumetric layouts

Understanding significance of above developments, we reformulate here the problematic exposed in Chapter 1 for volumetric purposes. Given a set of input triangulated meshes, we strive to find an isotopological trivariate isogeometric meshes population which respect to the four following properties:

- Pure hexahedrons with low distortion for the trivariate control lattice.

- Feature aligned with geometry inherited from the triangulated surface.
- Isotopological with homologous points into other geometric instances.
- Non-uniform isotropy for a morphing to all members of the population.

We then follow the Strategy 1.2 to compute required meshes. Same concepts have been already developed for 3D quadrilateral meshes in Section 5.1.

6.3.4.1 Isomorphic to isotopological homologous

We want to tackle here isotopological properties of volumetric meshes. Firstly, we introduce the notion of isomorphic meshes. Isomorphic meshes are meshes with the same number of n-simplices of each dimension n. Isomorphism is a structure preserving application admitting a continuous inverse function between the 2 considered simplicial complexes. In our definition, non-continuous functions are tolerated in the specific case of meshes. Figure 6.8 (A) and (B) illustrate the structure mismatching. Indeed, if we think with continuous manifolds, there exists a continuous transformation with a continuous function between two connected, compact and orientable volumes if and only if they have the same Euler characteristic and number of 2-dimensional boundary components with the same attached surface Euler characteristic and yielding to the same homotopy groups (we are not taking into account volumes created by more than one surface with $V_{\mathbb{C}}$). Remark that, in the general case, homotopy groups are not sufficient to classify topological spaces up to homotopy equivalence: it has to be deeply studied with papers in the related field. Interesting considerations are made in the topological space $\mathbb{R}^3$. We also notice that Betti numbers do not inform on isomorphism properties since the cylinder $\mathbf{C}^3$ and the sphere $\mathbf{S}^2$ have the same Betti numbers. Homology and homotopy groups are relevant information to state the homeomorphic properties between two topological spaces, but they are not sufficient. However and fortunately, the inverse is true [Hatcher 2001; Damiand 2010]: homeomorphic spaces have the same homotopy and homology groups.

Isotopological meshes are isomorphic meshes with a continuous inverse function and holding the same element connectivity as presented in Figure 6.8 (C). Homologous property is not directly evident. The structure has to respect the same feature location, i.e., we can compare the same node identificator in the same interesting zone among all instances of related meshes. It is done by constraining the disposal of the volumetric layout and taking into account principal curvature directions. This concept, similar with quadrilateral meshes is shown in Figure 6.8 (D) and (E).

6.3.4.2 Population constraints

To build isotopological meshes for a specific set of related meshes, the discretization sampling is based on one representative member of the population: the α-*member*.

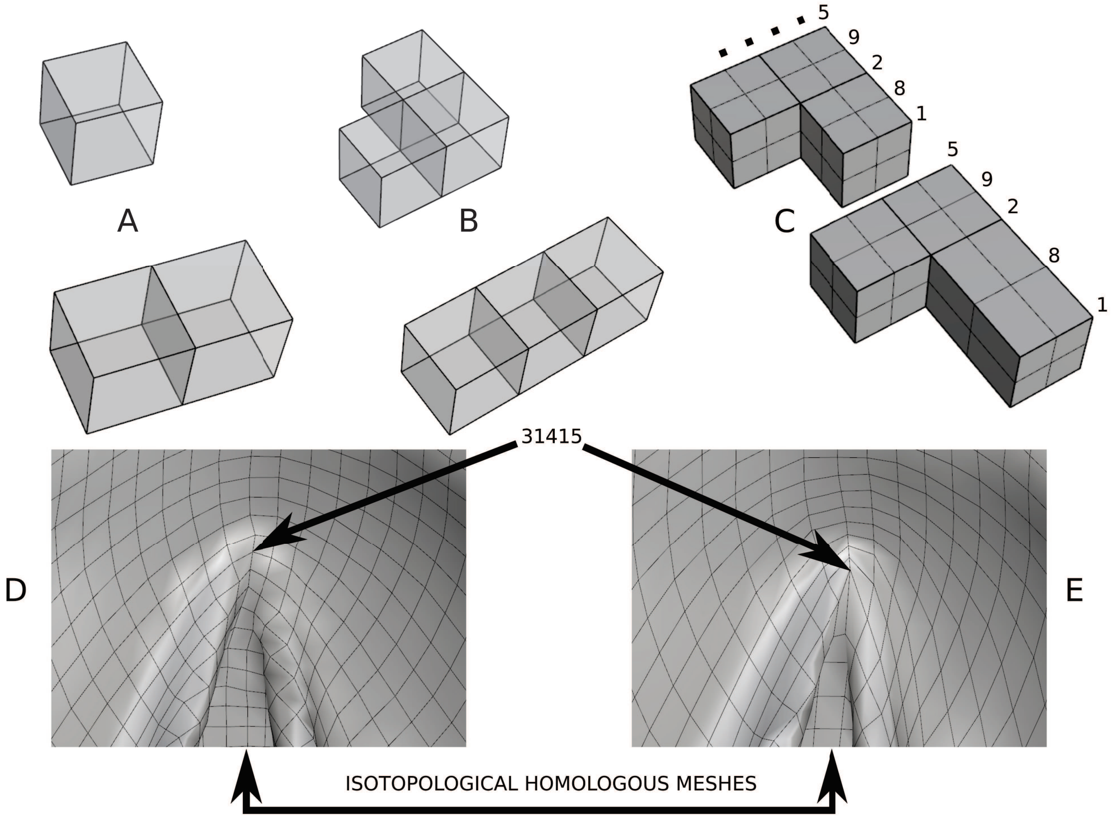

Figure 6.8: Isotopological homologous properties of volumetric meshes. (A) Non-isomorphic volumetric layouts. (B) Isomorphic layouts with a discontinuous mapping function. (C) Isotopological trivariate isogeometric meshes. (D) and (E) are representing the homologous concept for an aortic valve using quadrilateral meshes.

This idea was already conceptualized in Section 5.1 for quadrilateral meshes. Taking into consideration features and geometry of the α-*member* mesh, isotopological and homologous constraints are then settled for all members. Non-uniform isotropy is therefore intrinsically set because of volume number, connectivity and discretization. We recall that for mechanical applications with geometrical parameters, the α-*member* is chosen as the middle of all designing parameters. Constraints and relations between the volumetric layout, mesh isogeometric discretization and an arbitrary representative member are depicted in Figure 6.9. This process is then used in our following developments to construct reduced order models based on geometrical design rules. It is emphasized that for reduced order modeling objectives developed in Chapter 7, meshes must not differ by a rigid body transformation.

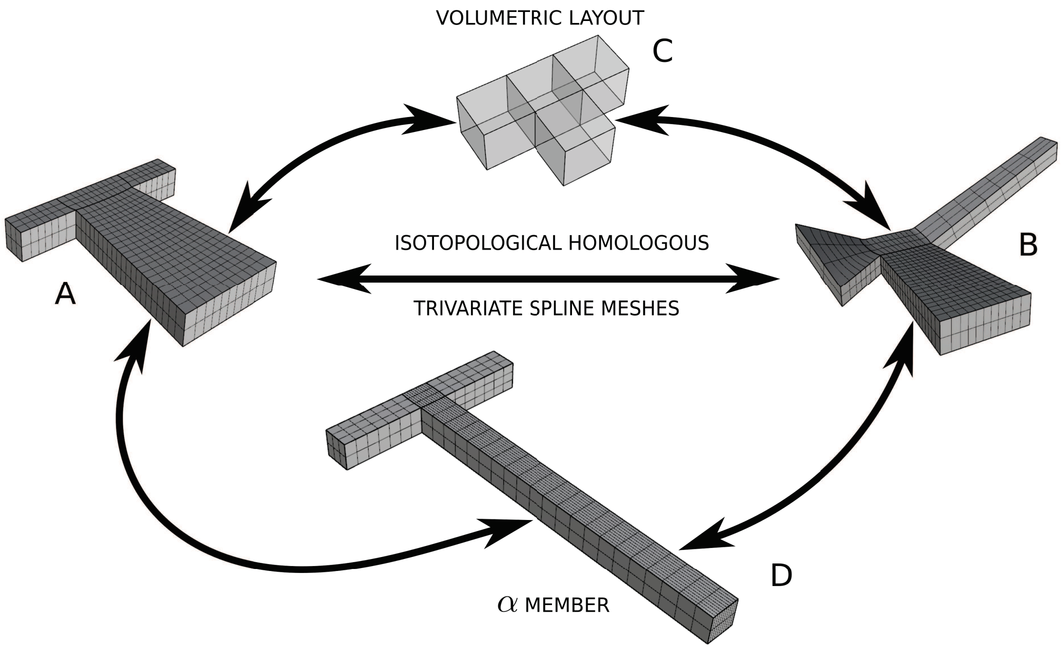

Figure 6.9: Isotopological isogeometric meshes constraints for reduced order modeling. (A) Isogeometric mesh with a geometry A. (B) Isogeometric mesh with a geometry B. (C) Associated volumetric layout of reference. (D) α-*member* chosen to represent the whole population.

6.3.5 B-Spline volume reconstruction

In order to generate a volumetric parameterization of given solids models, different steps have to be considered. Our input is generated thanks to a global parameterization aligned with a cross field. Using the quadrilateral mesh generated from this parameterization as done in Chapter 4, a structured grid of points is extracted on each patch of the cuboid configuration $\mathbb{C}_c$. Such grids are then used to fit B-Spline surfaces. Depending on the volumetric layout $V_{\mathbb{C}}$, missing surfaces are evaluated with curves embedded into the volume or into the volume's boundary. A technique close to the Coons patch surface reconstruction is endorsed [Farin and Hansford 1999; Piegl and Tiller 2012]. In the context of this thesis, the software [McNeel 2017b] and related library [McNeel 2017c] were adopted for surface determination and manipulation.

Once all mathematical surfaces are provided, we can now proceed to volumetric parameterization. Since the volumetric layout structure is regular, it serves as the parametric domain required for tensor product trivariate B-Spline surfaces. For each cube contained in $V_{\mathbb{C}}$, the B-Spline patch solid is obtained using reconstructed B-spline surfaces as boundary conditions. Keeping the boundary control points fixed, the interior control points of the B-Spline solid are computed with trivariate Coons interpolation. We follow the method of [Wang and Qian 2014] recovered by

[Al-Akhras 2016] to compute such volumetric designing. To improve isogeometric trivariate mesh quality, control points can be adjusted [Ma and Kruth 1995; Wang and Qian 2014] and potential G1 smoothness between patches could be settled. To illustrate the process, we consider a mechanical part, see, e.g. Figure 6.10. In this example only harmonic parameterization is used to compute B-Spline boundary surfaces [Tong et al. 2006; Martin, Cohen, and M. Kirby 2009]. Figure 6.10 (A) shows the B-Splines arising from surface parameterization. Thereafter, missing surfaces are determined to form volumetric cubes composed by 6 surface entities in Figure 6.10 (B). In Figure 6.10 (C) volume is achieved with a Coons 3D interpolation technique.

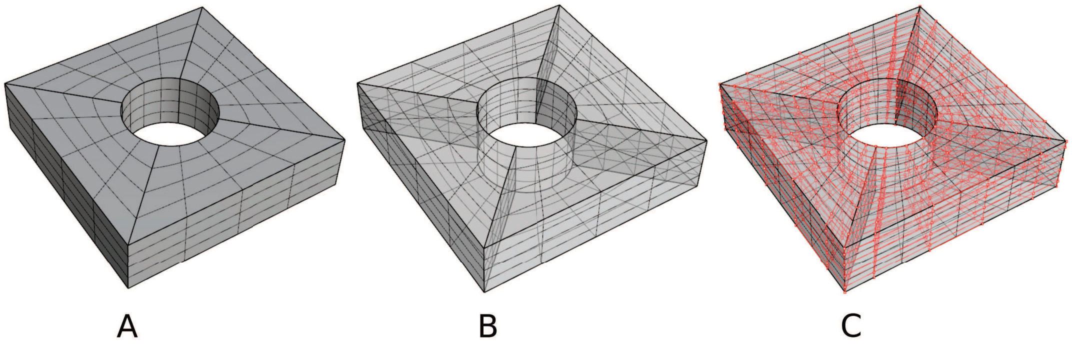

Figure 6.10: Trivariate B-Spline volume construction from B-Spline surfaces. (A) B-Spline surfaces extracted thanks to the parameterization. (B) Reconstructed missing interior surfaces needed for the trivariate parametric domain. (C) Interpolated trivariate isogeometric control lattice (depicted in red).

6.4 Conclusion

We have presented new useful mathematic material to convert surface parameterization into structured volumetric one. Rigorous definitions and properties of topological quantities have been given when passing in the third dimension. Indeed, from the quadrilateral layout to the volumetric layout $V_{\mathbb{C}}$, invariant properties and constraints were analyzed with strong mathematical tools arised from the topology field. According to these developments, we are able to know if the surface to volumetric transformation is possible and what characteristics are expected. This was mainly achieved thanks to the cuboid configuration $\mathbb{C}$. Thus, these properties help us to correctly determine volumetric layouts required for trivariate isogeometric B-Spline construction.

We have also introduced isotopological constraints and the homologous concept in order to build suitable isogeometric meshes for reduced order modeling purposes. In fact, addressing the same parameterization for all geometrical instances to be compared, avoids a projection step and brought us to accurate further mesh comparison. That's what we will demonstrate in the next Chapter 7.

Chapter 7

Trivariate isogeometric reduced order modeling applications

This chapter presents applications focusing on reduced order models built using isogeometric analysis [Maquart et al. 2019b].

Contents

7.1 Hexahedral remeshing

This section presents pure hexahedral meshing from trivariate B-Spline solids and a related meshing application for reduced order modeling. We will first describe how hexahedral meshes are constructed from such mathematical solids. In a second time, a standard FEA code is modified to show that our worflow is well-suited for remeshing purposes during analysis. Isotopological meshing process is naturally adapted to this kind of problematic. The method explicited in Chapter 1 will be used for hexahedral meshes generation.

7.1.1 Hexahedral sampling method from B-Spline surfaces

As well as aiming to build trivariate B-Spline solids from a surface global parameterization, we give a similar method to obtain hexahedral meshes from B-Spline surfaces. 6 surfaces are being considered and form the boundary of an isogeometric volume. We proceed patch by patch like as presented in Section 6.3. For each set of 6 compatible boundary spline surfaces, the hexahedral patch is obtained using reconstructed quadrilateral meshes from surfaces as boundary conditions. Compatibility of surfaces is achieved with same the surface degree, number of knots and control points. Degree could be different if global parametric directions for the new volume are taken into account. In addition, at each surface interface, physical locations of the control points must be the same. A simplified procedure from [Wang and Qian 2014] is adopted. By sampling linearly the square parametric domain of surfaces, we obtain a parametric grid as a function of the number of control points. Technically speaking, we sample with n and m points in the first and second parametric directions, resulting in $n-1$ and $m-1$ quadilateral elements; n and m being the number of control points in u and v parametric directions respectively. Sampling is explicited in Equation (7.1) for a degree 2 surface with uniform open knot vectors $\mathcal{U}$ and $\mathcal{V}$ as defined in Chapter 1. The 6 quadrilateral meshes are extracted with physical positions of previously computed parametric values $\mathcal{U}_q$ and $\mathcal{V}_q$. A finer grid can be computed if a refinement is needed.

$$\begin{cases} p = 2 : \mathcal{U} = \{0,0,0,1,2,3,4,5,6,6,6\}, \\ p = 2 : \mathcal{V} = \{0,0,0,1,2,3,4,5,6,6,6\}, \\ n = 8 : \mathcal{U}_q = \{0, \frac{6}{7}, \frac{12}{7}, \frac{18}{7}, \frac{24}{7}, \frac{30}{7}, \frac{36}{7}, 6\}, \\ n = 8 : \mathcal{V}_q = \{0, \frac{6}{7}, \frac{12}{7}, \frac{18}{7}, \frac{24}{7}, \frac{30}{7}, \frac{36}{7}, 6\}. \end{cases} \tag{7.1}$$

As surfaces come from a global parameterization, they are mathematical surfaces fitted from an arranged grid of points derived from the triangulated B-Rep surface. Estimating a new structured grid on a physical spline surface allow us to better capture the major trends of curvature, especially for scanned geometries provided from medical imaging. Figure 7.1 shows the method based on the sampling vectors $\mathcal{U}_q$ and $\mathcal{V}_q$ of Equation (7.1). In the final stage in Figure 7.1 (C) the position of the interior control points are then adjusted by minizing a Laplacian based energy.

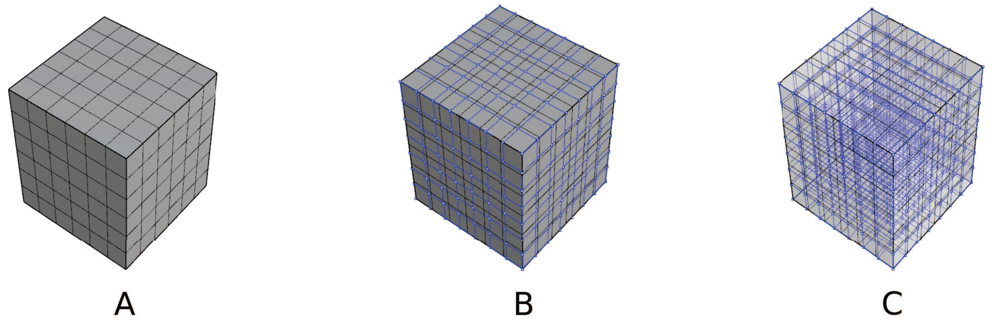

Figure 7.1: Hexahedral sampling method from B-Spline surfaces of degree 2. (A) 6 compatible B-Spline surfaces that bound a volume. Black lines delimit surfaces elements. (B) 6 quadrilateral meshes evaluated at physical positions of parametric values contained in vectors $\mathcal{U}_q$ and $\mathcal{V}_q$ of Equation (7.1) (quadrilateral meshes and points are depicted in blue). (C) Blue hexahedral patch computed using Coon's interpolation.

7.1.2 Large deformations: neo-hookean material application

7.1.2.1 Introduction to meshing during large deformations

The following developments present a remeshing application for large deformation during a mechanical analysis. We study the use of our algorithms to perform the isotopological remeshing during a hyperelastic simulation. Although no reduced order model is introduced in this example, hyperelastic large strain calculation is a case in which classical a posteriori reduced order models are not efficient because of the needed remeshing during the calculation of a given snapshot. Indeed when high strains are encountered, standard finite element meshes often lead to poor element shapes during the computation, and remeshing is unavoidable to be able to perform the simulation until the end. As for geometric parametric studies, the use of isotopological meshes is required for ROM algorithm to perform efficiently when remeshing is needed. This example is presented to show that our meshing pipeline described in previous Chapters 3, 4 and 6 has a real ability for isotopological remeshing purposes during computations. It can be further applied to overcome computation halt under excessive element deformation due to specific mechanical conditions, as observed for example by [Elguedj et al. 2008] and [Lipton et al. 2010].

7.1.2.2 Mechanical problem description

In this example, we consider a simple compressible Neo-Hookean material, see e.g. [Lemaitre and Chaboche 1994; Simo and Hughes 2006], and use our mesh generation algorithms on a half-seal part composed by one pants patch. For this particular case, we consider degree 1 B-Splines which are nothing more than standard piecewise linear hexahedrons classically used in FEA. The corresponding isogeometric parameterization involving our method, resulting in a trivariate B-Spline is presented in Figure 7.2. The same parameters (cuboid configuration, singular points, number of nodes and connectivity) will be used to create a deformed mesh of the model at a given time of the simulation. The input mesh and boundary conditions are given in Figure 7.3 (A). We consider a quasi static computation with a ramp loading from $t = 0$ to $t = 1$ and use the following values for the material parameters: $\mu = 3$ MPa and $\kappa = 20$ MPa for the shear and bulk modulus respectively. These material parameters imply a Poisson's ratio equal to $\nu = 0.3636$, which correspond to a compressible material. Lower values than $\nu = 0.45$ are recommended to avoid non desired element locking. The finite element calculation is classically performed using a total Lagrangian approach [Bower 2012; Belytschko et al. 2013], again see e.g. [Simo and Hughes 2006].

For a hyperlastic material, the first Piola-Kirchhoff stress tensor $\bar{\bar{P}}$ can be expressed in terms of the Helmholtz free energy W. This energy function depends locally only on the deformation gradient $\bar{\bar{F}}(\bar{\bar{X}})$. Thus we use $W(\bar{\bar{X}}, \bar{\bar{F}}(\bar{\bar{X}}))$ to define the stress tensor in Equation (7.2). Indeed, an objective formulation of the hyperelastic density energy is adopted, i.e., the polar decomposition allows us to write W as a function of $\bar{\bar{C}}$; $\bar{\bar{C}}$ being the right Cauchy-Green tensor.

$$\bar{\bar{P}}(\bar{\bar{X}}) = \frac{\partial W(\bar{\bar{X}}, \bar{\bar{F}}(\bar{\bar{X}}))}{\partial \bar{\bar{F}}(\bar{\bar{X}})}. \tag{7.2}$$

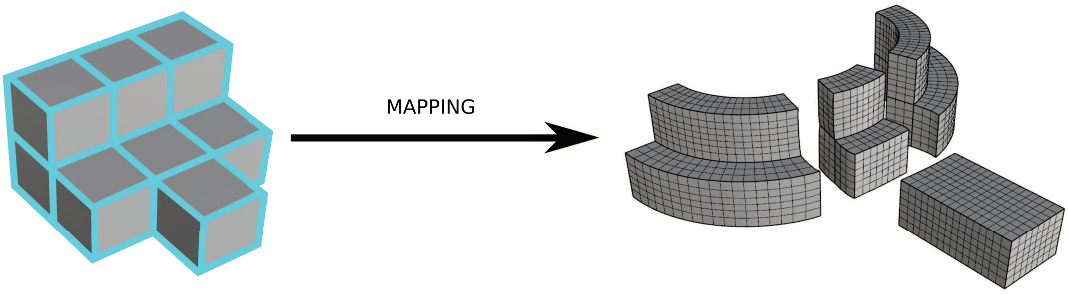

Figure 7.2: Volumetric isogeometric parameterization of the half-seal part for remeshing purposes. It is a genus-0 geometry with sharp features. Euler characteristic is $\chi = -1$ for the mesh with 3 specially located boundaries. During the remeshing step, the parameterization is still the same whereas the geometry is changing under loading.

7.1.2.3 Proposed remeshing method

The main steps of our remeshing strategy are described taking into account the material behavior. A simplified description is depicted in Figure 7.4. Based on the results of the full calculation without remeshing, we observe that element quality metrics of the deformed mesh start to deteriorate significantly after $t = 0.5$. Consequently, we extract the deformed geometry at this particular time and use our algorithms to create a new isotopological mesh to improve element aspect ratio and overall quality. The new mesh used form $t = 0.5$ can be seen in Figure 7.3 (A). In order to evaluate mesh quality, we use as a metric the element shape ratio S_r classically available in commercial softwares such as ANSYS. $S_r = \frac{A}{B}$ measures the stretching of the element, where A is the maximum distance from the hexahedral centroid to one of the eight corners and B is computed as the minimum value of the normal distance between the cell centroid and face centroids (computed as a dot product of the distance vector and the face normal). Therefore, for a unit cube we have $S_r = 1.732$.

In our calculation with remeshing, once we have created the new mesh with the strategy from Chapter 1, the displacement field is mapped from the old to the new mesh using standard techniques. The finite element calculation is resumed by considering an initial deformation state computed using the deformation gradient after projection onto the new mesh.

Element shape ratio computed at $t = 0.5$ and $t = 1$ on both meshes are shown in Figure 7.3 (B) and Figure 7.3 (C). We can observe that at $t = 0.5$ the remeshing reduces the maximum value of S_r by approximately 30%. A similar observation can be done at the final time $t = 1$, where the element shape ratio is even further reduced compared to the full simulation with the initial mesh.

With above developments coming from Chapter 6 and understanding large variety of element quality criteria, we have chosen to investigate a new quality criterion based on topological aspects. Although S_r was used here to fulfill our discussion, we invite the readers to take a look in Appendix C.

All different transformations are summarized in Equation (7.3) using composition, i.e., simply contracted matrix product yielding to a total deformation gradient $\bar{\bar{F}}_{tot}$; this task involving 4 transformations as shown in Figure 7.4. $\bar{\bar{F}}_r$ and $\bar{\bar{F}}_i$ are relative to the remeshing and displacement interpolation accuracy respectively. $\bar{\bar{F}}_b$ is the deformation from $t = 0$ to $t = 0.5$ whereas $\bar{\bar{F}}_f$ is related for the second final loading time until $t = 1$.

$$\bar{\bar{F}}_{tot} = \bar{\bar{F}}_f \bar{\bar{F}}_i \bar{\bar{F}}_r \bar{\bar{F}}_b. \tag{7.3}$$

7.1.2.4 Mechanical results discussion

We seek to compare the Von-Mises stresses at the final time for both cases to check that the remeshing and mapping steps lead to the correct solution. Figure 7.5 shows

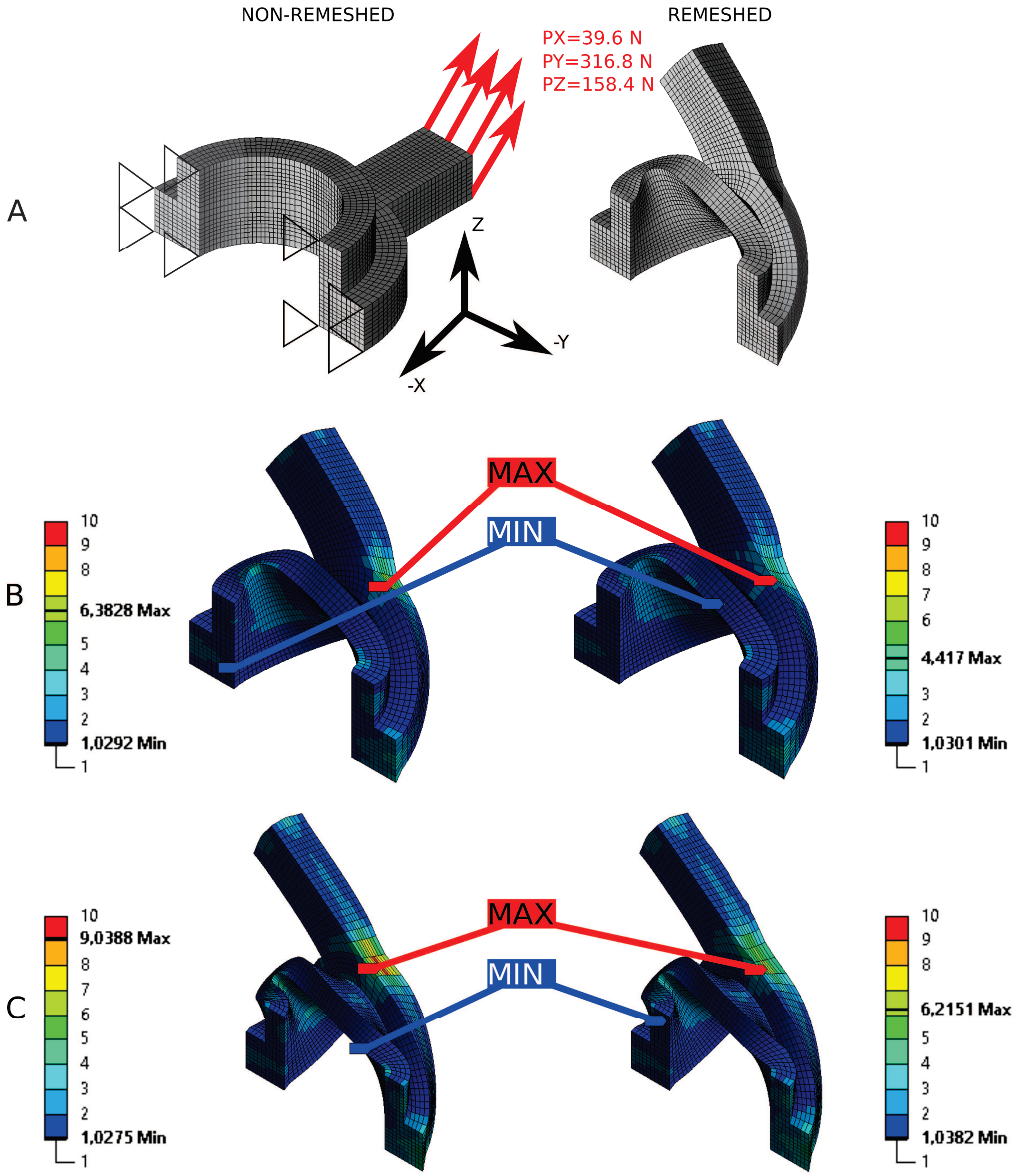

Figure 7.3: Element quality comparison under loading for the half-seal part. (A) The initial mesh at $t = 0$ with boundary conditions (left). The remeshed case at $t = 0.5$ (right). (B) Element shape ratio at $t = 0.5$ without remeshing process (left). Element shape ratio at $t = 0.5$ with remeshing process (right). (C) Element shape ratio at the last loading increment without remeshing process, $t = 1$ (left). Element shape ratio at the last loading increment with remeshing process, $t = 1$ (right). All deformed shapes are given with a scale factor of 1.

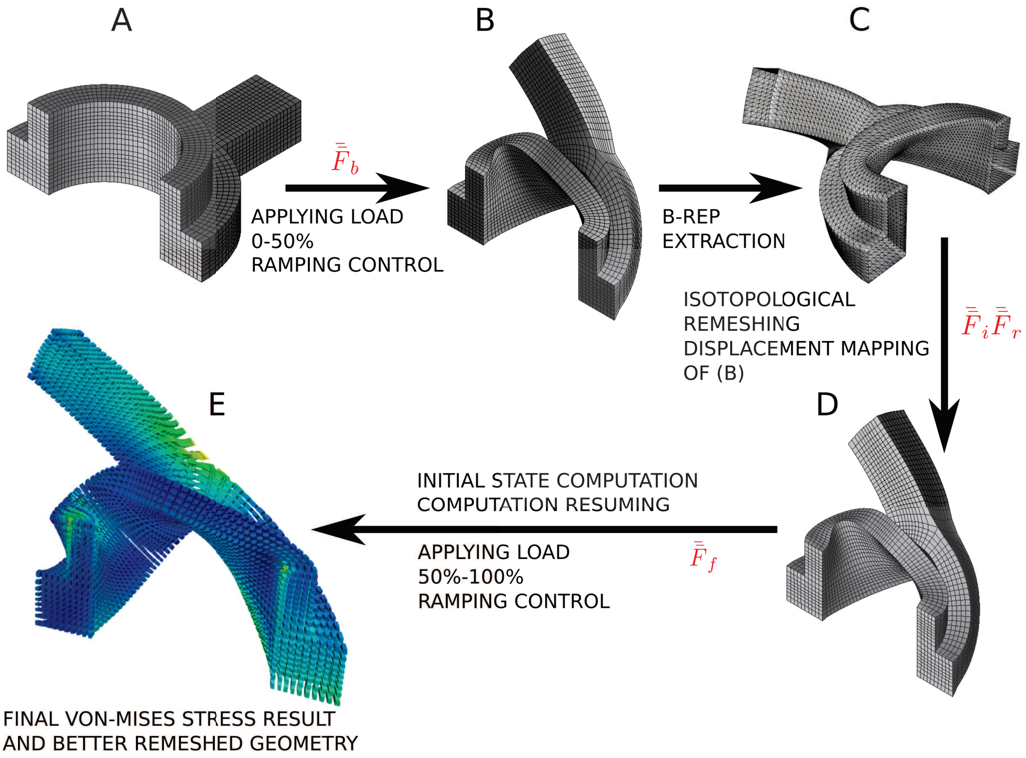

Figure 7.4: Remeshing method. (A) Initial mesh at $t = 0$. (B) Deformed unremeshed mesh at $t = 0.5$ calculated with a modified standard FEA code [Bower 2012]. (C) B-Rep extraction of the geometry (B) using ABAQUS and Rhinoceros 5. Please remark that the surface is homeomorphic to a pant with 3 specific boundaries. (D) Isotopological remeshing is done with our mapping method. The displacement solution obtained at step (B) is mapped back on the new remeshed geometry. (E) Final Von-Mises stress Paraview results at physical Gauss points. Initial state computation is based on the deformation gradient $\bar{\bar{F}}$. The modified FEA code is then used to resume the calculation.

the corresponding results for the unremeshed case (A) and remeshed case (B) at final time $t = 1$. For visualisation and comparison purposes, we build an associated linear hexahedral mesh which geometry is described by the Gauss points of the underlying FE mesh. We can see that for both cases the closest Gauss point near the corner have very similar Von-Mises stress values, in the same difference range as can be observed by comparing simulation results using commercial FE packages such as ANSYS and ABAQUS (see Figure 7.6) for the same example with the same mesh density. For instance, we correlate the Von-Mises values of the two unremeshed cases for the same physical Gauss point identificator in a high deformed zone. A value of 14.93 is found instead of 13.79 with our FEA code in the unremeshing process, which are slightly different of 8%. The remeshing process holds 15% of difference with the commercial simulation.

These results clearly show the efficient of our method to improve the mesh quality during a highly deformed hyperelastic simulation while preserving correctness of the finite element solution. In addition, for large deformations, remeshing avoid a very bad element geometry which can lead to a computation halt.

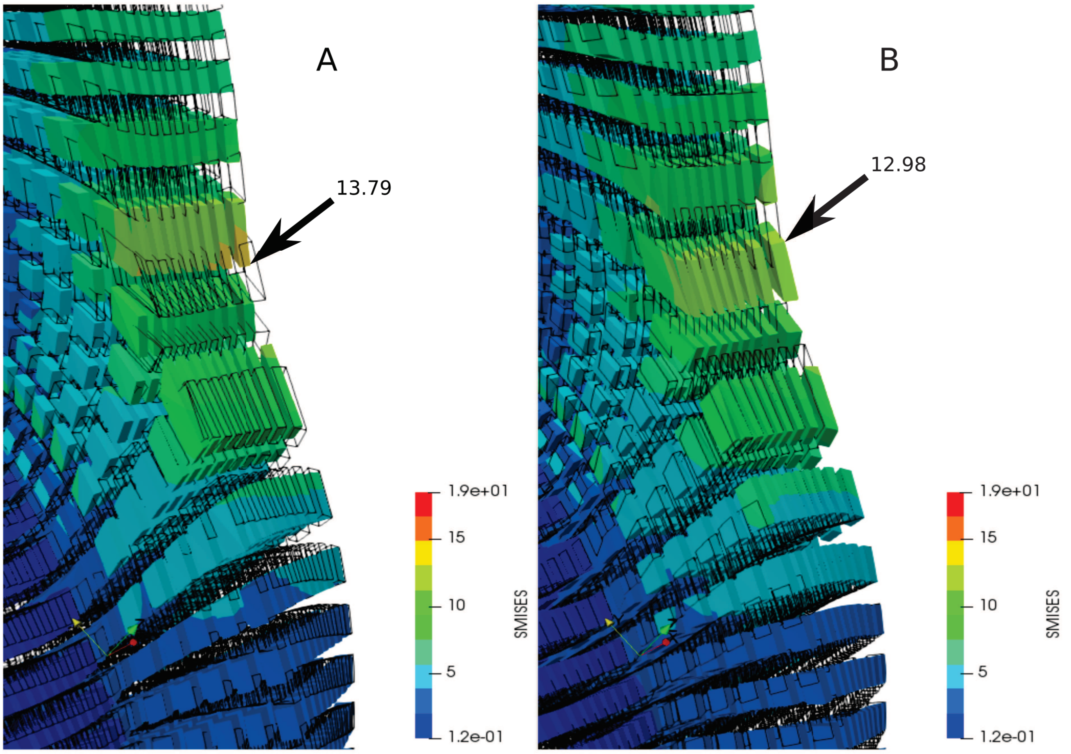

Figure 7.5: Details of Von-Mises stress comparison at Gauss points. For each hexahedral element, we build an associated linear hexahedral element which geometry is described by its related Gauss points. (A) Stress for the unremeshed case at $t = 1$. Elements made by Gauss points of the remeshed part are depicted in black wireframe. (B) Stress for the remeshed case at $t = 1$. Elements made by Gauss points of the unremeshed part are depicted in black wireframe.

7.2 Trivariate B-Spline reduced order models

In this section we deal with reduced order models whose snapshots are computed using isogeometric analysis [Hughes, Cottrell, and Bazilevs 2005; Cottrell, Hughes, and Bazilevs 2009; Al Akhras et al. 2017; Lai et al. 2017]. Only linear elastic problems are considered. Reduced order models based on an a posteriori approach are built from standard algorithms. Demonstrations on models solutions evaluation in near real-time will be given. The method explicited in Chapter 1 will be used for volumetric B-Spline models generation.

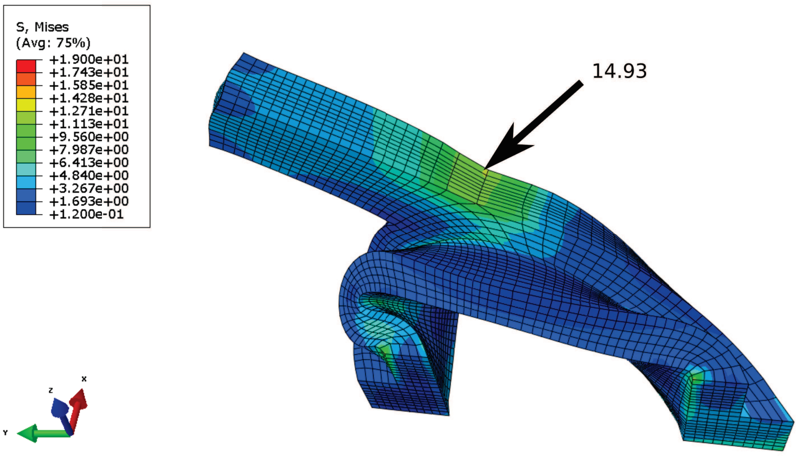

Figure 7.6: ABAQUS Von-Mises stress results on the unremeshed half-seal part. Notice that values are averaged on hexahedral elements nodes and the color scale is interpolated at scalar values embedded on these nodes. The Von-Mises value of 14.93 is not averaged and resides at a physical Gauss point.

7.2.1 Pipeline introduction

7.2.1.1 Algorithms

Triangulated B-Rep CAD to reduced order model evaluation algorithm is entirely incorporated into a Rhinoceros 5 [McNeel 2017b] Plug-In implemented in VB.NET. C++ processes are called from the Plug-In. For more details, we refer the readers to Appendix B. Some prerequisites are mandatory, such as a consistent pants-to-cuboids decomposition, as developed in Chapter 3. Cuboid decomposition templates per pant have to be correctly handled for special complex geometry cases. We use for that purpose the ROM builder proprietary software developed by ANSYS. This ROM solution works using classical SVD algorithms. Response surfaces reconstruction are made with kriging tools. Figure 7.7 gives the standard principle of operation. Related research done by ANSYS employees exists [Hraiech 2010; Galland 2011; Galland et al. 2011; Grassi et al. 2014]. For other purposes under dynamic loads, the problem is currently tackled in the ANSYS research team. Recently, this builder has been used to prevent excessive compression of buttock's soft tissues by bony structures [Luboz et al. 2018] in real-time for paraplegic persons.

7.2.1.2 Workflow reminder

Using our technique of pants-to-cuboid decomposition understanding features of input triangulated meshes, a cuboid configuration $\mathbb{C}_c$ template is associated to each pant composing the B-Rep surface geometry as presented in Chapter 3. Aligned global parameterization (see developments in Chapter 4) is computed and boundary

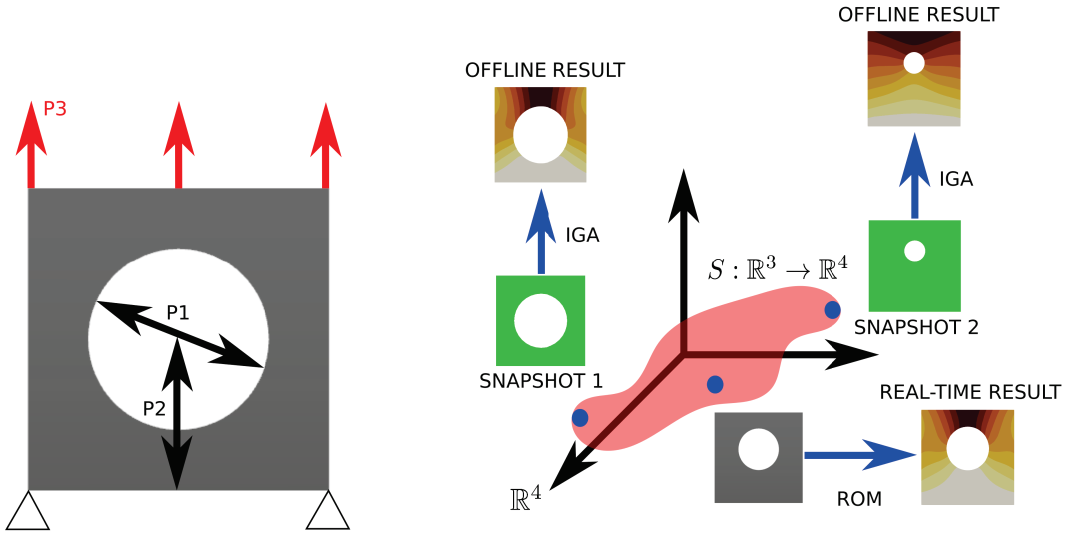

Figure 7.7: Reduced order model building and evaluation for a plate with one hole. Snapshots are calculated using isogeometric analysis. $P1$ and $P2$ are geometrical parameters defining respectively the diameter and the position of the hole along his height. $P3$ is a loading parameter. Response surfaces S are embedded in 4-dimensional space. There are as many surfaces as there are modes in the reduced basis.

B-Spline surfaces are fitted. We then extract an isotopological homologous volumetric parameterization of our input geometries due to the properties of $V_{\mathbb{C}}$ as formulated in Chapter 6.

7.2.2 Snapshots sampling

Sampling of geometrical parameters is done with a sparse grid technique, the same used before for quadrilateral meshes in Section 5.2 explicited in Figure 5.5. However, due to high-dimensional problems that we are going to deal with, a larger amount of relevant snapshots are required. We want to tackle here reduced basis constructed with both geometrical and mechanical parameters. We sample as follows: for each isotopological geometry, for each loading parameters and then for each mechanical properties, a snapshot is produced and resolved using IGA. This process is depicted in Figure 7.8. Range of parameters and sampling along parameters's axis refer to the sparse grid technique with the existence of a hypercenter of the n-dimensional space. Hypercenter is naturally the set composed by averaged values of parameters. We design a α-*member* of the geometrical population as being the isotopological snapshot of averaged values of geometrical parameters (see Section 5.1 and Section 6.3 for the α-*member* definition or properties). Equation (7.4) is showing the distribution of parameters. G refers to the number of different isotopological geometries, P to the number of loading cases and M is the number of material cases. Sampling is resulting in a tensorial form between 3 different quantities. This strategy yields a designing of N_s snapshots. First refinement of the level 1 sparse grid is then adopted for the following. Each snapshot is a vector in the $\mathbb{R}^{6n}$ space due to the displacement vectors supplementary information.

$$\dim\left(G \otimes P \otimes M\right) = \dim\left(G\right) \times \dim\left(P\right) \times \dim\left(M\right) = N_s. \tag{7.4}$$

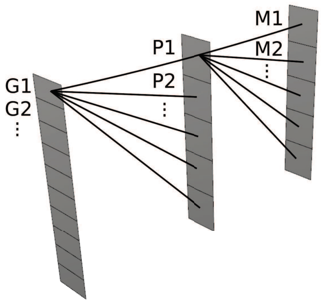

Figure 7.8: Parameters tensorial product. For each geometrical cases G, we associate all loading cases P. Each loading parameter is then combined with all mechanical cases M. This method resulting in $\dim\left(G\right) \times \dim\left(P\right) \times \dim\left(M\right)$ snapshots.

7.2.3 Pant part

Parameterization is performed with useful tools previously presented. Pant parameterization of a genus-0 surface with 3 boundaries is given as a key example for reduced order modeling with geometric parameters. Firstable, a cuboid configuration is choosen to suit the initial geometry, i.e., to fit as well as possible the sharp features of the B-Rep geometry. After few steps, an isogeometric volume with appropriate sharp features is created. The process is shown in Figure 7.9.

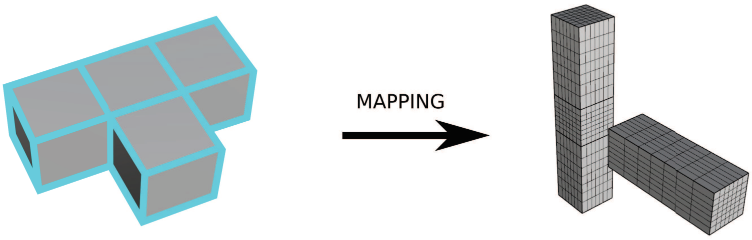

Figure 7.9: Volumetric isogeometric parameterization of the pant part. It is a genus-0 geometry with sharp features. Euler characteristic is $\chi = -1$ for the associated mesh M with 3 boundaries. We apply the same parameterization among all members of the population to obtain isotopological comparable isogeometric meshes.

Snapshots sampling is done involving 9 geometrical parameters G and 1 loading parameter P. Blue basis define the parameters G based on the hypercenter of the sparse grid constructed with only geometrical parameters. Loadings have been settled along the $Y+$ axis. Figure 7.10 (A) and (C) explain the distribution of parameters whereas (B) present the cuboid decomposition of the 37 different geometries. 222 isogeometric simulations were computed. Reduced order model is built and evaluations are determined in near real-time, e.g. Figure 7.11 is estimated with a random set of parameters.

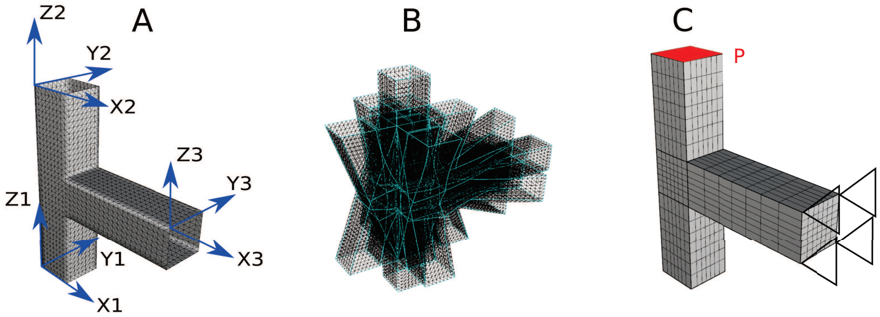

Figure 7.10: Pant part distribution of parameters and snapshots. (A) 9 geometrical parameters are settled. Geometrical parameters are defined into blue local basis. (B) Snapshots cuboid decomposition population. (C) 1 load parameter P is applied on the isogeometric model. We use a constant Young's modulus $E = 210$ GPa and Poisson's ratio $\nu = 0.3$. Loads and boundary conditions are distributed on concerned nodes.

Pant part range	Min	Max
X1 boundary 1	-40	40
Y1 boundary 1	-40	40
Z1 boundary 1	-35	35
X2 boundary 2	-40	40
Y2 boundary 2	-40	40
Z2 boundary 2	-35	35
X3 boundary 3	-40	40
Y3 boundary 3	-40	40
Z3 boundary 3	-35	35
Load intensity	50 N	300 N

Table 7.1: Range of parameters used for the pant part reduced order model.

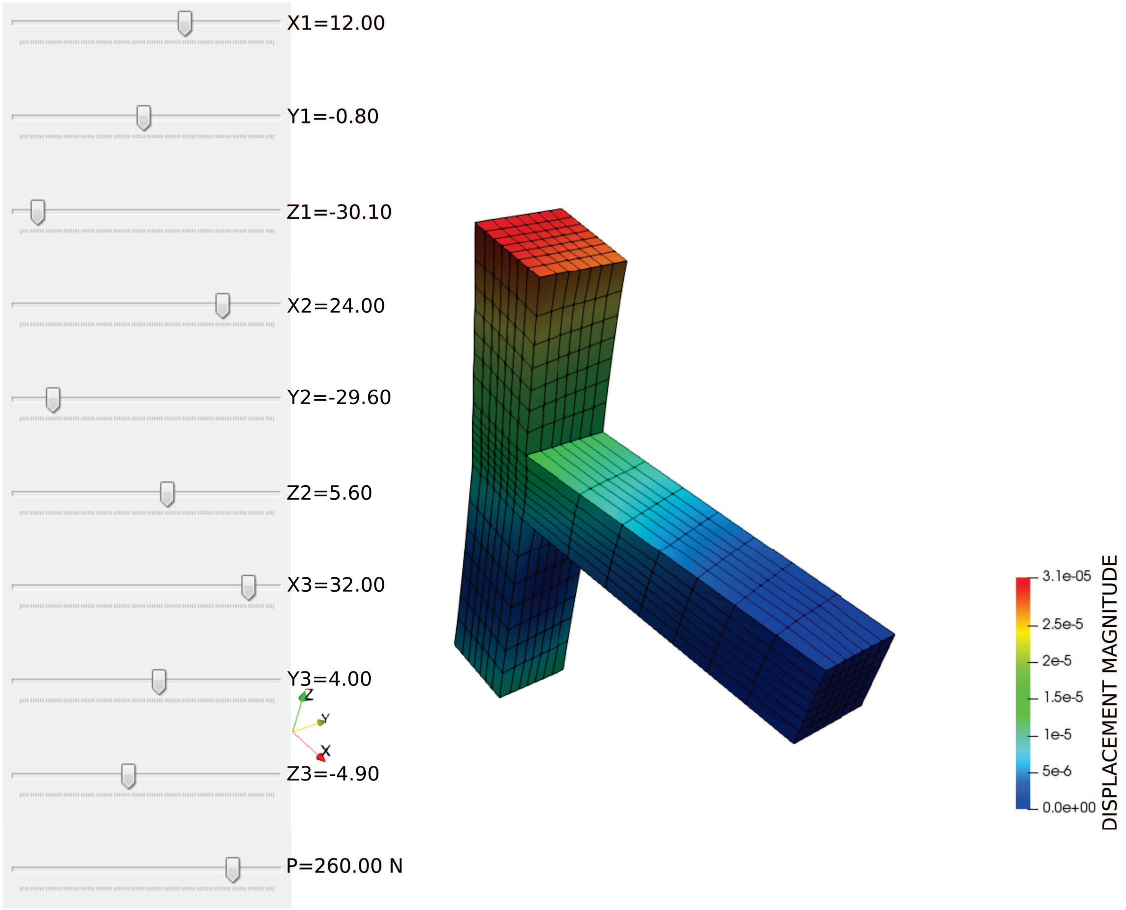

X1=12.00

Y1=-0.80

Z1=-30.10

X2=24.00

Y2=-29.60

Z2=5.60

X3=32.00

Y3=4.00

Z3=-4.90

P=260.00 N

Figure 7.11: Pant reduced order model real-time evaluation. A 10-dimensional manifold built by kriging tools is evaluated to find preponderant coefficients attached to the first 60 modes. Isogeometric elements are sampled with one hexahedron per element for viewing purposes in Paraview. Used range of parameters is detailed in Table 7.1.

7.2.4 Seal part

Seal part has a more complex topology and geometry than the pant. It is a genus-1 surface due to its 1-torus topology. By choosing a specific pant decomposition and analyzing symmetry properties, a reliable volumetric parameterization is extracted (see Figure 7.12).

This example holds 6 geometrical parameters G, 1 loading parameter P and 1 mechanical parameter M. Loadings have been settled along the $X+$ axis. Figure 7.13 presents parameters attributes. 400 snapshots were simulated. Evaluation of the constructed reduced order model is done in Figure 7.14.

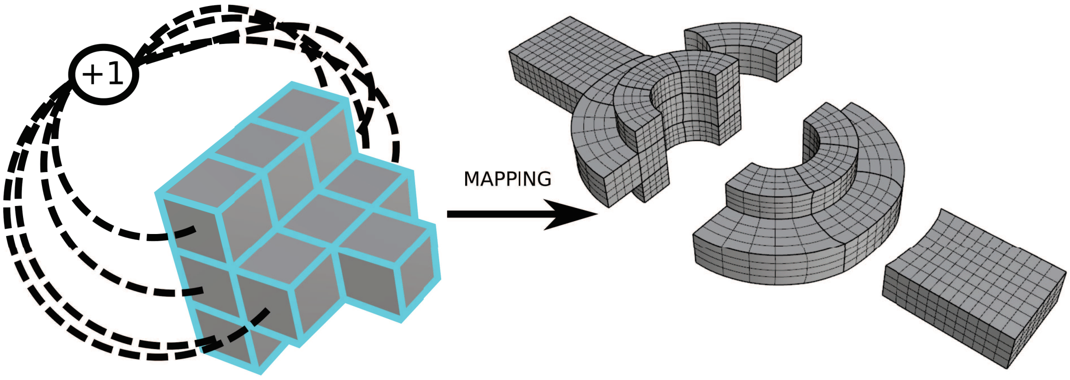

Figure 7.12: Volumetric isogeometric parameterization of the seal part. It is a genus-1 geometry with sharp features. Euler characteristic is $\chi = 0$ for the associated closed mesh M_c. We apply the same parameterization among all members of the population to obtain isotopological comparable isogeometric meshes.

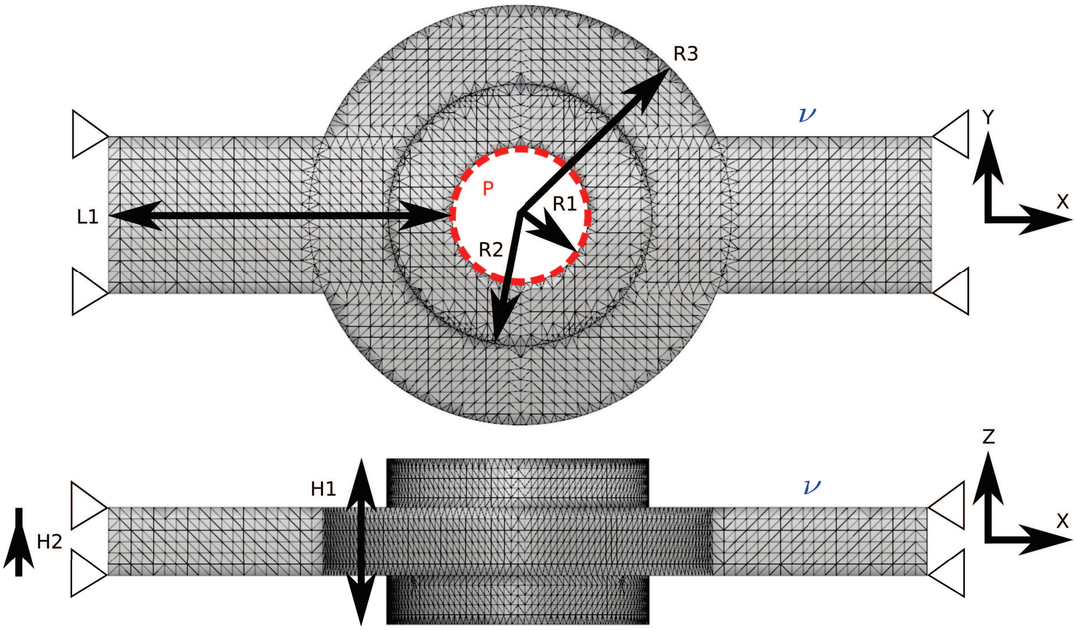

Figure 7.13: Seal part distribution of parameters. 6 geometrical parameters are settled. 1 load parameter P is applied and Poisson's ratio ν is devoted to be a mechanical parameter. We use a constant Young's modulus $E = 210$ GPa. Loads and boundary conditions are distributed on concerned nodes.

7.2.5 Wheel part: large geometrical reduced order model

Targeting the same worflow as for the seal part but with a higher complexity, the parameterization of the wheel part is illustrated in Figure 7.15. Genus-3 wheel is

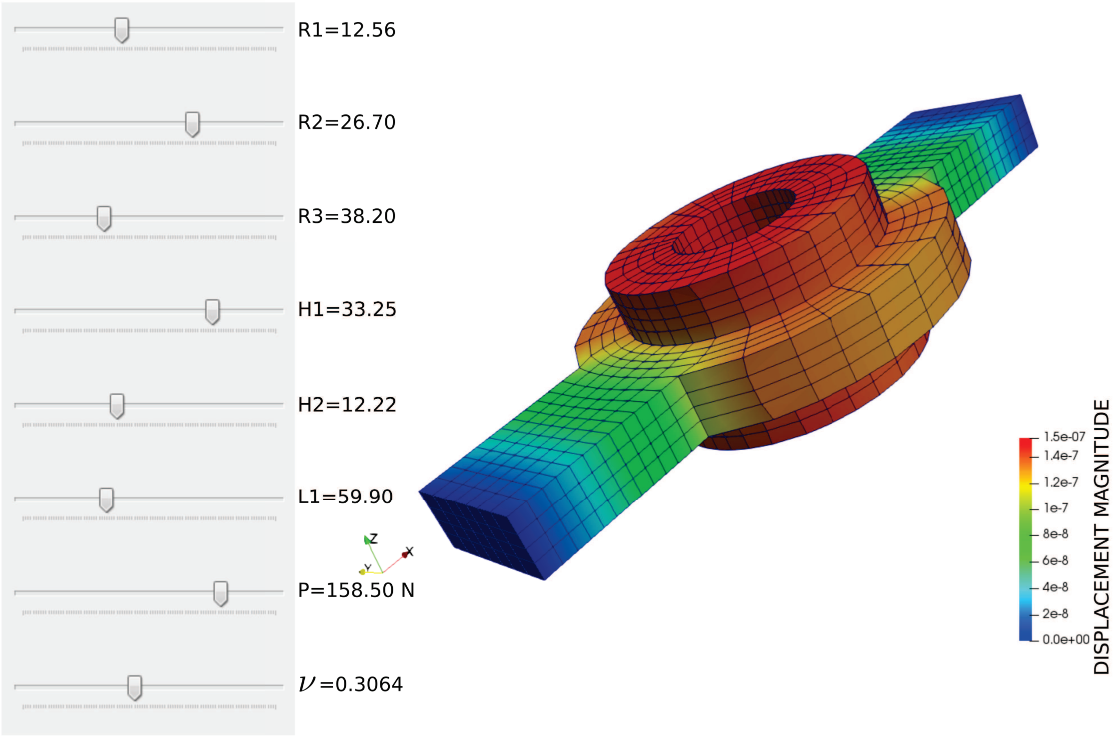

Figure 7.14: Seal reduced order model real-time evaluation. A 9-dimensional manifold built by kriging tools is evaluated to find preponderant coefficients attached to the first 50 modes. Isogeometric elements are sampled with one hexahedron per element for viewing purposes in Paraview. Used range of parameters is detailed in Table 7.2.

Seal part range	Min	Max
Radius 1	11	15
Radius 2	20	30
Radius 3	35	45
Height 1	28	35
Height 2	10	16
Length 1	50	80
Load intensity	100 N	175 N
Poisson's ratio	0.28	0.34

Table 7.2: Range of parameters used for the seal part reduced order model.

considerably more complex than others examples. On the one hand, the geometry and topology are fundamentally different and refer, for instance, to much more pants-to-cuboid decomposition possibilities. Indeed, parameterization workflow imply a computation time which is increased when treating these larger geometries. On the other hand, 9 geometrical parameters coupled with 2 naturally different parameters represent a large amount of snapshots of 592. It takes a real effort during offline simulations. Figure 7.16 informs on parameters assignation. Loadings have been settled along the $Z+$ axis. Evaluation in near real-time is done in Figure 7.17.

Wheel part range	Min	Max
Radius 1	7.8	9.75
Radius 2	13.65	16.25
Radius 3	25.35	29.9
Radius 4	62.725	67.275
Radius 5	73.775	80.275
Radius 6	86.625	91.975
Height 1	26	32.5
Height 2	8.125	9.75
Length 1	39	43.875
Load intensity	100 N	175 N
Young's modulus	200 GPa	230 GPa

Table 7.3: Range of parameters used for the wheel part reduced order model.

7.2.6 Results discussion

Snapshot production is done by considering a standard B-Rep CAD as input. Depending on the triangle discretization of the CAD geometry, our segmentation algorithms such as the pants-to-cuboids decomposition take more or less computing time. We mean in particular that the algorithmic complexity is high during specific steps. For instance, the number of pants decomposition possibilities to be tested increase in a factorial way with the Euler characteristic as demonstrated in Section 3.1. Cuboid decomposition is mainly based on a harmonic parameterization of a triangulated domain. SuperLU [Demmel et al. 1999] is used to solve these sparse linear systems. In addition, for solving other sparse linear systems for direction field generation and surface parameterization, CHOLMOD [Chen et al. 2008] and CoMISo [Bommes, Zimmer, and Kobbelt 2010]. Notice that it is a non-exhaustive list of used solvers. To summarize, due to large various solvers needed to support our workflow, minutes are required to obtain a surface parameterization to be transformed into a volumetric isogeometric one, helped with the volumetric layout $V_{\mathbb{C}}$. Technically speaking, for the genus-3 wheel part, 4 minutes are necessary to obtain a surface quadrilateral mesh snapshot.

ROM evaluations were done in near real-time, i.e., few seconds for above presented examples. It takes around 2 seconds for the pant part and a few more seconds

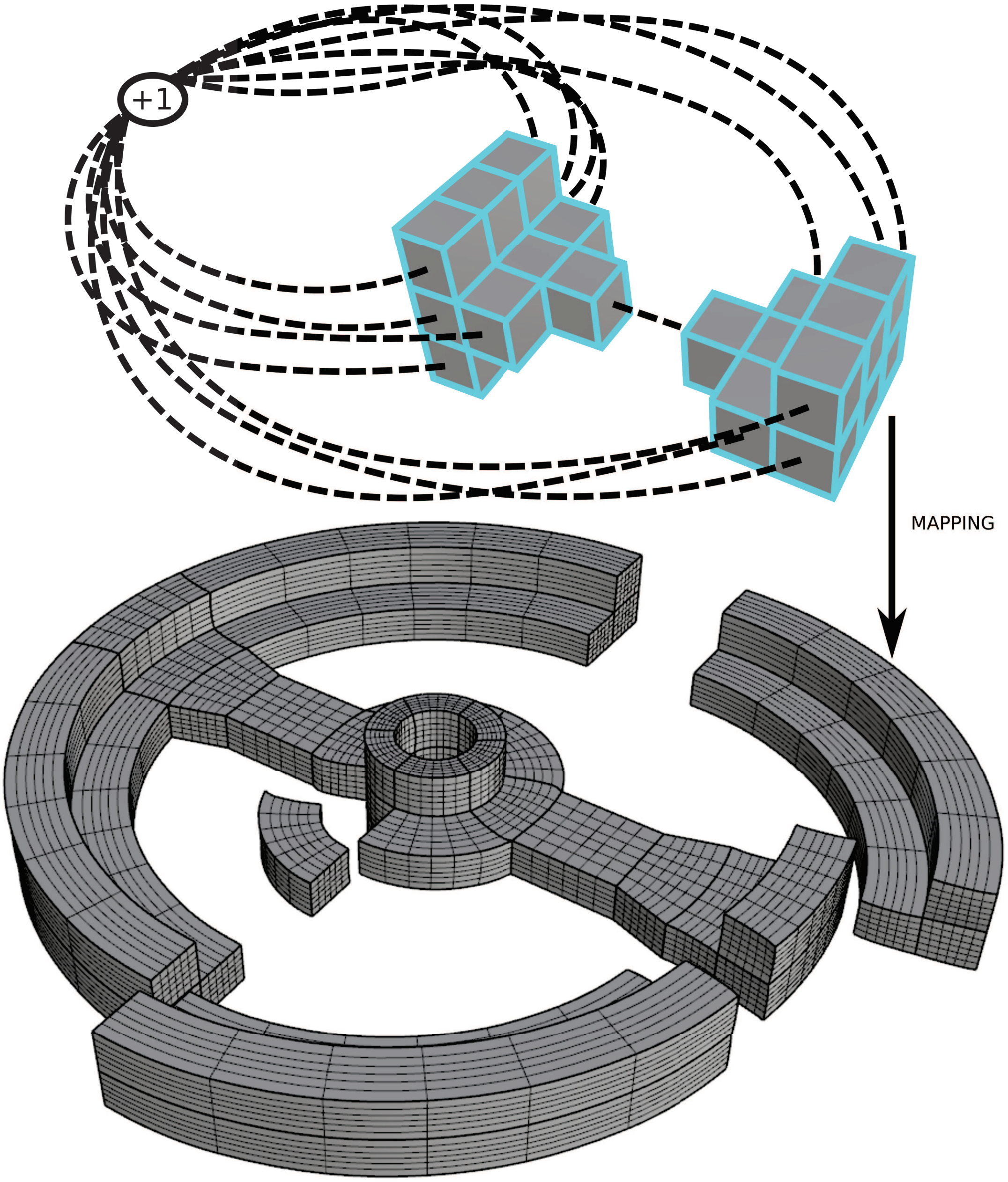

Figure 7.15: Volumetric isogeometric parameterization of the wheel part. It is a complex genus-3 geometry with sharp features. Euler characteristic is equal to $\chi = -4$, involving a decomposition in 4 pants. We apply the same parameterization among all members of the population to obtain isotopological comparable isogeometric meshes.

for the wheel part example with 11 parameters. Indeed, the wheel part holds 9 geometrical parameters and 2 mechanical ones, thus the response surfaces are embedded

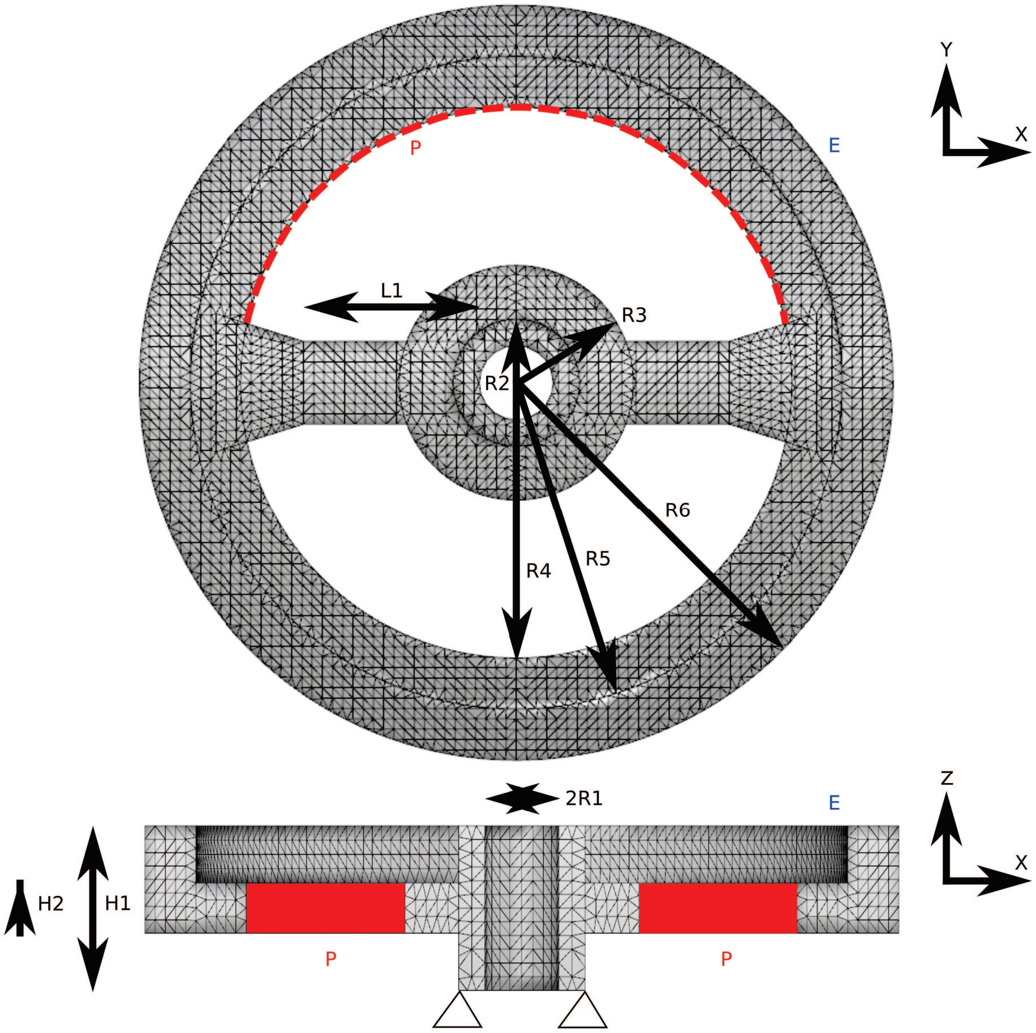

Figure 7.16: Wheel part distribution of parameters. 9 geometrical parameters are settled. 1 load parameter P is applied and Young's modulus E is devoted to be a mechanical parameter. We use a constant Poisson's ratio $\nu = 0.3$. Loads and boundary conditions are distributed on concerned nodes.

in a higher dimensional space than other examples. In addition, more complex the geometry is, more the solution vectors are lengthy. Reduced basis are composed by the first 50 modes for the seal and wheel part respectively, leading to 50 coefficients to be determined.

Fortunately, isotopological meshes are efficient in terms of point per point comparison because they are synonymous of structured data. Intermediate computation such as mesh interpolation, or hazardous structured morphing is unnecessary. Accuracy of evaluations, including geometry and mechanical fields is greatly improved thanks to homologous meshes.

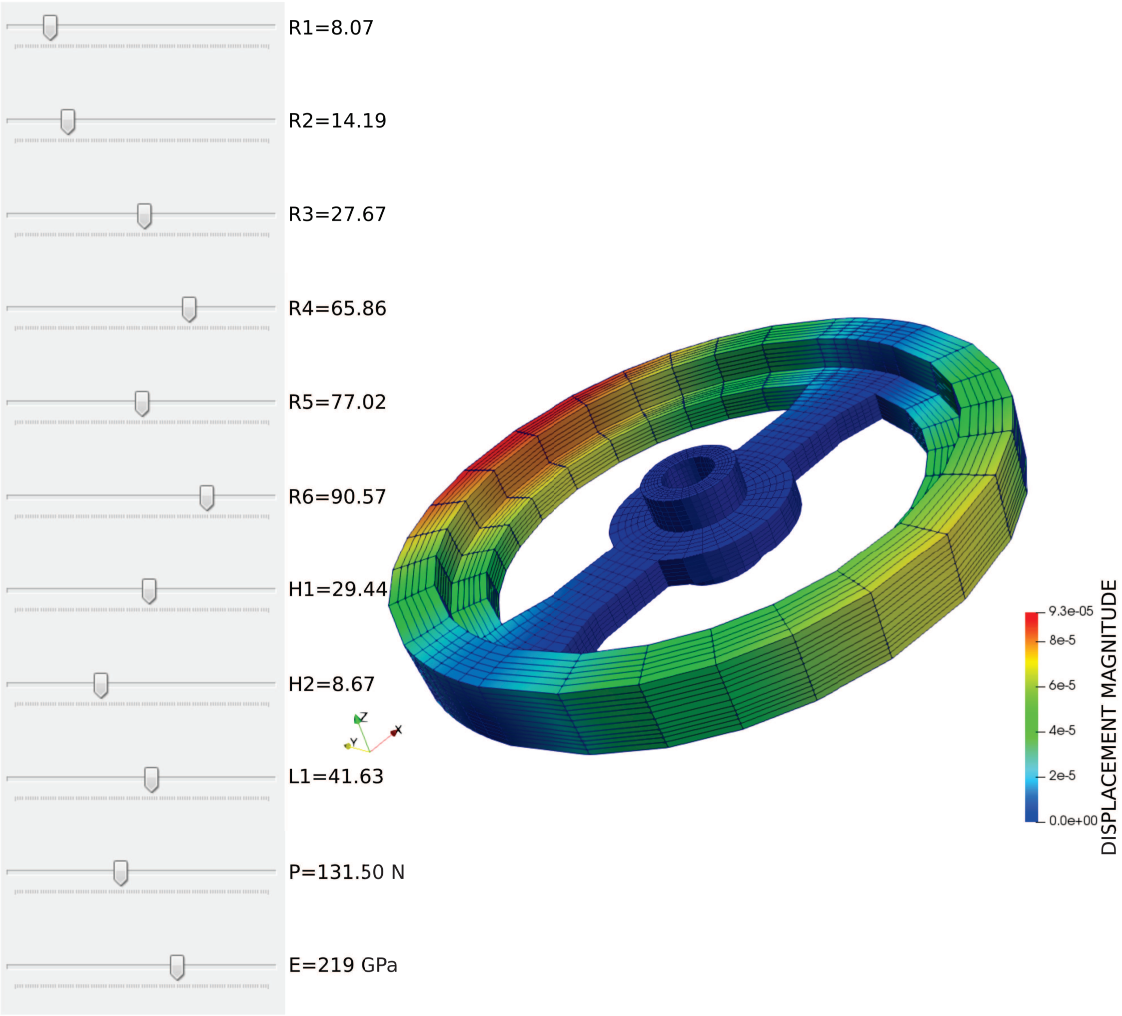

Figure 7.17: Wheel reduced order model real-time evaluation. A 11-dimensional manifold built by kriging tools is evaluated to find preponderant coefficients attached to the first 50 modes. Isogeometric elements are sampled with one hexahedron per element for viewing purposes in Paraview. Used range of parameters is detailed in Table 7.3.

7.3 Conclusion

Thanks to isotopological meshes, we have introduced many geometrical parameters into the learning process of mechanical reduced order modeling. Results are shown for geometrical virtual charts that can be used for shape optimization or an industrial sizing purpose. Comparing mechanical fields efficiently is done by adressing the same parameterization for different geometrical instances. We constrain the parameterization among all meshes composing the population to be reduced. Projection steps are thus avoided. In fact, avoiding a projection step with structured information and setting homologous parameterizations yield to accurate reduced order models. In addition for accuracy, homologous concepts allow to compare information at the same location, i.e., in a the same relevant geometry zone for all geometrical instances. Moreover, introducing geometrical parameters enables shape optimization that is useful nowadays in a part weight reduction objective. Multidimensional models are more and more encountered and today's physicists have to deal with. We gave answers to sample large parameter spaces formed by many geometrical designing parameters. Presented near real-time evaluations demonstrate the robustness and the reliability of the developed method.

Conclusions

We have presented in this thesis a volumetric isotopological mesh generation method from B-Rep CAD. The input is a standard model with a triangulated geometry. For most of them, CAD softwares are not able to represent real mathematical volumes. We give answers to a widely studied problematic. By using surface segmentation approaches, a cuboid decomposition splits the surface. Splitting is done with respect to the input surface topology and theorems related on embedded fields on surfaces. This segmentation serves to parameterize the entire B-Rep of the solid's boundary. Cuboid decomposition is then topologically analyzed in the way to construct a consistent volumetric layout. Understanding all mathematical properties and constraints among all steps of this process, a volumetric parameterization is extracted. The final goal is then fulfilled thanks to the B-Rep mapping and constructed relevant volumetric layout.

We have shown that our meshing strategy is well-suited for reduced order modeling with geometric parameters. Comparing mechanical fields efficiently is done by adressing the same parameterization to different geometrical instances. In fact, avoiding a projection step and setting homologous parameterizations yield to accurate reduced order models. Moreover, introducing geometrical parameters into a reduced order model enables shape optimization that is useful nowadays in a part weight reduction objective. A real benefit for the computational mechanics community has been deployed by defining a generic method to overcome the difficulty to generate isotopological meshes. Our method is introduced to solve the problem in a universal form. This helps us to define a set of 3D volumetric isotopological homologous meshes. Presented real-time evaluations demonstrate the robustness and the reliability of the developed method.

A first key contribution is done in the segmentation of the input surface provided by the CAD. We have drastically enhanced the pants decomposition process by giving more geometrical tools. Surface decomposition theory is an essential tool to fulfill our objectives. We strive to understand both geometry and topology during this step. A second improvement is to position the singularities in the best possible way. Gaussian curvature distribution is naturally defined to locate them if curvature is sampled in a few vertices on the mesh. In fact, the cuboid decomposition is not anymore chosen just involving topology criteria but with coupled topological and geometrical ones.

After performing the proposed smart segmentation approaches, the next step toward a volumetric parameterization is the surface parameterization. We parameterize the B-Rep triangulated mesh using well-known global parameterization techniques [Campen and Kobbelt 2014]. Aligned global parameterization adapts the mapping by fitting its gradient to a smooth cross field. Computing a global parameterization is reduced to defining a suitable topological and geometrical cross field interpolating relevant features. That is why it is crucial to understand such fields behavior on surfaces. Into a third enhancement, programming work has been done to couple these algorithms with our developments for futher reduced order modeling needs. In fact, automatic meshing process are appreciated for reduced order modeling applications related to different geometries.

Chapter 6 is one of our biggest contribution for the computational mechanics community. We gave new mathematical tools to understand properties during surface to volume conversion. Such hard conversion problematic continues to find a certain interest in geometry processing and physics communities. We have shown that controlling topological properties during the conversion process is fundamental. Indeed, topology and mathematical features of manifolds have to be considered at the highest level. Invariant information transmitted from the surface to the volume is essential to build volumetric meshes needed by our method.

The efficiency and the robustness of the proposed approach are illustrated by several examples coming from the mechanical and medical domains. Applications involving statistical shape analysis techniques were given. Evaluations of reduced order models have demonstrated the ability of the method for geometric parametric analysis problems. For instance, the wheel reduced order model has 11 parameters which 9 are purely geometric ones. Smart sampling of snapshots coupled with our isotopological volumetric parameterization method yields to an accurate model reduction. Moreover, it has been successfully applied to B-Rep models with features and non-trivial geometry. We have given a robust and approved method to study geometrical differences of a population.

Limitations

Despite the abilities of our algorithms and tools presented in this thesis, treating any arbitrary and complex CAD geometry automatically is still a challenge. For complex cases with an arbitrary geometry, pants decomposition can be not consistent: [Zhang and Li 2014] has shown that topological pants decompositions are not always geometry-aware. Moreover, the pant topology is not always adapted to the geometry. Indeed, pants patches are topologically equivalent to 3-way pipes. But this is in general not suitable for the following cuboid decomposition. In fact, distorted pants lead to poor volumetric parameterization quality. Chapter 3 gives some alternatives using the n-pant topology. Specific user proposals incorporated into the automatic process can help.

Cuboid decomposition is dependent on a fixed border harmonic parameterization. For highly curved shapes or disproportionate geometries, numerical computation of square parametric domains is misfit. Free border or ARAP (As Rigid As Possible) mappings are a possible answer.

During the surface parameterization, the positioning of irregular nodes of the quadrilateral layout is crucial. Indeed, they lead the surface topology but also the link with features if hard constraints are settled. Thus, a suitable mapping solution is not always found due to sharp edges constraints or unadapted layouts. Nodes embedding optimization is limited in the way that moving regular nodes does not necessarily minimize the parameterization energy; but their location is essential. Spacement constraints or non-integer grid maps could solve partially these issues.

Generated cuboid decompositions are adapted to surface definition resulting in an arbitrary definition of the interior volume. In Chapter 6, we have given mathematical properties conserved during surface to volume conversion. Nevertheless, it has shown that there is a lack of topological information. It has been clearly shown that the interior volumetric parameterization has an infinite number of possiblities given an arbitrary surface as input.

To finish, we need a stronger link between geometry and topology. It has been shown a long time ago that the Gauss-Bonnet theorem is helpful. But triangulated surface to structured surface reconstruction remains a big current challenge.

Perspectives

To extend the presented work, we give several perspectives or possible improvements that can be studied to go further. Indeed, progresses have been made for modeling with geometric parameters by given methods in this thesis. But, aiming to go forward, some reflexions are detailed.

- We believe strongly in IGA. Current computational mechanics methods have to evolve. Due to the craze in this field, powerful IGA meshing solutions will be found in the next years, see e.g. [Coreform 2019; Geomiso 2019]. This momentum has several benefits. First, it allows to change used techniques which have decades and enables the construction of smart mathematical models to solve mechanics. Secondly, structured data extraction will be straightforward due to the intrinsic parameterization of these new methods. So, learning approaches are served.

- In order to build reduced order models for dedicated applications, we recommend today to start directly with parameterized solids if it is possible. Commercial softwares exist for feature-based modeling applications. We can use [McNeel 2017a] to script a modeling with geometrical parameters. More and more editors implement reverse engineering techniques. SpaceClaim and solidThinking are some of growing tools for industrial uses.

- To obtain more topological information for volumetric parameterization involving presented methods in this thesis, starting with a tetrahedral mesh instead of triangulated one will be a possibility. Nowadays mesh generation algorithms are robust enough so as to generate a volumetric unstructured tetrahedral mesh from a B-Rep CAD. In fact, used cuboid decomposition and surface parameterization techniques do not give a definition of the interior volume. Thus, the volumetric parameterization is far to being unique for a given surface and cuboid decomposition. Recent trends are to compute octahedral fields, i.e., fields embedded in volumes [Ray and Sokolov 2015; Sokolov et al. 2016; Solomon, Vaxman, and Bommes 2017; Liu et al. 2018]. Notice that recent automatic techniques for polycube decomposition exist [Fang et al. 2016].

- In a reduced order model designing goal for large variations of parameters or complicated geometry, immersed methods are attractive. They can conserve a specific mesh structure between different geometrical instances, see e.g. [Courard 2016]. Immersogeometric applications exist [Kamensky et al. 2017].

Appendix A

Mathematical notations and algebraic operators

We describe, in this appendix, the main used notations in the manuscript together with algebraic operators.

Contents

A.1 General notations and operators

Main used notations are summarized in Table A.1. Following conventions are generally respected for notations and algebraic operators:

- The scalar values are written with normal typology or in capital letters. (a, b, A, B,).
- Vectors are written in bold or in calligraphy mode for capital letters. ($\mathbf{a}$, $\mathbf{b}$, $\mathcal{A}$, $\mathcal{B}$).
- Matrices are written in bold and capital letters. ($\mathbf{A}$, $\mathbf{B}$).
- Second order tensors for mechanical purposes are written in capital letters with double bars. ($\bar{\bar{A}}$, $\bar{\bar{B}}$).
- Parameters spaces, topological spaces, layouts and configurations are written in doubled capital letters. ($\mathbb{A}$, $\mathbb{B}$).
- Matrix product between two second order tensors is denoted without any operator: $\bar{\bar{A}} = \bar{\bar{B}}\bar{\bar{C}}$.
- Tensorial product is classically denoted: $\otimes$.
- Scalar product is classically denoted with a point: ., it is also denominated dot product.
- Vector product is classically denoted: $\times$.

Global symbol	General description	Example	Description
a	Scalar	p	First B-Spline degree
A	Scalar	K	Gaussian curvature
$\mathbf{a}$	Vector	$\mathbf{d}$	Vector or direction field
$\mathcal{A}$	Vector	$\mathcal{U}$	Knot vector u
$\mathbf{A}$	Matrix	$\mathbf{U}$	Snapshot matrix
$\bar{\bar{A}}$	Second order tensor	$\bar{\bar{F}}$	Deformation gradient
$\mathbb{A}$	Topological information	$\mathbb{R}^3$	3D topological space

Table A.1: Main used notations.

A.2 Non-exhaustive lists of used notations

Reserved letters and notations are described in Tables A.2 and A.3. Some of notations can refer to multiple notions in other chapters. Multiple notations can describe same notions in different contexts.

Letter	Description	Letter	Description
M_d	Disk-like mesh	t_{ij}	Integer translations
m_{ij}	Matching rotation	A_f	Area of face f
G	Cut graph	G	Graph or tree graph
Ω	Domain	α	Direction angle
f_i	Face i	${}^{p}\kappa_{\mathcal{C}}$	Field curvature p
${}^{c}\kappa_{\mathcal{C}}$	Field curvature c	k_1	Principal curvature dir. 1
k_2	Principal curvature dir. 2	T_γ	Turning number along γ
n_a	Number of arcs	n_n	Number of nodes
δ_γ	Holonomy along γ	γ	Cycle
γ_c	Closest homotopic cycle	s_i	Signs
n_t	Total number of triangles	k_i	Discrete angles
kg	Geodesic curvature	$l(s)$	Loop
K	Gaussian curvature	v	Vertex
G_i	Gravity center of f_i	$\mathcal{V}_e$	End vector
$E(\mathcal{C})$	Cross field energy	κ_{ij}	Angle difference
s_{ij}	Seed point ij	D	Set of boundary points
O	Set of common points	C	Set of cutting points
U_k	Square map k	B_i	Boundary i
W_{S1}	Sharp cutting curve $S1$	P_{Tk}	Temporary patch k
f_i	Harmonic function i	C_T	Time complexity
p_i	Point i	w_{ij}	Cycle for pants ij
w_i	Cycle for pants i	w_j	Cycle for pants j
S	Sharp points	T_i	Pant patch i
N_c	Set of combinations	W	Set of boundaries
h_i	Handle loop i	w_{ij}	Parameterization weights
δ_{ij}	Angle for weights	γ_{ij}	Angle for weights
$T_{\mathbf{d}}$	Turning number of $\mathbf{d}$	n_t	Total number of vertices
K_v	Vertex Gaussian curvature	R_{v_1}	Ring 1 of vertex v
b_i	Boundary i	$H^1(M)$	First homology group
$\pi_1(M,x)$	First homotopy group	γ_i^H	Cycle in $H^1(M)$
$\mathbb{I}$	Bounded space	$\mathbb{O}$	Unbounded space
$\mathbf{C}(\xi)$	B-Spline curve	$\mathbf{S}(\xi,\eta)$	B-Spline surface
$\mathbf{V}(\xi,\eta,\zeta)$	B-Spline volume	$\mathbf{B}_i$	Control point i
$N_{i,p}(\xi)$	First B-Spline basis	Ξ	First knot vector

Table A.2: Table 1 of reserved letters.

Letter	Description	Letter	Description
S	Surface	D	2-manifold disk
M	Set of mechanical param.	M	Mesh
M	n-dimensional manifold	I	Index of singularity
N_s	Number of snapshots	Q_h	$\frac{3\pi}{2}$ Gaussian quality criterion
$\mathbf{C}^3$	3-manifold cylinder	$\mathbb{Q}$	Quadrilateral layout
$\mathbb{C}$	Cuboid configuration	$\mathbb{C}_c$	Closed cuboid configuration
χ	Euler characteristic	$V_{\mathbb{C}}$	Volumetric layout of $\mathbb{C}_c$
n_s	Number of singularities	n_i	Interior singularities num.
$\mathbf{d}$	Vector or n-direction field	n_b	Boundary singularities num.
$\mathbf{H}^n$	Cohomology groups	k_i	CW-complex entities
b_i	Betti numbers	$\mathbf{S}^3$	3-manifold sphere
$\mathbf{B}^3$	3-manifold disk	v_i	Vertices valencies
v_i	Vertices or vertex i	v_i^m	Interior vertices
v_i^b	Boundary vertices	g	Genus of a 2-manifold
b	Number of boundaries	M_c	Closed mesh
$n_{\mathbb{Q}}$	Number of nodes of $\mathbb{Q}$	$\gamma_{\mathbb{Q}}$	Cycle of $\mathbb{Q}$
$U_{V_{\mathbb{C}}}$	Set of non-isomorphic $V_{\mathbb{C}}$	n_V	Nodes of the vol. layout V
$\partial V_{\mathbb{C}}$	Boundaries of $V_{\mathbb{C}}$	∂M	Boundaries of the M manifold
$\mathbf{B}^n$	n-manifold disk	$\mathbf{S}^n$	n-manifold sphere
$\dim(M)$	Dimension of M	$\|M\|$	Num. of components of M - 1
$\varepsilon_j(R_i)$	Strain of edge j at R_i	M_d	Disk-like mesh
s	Index of singularity	M^*	Dual mesh
V^*	Set of dual vertices	E^*	Set of dual edges
e^*	Dual edge	E	Set of edges
V	Set of vertices	$\mathcal{C}$	Cross field
$\mathcal{U}_c$	First direction of $\mathcal{C}$	$\mathcal{V}_c$	Second direction of $\mathcal{C}$
p	Period jump	w_{ij}	Connection angle
p	First B-Spline degree	q	Second B-Spline degree
r	Third B-Spline degree	∇u	Parametric gradient u
$\mathcal{H}$	Second knot vector	$\mathcal{Z}$	Third knot vector
G_1	Geometry 1	$\mathbf{U}$	Snapshot matrix
$\mathbb{B}$	Subspace	P	Set of parameters
α_k^j	SVD coefficient	$\mathbf{\Psi}_k$	Mode k
σ_k	Singular value k	$\mathbf{\Phi}$	Right sing. matrix

Table A.3: Table 2 of reserved letters.

Appendix B

IGA_ROM PlugIn

IGA_ROM PlugIn presentation and associated algorithms.

Contents

B.1 IGA_ROM PlugIn flowchart

B.1.1 PlugIn context and simplified flowchart

In order to manipulate various types of geometrical objects and also for visualization purposes a relevant software has to be chosen. Our choice was therefore focused on Rhinoceros 5. Indeed, we want an integrated environment where NURBS, B-Splines and meshes can already been represented. Moreover, additional requirements are the availability of scripting and debugging into an existing operating system. Rhinoceros 5 has these needed skills. PlugIns can be developed in VB.NET or C#.

Secondly, for ROMs computations, automatic workflows are mandatory. Handling large amounts of snapshots requires communication between entities and external softwares. User interactions and inputs have to be drastically reduced to the minimum. That is why, significant time was spent in this thesis to integrate automatic processes. The quantity of provided programming work is explained in Figure B.1. Remark that for ROMs computations using IGA, reduced order models can not be directly computed through the PlugIn. Thus, dedicated applications have to be constructed using programmed objects and classes.

In Figure B.1, code metrics such as number of lines were estimated in debug mode, i.e., by counting useful lines of code into the VB.NET text editor. The cyclomatic complexity is usually given to state about a program complexity. In other words, it is created by calculating the number of different code paths in the flow of the program. A program that has a complex flow will requires more tests to achieve good code coverage. VB.NET and C++ objects are formulated respecting the programming standards as well as possible into a research context.

B.1.1.1 IGA_ROM.dll

IGA_ROM.dll is the PlugIn library containing new commands which can be operated directly in Rhinoceros. This library provides modules, functions and graphics related to the previous commands. Moreover, some of demonstrated applications in this thesis are dedicated and thus included in IGA_ROM.dll: it is the case for ROMs using volumetric B-Splines. Main objects and classes are called from this file.

B.1.1.2 IGAExt.dll

IGAExt.dll contains newly developed objects in relation with volumetric layouts and its properties but also on B-Splines objects. This file provides important isotopological information needed for ROM computations and isogeometric volumes definition. Moreover, one of its capabilities is to automatically class geometrical objects while conserving topological properties. It is done by parallel programming and smart nested classes.

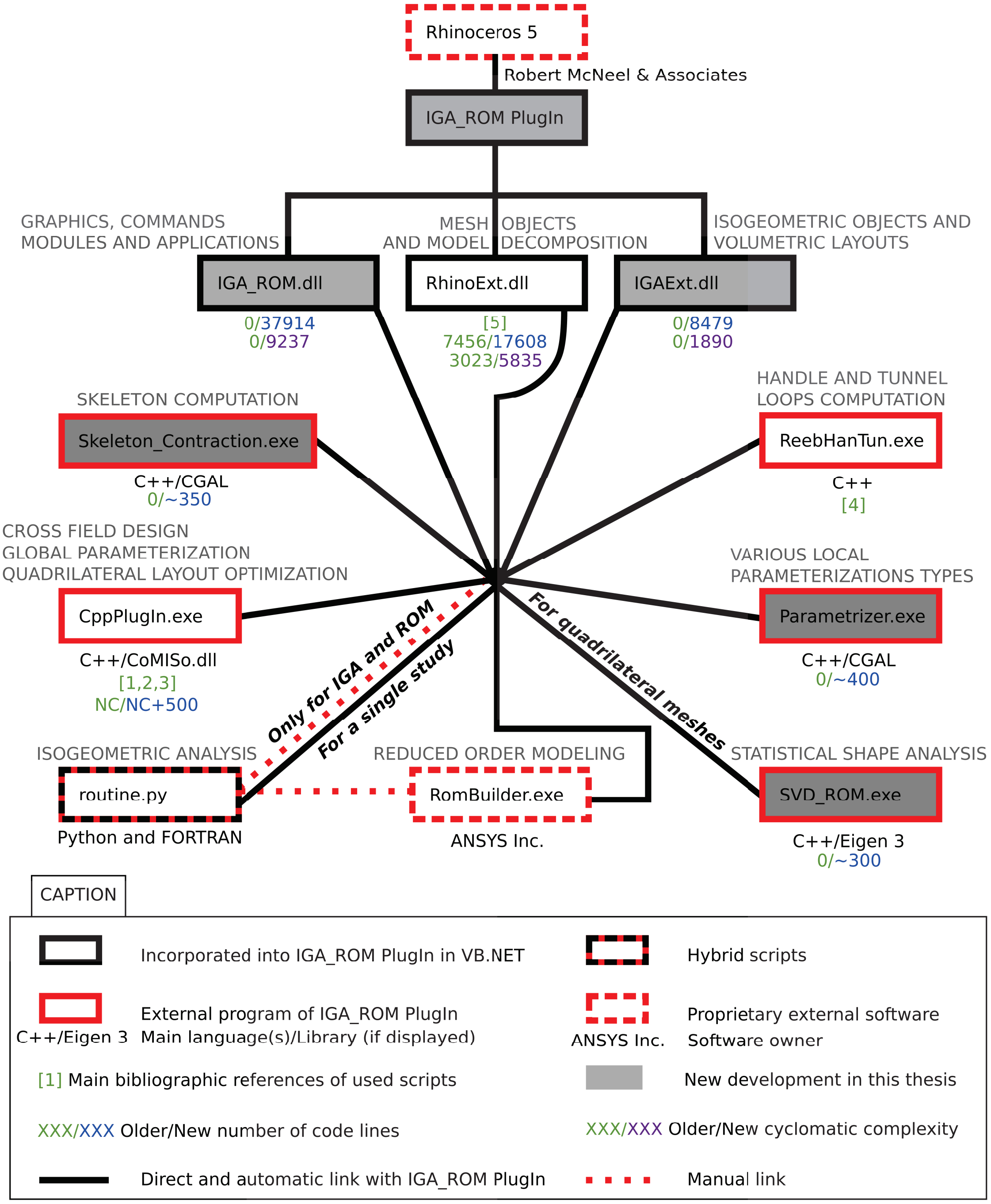

Figure B.1: Simplified flowchart of the IGA_ROM PlugIn. New developments made in this thesis are depicted with a gray background. [1]: [Campen and Kobbelt 2014]. [2]: [Bommes, Zimmer, and Kobbelt 2010]. [3]: [Crane, Desbrun, and Schröder 2010]. [4]: [K. Dey, Fan, and Wang 2013]. [5]: [Al-Akhras 2016]. NC stands for Non Communicated. Real names of used scripts or programs are given whatever it is english or not. Lot of dependencies are related to all named softwares and scripts.

B.1.1.3 RhinoExt.dll

RhinoExt.dll has been originally developed by [Al-Akhras 2016]. It provides mesh objects and also classes for cross field representation and global parameterization post-processing. Initial model segmentation techniques were implemented. New scripting was brought by improving segmentation algorithms, such as pants and cuboid decomposition. Several new objects have been developed in order to optimize existing ones. Most of automatic processes and links between external programs are programmed and called from this file.

B.1.2 PlugIn external scripts and softwares

Diverse scripts or research codes are linked to the PlugIn. For instance, CppPlugIn.exe is coming from the graphics and geometry communities. It serves to compute a constrained cross field which properties are derived from the quadrilateral layout; but also for determining a global parameterization and optimizing it. File routine.py is used for isogeometric analysis. At the beginning, the LaMCoS (Laboratory of Structural Mechanics and Contacts) developed an user interface and subroutine integrated into ABAQUS for IGA purposes [Elguedj et al. 2012]. Named abqNURBS, it is scripted in C++, Python and FORTRAN. The file routine.py is partially based on these internal laboratory developments but only FORTRAN routines are kept from the original project. These FORTRAN routines holding main NURBS properties have been later wrapped and integrated into Python scripts for IGA based shape optimization problems [Hirschler et al. 2018]. According to this recent work, slight modifications have been brought to Python files in order to use isogeometric analysis for reduced order models presented in this thesis. Thus, we name routine.py a hybrid software in Figure B.1.

B.2 Highlighted PlugIn functionalities

Presented functionalities can describe a part of the work related to previous chapters but also other independent capabilities. A non-exhaustive list is given and only few relevant scripts are explained.

B.2.1 Arbitrary non-arranged B-Spline surfaces to B-Splines volumes

Efforts have been deployed for isogeometric analysis concerning pre-processors, integrated analysis (like abqNURBS presented above) and post-processors. A IGA weakness is the availability of automatic model generation. As already explained in Chapter 1, various properties are required to perform an analysis trough a classic CAD design. Here, we contribute by adding a pre-processor tool. Proposed algorithm converts B-Spline surfaces into volumetric splines in a fully automatic manner without any user interaction as depicted in Figure B.2. Properties are required when designing boundary surfaces; same number of control points at surface interfaces and same polynomial degrees are mandatory. Moreover, each volume must have exactly 6 boundary surfaces. Despite these strong requirements, the input pre-processor files (for abqNURBS or other softwares) are automatically generated. A consistent isogeometric volume is created and will be analysis suitable even if:

- Surface knot values are different for a same parametric direction.
- Borders of surfaces are not geometrically compatible (we need at least 2 interpolation control points).
- There is duplicated surfaces.
- Surfaces are not particularly oriented.
- Surfaces are selectionned in a group or in an arbitrary manner.

Script is based on combination properties between surfaces, volumes but also on volume orientation possibilities. Useful graphs are determined so as to arrive to a consistent volumetric solution. This algorithm does not conserve isotopological informations between different trivariate isogeometric instances. Since it is fully automatic, we need at least one user input which will be distributed among all meshes of the population. Additional requirements are thus mandatory. An example of such fast isogeometric model construction is given in Figure B.3.

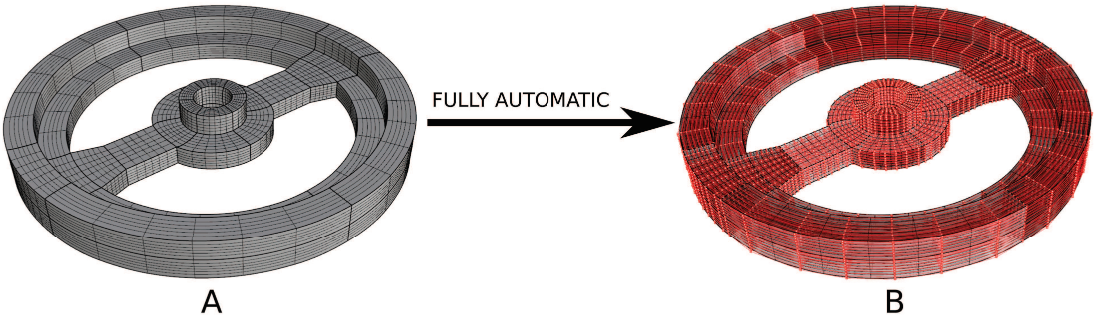

Figure B.2: Wheel fully automatic trivariate isogeometric parameterization. (A) Surfaces with required properties from CAD. (B) Computed trivariate parameterization. Boundary surfaces of the parameterization are represented in semi-transparent: color could be different depending on the normal orientation. CAD to isogeometric analysis suitable model is achieved in 15 seconds.

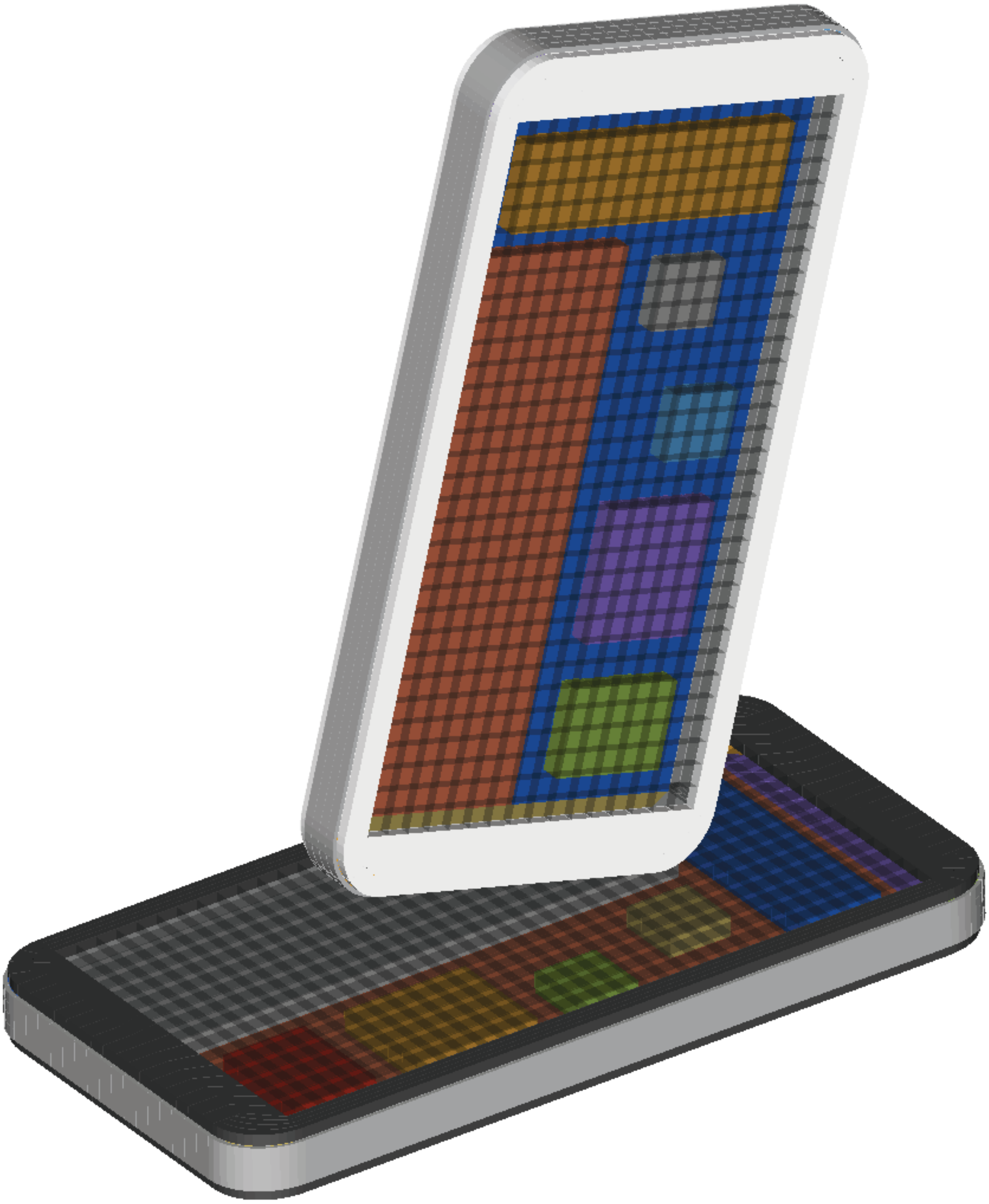

Figure B.3: Hybrid FEA/IGA model solved in RADIOSS [Occelli 2018]. Trivariate parameterization of curved parts was partially made by our IGA_ROM PlugIn.

B.2.2 Isotopological abqNURBS input file generation algorithm

This robust algorithm aims to generate pre-processor files (for abqNURBS or other softwares) from independent but compatible isogeometric connected volumes. In other words, given a set of trivariate isogeometric control lattices, it determines the global connectivity, class the geometrical entities and obtain global trivariate parametric directions of a complex part. It is done in parallel taking into account isotopological considerations: manipulated datas are stored into thread-safe VB.NET objects during concurrent accesses. In addition, powerful well-known cryptography hashing algorithms are ensured that the isotopological information is kept. This algorithm is incorporated into the PlugIn and used for above pre-processing purposes but also to determine files for routine.py (see Figure B.1). Simple boundary conditions and loads can be added to the model directly into Rhinoceros while computing the pre-processing files. Figure B.4 illustrates the study inputs of the seal part.

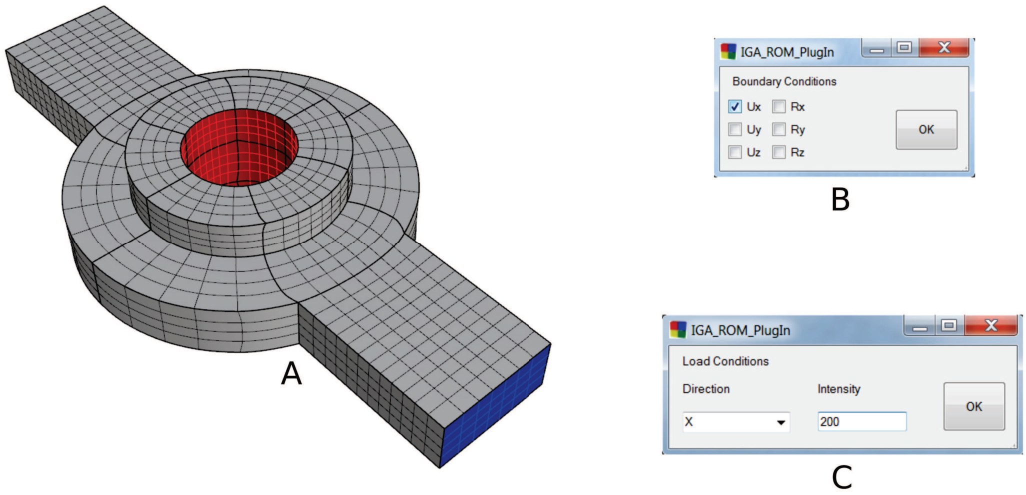

Boundary Conditions
☑ Ux ☐ Rx
☐ Uy ☐ Ry
☐ Uz ☐ Rz

Load Conditions
Direction: X
Intensity: 200

Figure B.4: Inputs of a volumetric isogeometric model in order to build pre-processing files. Conditions are settled directly into Rhinoceros 5. (A) Boundary conditions and loads applied to the trivariate isogeometric model boundary surfaces. (B) Blue surface holding boundary conditions. Red surfaces are subject to loads in (C).

B.2.3 Reduced order model evaluation

Trivariate isogeometric reduced order model evaluation is made directly into the PlugIn interface embedded into Rhinoceros. Dedicated form with appropriated scrolling bars is automatically generated, e.g. see Chapter 7. During this process the software RomBuilder.exe (see Figure B.1) from ANSYS (U.S. patent application 16/253,635 filed January 22, 2019) is interrogated and a solution vector is provided. Then, other

Python routines are called to reconstruct the isogeometric model with required properties from evaluation; thus generating a VTU (Visualization Toolkit Unstructured) file for Paraview.

B.2.4 IGA_ROM PlugIn main tabs

Figure B.5: File tab.

Figure B.6: Mesh tab.

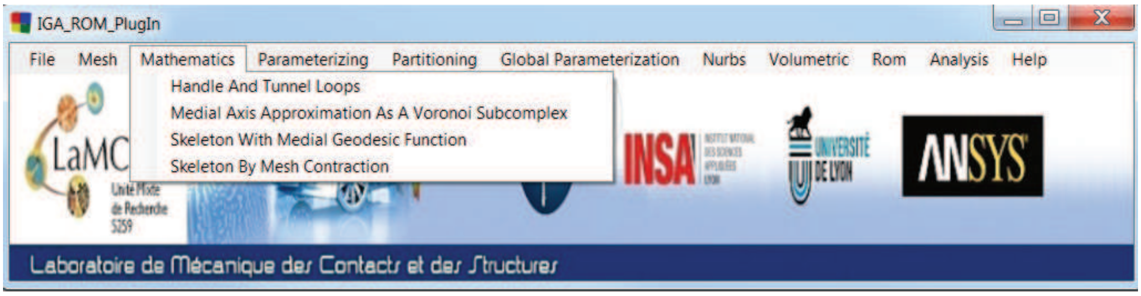

Figure B.7: Mathematics tab.

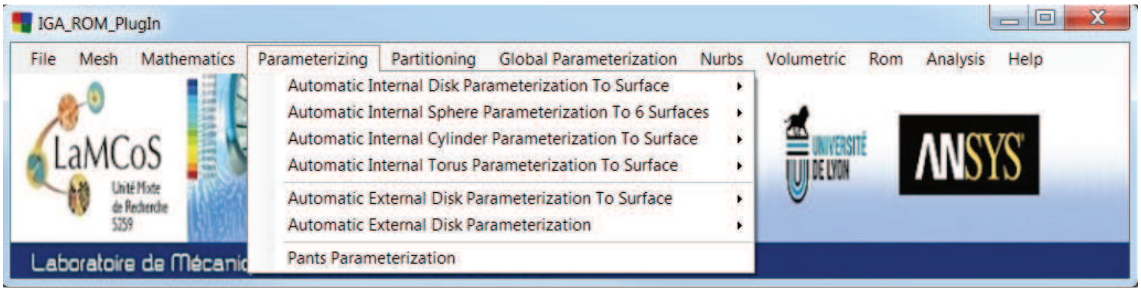

Figure B.8: Parameterizing tab.

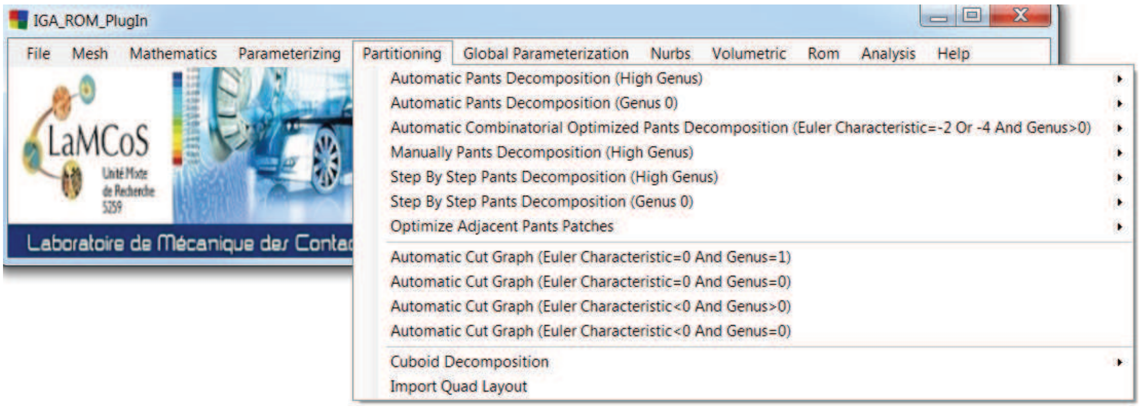

Figure B.9: Partitioning tab.

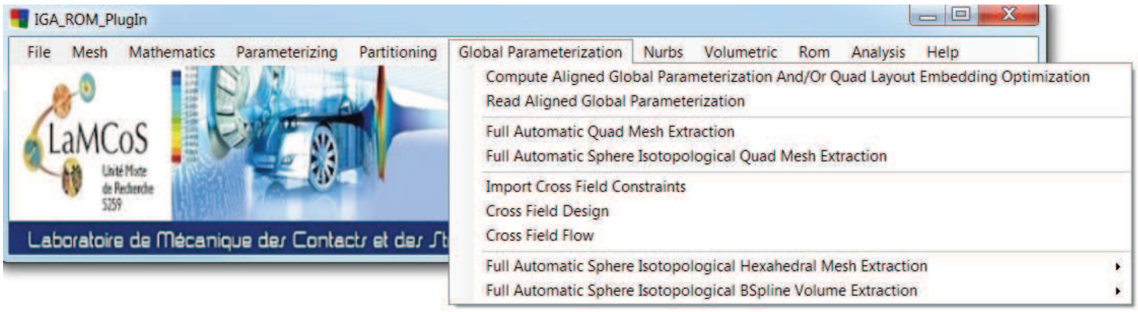

Figure B.10: Global parameterization tab.

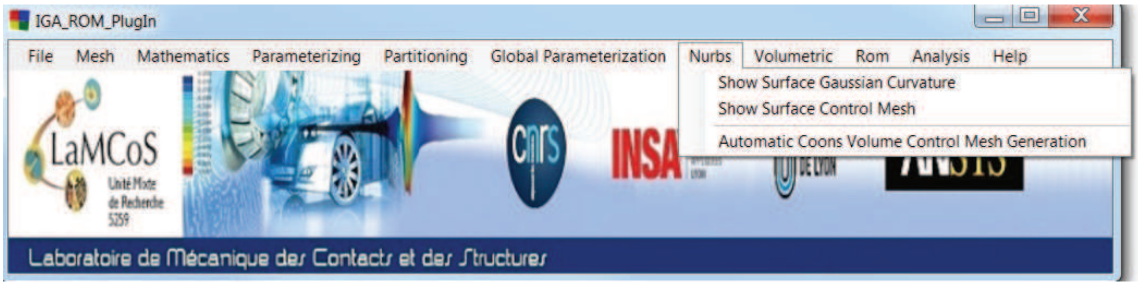

Figure B.11: Nurbs tab.

Figure B.12: Volumetric tab.

Figure B.13: Rom tab.

Figure B.14: Analysis tab.

Figure B.15: Help tab.

Appendix C

Additional developments

Additional developments of the manuscript.

Contents

C.1 Quadrilateral layout arcs embedding optimization

Firstable, we refer the readers to the work of [Myles et al. 2010]. We briefly develop the constraints attached to an isoparametric curve of the quadrilateral layout $\mathbb{Q}$ used in surface mesh global parameterization (see Chapter 4). Into a disk-like parameterization embedded in $\mathbb{R}^2$, when spanning a seam, connection between 2 nodes n_1 and n_2 is related by rigid body motion in $\mathbb{R}^2$. This is the reasoning behind Equation (C.1). We notice that in general, disk-like parameterizations may contain overlapping areas depending on the Gaussian curvature and kind of surface parameterization.

$$n_{2u,v} = R_1 n_{1u,v} + t^1_{u,v}, \text{ across one seam,} \tag{C.1a}$$

$$n_{2u,v} = R_2[R_1 n_{1u,v} + t^1_{u,v}] + t^2_{u,v}, \text{ across two seams,} \tag{C.1b}$$

$$n_{2u,v} = R_3[R_2[R_1 n_{1u,v} + t^1_{u,v}] + t^2_{u,v}] + t^3_{u,v}, \text{ across three seams,} \tag{C.1c}$$

$$n_{2u,v} = R_3 R_2 R_1 n_{1u,v} + R_3 R_2 t^1_{u,v} + R_3 t^2_{u,v} + t^3_{u,v}, \text{ with reorganization.} \tag{C.1d}$$

This is done successively among all seams crossed by an arc. This yielding to the generalized form given in Equation (C.2). Remark that either u or v parameter can be taken into account. Parametric rotations R are restricted to $\frac{\pi}{2}$ due to the 4-symmetry nature of the field. Translations t are integers. $m+1$ is the number of crossed seams.

$$n_{2u,v} = [(\prod_{i=0}^{m} R_{(m-i)+1}) n_{1u,v} + (\sum_{i=0}^{m-1} (\prod_{j=0}^{m-1-i} R_{(m-j)+1}) t^{i+1}_{u,v}) + t^{m+1}_{u,v}]. \tag{C.2}$$

C.2 Quadrilateral layout nodes embedding optimization

Needed moving directions of nodes of $\mathbb{Q}$ in order to minimize Equation (4.14) will be explained. We invite the readers to read the appendix of [Campen and Kobbelt 2014] for more details. Objective function is defined in Equation (C.3) per 1-ring with triangles T of the interesting node. $E_p(x, y)$ refers to the parameterization energy for the 1-ring. The gradient descent vector coordinates which give the direction of moving are formulated in Equation (C.4). Remember that a geodesic polar map is used [Welch and Witkin 1994], and for the sake of simplicity dependent variables will be denoted as x and y for the related node of $\mathbb{Q}$.

$$E_p(x,y) = \sum_{f\in T}[\|\nabla u - \mathbf{u}^{\mathcal{C}}\|^2 A_f(x,y) + \|\nabla v - \mathbf{v}^{\mathcal{C}}\|^2 A_f(x,y)], \tag{C.3}$$

$$\begin{aligned}\frac{\partial E_p^T(x,y)}{\partial x} = [&\frac{\partial A_f(x,y)}{\partial x}\|\nabla u - \mathbf{u}^{\mathcal{C}}\|^2 + \frac{\partial A_f(x,y)}{\partial x}\|\nabla v - \mathbf{v}^{\mathcal{C}}\|^2 + \\ &2(\nabla u - \mathbf{u}^{\mathcal{C}}).\frac{\partial \nabla u}{\partial x}A_f(x,y) + 2(\nabla v - \mathbf{v}^{\mathcal{C}}).\frac{\partial \nabla v}{\partial x}A_f(x,y),\end{aligned} \tag{C.4a}$$

$$\begin{aligned}\frac{\partial E_p^T(x,y)}{\partial y} = [&\frac{\partial A_f(x,y)}{\partial y}\|\nabla u - \mathbf{u}^{\mathcal{C}}\|^2 + \frac{\partial A_f(x,y)}{\partial y}\|\nabla v - \mathbf{v}^{\mathcal{C}}\|^2 + \\ &2(\nabla u - \mathbf{u}^{\mathcal{C}}).\frac{\partial \nabla u}{\partial y}A_f(x,y) + 2(\nabla v - \mathbf{v}^{\mathcal{C}}).\frac{\partial \nabla v}{\partial y}A_f(x,y).\end{aligned} \tag{C.4b}$$

Thus, an embedded node a of $\mathbb{Q}$ of coordinates (x, y) (computed in a specific coordinate system) of $\mathbb{Q}$ has be moved in the direction given in Equation (C.5). This direction $\mathbf{d}(a)$ is expressed for the 1-ring, with summation over the triangles $f \in T$ incident to the node a.

$$\mathbf{d}(a) = -(\frac{\partial E_p(x,y)}{\partial x}, \frac{\partial E_p(x,y)}{\partial y}) = -\sum_{f\in T}(\frac{\partial E_p^T(x,y)}{\partial x}, \frac{\partial E_p^T(x,y)}{\partial y}). \tag{C.5}$$

C.3 New topology based element quality criterion

Several mesh metrics exist to quantify hexahedral mesh quality such as aspect ratio, scaled Jacobian, distortion, parallel deviation and so on. Jacobian ratio is widely used and indicates if the mapping between element space and real space is becoming computationally unreliable. For a hexahedral element, this is in general the ratio of the maximum to the minimum sampled value of R_i. R_i are scalar values at given points and represent the magnitude of the mapping function between element natural coordinates and real space. They are sampled in corner nodes of the hexahedral element. In an ideally shaped element, R_i are relatively constant over the element, and do not change sign.

Here, we want to explicit a new formulation of hexahedral element quality based on topological properties of the 8-node brick. By topological we mean topology, i.e., the link between geometry and topology for the element. Indeed, we want to tackle and characterize the difference between the parametric space and physical space of the element. This approach is quite similar to the Jacobian ratio, but it can be measured from the point of view of the Gauss-Bonnet theorem (see Theorem 2.3). In this spirit, we define the $\frac{3\pi}{2}$ Gaussian curvature quality metric. It estimates at each hexahedral node the angle deviation from the classic cube angle of $\frac{3\pi}{2}$. Element quality scalar value is then determined by the deviation summation over the 8 nodes. Values are ranking from 0 to 6π. Equation (C.6) establishes the Gauss-Bonnet theorem for a single brick of 8 nodes both in the continuous and discrete case:

$$\int_S K dS = 2\pi\chi(S) = \sum_{i=1}^{8} \left[2\pi - \sum_{j=1}^{3} \beta_i^j\right] = 4\pi, \tag{C.6}$$

where S is the boundary surface of the element, $\chi(S)$ the Euler characteristic of the hexahedral simplicial complex, K the Gaussian curvature and β_i^j the angle related to the node i between all of its 3 incident edges, $j \in \{1, 2, 3\}$. The new quality metric Q_h is expressed in Equation (C.7).

$$Q_h = \sum_{i=1}^{8} |\frac{3\pi}{2} - \sum_{j=1}^{3} \beta_i^j|. \tag{C.7}$$

For a perfect cube, $Q_h = 0$ is trivial. Q_h^{max} is not immediatly obvious. In $\mathbb{R}^3$, by concentrating the Gaussian curvature at 2 nodes on a brick, we obtain $Q_h^{max} = 6\pi$ as written in Equation (C.8b). Each of the 2 nodes collecting all the Gaussian curvature in $\mathbb{R}^3$, whether $K = 0$ for concerned nodes in Equation (C.8a) in order to respect theorems.

$$\int_S K dS = \sum_{i=1}^{2} 2\pi - 0 + \sum_{i=3}^{8} 2\pi - 2\pi = 4\pi, \tag{C.8a}$$

$$Q_h^{max} = \sum_{i=1}^{2} |\frac{3\pi}{2} - 0| + \sum_{i=3}^{8} |\frac{3\pi}{2} - 2\pi| = 6\pi. \tag{C.8b}$$

In other words, it is geometrically a line embedded in the $\mathbb{R}^3$ space. A quality metric value example Q_h^b can be demonstrated by flattening the hexahedral element into the $\mathbb{R}^2$ plane. Equation (C.9) refer to maximum value admissible with this metric in practical cases. Figure C.1 shows an example of the metric applied to large deformations.

$$Q_h^b = \sum_{i=1}^{4} |\frac{3\pi}{2} - 2\pi| + \sum_{i=5}^{8} |\frac{3\pi}{2} - \pi| = 4\pi. \tag{C.9}$$

Depending on the geometry, this criterion does not always capture element volume variation in particular when stretching along faces normals, if considering a perfect cube.

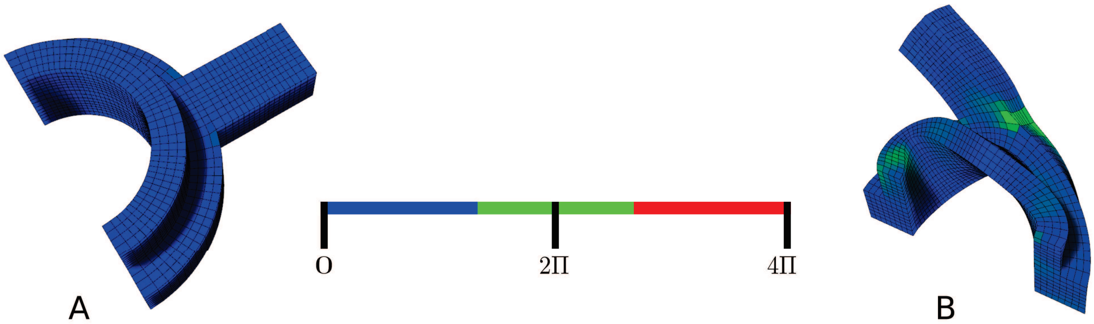

Figure C.1: $\frac{3\pi}{2}$ Gaussian curvature element quality metric. Example is shown using meshes from Chapter 7. (A) Element quality for the half-seal undeformed shape. (B) Element quality for the associated deformed shape of (A) at the intermediate loading step, $t = 0.5$. Element quality has been computed by our IGA_ROM PlugIn (see Appendix B).

Bibliography

Eckart, Carl and Gale Young (1936). “The approximation of one matrix by another of lower rank”. *Psychometrika* 1.3, pp. 211–218.

Dijkstra, Edsger W (1959). “A note on two problems in connexion with graphs”. *Numerische mathematik* 1.1, pp. 269–271.

Tutte, William Thomas (1963). “How to draw a graph”. *Proc. London Math. Soc* 13.3, pp. 743–768.

Pugh, Charles C (1968). “A generalized Poincaré index formula”. *Topology* 7.3, pp. 217–226.

Stillwell, John (1993). “Classical Topology and Combinatorial Group Theory”. Ed. by Springer-Verlag New York. Springer-Verlag New York.

Lemaitre, Jean and Jean-Louis Chaboche (1994). *Mechanics of solid materials.* Cambridge university press.

Welch, William and Andrew Witkin (1994). “Free-form shape design using triangulated surfaces”. *Proceedings of the 21st annual conference on Computer graphics and interactive techniques.* ACM, pp. 247–256.

Feßler, RE (1995). “A generalized Poincaré index formula”. *Journal of Differential Equations* 115.2, pp. 304–324.

Ma, Weiyin and Jean-Pierre Kruth (1995). “Parameterization of randomly measured points for least squares fitting of B-spline curves and surfaces”. *Computer-Aided Design* 27.9, pp. 663–675.

Demmel, James W et al. (1999). “A supernodal approach to sparse partial pivoting”. *SIAM Journal on Matrix Analysis and Applications* 20.3, pp. 720–755.

Farin, Gerald and Dianne Hansford (1999). “Discrete Coons patches”. *Computer Aided Geometric Design* 16.7, pp. 691–700.

Hatcher, Allen, Pierre Lochak, and Leila Schneps (2000). “On the teichmüller tower of mapping class groups”. *Journal Für Die Reine Und Angewandte Mathematik* 521, pp. 1–24.

Praun, Emil, Adam Finkelstein, and Hugues Hoppe (2000). “Lapped textures”. *Proceedings of the 27th annual conference on Computer graphics and interactive techniques.* ACM Press/Addison-Wesley Publishing Co., pp. 465–470.

Rogers, David F (2000). *An introduction to NURBS: with historical perspective.* Elsevier.

Hatcher, Allen (2001). “Algebraic Topology”. *http://www.math.cornell.edu/hatcher.*

Kunisch, Karl and Stefan Volkwein (2001). “Galerkin proper orthogonal decomposition methods for parabolic problems”. *Numerische mathematik* 90.1, pp. 117–148.

Turk, Greg (2001). “Texture synthesis on surfaces”. *Proceedings of the 28th annual conference on Computer graphics and interactive techniques.* ACM, pp. 347–354.

Dischler, J-M et al. (2002). “Texture particles”. *Computer Graphics Forum.* Vol. 21. 3. Wiley Online Library, pp. 401–410.

Farin, Gerald E (2002). *Curves and surfaces for CAGD: a practical guide.* Morgan Kaufmann.

Alliez, Pierre et al. (2003). “Anisotropic polygonal remeshing”. *ACM Transactions on Graphics (TOG).* Vol. 22. 3. ACM, pp. 485–493.

Floater, Michael S. (2003). “Mean value coordinates”. *Computer Aided Geometric Design* 20, pp. 19–27.

Bungartz, Hans-Joachim and Michael Griebel (2004). “Sparse grids”. *Acta numerica* 13, pp. 147–269.

Erickson, Jeff and Sariel Har-Peled (2004). “Optimally Cutting a Surface into a Disk”. *Discrete & Computational Geometry* 31.1, pp. 37–59.

Marinov, Martin and Leif Kobbelt (2004). “Direct anisotropic quad-dominant remeshing”. *Computer Graphics and Applications, 2004. PG 2004. Proceedings. 12th Pacific Conference on.* IEEE, pp. 207–216.

Tarini, Marco et al. (2004). “Polycube-maps”. *ACM transactions on graphics (TOG).* Vol. 23. 3. ACM, pp. 853–860.

Erickson, Jeff and Kim Whittlesey (2005). “Greedy optimal homotopy and homology generators”. *16th Annual ACM-SIAM Symposium on Discrete Algorithms*, pp. 1038–1046.

Floater, Michael S and Kai Hormann (2005). “Surface parameterization: a tutorial and survey”. *Advances in multiresolution for geometric modelling.* Springer, pp. 157–186.

Hughes, T.J.R., J.A. Cottrell, and Y. Bazilevs (2005). “Isogeometric analysis: CAD, finite elements, NURBS, exact geometry and mesh refinement”. *Computer Methods in Applied Mechanics and Engineering* 194.39-41, pp. 4135 –4195.

Lee, Yunjin et al. (2005). “Mesh scissoring with minima rule and part salience”. *Computer Aided Geometric Design* 22.5, pp. 444–465.

Verdière, Éric Colin de and Francis Lazarus (2005). “Optimal System of Loops on an Orientable Surface”. *Discrete & Computational Geometry* 33.3. A conference version appeared in *Proc. IEEE Symp. on Foundations of Computer Science (FOCS)*, 2002. A preliminary version appeared in *Abstr. Europ. Workshop on Computational Geometry (EuroCG)*, 2002, pp. 507–534.

Dong, Shen et al. (2006). “Spectral surface quadrangulation”. *ACM Transactions on Graphics (TOG).* Vol. 25. 3. ACM, pp. 1057–1066.

Hornung, Alexander and Leif Kobbelt (2006). “Robust reconstruction of watertight 3 d models from non-uniformly sampled point clouds without normal information”. *Symposium on geometry processing*, pp. 41–50.

Li, Wan-Chiu et al. (2006). "Representing higher-order singularities in vector fields on piecewise linear surfaces". *IEEE Transactions on Visualization and Computer Graphics (2006)* 12.5.

Ray, Nicolas et al. (2006). "Periodic global parameterization". *ACM Transactions on Graphics (TOG)* 25.4, pp. 1460–1485.

Ryckelynck, David et al. (2006). "On the a priori model reduction: overview and recent developments". *Archives of Computational methods in Engineering* 13.1, pp. 91–128.

Simo, Juan C and Thomas JR Hughes (2006). *Computational inelasticity*. Springer Science & Business Media.

Tong, Y et al. (2006). "Designing quadrangulations with discrete harmonic forms". *Eurographics Symposium on Geometry Processing*, pp. 1–10.

K. Dey, Tamal, Kuiyu Li, and Jian Sun (2007). "On Computing Handle and Tunnel Loops". *International Conference on Cyberworlds*, pp. 357–366.

Kälberer, Felix, Matthias Nieser, and Konrad Polthier (2007). "QuadCover-Surface Parameterization using Branched Coverings". *Computer Graphics Forum*. Vol. 26. 3. Wiley Online Library, pp. 375–384.

Simsek, Alp, Asuman Ozdaglar, and Daron Acemoglu (2007). "Generalized Poincare-Hopf theorem for compact nonsmooth regions". *Mathematics of Operations Research* 32.1, pp. 193–214.

Verdière, Éric Colin de and Francis Lazarus (2007). "Optimal pants decompositions and shortest homotopic cycles on an orientable surface". *Journal of the ACM* 54.4. A conference version appeared in *Proc. Int. Symp. on Graph Drawing (GD)*, 2003. A preliminary version appeared in *Abstr. Europ. Workshop on Computational Geometry (EuroCG)*, 2003, Article No. 18.

Alliez, Pierre et al. (2008). "Recent advances in remeshing of surfaces". *Shape analysis and structuring*. Springer, pp. 53–82.

Bommes, David, Tobias Vossemer, and Leif Kobbelt (2008). "Quadrangular parameterization for reverse engineering". *International Conference on Mathematical Methods for Curves and Surfaces*. Springer, pp. 55–69.

Chen, Yanqing et al. (2008). "Algorithm 887: CHOLMOD, supernodal sparse Cholesky factorization and update/downdate". *ACM Transactions on Mathematical Software (TOMS)* 35.3, p. 22.

Dey, Tamal K et al. (2008). "Computing geometry-aware handle and tunnel loops in 3D models". *ACM Transactions on Graphics (TOG)* 27.3, p. 45.

Elguedj, Thomas et al. (2008). "B-bar and F-bar projection methods for nearly incompressible linear and non-linear elasticity and plasticity using higher-order NURBS elements". *Computer methods in applied mechanics and engineering* 197.33-40, pp. 2732–2762.

Huang, Jin et al. (2008). "Spectral quadrangulation with orientation and alignment control". *ACM Transactions on Graphics (TOG)*. Vol. 27. 5. ACM, p. 147.

Lin, Juncong et al. (2008). "Automatic PolyCube-Maps". *Advances in Geometric Modeling and Processing*, pp. 3–16.

Niroomandi, Siamak et al. (2008). “Real-time deformable models of non-linear tissues by model reduction techniques”. *Computer methods and programs in biomedicine* 91.3, pp. 223–231.

Ray, Nicolas et al. (2008). “N-symmetry direction field design”. *ACM Transactions on Graphics (TOG)* 27.2, p. 10.

Wang, Hongyu et al. (2008). “Polycube splines”. *Computer Aided Design* 40.6, pp. 721–733.

Bommes, David, Henrik Zimmer, and Leif Kobbelt (2009). “Mixed-integer quadrangulation”. *ACM Transactions On Graphics (TOG)* 28.3, p. 77.

Cottrell, J Austin, Thomas JR Hughes, and Yuri Bazilevs (2009). *Isogeometric analysis: toward integration of CAD and FEA*. John Wiley & Sons.

Glotzer, Sharon C et al. (2009). *International assessment of research and development in simulation-based engineering and science. Panel report*. Tech. rep.

Jubin, Benoît (2009). “A generalized Poincaré-Hopf index theorem”. *arXiv preprint arXiv:0903.0697 (2009)*.

Li, Xin, Xianfeng Gu, and Hong Qin (2009). “Surface Mapping Using Consistent Pants Decomposition”. *IEEE Transactions on Visualization and Computer Graphics* 15.4, pp. 558–571.

Martin, Tobias, Elaine Cohen, and Robert M. Kirby (2009). “Volumetric Parameterization and Trivariate B-spline Fitting Using Harmonic Functions”. *Computer Aided Geometric Design* SPM ’08 26, pp. 648–664.

Ray, Nicolas et al. (2009). “Geometry-aware direction field processing”. *ACM Transactions on Graphics (TOG)* 29.1, p. 1.

Zeng, Wei et al. (2009a). “Generalized Koebe’s Method for Conformal Mapping Multiply Connected Domains”. *2009 SIAM/ACM Joint Conference on Geometric and Physical Modeling* SPM ’09. Pp. 89–100.

Zeng, Wei et al. (2009b). “Surface quasi-conformal mapping by solving Beltrami equations”. *IMA International Conference on Mathematics of Surfaces*, pp. 391–408.

Bommes, David, Henrik Zimmer, and Leif Kobbelt (2010). “Practical mixed-integer optimization for geometry processing”. *International Conference on Curves and Surfaces*. Springer, pp. 193–206.

Chinesta, Francisco, Amine Ammar, and Elías Cueto (2010). “Recent advances and new challenges in the use of the proper generalized decomposition for solving multidimensional models”. *Archives of Computational methods in Engineering* 17.4, pp. 327–350.

Cohen, E. et al. (2010). “Analysis-aware modeling: Understanding quality considerations in modeling for isogeometric analysis”. *Computer Methods in Applied Mechanics and Engineering* 199.5-8, pp. 334 –356.

Crane, Keenan (2010). “Discrete connections for geometry processing”. http://resolver.caltech.edu/CaltechTHESIS:05282010-102307125. MA thesis. California Institute of Technology.

Crane, Keenan, Mathieu Desbrun, and Peter Schröder (2010). “Trivial Connections on Discrete Surfaces”. *Computer Graphics Forum (SGP)* 29.5, pp. 1525–1533.

Damiand, Guillaume (2010). “Contributions aux cartes combinatoires et cartes généralisées: Simplification, modèles, invariants topologiques et applications”. *Habilitation à diriger des recherches, Université Claude Bernand Lyon 1, (2010).*

Hraiech, Najah (2010). “Morphing de maillage et indexation de forme pour la modélisation du fémur humain”. PhD thesis. Rennes 1.

K. Dey, Tamal, Jian Sun, and Yusu Wang (2010). “Approximating Cycles in a Shortest Basis of the First Homology Group from Point Data”. *ACM 26th Annual Symposium on Computational Geometry*, pp. 166–175.

Lai, Yu-Kun et al. (2010). “Metric-driven rosy field design and remeshing”. *IEEE Transactions on Visualization and Computer Graphics* 16.1, pp. 95–108.

Li, Bo et al. (2010). “Generalized PolyCube Trivariate Splines”. *Shape Modeling International Conference (SMI), 2010*, pp. 261–265.

Lipton, Scott et al. (2010). “Robustness of isogeometric structural discretizations under severe mesh distortion”. *Computer Methods in Applied Mechanics and Engineering* 199.5-8, pp. 357–373.

Myles, Ashish et al. (2010). “Feature-aligned T-meshes”. *ACM Transactions on Graphics (TOG).* Vol. 29. 4. ACM, p. 117.

Zhang, Muyang et al. (2010). “A wave-based anisotropic quadrangulation method”. *ACM Transactions on Graphics (TOG).* Vol. 29. 4. ACM, p. 118.

Bommes, David, Timm Lempfer, and Leif Kobbelt (2011). “Global structure optimization of quadrilateral meshes”. *Computer Graphics Forum.* Vol. 30. 2. Wiley Online Library, pp. 375–384.

Chinesta, Francisco, Pierre Ladeveze, and Elías Cueto (2011). “A short review on model order reduction based on proper generalized decomposition”. *Archives of Computational Methods in Engineering* 18.4, p. 395.

Escobar, JM et al. (2011). “A new approach to solid modeling with trivariate T-splines based on mesh optimization”. *Computer Methods in Applied Mechanics and Engineering* 200.45, pp. 3210–3222.

Galland, Florent (2011). “An adaptive model reduction approach for 3D fatigue crack growth in small scale yielding conditions”. PhD thesis. INSA de Lyon.

Galland, Florent et al. (2011). “A global model reduction approach for 3D fatigue crack growth with confined plasticity”. *Computer Methods in Applied Mechanics and Engineering* 200.5, pp. 699–716.

Huang, Jin et al. (2011). “Boundary aligned smooth 3D cross-frame field”. *ACM transactions on graphics (TOG).* Vol. 30. 6. ACM, p. 143.

Kerfriden, Pierre et al. (2011). “Bridging proper orthogonal decomposition methods and augmented Newton–Krylov algorithms: an adaptive model order reduction for highly nonlinear mechanical problems”. *Computer Methods in Applied Mechanics and Engineering* 200.5, pp. 850–866.

Amsallem, David, Matthew J Zahr, and Charbel Farhat (2012). “Nonlinear model order reduction based on local reduced-order bases”. *International Journal for Numerical Methods in Engineering* 92.10, pp. 891–916.

Bommes, David (2012). “Quadrilateral Surface Mesh Generation for Animation and Simulation”. PhD thesis. Bommes.

Bower, Allan (2012). *Applied Mechanics of Solids.* http://solidmechanics.org/FEA.php, 2018.

Campen, Marcel, David Bommes, and Leif Kobbelt (July 2012). “Dual loops meshing: quality quad layouts on manifolds”. *ACM Trans. Graph.* 31.4, 110:1–110:11.

Elguedj, T et al. (2012). “Abaqus user element implementation of NURBS based isogeometric analysis”. *6th European congress on computational methods in applied sciences and engineering, Vienna, Austria*, pp. 10–14.

Myles, Ashish and Denis Zorin (2012). “Global parametrization by incremental flattening”. *ACM Transactions on Graphics (TOG)* 31.4, p. 109.

Piegl, Les and Wayne Tiller (2012). *The NURBS book.* Springer Science & Business Media.

Zhang, Yongjie, Wenyan Wang, and Thomas JR Hughes (2012). “Solid T-spline Construction from Boundary Representations for Genus-Zero Geometry”. *Computer Methodsin Applied Mechanics and Engineering* 201.

Belytschko, Ted et al. (2013). *Nonlinear finite elements for continua and structures.* John wiley & sons.

Bommes, David et al. (2013a). “Integer-grid maps for reliable quad meshing”. *ACM Transactions on Graphics (TOG)* 32.4, p. 98.

Bommes, David et al. (2013b). “Quad-Mesh Generation and Processing: A Survey”. *Computer Graphics Forum.* Vol. 32. 6. Wiley Online Library, pp. 51–76.

Boucinha, Lucas, Anthony Gravouil, and Amine Ammar (2013). “Space–time proper generalized decompositions for the resolution of transient elastodynamic models”. *Computer Methods in Applied Mechanics and Engineering* 255, pp. 67–88.

Ebke, Hans-Christian et al. (2013). “QEx: Robust Quad Mesh Extraction”. *Proceedings of the 2013 SIGGRAPH Asia Conference.* SA ’13. Hong Kong, Hong Kong: ACM, 168:1–168:10.

K. Dey, Tamal, Fengtao Fan, and Yusu Wang (2013). “An efficient computation of handle and tunnel loops via Reeb graphs”. *SIGGRAPH.*

Knöppel, Felix et al. (2013). “Globally optimal direction fields”. *ACM Trans. Graph. (2013)* 32.4.

Kowalski, Nicolas, Franck Ledoux, and Pascal Frey (2013). “A PDE Based Approach to Multidomain Partitioning and Quadrilateral Meshing”. *Proceedings of the 21st International Meshing Roundtable.* Ed. by Xiangmin Jiao and Jean-Christophe Weill. Berlin, Heidelberg: Springer Berlin Heidelberg, pp. 137–154.

Li, Bo et al. (2013). “Surface Mesh to Volumetric Spline Conversion with Generalized Poly-cubes”. *IEEE Transactions on Visualization and Computer Graphics* 99.PrePrints, p. 1.

Myles, Ashish and Denis Zorin (2013). “Controlled-distortion constrained global parametrization”. *ACM Transactions on Graphics (TOG)* 32.4, p. 105.

Wang, Wenyan et al. (2013). “Trivariate solid T-spline construction from boundary triangulations with arbitrary genus topology”. *Computer-Aided Design* 45, pp. 351–360.

Yu, Wuyi et al. (2013). “Optimizing Polycube Domain Construction for Hexahedral Remeshing”. *Computer-Aided Design*.

Campen, Marcel and Leif Kobbelt (2014). “Quad layout embedding via aligned parameterization”. *Computer Graphics Forum*. Vol. 33. 8. Wiley Online Library, pp. 69–81.

Giacoma, Anthony (2014). “Efficient acceleration techniques for nonlinear analysis of structures with frictional contact”. PhD thesis. INSA de Lyon.

Grassi, Lorenzo et al. (2014). “Comprehensive evaluation of PCA-based finite element modelling of the human femur”. *Medical Engineering and Physics* 36.10, pp. 1246–1252.

Li, Xin and S. S. Iyengar (Dec. 2014). “On Computing Mapping of 3D Objects: A Survey”. *ACM Comput. Surv.* 47.2, 34:1–34:45.

Liu, Lei, Yongjie Zhang, and Thomas JR Hughes (2014). “Volumetric T-spline construction using Boolean operations”. *Engineering with Computers* 30, pp. 425–439.

Myles, Ashish, Nico Pietroni, and Denis Zorin (2014). “Robust field-aligned global parametrization”. *ACM Transactions on Graphics (TOG) - Proceedings of ACM SIGGRAPH 2014* 33 Issue 4.135.

Wang, Xilu and Xiaoping Qian (2014). “An optimization approach for constructing trivariate B-spline solids”. *Computer-Aided Design* 46, pp. 179–191.

Zhang, K. and X. Li (2014). “Searching Geometry-aware Pants Decomposition in Different Isotopy Classes”. *Geometry, Imaging, and Computing, Vol. 1, No. 3*, pp. 367–393.

Campen, Marcel, David Bommes, and Leif Kobbelt (2015). “Quantized global parametrization.” *ACM Trans. Graph.* 34.6, p. 192.

Liu, Lei et al. (2015). “Feature-preserving T-mesh construction using skeleton-based polycubes”. *Computer-Aided Design* 58, pp. 162–172.

Morganti, S et al. (2015). “Patient-specific isogeometric structural analysis of aortic valve closure”. *Computer Methods in Applied Mechanics and Engineering* 284, pp. 508–520.

Ray, Nicolas and Dmitry Sokolov (2015). “On smooth 3d frame field design”. *arXiv preprint arXiv:1507.03351 (2015).*

Razafindrazaka, Faniry H, Ulrich Reitebuch, and Konrad Polthier (2015). “Perfect matching quad layouts for manifold meshes”. *Computer Graphics Forum*. Vol. 34. 5. Wiley Online Library, pp. 219–228.

Al-Akhras, Hassan (2016). “Automatic Isogeometric Analysis Suitable Trivariate Models Generation - Application to Reduced Order Modeling”. PhD thesis. INSA de LYON, École Doctorale MEGA ED 162.

Al-Akhras, Hassan et al. (2016). “Isogeometric analysis-suitable trivariate NURBS models from standard B-Rep models”. *Comput. Methods Appl. Mech. Engrg.* 307, pp. 256–274.

Alliez, Pierre, Sylvain Pion, and Ankit Gupta (2016). “Principal Component Analysis”. *CGAL User and Reference Manual.* 4.9. CGAL Editorial Board.

Courard, Amaury (2016). “PGD-Abaques virtuels pour l’optimisation géométrique des structures”. PhD thesis. Université Paris-Saclay.

Fang, Xianzhong et al. (2016). “All-hex meshing using closed-form induced polycube”. *ACM Transactions on Graphics (TOG)* 35.4, p. 124.

Fu, Xiao-Ming, Chong-Yang Bai, and Yang Liu (2016). “Efficient volumetric polycube-map construction”. *Computer Graphics Forum.* Vol. 35. 7. Wiley Online Library, pp. 97–106.

Hajij, Mustafa, Tamal K. Dey, and Xin Li (2016). “Segmenting a Surface Mesh into Pants Using Morse Theory”. *arXiv.org* arXiv:1608.06368v2.

Harmel, Maximilian, Roger A. Sauer, and David Bommes (2016). “Volumetric mesh generation from T-spline surface representations”. *Computer-Aided Design.*

Hu, Kangkang and Yongjie Jessica Zhang (2016). “Centroidal Voronoi tessellation based polycube construction for adaptive all-hexahedral mesh generation”. *Computer Methods in Applied Mechanics and Engineering* 305, pp. 405–421.

Kiazyk, Stephen, Sébastien Loriot, and Éric Colin de Verdière (2016). “Triangulated Surface Mesh Shortest Paths”. *CGAL User and Reference Manual.* 4.9. CGAL Editorial Board.

Lai, Yicong et al. (2016). “Rhino 3D to Abaqus: A T-Spline Based Isogeometric Analysis Software Framework”. *Advances in Computational Fluid-Structure Interaction and Flow Simulation: New Methods and Challenging Computations.* Ed. by Yuri Bazilevs and Kenji Takizawa. Cham: Springer International Publishing, pp. 271–281.

Lyon, Max, David Bommes, and Leif Kobbelt (2016). “HexEx: robust hexahedral mesh extraction”. *ACM Transactions on Graphics (TOG)* 35.4, p. 123.

Massarwi, Fady and Gershon Elber (2016). “A B-spline based framework for volumetric object modeling”. *Computer-Aided Design* 78, pp. 36–47.

Saboret, Laurent, Pierre Alliez, and Bruno Lévy (2016). “Triangulated Surface Mesh Parameterization”. *CGAL User and Reference Manual.* 4.9. CGAL Editorial Board.

Sokolov, Dmitry et al. (2016). “Hexahedral-dominant meshing”. *ACM Transactions on Graphics (TOG)* 35.5, p. 157.

Vy, Phuoc et al. (2016). “Review of patient-specific simulations of transcatheter aortic valve implantation”. *International Journal of Advances in Engineering Sciences and Applied Mathematics* 8.1, pp. 2–24.

Al Akhras, H et al. (2017). “Towards an automatic isogeometric analysis suitable trivariate models generation – Application to geometric parametric analysis”. *Computer Methods in Applied Mechanics and Engineering* 316, pp. 623–645.

Beaufort, Pierre-Alexandre et al. (2017). "Computing cross fields A PDE approach based on the Ginzburg-Landau theory". *Procedia Engineering* 203, pp. 219–231.

Campen, Marcel (2017). "Partitioning Surfaces Into Quadrilateral Patches: A Survey". *Computer Graphics Forum.*

Campen, Marcel and Denis Zorin (2017). "Similarity Maps and Field-Guided T-Splines: a Perfect Couple". *ACM Trans. Graph* 36.4.

Kamensky, David et al. (2017). "Immersogeometric cardiovascular fluid–structure interaction analysis with divergence-conforming B-splines". *Computer methods in applied mechanics and engineering* 314, pp. 408–472.

Lai, Yicong et al. (2017). "Integrating CAD with Abaqus: A practical isogeometric analysis software platform for industrial applications". *Computers & Mathematics with Applications.*

Lei, Na et al. (2017). "Quadrilateral and hexahedral mesh generation based on surface foliation theory". *Computer Methods in Applied Mechanics and Engineering* 316, pp. 758–781.

Lu, Ye (2017). "Construction d'abaques numériques dédiés aux études paramétriques du procédé de soudage par des méthodes de réduction de modèles espace-temps". PhD thesis. Université de Lyon.

Maquart, G et al. (2017). "Backbending in the pear-shaped Th 90 223 nucleus: Evidence of a high-spin octupole to quadrupole shape transition in the actinides". *Physical Review C* 95.3, p. 034304.

McNeel, Robert (2017a). *Grasshopper for Rhinocéros 5.* https://www.grasshopper3d.com/, 2017.

— (2017b). *Rhinocéros 5 3D.* https://www.rhino3d.com/, 2017.

— (2017c). *Rhinocommon DLL Documentation.* https://developer.rhino3d.com/api/, 2017.

Ray, Nicolas et al. (2017). "Hexahedral Meshing: Mind the Gap!"

Solomon, Justin, Amir Vaxman, and David Bommes (May 2017). "Boundary Element Octahedral Fields in Volumes". *ACM Trans. Graph.* 36.3, 28:1–28:16.

Chemin, Alexandre et al. (2018). "Representing three-dimensional cross fields using 4th order tensors". *arXiv preprint arXiv:1808.03999, (2018).*

Hirschler, Thibaut et al. (2018). "Isogeometric sizing and shape optimization of thin structures with a solid-shell approach". *Structural and Multidisciplinary Optimization*, pp. –.

Huang, Jingwei et al. (2018). "QuadriFlow: A Scalable and Robust Method for Quadrangulation". *Computer Graphics Forum.* Vol. 37. 5. Wiley Online Library, pp. 147–160.

Liu, Heng et al. (2018). "Singularity-constrained octahedral fields for hexahedral meshing". *ACM Transactions on Graphics (TOG)* 37.4, p. 93.

Lu, Y, N Blal, and A Gravouil (2018). "Adaptive sparse grid based HOPGD: Toward a nonintrusive strategy for constructing space-time welding computational vademecum". *International Journal for Numerical Methods in Engineering* 114.13, pp. 1438–1461.

Luboz, Vincent et al. (2018). “Personalized modeling for real-time pressure ulcer prevention in sitting posture”. *Journal of tissue viability* 27.1, pp. 54–58.

Maquart, Tristan (2018). “Disk-sphere field duality theorem”. *ArXiv : (2018).*

Occelli, Matthieu (2018). “Explicit Dynamics Isogeometric Analysis. LR B-Splines Implementation in the Radioss solver”. PhD thesis. INSA de LYON, École Doctorale MEGA ED 162.

Reberol, Maxence (2018). “Maillages hex-dominants: génération, simulation et évaluation”. PhD thesis. Université de Lorraine.

Coreform, LLC (2019). *Coreform Technologies*. https://coreform.com/, 2019.

Derek, Thomas et al. (2019). *U-splines: splines over unstructured meshes*. https://coreform.com/.

Geomiso (2019). *Geomiso, design and engineering remastered: fully integrated CAD/CAE software based on the new isogeometric method*. https://www.geomiso.com/, 2019.

Maquart, Tristan et al. (2019a). “3D B-Rep model partitioning and quadrilateral meshing for geometric parametric analysis”. *International Journal for Numerical Methods In Engineering: Submitted (2019).*

Maquart, Tristan et al. (2019b). “3D volumetric isotopological meshing for finite element and isogeometric based reduced order modeling”. *Computer Methods in Applied Mechanics and Engineering: Submitted (2019).*

Maquart, Tristan et al. (2019c). “Surface to volumetric manifolds for 3D structured mesh generation”. *Unsubmitted: June 11, 2019.*

Département FEDORA – INSA Lyon - Ecoles Doctorales – Quinquennal 2016-2020

SIGLE	ECOLE DOCTORALE	NOM ET COORDONNEES DU RESPONSABLE
CHIMIE	**CHIMIE DE LYON** **http://www.edchimie-lyon.fr** Sec. : Renée EL MELHEM Bât. Blaise PASCAL, 3e étage **secretariat@edchimie-lyon.fr** INSA : R. GOURDON	M. Stéphane DANIELE Institut de recherches sur la catalyse et l'environnement de Lyon IRCELYON-UMR 5256 Équipe CDFA 2 Avenue Albert EINSTEIN 69 626 Villeurbanne CEDEX **directeur@edchimie-lyon.fr**
E.E.A.	**ÉLECTRONIQUE, ÉLECTROTECHNIQUE, AUTOMATIQUE** **http://edeea.ec-lyon.fr** Sec. : M.C. HAVGOUDOUKIAN **ecole-doctorale.eea@ec-lyon.fr**	M. Gérard SCORLETTI École Centrale de Lyon 36 Avenue Guy DE COLLONGUE 69 134 Écully Tél : 04.72.18.60.97 Fax 04.78.43.37.17 **gerard.scorletti@ec-lyon.fr**
E2M2	**ÉVOLUTION, ÉCOSYSTÈME, MICROBIOLOGIE, MODÉLISATION** **http://e2m2.universite-lyon.fr** Sec. : Sylvie ROBERJOT Bât. Atrium, UCB Lyon 1 Tél : 04.72.44.83.62 INSA : H. CHARLES **secretariat.e2m2@univ-lyon1.fr**	M. Philippe NORMAND UMR 5557 Lab. d'Ecologie Microbienne Université Claude Bernard Lyon 1 Bâtiment Mendel 43, boulevard du 11 Novembre 1918 69 622 Villeurbanne CEDEX **philippe.normand@univ-lyon1.fr**
EDISS	**INTERDISCIPLINAIRE SCIENCES-SANTÉ** **http://www.ediss-lyon.fr** Sec. : Sylvie ROBERJOT Bât. Atrium, UCB Lyon 1 Tél : 04.72.44.83.62 INSA : M. LAGARDE **secretariat.ediss@univ-lyon1.fr**	Mme Emmanuelle CANET-SOULAS INSERM U1060, CarMeN lab, Univ. Lyon 1 Bâtiment IMBL 11 Avenue Jean CAPELLE INSA de Lyon 69 621 Villeurbanne Tél : 04.72.68.49.09 Fax : 04.72.68.49.16 **emmanuelle.canet@univ-lyon1.fr**
INFOMATHS	**INFORMATIQUE ET MATHÉMATIQUES** **http://edinfomaths.universite-lyon.fr** Sec. : Renée EL MELHEM Bât. Blaise PASCAL, 3e étage Tél : 04.72.43.80.46 **infomaths@univ-lyon1.fr**	M. Luca ZAMBONI Bât. Braconnier 43 Boulevard du 11 novembre 1918 69 622 Villeurbanne CEDEX Tél : 04.26.23.45.52 **zamboni@maths.univ-lyon1.fr**
Matériaux	**MATÉRIAUX DE LYON** **http://ed34.universite-lyon.fr** Sec. : Stéphanie CAUVIN Tél : 04.72.43.71.70 Bât. Direction **ed.materiaux@insa-lyon.fr**	M. Jean-Yves BUFFIÈRE INSA de Lyon MATEIS - Bât. Saint-Exupéry 7 Avenue Jean CAPELLE 69 621 Villeurbanne CEDEX Tél : 04.72.43.71.70 Fax : 04.72.43.85.28 **jean-yves.buffiere@insa-lyon.fr**
MEGA	**MÉCANIQUE, ÉNERGÉTIQUE, GÉNIE CIVIL, ACOUSTIQUE** **http://edmega.universite-lyon.fr** Sec. : Stéphanie CAUVIN Tél : 04.72.43.71.70 Bât. Direction **mega@insa-lyon.fr**	M. Jocelyn BONJOUR INSA de Lyon Laboratoire CETHIL Bâtiment Sadi-Carnot 9, rue de la Physique 69 621 Villeurbanne CEDEX **jocelyn.bonjour@insa-lyon.fr**
ScSo	**ScSo*** **http://ed483.univ-lyon2.fr** Sec. : Véronique GUICHARD INSA : J.Y. TOUSSAINT Tél : 04.78.69.72.76 **veronique.cervantes@univ-lyon2.fr**	M. Christian MONTES Université Lyon 2 86 Rue Pasteur 69 365 Lyon CEDEX 07 **christian.montes@univ-lyon2.fr**

*ScSo : Histoire, Géographie, Aménagement, Urbanisme, Archéologie, Science politique, Sociologie, Anthropologie

FOLIO ADMINISTRATIF

THESE DE L'UNIVERSITE DE LYON OPEREE AU SEIN DE L'INSA LYON

NOM : MAQUART DATE de SOUTENANCE : 06/06/2019

Prénoms : Tristan François

TITRE : **TRIVARIATE MODELS GENERATION FROM UNSTRUCTURED SURFACE MANIFOLDS FOR ISOGEOMETRIC ANALYSIS – APPLICATION TO REDUCED ORDER MODELING WITH GEOMETRIC PARAMETERS**

NATURE : Doctorat Numéro d'ordre : 2019LYSEI033

Ecole doctorale : MEGA ED162

Spécialité : Génie Mécanique

RESUME :
This work presents a generic framework to construct trivariate isogeometric meshes of complicated geometry and arbitrary topology required for reduced order model applications. Indeed, structured meshes such as isogeometric or pure hexahedral ones are difficult to obtain in an automatic manner. Statistical shape analysis and reduced order modeling require structured and ordered data to be efficient. For that purpose, we use the triangulated solid 3D model's boundary provided from B-Rep CAD (Boundary-Representation in Computer Aided Design) models. Firstable, the workflow includes an integration of a geometry-feature-aware pants-to-cuboids decomposition algorithm. The input triangulated mesh is decomposed into a set of cuboids in two steps: pants decomposition and cuboid decomposition. Cuboid decomposition splits a surface into a set of quadrilateral patches which can define a volumetric layout of the associated boundary surface. Cross fields, i.e., 4-symmetry direction fields are used to guide a surface aligned global parameterization. Optimizing this parameterization, patches of the quadrilateral layout inherited from the cuboid decomposition are re-positioned on the surface in a way to achieve low overall distortion. The optimization process is thought to design cross fields with topological and geometrical constraints. Using the optimized cuboid decomposition, a volumetric layout is extracted. Based on the global parameterization and the structured volumetric layout previously computed, a trivariate isogeometric parameterization is deducted. Learning generalized forms of theorems in the topology field, invariant topological properties are analyzed throughout the proposed process. To finish, for different geometrical instances with the same topology but different geometries, our method allows to have the same representation: trivariate isogeometric isotopological meshes holding the same connectivity. The efficiency and the robustness of the proposed approach are illustrated through several examples of reduced order models using IGA (IsoGeometric Analysis).

MOTS-CLÉS : IsoGeometric Analysis; Reduced Order Modeling; Statistical Shape Analysis; Topology; Parameterization; Cuboid Decomposition; Parametric Geometry.

Laboratoire(s) de recherche : Laboratoire de Mécanique des Contacts et des Structures
Université de Lyon, CNRS, INSA-Lyon UMR5259
27 bis avenue Jean Capelle - F69621 Villeurbanne Cedex France

Directeur de thèse : Thomas ELGUEDJ
Co-directeur de thèse : Anthony GRAVOUIL
Co-encadrant de thèse : Michel ROCHETTE

Président de jury : David NERON

Composition du jury :

LEGRAIN, Grégory	Maître de conférences HDR, École Centrale de Nantes	Rapporteur
RASSINEUX, Alain	Professeur, UTC Compiègne	Rapporteur
BARANGER, Thouraya	Professeur, UCBL	Examinatrice
NERON, David	Professeur, ENS Paris-Saclay	Examinateur et président
REMACLE, Jean-François	Professeur, Université Catholique de Louvain	Examinateur
ELGUEDJ, Thomas	Professeur, INSA de Lyon	Directeur de thèse
GRAVOUIL, Anthony	Professeur, INSA de Lyon	Invité et co-directeur de thèse
ROCHETTE, Michel	Docteur, ANSYS France	Invité et co-encadrant de thèse